NOVA SCHOOL OF SCIENCE & TECHNOLOGY

DEPARTAMENT OF PHYSICS

Solar Concentrators and Solar-pumped Lasers

Dário Machado Garcia

Master in Physics Engineering

DOCTORATE IN PHYSICS

NOVA University of Lisbon

March, 2023

NOVA SCHOOL OF SCIENCE & TECHNOLOGY

DEPARTAMENT OF PHYSICS

Solar Concentrators and Solar-pumped Lasers

Dário Machado Garcia

Master in Physics Engineering

Adviser: Dawei Liang
Associate Professor with Habilitation, Faculdade de Ciências e Tecnologia da Universidade Nova de Lisboa

Co-advisers: Paulo Morais,
Senior Researcher, Portuguese Institute of Welding and Quality

Examination Committee:

Chair: Orlando Manuel Neves Duarte Teodoro
Full Professor, Faculdade de Ciências e Tecnologia da Universidade Nova de Lisboa

Rapporteurs: Gonçalo Nuno Marmelo Foito Figueira
Associate Professor, Instituto Superior Técnico da Universidade de Lisboa

João Miguel Pinto Coelho
Auxiliar Researcher, Faculdade de Ciências da Universidade de Lisboa

Adviser: Dawei Liang
Associate Professor with Habilitation, Faculdade de Ciências e Tecnologia da Universidade Nova de Lisboa

Members: Joana Isabel Lázaro Almeida
Auxiliar Researcher, Faculdade de Ciências e Tecnologia da Universidade Nova de Lisboa

Orlando Manuel Neves Duarte Teodoro
Full Professor, Faculdade de Ciências e Tecnologia da Universidade Nova de Lisboa

DOCTORATE IN PHYSICS

NOVA University of Lisbon
March, 2023

Solar Concentrators and Solar-pumped Lasers

ACKNOWLEDGMENTS

This long journey would not have been possible without the help and support of many people. So, I would like to express my sincere gratitude to:

My supervisor, Prof. Dawei Liang. I would like to thank for his constant support, dedication, and friendship demonstrated during all these years. This was a rewarding experience, not only at scientific level but also at personal level, that will influence me throughout my life.

The thesis committee members: Prof. Orlando Teodoro, Prof. Gonçalo Figueira, Prof. João Coelho and Prof. Maria Adelaide Jesus, for their insightful comments and suggestions from various perspectives.

My colleagues in the Solar Laser Laboratory, Joana Almeida, Cláudia Vistas, Bruno Tibúrcio, Miguel Catela and Hugo Costa for their valuable support and honest acquaintanceship.

Dr. Emmanuel Guillot as the coordinator of SFERA II and SFERAIII European project in PROMES-CNRS, for the opportunity to access the solar facilities.

DAEPHYS and the Science and Technology Foundation of Portuguese Ministry of Science, Technology and Higher Education, for the attribution of the PhD fellowship.

All the Professors of FCT UNL that have provided me the necessary up to date knowledge to confront this PhD and to the futures issues to come.

Lastly, to my parents and siblings for all the sacrifices that have made on my behalf.

"I made it by being tougher than the toughies, and smarter than the smarties!
And I made it square!" (Carl Barks)

ABSTRACT

Innovative substitutions for Fresnel lenses concentrators by Elliptical shaped Fresnel lens (ESFL) and parabolic concentrators by ring array concentrator (RAC) models are presented, as well as, advances of solar-pumped lasers of Ce:Nd:YAG operation during a clean and clouded weather.

The design of the ESFL and RAC were modelled into Zemax® non-sequential ray-tracing software from well-defined mathematical equations. Most of the key parameters were analysed and the resulting outputs were compared and documented in publications.

The design parameters for solar-pumped lasers were optimized using Zemax®, and then the LASCAD™ laser cavity system software was used to further optimize the laser resonator parameters. A solar laser prototype was built with an active medium of Ce:Nd:YAG and tested using a heliostat-parabolic mirror system at both NOVA University of Lisbon and Procédés, Matériaux et Énergie Solaire - Centre National de la Recherche Scientifique (PROMES-CNRS) in Odeillo-Font Romeu, France.

The ESFL offers a 4.58 W/mm^2 increase in solar flux concentration compared to a Fresnel lens, which only achieves 2.66 W/mm^2 at the same size and focal distance. A 3.14 m^2 RAC with a focal length of 300 mm can capture over 18 W/m^2.

The first recorded Ce:Nd:YAG solar laser operating with a small collection area of 0.293 m^2 at the NOVA facility, produced a multimode output power of 11.2 W, resulting in a solar-to-laser power conversion efficiency of 3.37%, with a minimum threshold pump power of 66 W. The MSSF parabolic mirror from PROMES-CNRS achieved a lower threshold pump power of 32.4 W using a smaller collection area of 0.075 m^2, and during cloudy weather, a threshold pump power was further reduced to 29.2 W. Furthermore, cloud interference improved the solar-to-laser conversion efficiency to 6.32%, nearly tripling the 2.32% efficiency on a clear sky, while the solar laser conversion efficiency of 21.47 W/m^2 was nearly twice the value of 12.62 W/m^2 on a clear sky.

The research efforts performed during this work are explained. Experimental results are discussed, and future suggestions are proposed.

Keywords: Solar concentrator, Solar-pumped laser, Ce:Nd:YAG, Elliptical shaped Fresnel lens, Ring array concentrator

RESUMO

Inovações para substituições de concentradores de lentes de Fresnel por lentes de Fresnel elípticas (ESFL) e concentradores parabólicos por modelos de concentradores de matriz de anéis (RAC) são apresentados, bem como avanços de lasers solares de Ce:Nd:YAG operando no limiar mais baixo e durante o clima nublado. O projeto do ESFL e do RAC foi modelado incorporando as equações recém-deduzidas no software de rastreamento de raios não sequencial Zemax®. A maioria dos principais parâmetros foi analisada e as saídas resultantes foram comparadas e documentadas em publicações. Em relação aos lasers solares bombeados, todos os parâmetros de projeto foram otimizados e adaptados no Zemax® e o software de sistema de cavidade a laser LASCAD™ foi usado para otimizar os parâmetros do ressonador a laser. O protótipo de laser solar com o meio ativo de Ce:Nd:YAG foi construído e testado na instalação helióstato-parabólica na Universidade Nova de Lisboa e no forno solar de tamanho médio (MSSF) no Procédés, Matériaux et Énergie Solaire - Centre National de la Recherche Scientifique (PROMES-CNRS) em Odeillo-Font Romeu, França.

O ESFL oferece um aumento de 4,58 W/mm^2 na concentração de fluxo solar em comparação com uma lente de Fresnel, que alcança apenas 2,66 W/mm^2 no mesmo tamanho e distância focal. Um RAC de 3,14 m^2 com uma distância focal de 300 mm pode capturar mais de 18 W/m^2. O primeiro laser solar Ce:Nd:YAG registrado, operando com uma pequena área de coleta de 0,293 m^2 na instalação da NOVA, produziu uma potência de saída multimodo de 11,2 W, resultando em uma eficiência de conversão de energia solar para laser de 3,37%, com uma potência mínima de bombeamento de 66 W. O espelho parabólico MSSF do PROMES-CNRS alcançou uma potência de bombeamento de limiar mais baixa de 32,4 W usando uma área de coleta de 0,075 m^2 e, durante o tempo nublado, uma potência de bombeamento de limiar de 29,2 W foi registada. Além disso, a interferência das nuvens melhorou a eficiência de conversão de energia solar para laser em 6,32%, quase triplicando a eficiência de 2,32% em um céu claro, enquanto a eficiência de conversão de energia do laser solar de 21,47 W/m^2 foi quase o dobro do valor de 12,62 W/m^2 em um céu claro.

Palavras chave: Concentrador solar, Laser bombado por luz solar, lentes Fresnel de formato elíptico, concentrador de matriz de anel

CONTENTS

LIST OF FIGURES

LIST OF TABLES

ACRONYMS

AM1.5	Air Mass 1.5 atmospheres
ANU	Australian National University
ASTM	American Society for Testing and Materials
AR	Anti Reflection
AUTOCAD®	AUTO Computer Aided Design
BPM	Beam Propagation Method
CAD	Computer Aid Designs
CE	Collection efficiency
Ce:Nd:YAG	Cerium:Neodymium:Yttrium Aluminum Garnet
CENIM	Centro Nacional de Investigaciones Metalúrgicas
CSP	Concentrated solar plant
ESFL	Elliptical-Shaped Fresnel Lens
FEA	Finite Element Analysis
FFT	Fast Fourier Transform
FWHM	Full Width at Half Maximum
HFSF	High Flux Solar Furnace
HR	High reflection
IGES	Initial Graphics Exchange Specification
LASCAD	LASer Cavity Analysis and Design
MSSF	Medium Size Solar Furnace
MWSF	Mega Watt Solar Furnace
NIR	Near Infra-Red
NSC	Non-Sequential Component

NSTTF	National Solar Thermal Test Facility
PMMA	Poly Methyl Methacrylate
PR	Partial Reflection
PROMES-CNRS	Procédés, Matériaux et Énergie Solaire - Centre National de la Recherche Scientifique
PSA-CIEMAT	Plataforma Solar de Almería- Centro de Investigaciones Energéticas
RoC	Radius of Curvature
SAT	Standard ACIS Text
SE	Slope efficiency
SLCE	Solar-to-laser conversion efficiency
STEP	Standard for the Exchange of Product Data
STL	Standard Triangle Language
TEM	Transverse mode
UV	Ultraviolet
ZOF	Zemax® Object Format
ZPL	Zemax® Programming Language

SYMBOLS

A	Effective collection area
a, r	Radial aperture
a_{in}	Ring inner aperture (RAC)
a_{out}	Ring outer aperture (RAC)
A_r	Surface area
B	Constant Probability
c	Curvature
cw	Continuous wave
c_l	Speed of light
d_a	Accepted effective size
d_E	Effective size of the solar-terrestrial image
D_{loss}	Diffraction loss
d_t	Mirror/lens thickens (RAC/ESFL)
d_w	Initial ring width variable (RAC)
E	Energy
G_x G_y	Gaussian distribution in X and Y axis
h	Planck constant
h_f	Focal length
h_l	Lens height (ESFL)
I	Intensity
k	Conic constant
l	Length
N, n	Integer number
N_i	Population

n_λ	Refraction index
$\varnothing$	diameter
P	Power
R	Base radius (RAC)
$r_{fresnel}$	Fresnel lens radius
T	Transmission
T_h	Threshold power
v	Phase velocity
x,y,z	Coordinates
z	Sag
α_l	Aspheric coefficients
α_s	Scattering coefficient
α_λ	Absorption coefficient of the material
δ_{RMS}	Root-Mean-Square Width
$\delta\omega$	Division angle (ESFL)
ε	Emissivity
η	Efficiency
θ	Angle
θ_a	Solar acceptance half-angle
θ_E	Terrestrial solar half-angle
θ_p	Pitch angle
λ	Wavelength
$\rho(\lambda)$	Energy density
σ^2	Standard deviation
τ	Relaxation rate
τ	Rod thickness
φ	Angular rotation
ω	Aperture angle or rim angle

1

INTRODUCTION

1.1 Background and motivation

The utilization of solar energy is of utmost importance in today's world as it is a crucial source of renewable energy. This sustainable energy source offers several advantages, such as being cost-effective, accessible, and eco-friendly as it does not emit harmful greenhouse gases. Additionally, the technology used to harness solar energy is continuously improving, making it a promising option for the future. The adoption of solar energy can contribute significantly to a sustainable future, making it an essential option for energy generation.

Solar concentrators are a critical technology in the renewable energy industry as they increase the efficiency of solar power generation. These devices concentrate sunlight onto a small area, producing a higher concentration of solar energy that can be utilized for various applications. Concentrated solar power (CSP) plants use this technology to generate electricity, which can be stored and distributed even when the sun is not shining. This makes solar concentrators a reliable and continuous source of energy that can reduce our dependence on fossil fuels and decrease carbon emissions. Furthermore, solar concentrators can be used for heating and cooling, making them suitable for a range of industrial and residential applications. In conclusion, solar concentrators have the potential to revolutionize the way we generate and use energy, making them a vital technology for our lives.

Researchers, power companies, and policymakers are interested in the ability of concentrating solar power to generate large amounts of continuous electricity, which can overcome the intermittency issues associated with solar resources. One common approach to identifying potential locations for the CSP plants worldwide is by analysing the global distribution of Direct Normal Irradiance (DNI). This analysis reveals that the "Sun Belt" regions of North Africa, the Middle East, the Mediterranean, and American continent, are highly suitable for CSP plants due to their abundant solar radiation. These regions' large land areas with high solar irradiation offer an excellent opportunity to install multiple solar-energy harvesting systems.

Solar research facilities provide a platform for both academic and industrial researchers to investigate and test commercial prototypes in various fields. These fields include solar thermal electricity generation technologies [1, 2], solar fuel production such as H_2, synthesis gas, liquid and gas hydrocarbons [3, 4], cycles for chemical storage of solar energy using ZnO, CeO_2, iron, silica, and other materials [5], solar water treatment techniques such as desalination, disinfection, and decontamination [6, 7], solar heating and cooling of buildings [8], synthesis of high-value materials and coatings of nanomaterials, new ceramics or metals, foams, and catalytic layers [9], high-flux photochemistry [10], photo-physics, characterization of materials under extreme conditions [11], and solar pumping of laser for industrial and space applications[12, 13].

To achieve the goals mentioned above, this study aimed to investigate innovative solar concentration systems, namely the ring array concentrator (RAC) and elliptical shaped Fresnel lens (ESFL), as alternatives to the commonly used parabolic mirrors and Fresnel lenses. The potential benefits of these novel concentrators in various applications were explored. Additionally, the study proposed the utilization of a solar pumping prototype with Ce:Nd:YAG in an end-side-pump configuration. The design and parameters of the solar furnace were conceptualized in Mathematica and numerically optimized using Zemax®. The findings of this research were published in peer-reviewed journals.

Solar lasers are an emerging technology for applications where sunlight is abundant and other energy sources are scarce, particularly in space-based operations. Solid-state lasers can be pumped by solar energy either directly or indirectly, with direct solar pumping being more efficient, simple, and reliable. However, semiconductor arrays used in indirect pumping (light converted with electricity) have generally a limited lifetimes and performance degradation over time. Direct solar pumping of solid-state lasers can overcome these limitations and enable reliable space-borne laser operation over multiple years. In space, solar energy is a continuous source of energy, and solar lasers offer potential applications in remote sensing, deep space communications, wireless space power laser beaming [14], asteroid deflection, fuel-free photonic thrusters [15], and orbital space debris removal. Solar lasers also have potential terrestrial applications in material processing, micro/nano-material production, and renewable energy cycles, such as the renewable magnesium-hydrogen cycle [16]. Mg has a high energy storage density, and when combined with water, produces both H_2 and thermal energy. However, temperatures exceeding 4000 K are required for MgO reduction, and solar-powered lasers with excellent beam quality can easily reach this temperature, refining MgO back to Mg for fuel cell vehicle applications [17]. Overall, solar lasers present an exciting opportunity for sustainable energy production and innovation in both space and terrestrial applications.

The design of solar pumped laser was firstly numerically optimized through Zemax® then LASCAD™ software, respectively. The set-ups design and build in Lisbon, according to the optimized parameters of the numerical analysis. The testing of the solar laser performance was carried out at NOVA university and at PROMES-CNRS, through the participation in R&D projects supported by SFERA III projects (Solar Facilities for the European Research Area, 7th Framework Program of the EU). Both facilities collect the solar energy through a heliostat-parabolic parabolic system. At 2022, the solar laser prototype was performed in February at the NOVA facility, then in September at PROMES-CNRS.

Significant progresses in both solar laser efficiency, threshold power reduction through small collection area and its comparison under cloudless/cloudy sky are explained in detail in Chapter 7.

1.2 Outline

This dissertation is divided into 8 chapters:

Chapter 2 covers the fundamental concepts of solar concentrators. The generalized relationship of the Sun with the concentrating media are described.

Chapter 3 presents the modelling tools for the numerical optimization of the proposed solar concentrators and laser schemes.

Chapter 4 provides a comprehensive overview of the Elliptical shaped Fresnel lens (ESFL) model, as reported in the paper XIII of the list of publication.

Chapter 5 provides a comprehensive overview of the Ring Array Concentrator model, as reported in the paper XXVIII and XIX of the list of publication.

Chapter 6 covers the fundamental concepts of solid-state lasers. The solar-pumped lasers concept is also described, including an overview of the suitable laser materials for solar-pumped lasers and a State-of-the Art.

Chapter 7 describes the efforts for enhancing the solar-pumped laser with Ce:Nd:YAG under both cloudless and cloudy conditions for both TEM_{00} mode and multimode laser output, as reported in the paper IX, X, and XI of the list of publication.

Chapter 8 is the conclusion and the futures vision.

The highlights and publications obtained during the PhD project are presented in the Annexes.

2

SOLAR ENERGY AND CONCENTRATION SYSTEMS

2.1 General concept

The use of optical devices such as concentrators offers the advantage of collecting solar energy into a concentrated form, which is highly beneficial for certain high-temperature applications. However, the degree of energy concentration achieved is subject to several uncontrollable factors, such as the unpredictable atmospheric conditions on Earth or the degradation of the concentrator material over time.
The speed of light is a constant of 299792458 m/s when traveling in a vacuum, with a refractive index of n_λ=1. When the propagating ray enters a different refractive material (n_λ>1), it reduces the phase velocity by $v=c/n_\lambda$. Typical values of n_λ for air at normal pressure are around 1.0003, 1.33 for water, and 1.45-1.8 for glass and plastics, respectively. Moreover, the n_λ is different for each wavelength.

2.1.1 Snell's law

Snell's law of refraction follows the principle of least time (from Fermat's principle). The refracted incident ray travels from the interface between the refractive index media of n_1 and n_2, as shown in Equation (2.1).

$$n_i \, sin(\theta_i) = n_t \, sin(\theta_t) \tag{2.1}$$

where θ_i is the incidence angle normal at medium *i* and the refracted angle θ_t measured at the normal on medium *t*. The incident beam splits into a reflected beam and a transmitted beam, both subject to Snell's Law, as shown in Figure 2.1.

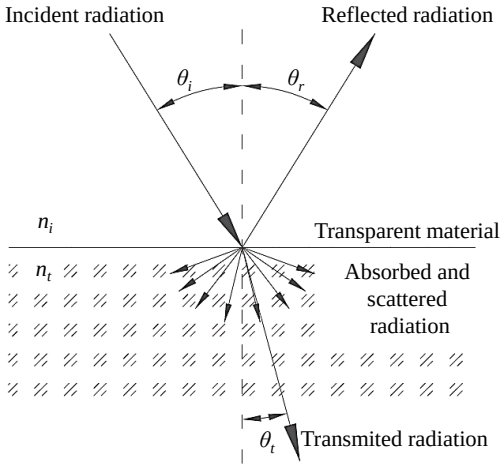

Figure 2.1 — Incident radiation is incoming from angle θ_i normal to the surface of the material. Reflected radiation bouncing with θ_r (same value as θ_i). The transmitted radiation shifts θ_t in its trajectory due to snell's law. The intensity of the transmitted radiation is reduced due to the absorption and scattering nature of the refractive medium.

2.1.1.1 Refraction

A portion of incident radiation is transmitted through the next interface from the previous. If the second interface (medium) has the same refraction index (i.e., $n_i = n_t$), then the ray continues to travel without changing its course, i.e., $\theta_i = \theta_t$. If $n_i < n_t$, due to Snell's law, then the refractive radiation will have a slight bent or a deviation of the angle about the normal axis, as shown in Figure 2.1. Refractive materials such as fused silica lenses with $n_\lambda \approx 1.47$ and poly methyl methacrylate (PMMA) at $n_\lambda \approx 1.49$ are commonly used in solar-pumped lasers.

2.1.1.2 Absorption

Light with a certain energy, intensity, and wavelength passing through a medium (other than in vacuum) would have small or sizable portions of its energy absorbed by the material. The transmitted wavelength intensity ($I_{t(\lambda)}$) is proportional to the standard exponential decay of the incident intensity ($I_{i(\lambda)}$) by the coefficient of absorption of the material (α_λ) at a depth length (l):

$$I_t(\lambda) = I_i(\lambda)\, e^{-\alpha_\lambda l} \tag{2.2}$$

2.1.1.3 Reflection

The reflected radiation remains the same n_i section after interacting with the reflective medium. A small portion of the reflected energy is lost due to the absorption of the material. The reflected angle is mostly the same as the angle of incidence, $\theta_i = \theta_r$.

2.1.2 Mirror

The mirror is an optical device with the primary function of reflecting light. Most mirrors found in the market are flat and through special demand, curved-shaped mirrors can be obtained. The amount of energy reflected by the mirror measures the reflectivity, i.e., the amount of energy reflected compared to the initial energy. Front surface mirrors (or first surface mirrors) are metal-coated mirrors with a thin

layer of metal coating, mostly produced by vacuum evaporation or by a sputtering technique. The metallic coating adheres to a substrate, mostly glass (fused silica), as shown in Figure 2.2 a). Mirror coating of aluminium, silver, or gold is commonly found in the market, and less common materials such as beryllium, copper, chrome, or nickel/chrome alloys are more difficult to acquire. Dielectric layers are often used to protect or/and enhanced the metallic coating. Metallic mirror (first surface mirror) provides larger reflective broadband, negligible low achromatic dispersion, and weak angular dependency on reflectivity.

Another type of mirror is the back surface metallic mirror, which has an added protective glass layer on top of the metallic surface, as shown in Figure 2.2 b). Household mirrors are silver coated on the back.

Advantages of first surface mirrors compared to back surface mirrors:

- The substrate of the mirror does not contribute to the reduction of reflectivity by absorption in certain broadband regions. This type of mirror has a much lower loss of reflection band in the infrared region.
- Wavefront distortion from reflection caused by inhomogeneities of the substrate cannot occur.
- In non-normal incidence light. It does not generate ghost images due to the weaker front surface reflection from the mirror surface.
- Light in normal incidence. It does not cause strong chromatic dispersion based on the interference contribution from the front and back surface reflection of the glass substrate.

Disadvantages:

- The touched surface creates fingerprints that can easily cause oxidation. It may not be possible to clean such mirrors, losing the optical quality.
- Moisture and aggressive gases may cause oxidation in the mirror coating.
- The degradation of reflectivity in the function of time is faster than that of the back surface mirror.
- Harder to clean.

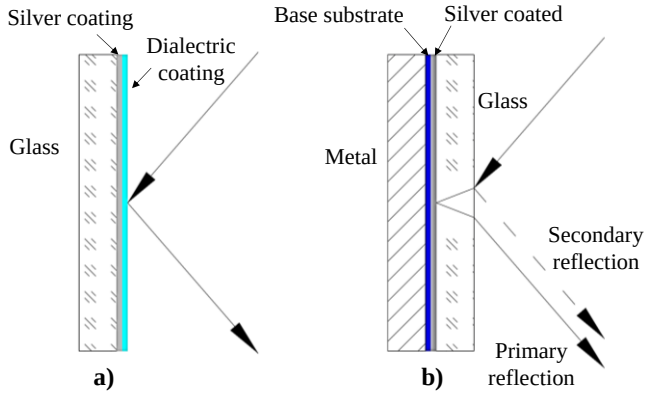

Figure 2.2 — (a) First surface and (b) back surface mirrors.

2.1.3 Solar spectrum

Figure 2.3 shows both the global and the direct reference spectra ASTM (American Society for Testing and Materials) G173 at Air Mass 1.5 (AM1.5) [18]. In Zemax®, 21 wavelengths were selected as the solar spectrum data, each normalized as a function of its weight. The weight determines the intensity/power of each solar ray, which is dependent on the power attributed to the emitting source.

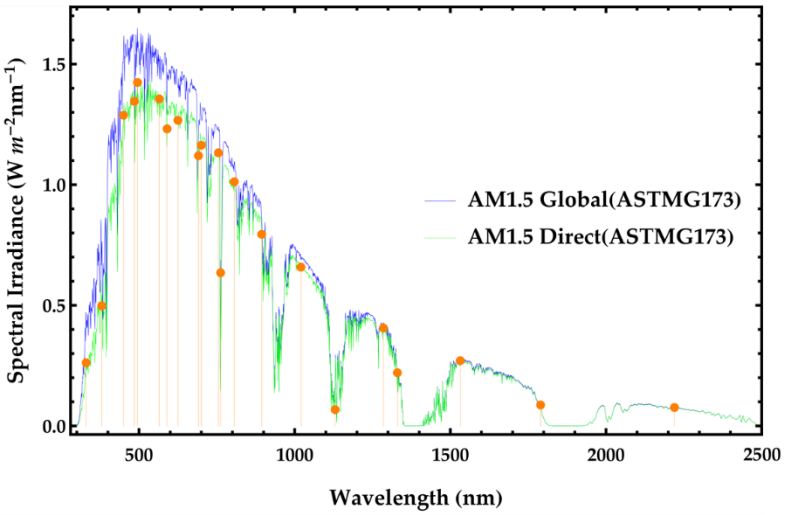

Wavelenght (nm)	Weight
330	0.18255
380	0.34675
450	0.89776
485	0.9379
495	0.99233
565	0.94473
590	0.85838
625	0.88284
691	0.78067
700	0.81098
755	0.78903
762	0.44251
806	0.70546
894	0.55348
1020	0.45887
1130	0.047092
1285	0.28281
1330	0.15369
1532	0.18845
1790	0.060518
2220	0.053409

Figure 2.3 — Global and direct solar spectra ASTMG173 at AM1.5, with the selected wavelength used for ray tracing in Zemax® and its respective weight value.

2.1.4 Sun shaped by angle

It is crucial to consider the shape of the Sun when conducting research and developing solar-based technologies. The acceptance half-angle, which determines the angle at which solar rays reach the Earth's atmosphere, is dependent on the size of the Sun and its distance from the Earth. The widely accepted value for the Sun-Earth subtended acceptance half-angle is 0.27°, which has been determined mathematically and theoretically [19, 20]. This value is commonly used by researchers in the field of solar energy concentration [3, 20-34].

The angle mentioned above is only accurate in the absence of Earth's atmosphere. When solar rays enter the atmosphere, their trajectory is significantly altered due to the law of refraction. These rays traverse different atmospheric layers, including the troposphere, stratosphere, mesosphere, and thermosphere, resulting in scattering, dispersion, and absorption. Therefore, the original solar intensity from the Sun decreases, leading to diffuse sky radiation [20]. The intensity of radiation decreases mainly due to the absorption of ozone (O_3) and water vapor in the atmosphere. Ozone absorbs at the ultraviolet band, while water vapor absorbs at the near-infrared band. The refractive index of each gaseous layer affects the refraction angle. Additionally, the acceptance of the half-angle of the Sun's rays can vary depending on various factors such as geographical location, time zone, and local atmospheric conditions, such as the presence of clouds, humidity, sand particles, and pollution in the troposphere. Thus, it is necessary for the acceptance half-angle to be greater than 0.27° at the Earth's surface, considering the intricate factors that influence the refraction of sunlight in the Earth's atmosphere. Despite this, many researchers in the field have overlooked these complex systems and instead relied on the 0.27° half-angle as the universal standard in their works [3, 20-35].

2.1.5 Sun shape Gaussian distribution

The Sun shape image can be inconsistent, and it is difficult to analyse due to unpredictable and uncontrollable atmospheric factors. The systematic and the averaging measurement of the image size approximates a near-exact representation of the image of the Sun. One of the alternative approximations was done by Vittitoe and Biggs [36], which treats the Sun as a superposition of six Gaussian terms.
The approximation of the Sun shape in Gaussian distribution form is described in Equation (2.3). This Gaussian form sets the behaviour of the Sun distribution of the solar radiation emitting from a generic source:

$$I(l,m) \approx I_0 e^{-(G_x l^2 + G_y m^2)} \tag{2.3}$$

Where l and m are the direction cosines of the rays in the X and Y axis direction with G_x and G_y as the Gaussian distribution in function of the root-mean-square width (δ_{RMS}), given by Equation (2.4):

$$G_x = G_y = \frac{1}{2 \times {\delta_{RMS}}^2} \tag{2.4}$$

The larger the value of G_x and G_y, the narrower the distribution in that respective direction. The overall distribution collimated form when both G_x and G_y are infinite (values of zero in Zemax®).
The δ_{RMS} described and obtained by [36], where the correlation of δ_{RMS} with the solar irradiation (I) is shown in Figure 2.4, where the curve is given by

$$\delta_{RMS} \times 10^3 \approx 3.7648 - 0.0038413(I - 1000) + 1.5923 \times 10^{-5}(I - 1000)^2 \tag{2.5}$$

with I is the solar irradiance in W/m^2. This curve is a generalized reference to the Sun's shape at a given solar irradiance. The actual δ_{RMS} value may change dependently not only through the current measured irradiation, but also the time and location where the measurement was carried out, as referenced in [36].

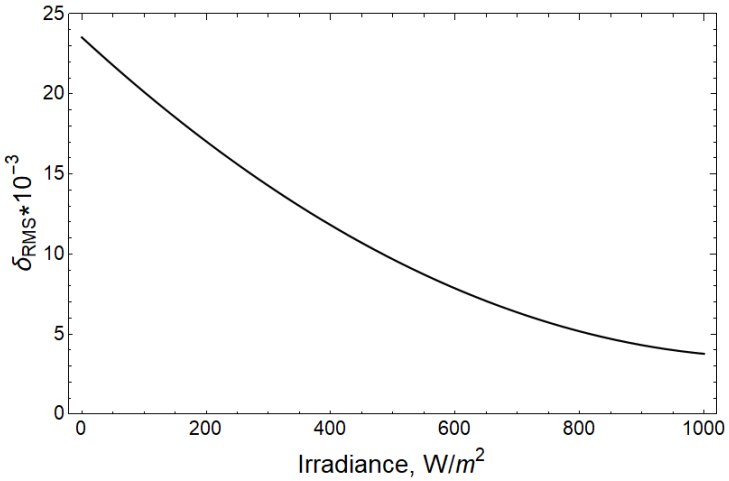

Figure 2.4 — Variation of δ_{RMS} at different solar irradiances.

Zemax® ray tracing software approximates the Sun shape in a mathematical and computational form. Considering a parabolic mirror of 2 m diameter, a focal length of 850 mm, and a reflectivity of 59% [12], the same as the medium-sized solar furnace (MSSF) parabolic mirror in PROMES-CNRS, where a typical local irradiance of 1000 W/m^2 is normally attained on a normal clear day [37, 38]. The Sun shape image of this concentrator would have a δ_{RMS} of 0.0037648 according to Equation (2.5) then the

G_x and the G_y would be 35276.6 through Equation (2.4). Alternatively, the Gaussian distribution of G_x and G_y can be manually adjusted in Zemax® until the simulated result is the same as the experimental measurements [39].

The terrestrial solar half-angle (θ_E) found by using the effective size of the solar-terrestrial image (d_E) at a distance (L), as represented in Equation (2.6).

$$\theta_E = tan^{-1}\left(\frac{0.5\, d_E}{L}\right) \tag{2.6}$$

θ_E calculated through a simple simulation in Zemax® by using a detector at a distance (L) away from a small solar light source, as shown in Figure 2.5 a). For example, consider a 0.002 mm diameter source (a small hole) at L = 10 m away from a rectangular detector of 150 × 150 mm^2 with a precision of 1001 × 1001 pixels. The calculation of θ_E is independent of the distance L since d_E is adjusted by the inverse-square law.

Figure 2.5 b) shows the solar distribution in Zemax® of a solar source by using the G_x = G_y = 35276 as the Gaussian distribution calculated from Equation (2.4) at a consideration of 1000 W/m^2 irradiance. For a correct calculation of the terrestrial solar angle, considering 95% of the total distribution then a width of d_E = 91 mm, which is equivalent to θ_E = 0.52°, which is very close to that of measured by others published papers [40, 41]. It is important to note that the acceptance half-angle (θ_a) of 0.27° can be found at the accepted effective size (d_a) at 56% effective of focal Gaussian distribution [42].

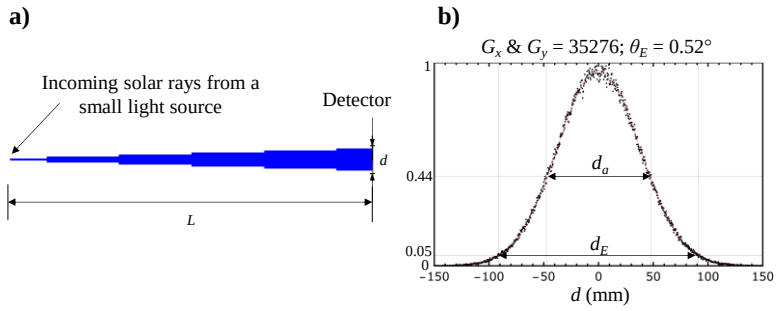

Figure 2.5 — (a) Light propagation from a small light source towards a detector of size d at a distance L. (b) Solar-terrestrial image with solar half-angle (θ_E) of 0.52° calculated from d_E and acceptance solar half-angle (θ_a) of 0.27° calculated from d_a.

2.1.6 Sun shape size deviation

The determination of the Sun's shape is influenced not only by the unpredictable fluctuations in the atmosphere but also by the physical imperfections of a non-ideal concentrator. For instance, in the case of a parabolic concentrator, factors such as the surface's curvature, waviness errors, the placement of the concentrator by the tracking mechanism, and the relative position of the concentrator and/or detector all play a role. The combined effect of all these non-systematic errors can be approximated using a simple standard deviation, $\sigma^2 = \Sigma\sigma^2_i$. The resulting image is referred to as the degraded Sun shape [20]. The real image of the Sun shape, through Central Limit Theorem, the Gaussian shape is the sum of the errors added in square, described by Equation (2.7):

$$\sigma^2_{sunshape} = \sigma^2_{optical} + \sigma^2_{Sun} \tag{2.7}$$

The σ_{Sun}^2 depends on the solar Gaussian distribution of the current irradiance intensity. The $\sigma_{optical}^2$ is the joint optical error generally found at any concentrator, represented by

$$\sigma_{optical}^2 = \sigma_{contour}^2 + \sigma_{specular}^2 + \sigma_{displacement}^2 + \sigma_{tracking}^2 + \sigma_{human}^2 \qquad (2.8)$$

The optical errors arising from several sources, and each type of errors itself contributes to: the deformity of the mirror surface (contour error, $\sigma_{contour}^2$); the imperfection and rugosity of the mirror surface which are observable in microscopic level ($\sigma_{specular}^2$); the displacement of the concentrator as a whole can largely influence the outcome of the Sun shape ($\sigma_{displacement}^2$); and the tracking error of the tracking machine ($\sigma_{tracking}^2$); the human error of positioning the mirror or the combined-mirror system. The representation of the optical error is shown in Figure 2.6.

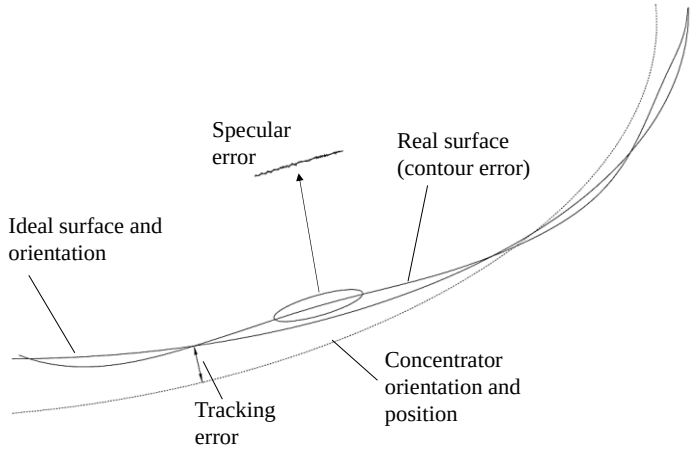

Figure 2.6 — Optical error of a real mirror concentrator comparing with an ideal mirror surface. The real surface mirror has error in orientation, specular, contour and tracking error.

2.2 Parabolic concentrator

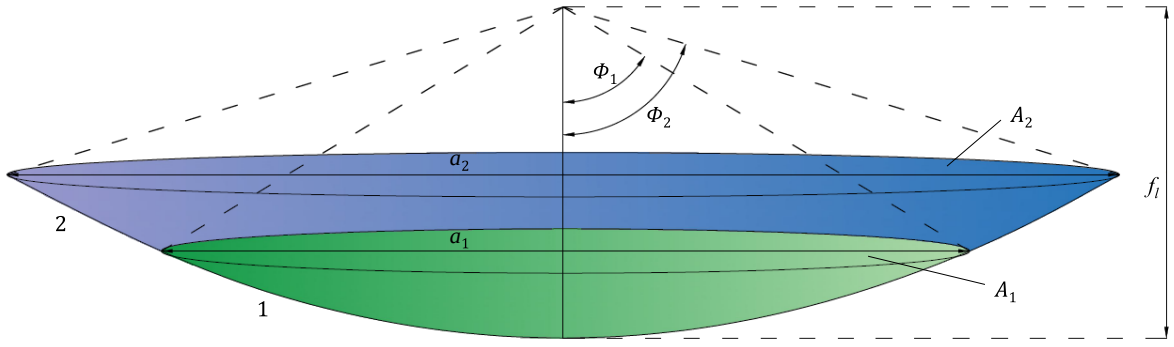

Figure 2.7 — Parabolic geometry. Each parabolic concentrator has the same focal length with different aperture sizes.

A reflector shaped like a parabolic dish is considered the most efficient and simplest solar concentrator. This type of reflective concentrator reflects all paraxial rays that hit its surface towards a common focal spot. The parabolic shape is easy to analyse, relatively easy to construct (depending on its size), material-efficient, and provides a sufficient concentration ratio for many high-power applications [43].

The sag Equation (2.9) generalizes the parabolic shape in the x-z plane, considering z pointing toward the Sun.

$$z = \frac{c\,a^2}{1+\sqrt{1-(1+k)c^2a^2}} + \sum_{i=1}^{M} \alpha_i a^i \tag{2.9}$$

Where c is the curvature of the surface, k is the conic constant, a is the radial aperture coordinate, and the terms α are aspheric coefficients. A pure parabolic geometry attained by k = -1 and considered the coefficients α as zero, then the simplify equation shows as:

$$z = \frac{c\,a^2}{2} = \frac{a^2}{2\,RoC} = \frac{a^2}{4\,f_l} \tag{2.10}$$

Most concave geometry uses the radius of curvature (*RoC*) to design its surface line, which is the inverse of c. In this case, the *RoC* would be twice the value of the focal length (f_l), as shown in Figure 2.8.

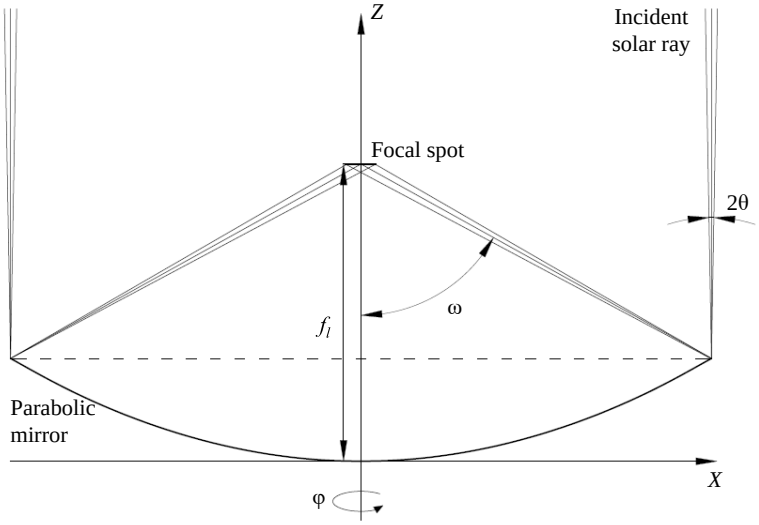

Figure 2.8 — Parabolic geometry. ω is the rim angle or aperture angle, f_l is the focal length, the θ half solar angle, and φ the angular rotation of the lens.

The Figure 2.9 a) shows a medium size solar furnace (MSSF) parabolic mirror with a source emitting twenty blue layout rays. The MSSF is a parabolic mirror concentrator found and used in PROMES-CNRS, France. This concentrator has a maximum radial aperture of 1000 mm diameter, minimum radial aperture of 150 mm, a focal length of 850 mm, which is equivalent to a 1700 mm radius of curvature. Figure 2.9 b) shows the focal distribution (Sun shape) in incoherent irradiance on the *Detector viewer*. The concentrated solar flux of 16.2 W/mm^2 and 15 mm diameter at 5 mm FWHM (full width at half maximum) in size, were in a very similar range claimed by [37, 38] and [44], under a clear day at with a solar irradiance of 1000 W/m^2.

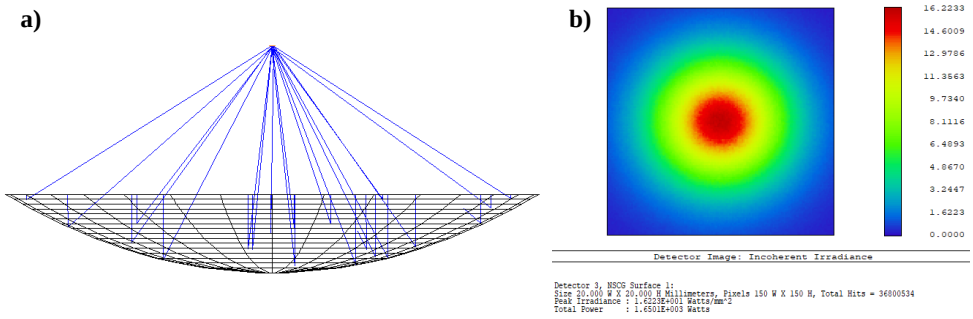

Figure 2.9 — (a) Zemax® NSC 3D layout representation of the parabolic concentrator of 1 m radius and a focal length of 0.85 m. (b) Focal spot of a rectangular detector of 20 × 20 mm^2 with 150 × 150 pixels at the focal spot of the MSSF parabolic concentrator with 40 million analysis rays, at typical solar irradiance of 1000 W/m^2.

2.3 Fresnel lenses

The Fresnel lens is a refractive optical apparatus with few millimetres in thickness. This concentrator conceptually produced by removing the non-essential parts of dielectric material from a conventional lens, as shown in Figure 2.10. The dielectric surface of the resulting thin facetted lens intercepts the rays of light with the same incidence angle as the original would have and performs identical refractive and focus functions.

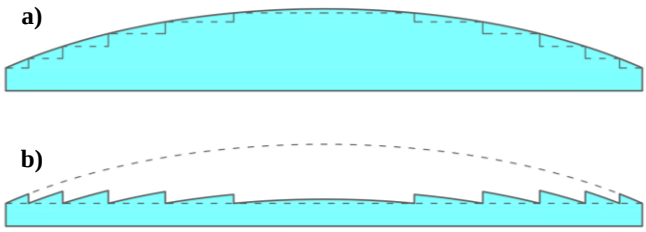

Figure 2.10 — (a) Standard focusing lens and dashed lines divide the steeped surface design by Buffon. (b) Fresnel lens uses the stepped surface onto a thin substrate.

Both the standard lens and the Fresnel lens use the same sag equation as described in Equation (2.9). However, while the standard lens uses refractive optics to focus light based on the law of refraction, the Fresnel lens utilizes refractive optics in conjunction with discrete concentric rings to focus the light. Despite this difference, both types of lenses suffer from chromatic aberrations due to the broad range of wavelengths present in sunlight.

Prior to 1950, Fresnel lenses were typically made of glass or silica and were manufactured by grinding and polishing grooves into the material. Later, a more cost-effective method of casting and pressing glass into moulds was introduced. However, this method did not receive further treatment, resulting in lower optical quality lenses. Furthermore, the high surface tension of glass during solidification posed challenges in creating rounded grooves and tips.

Currently, advancements in plastics, moulding techniques, and computer-aided diamond-turning machines have significantly enhanced the quality of Fresnel lenses. The use of these materials and techniques has allowed for lighter and more affordable lenses, expanding their applications. Plastic Fresnel lenses can be produced through pressure moulding, injection moulding, cutting, or extrusion. These

lenses have been used in various applications such as overhead projectors, copy machines, camera screens, magnifiers, reading lenses, holography, data transfer, lighthouses, solar collectors for thermal and photovoltaic purposes, and solar-pumped lasers.

The two design orientations of the flat Fresnel lens are the “grooves-in” orientation, with the grooved facet facing towards the target, and the “grooves-out” orientation, with the grooved facet facing towards the Sun, as depicted in Figure 2.11a) and b), respectively. The grooves-out design boasts enhanced optical efficiency, as the trajectory of the traveling light undergoes modification at both the entering and exiting mediums in accordance with Snell's law. In contrast, the groove-in design only redirects the light at the exit groove, given that the incoming light is perpendicular to the lens’s input face. However, grooves-in designs are less prone to soiling problems and are easier to clean and maintain.

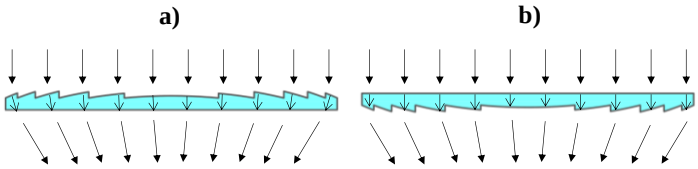

Figure 2.11 — Fresnel lens. (a) grooves-out design and (b) grooves-in design.

Prolonged exposure to different temperatures can cause changes in the refractive properties of the material, which can impact the effectiveness of a Fresnel lens. These changes can lead to variations in the focal distance and size of the focal spot. Moreover, thermal expansion of the lens can cause further deformation of its image profile. Therefore, it is important to consider the operating temperature of the lens during the design phase. Additionally, prolong exposure to high temperatures can decrease the lifetime of the concentrator [45].

Different manufacturers of Fresnel lenses may produce lenses with varying efficiency, even if the lens specifications are identical, due to factors such as the manufacturing process, type and amount of material used, lens thickness, and finishing processes. Removing the lens from the mould or machining process can result in a rough surface (as shown in Figure 2.12 a)) due to detachment, and the pitch angle required to remove the lens from the mould (represented in Figure 2.12 b)) can cause optical loss. A pitch angle of around 2 degrees is commonly used. The production process can also produce defects such as rounded facets at the peaks (shown in Figure 2.12 c)) and valleys (shown in Figure 2.12d)), which are generally caused by poor plastic injection or cutting tool edges during machining. The ideal

grove is represented as Figure 2.12 e). Therefore, it is important to consider the quality of the manufacturing process when selecting a Fresnel lens.

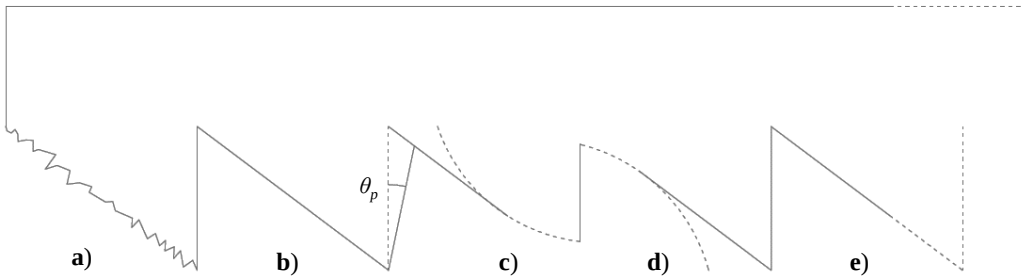

Figure 2.12 — Real physical flaws or errors of Fresnel lens. (a) roughness of the groove's facet surface. (b) pitch angle θ_p. (c) peak round facet, (d) valley round facet and (e) the ideal grove.

Most of the Fresnel lens modelling sequences and parameters found in the industry, including the Zemax® Fresnel lens are based on Claytor's patent [46, 47], shown in Figure 2.13. These variables are:

- *r*, the aperture defines the radial size of the Fresnel lens.
- *RoC*, the radius of curvature defines the focal length.
- *k*, the conic curvature constant defines the shape of the Fresnel lens facet.
- d_t, is the thickness of the substrate below the grooves.
- θ_p, pitch (degrees) defines the "inactive" faces (those faces nominal parallel to the local z-axis).
- d_m, the frequency of the grooves per lens diameter defines the total number of slope facets and their size.

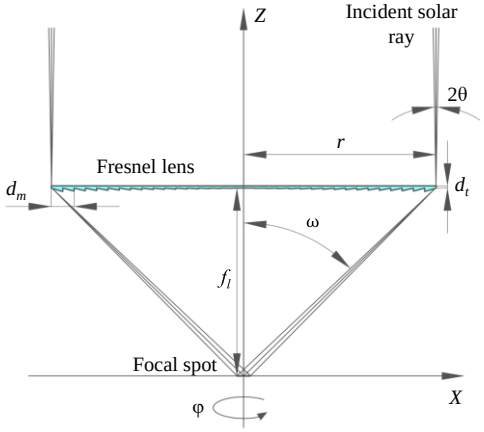

Figure 2.13 — Fresnel lens with radial aperture (*r*) with an incident solar ray at the edge with a solar half-angle of θ, and φ the angular rotation of the lens. The f_l is the focal length of the lens, ω is the rim angle, d_t is the thickness of the lens and d_m is the groove frequency.

The Fresnel lens's focal image is wavelength sensitive due to the chromatic Snell's deviation caused by the difference in refraction index. Figure 2.14 shows the achromatic aberration of wavelengths from 0.3 μm to 1.5 μm. The Y = 0 mm is the mathematical focus calculated for 0.5 μm (red line) and all other wavelengths scattered around on its focus. The position Y = 100 mm has the sharpest concentration size and the highest concentration intensity.

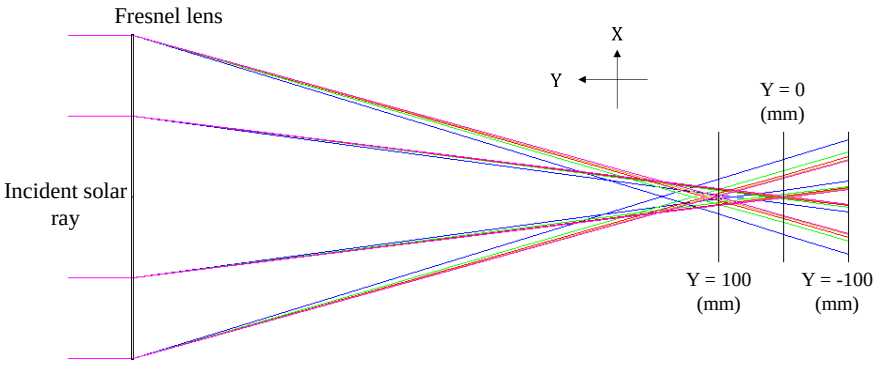

Figure 2.14 — Achromatic aberration is caused by various collimated wavelengths by a Fresnel lens.

A focal characteristic of a simulated Fresnel lens in Zemax® with the same specification of 889 mm diameter, focal length of 757 mm, thickness of 3.17 mm and grooves numbers of 50 in 25 mm faced toward the focus used in *Centro Nacional de Investigaciones Metalúrgicas* (CENIM) in Complutense University of Madrid [48-50] is shown in Figure 2.15. This Fresnel lens had generated over 2.60 W/mm^2 of concentrated solar flux with a focal size of 8 mm diameter, under a clear day at with a solar irradiance of 1000 W/m^2.

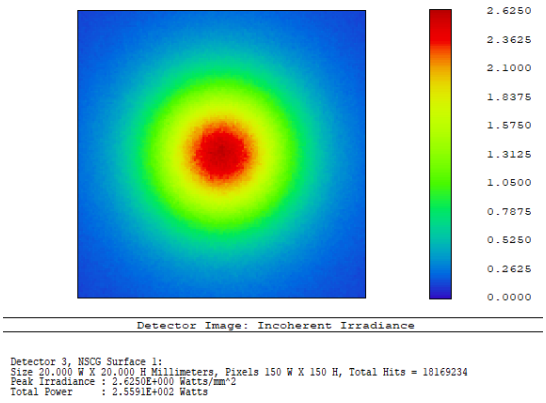

Figure 2.15 — Focal spots of a rectangular detector of 20 × 20 mm^2 with 150 × 150 pixels at the focal spot of the CENIM Fresnel lens with 40 million analysis rays, at typical irradiance of 1000 W/m^2.

3

NUMERICAL TOOLS FOR DESIGNING SOLAR CONCENTRATORS AND SOLAR-PUMPED LASER MODELS

3.1 Introduction

In this chapter, we delve into the essential numerical tools employed in the design processes of solid-state lasers and solar concentrators. The initial focus is on the non-sequential Zemax® ray-tracing analysis, a crucial tool for optimizing the design parameters of solid-state lasers. Furthermore, the chapter explores the Laser Cavity Analysis and Design (LASCAD™) software, employed for evaluating the performance of laser output. To complement these discussions, the chapter concludes with a brief introduction to the ANSYS™ software, which facilitates temperature calculations using the output data file generated by Zemax®.

3.1.1 Non-Sequential Component (NSC) editor

The *Non-Sequential Component Editor* window or *NSC editor* window serves as a central workbench for modelling an optical system. This window works similarly to a Microsoft Excel spreadsheet, as shown in Figure 3.1. Each **row** is equivalent to an **object** and each **column** within a row represents a specific **parameter** of that object. An intersection of a row and a column forms a cell. A single cell (asides from the first and second column) is subdivided into two rectangles, the larger input rectangle is reserved for data input and the smaller one is for the cell-solving condition. The highlighted cell has a black background. The arrow key from the keyboard or left-clicking the mouse serves as a navigation tool to select the intended cell. All column's widths are modified by hovering on the dividing line between two columns at the top row (white row).

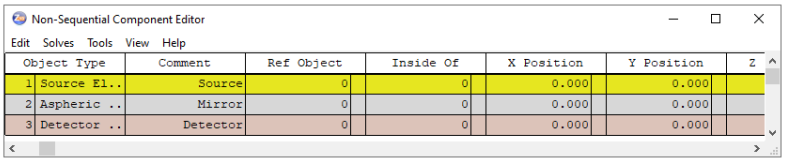

Figure 3.1 — *Non-Sequential Component Editor* window, listing three objects. The first object is Source Eclipse (Yellow), the second object is Aspheric Surface (Grey), and the third object is Detector Rectangle (Purple).

3.1.1.1 Common parameters cells

All the objects within the *NSC editor* share the same type of cell composition in the first eleven columns.

- Column 1 – Object Type: It indicates the type of object selected for that row. Right-clicking on this cell opens the *Object row <number> Properties* dialog box.
- Column 2 – Comment: It uses for comments, it can accept no more than 225 characters.
- Column 3 – Ref Object: It copies the position and orientation of the target object row number. The referenced number must be lower than the current object number.
- Column 4 – Inside of: Puts the current object inside of the target object row number. The referenced number must be lower than the current object number.
- Column 5 – X Position: X coordinate position of the object in millimetres.
- Column 6 – Y Position: Y coordinate position of the object in millimetres.
- Column 7 – Z Position: Z coordinate position of the object in millimetres.
- Column 8 – Tilt about X: X rotation at the X plane at a degree angle.
- Column 9 – Tilt about Y: Y rotation at the Y plane at a degree angle.
- Column 10 – Tilt about Z: Z rotation at the Z plane at a degree angle.
- Column 11 – Material: Defines the material of the current object if applicable. The material written by the use must be a valid named material found in the "Glass Catalog" list.

3.1.1.2 NSC editor: cell

Each cell apart from the first two columns ("Object type" and "Comments") subdivides into a larger rectangular cell (left) and a smaller rectangular cell (right).

- Large rectangular cell – Input text box which accepts integer numbers, decimal numbers, or a string of words depending on the cell's specification.

  A numerical cell can do basic arithmetic functions of plus (+), minus (-), multiplication (*), and division (/). For example, adding "+5.5" onto an existing "20" within the cell will result in a "25.5" when pressing the Enter key or by moving to another cell.

  Note: To subtract a number, the sequence starts with a plus before a minus. For example, "+-10".

- Small rectangular cell – Shows the solve condition of the parameter. Zemax® offers four solve types, as shown in Figure 3.2:
  - Empty: The parameter is a fixed solve type.
  - V: The parameter is a variable solve type.
  - P: The parameter is a pickup solve type.
  - Z: The parameter run by a ZPL macro.

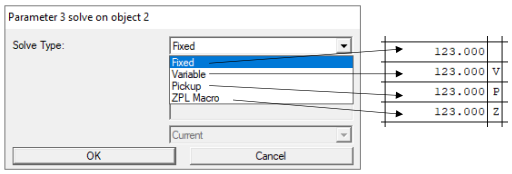

Figure 3.2 — Solve type dialog box of parameter 3 on object 2.

3.1.1.3 Object nesting volumes and surfaces

The order in which the objects are placed in the *NSC Editor* window has a significant role in the ray-objects interaction. The number of nesting objects by default in Zemax® is five and the minimum is four, special models may need a higher nesting number to function properly. The nesting object limit is changeable in the *Main menu* → *System* → *General…* → *Non-sequential* tab.

3.1.1.3.1 Nesting volumes:

Volumetric objects are often refractors. Zemax® keeps tracking the index of refraction through which the ray is propagating from one object to another.

The general rules are:

If a ray strikes more than one object at the exact point in space; the last object listed in the *NSC Editor* determines the properties of the surface or volume at that point.

Considered a silica sphere with a cylindrical hole in the middle, and continuously pumped by a collimated light source in the air, as shown in Figure 3.3. In the *NSC editor* window, the order of source object placed before the other two objects. According to the nesting rule, the cylinder volume (#2) of vacuum material must place **after** the sphere object (#1) of silica material in the *NSC editor* window, as shown in Figure 3.3 a).

The difference between Figure 3.3 a) and Figure 3.3 b) is evident. In Figure 3.3 a), the light passes normally through the cylindrical hole, while the rays inside of the silica sphere reflects due to the difference in the refraction index of both silica and air. Figure 3.3 b) shows the incorrect nesting procedure since the passing ray continues as if no hole is present.

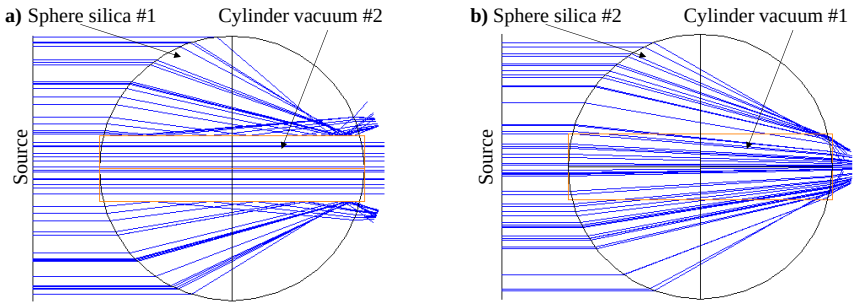

Figure 3.3 — Nesting order of a Sphere in silica with a cylinder volume in a vacuum. (a) the correct object nesting order, (b) the wrong nesting order.

3.1.1.3.2 Nesting surfaces:

The nesting surface rules are the same as the nesting volumes.

If a ray strikes more than one object at the same point in space; the last object listed in the *NSC Editor* determines the properties of the surface at that point.

For nesting surfaces, additional rules should consider when there is more than one surface existing at the ray intercepting point:

1) The last surface listed will determine the properties of the surface.
2) If the last surface listed is a mirror, then the ray will reflect.
3) If the last surface listed is an absorber, then the ray will absorb.
4) If the last surface listed is neither a mirror nor an absorber, the ray will ignore the surface.
5) Surface objects may not share boundaries with volume objects unless the surface object is reflective or absorbing, or unless the volume object listed after the surface object; in which case the volume defines the properties of the common boundary.

3.1.1.4 Wavelength data window

The system's wavelength is configurable in *Wavelength Data* dialog box, shown in Figure 3.4, access from *Main menu → System → Wavelengths*. A total of 24 wavelength entries can be accepted at a time. Each wavelength has its respective unitless weight. Each tick box activates and deactivate the selected wavelengths or to sort, save and load the wavelength data. A minimum and maximum computational wavelength can be set for the system. The list of wavelengths can be saved and loaded from a *.WAV file. This file is editable by any text editor software, such as Notepad.

The wavelength measured in micrometres and referenced to the system's air temperature and pressure. The default system temperature is set at 20 degrees Celsius, and the default air pressure is at 1.0 atmospheres. If a new system with modified temperature and pressure, then a new set of wavelengths must be manually adjusted.

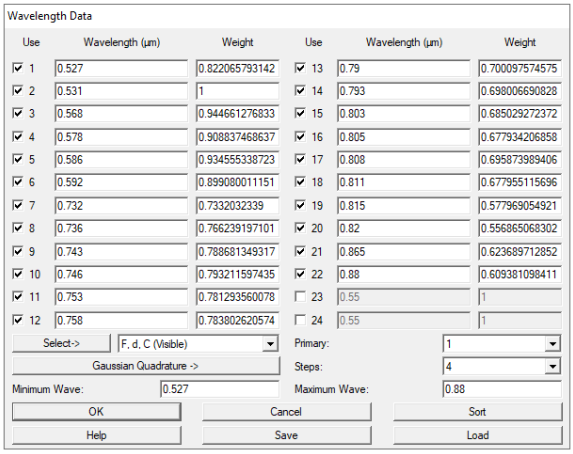

Figure 3.4 — *Wavelength Data* dialog box. 22 solar wavelengths with their respective weights selected from the solar spectrum overlapped with the absorption bands of Nd:YAG.

3.1.1.5 Spectrum file

The *Wavelength Data* dialog box is the most direct and common way to introduce wavelengths into the ray tracing system, however, it can only accept up to a maximum of 24 wavelengths. Spectrum file is an alternative method to increase the number of system wavelengths, up to 200 and no less than 3 sets. Notepad with *.SPCD extension is used for Spectrum files, and by default placed in the Object *\Sources\Spectrum Files* folder. The Spectrum file consists of two sets of columns, a column of wavelength in micrometres and other columns as a dimensionless relative weight value, shown in the following format:

```
# comment <optional>
wavelength1 weight1
wavelength2 weight2
etc...
```

Any blank line or a line starting with the "#" or "!" symbol assumed to be a comment and ignored.

The spectrum file can only be accessed from the object's property under the *Sources* tab and by selecting the dropdown box of "Source color". The "System Wavelengths" is the default option and the "Spectrum file" option selected from that dropdown box, which enables a new dropdown list menu of spectrum files with *.SPCD extension. Any spectrum file selected will supersede the default system wavelength data. Figure 3.5 a) shows the resulting 200 wavelengths and weight distribution of a direct AM 1.5 solar spectrum.

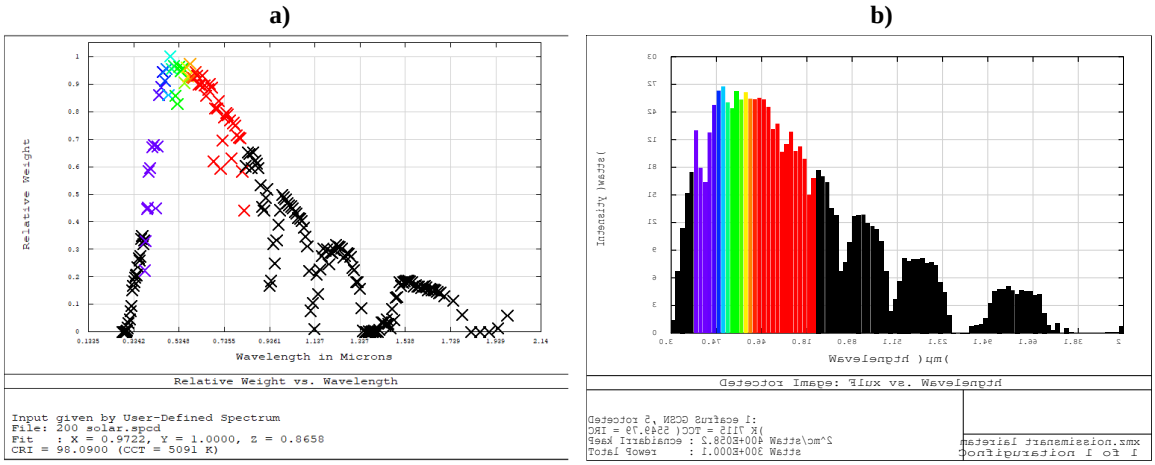

Figure 3.5 — **(**a) Spectrum file with 200 spectral lines from the direct AM 1.5 solar spectrum. (b) Solar spectrum distribution measured from a source of 1000 W with the loaded spectrum file of (a).

3.1.1.6 Ray selection from a spectrum

Once a spectrum is defined either from *wavelength data* or from a *spectrum file*, the ray tracing process randomly chooses wavelengths from the spectrum based on their relative weight. A wavelength with twice the relative weight as another wavelength will be traced twice more often, and therefore twice of that wavelength will be traced. If a wavelength has a low relative weight, fewer rays are traced. If the source units are in Watts or Joules, every ray would have the same amount of power (or energy). The power distribution resulting from the weight at each wavelength from a 1000 W source with the solar Spectrum file of Figure 3.5 a) can be seen in Figure 3.5 b). Wavelengths with higher weights have a higher power distribution due to the larger number of wavelengths hitting the detector, and vice versa for wavelengths with a lower weight. The combined total power of all wavelengths on the detector is equal to the initial power from the source, which is 1000 W.

3.1.1.7 Glass Catalog dialog box and Glass table

Every physical and optical aspect of the material found in Zemax® can be consulted and edited. An optical material is called "glass". Zemax® provides pre-existing standard Catalogs from various prominent optical companies. New glasses and Catalogs are created, added, and shared. Any objects with

volume may attribute a glass material by writing the glass name into the "Material" column, for example, WATER, which Zemax® will look for the matching name in the glass Catalog or the glass table.

Glass Catalog

The *Glass Catalog* dialog box, as shown in Figure 3.6, accessed from the *Main menu → Tools → Catalogs → Glass Catalogs…*. Distinct groups of glass lists can be accessed at different Catalog lists. Each glass may have a separate set of parameters that tie to its dispersion formulas; refraction index; operating temperature; maximum and minimum wavelength; etc... Each parameter within this dialog box is editable and saved into a separate glass Catalog.

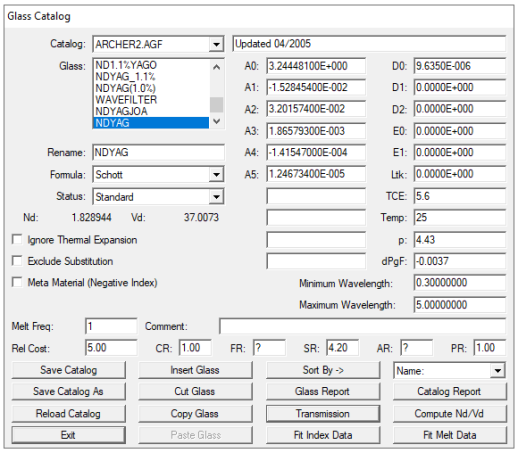

Figure 3.6 — *Glass Catalog* dialog box. "NdYAG" as the selected material.

The transmission at a different wavelength within the material consulted and edited in the *Transmission Data* dialog box, through the *Transmission* button, as shown in Figure 3.7.

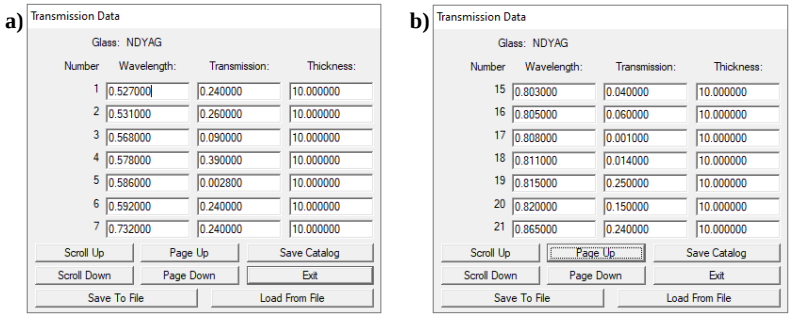

Figure 3.7 — *Transmission Data* dialog box of Nd:YAG. (a) is the transmission of wavelengths at 10 mm thickness for the initial batch of seven wavelengths starting from 0.2 micrometres to (b) as the 15-21 bulk of wavelength data.

The first column is the wavelength, the second column is the transmission weight calculated through the normalized Beer's law Equation (3.1) at a known thickness (τ) in mm. The absorption coefficient (α) is a measured identity tied to a respective wavelength.

$$t(\lambda) = e^{-\alpha(\lambda)\tau} \tag{3.1}$$

Material: Nd:YAG

The material "Nd:YAG" is not included in the Zemax® Catalog. However, the S-LAM60M material in the ARCHER Catalog has the same refractive index as an Nd:YAG crystal. To use this material as NdYAG in Zemax®, the user should copy and rename it as "Nd:YAG" and then replace the transmission

data with that of Nd^{3+} ions at the correct concentration. The Table 3-1 shows the calculated transmission weight per wavelength for a Nd(1%):YAG calculated from Equation (3.1) by using the absorption co-efficient distribution in [51].

Table 3-1 — Nd(1%):YAG absorption band [51] and the related transmission weight at 10 mm material length.

Wavelength (nm)	Transmission weight
527	0.24
531	0.26
568	0.09
578	0.39
586	0.0028
592	0.24
732	0.24
736	0.09
743	0.16
746	0.002
753	0.024
758	0.039
790	0.35
793	0.056
803	0.04
805	0.06
808	0.001
810	0.014
815	0.25
820	0.15
865	0.24
880	0.40

3.1.2 Pumping sources

A pumping source or simply source is a ray-emitting object in Zemax® that spreads rays at a predefined intensity, angle, and wavelength. A Zemax® model without a source object cannot do any ray tracing. In solar-pumped laser modelling, only the surface-type sources were used:

- Source Ellipse – An elliptical surface that emits light from a virtual source point.
- Source Rectangle – A rectangular surface that emits light from a virtual source point.

Source Ellipse:

The *Source Ellipse* is a flat elliptical (and optionally annular) surface. The rays launched lie on the surface of the ellipse with a uniform distribution. The distribution of the ray direction follows a Gaussian distribution from the following Equation (3.2):

$$I(l,m) \approx I_0 e^{-(G_x l^2 + G_Y m^2)} \tag{3.2}$$

Where l and m are the direction cosine of the rays in the X and Y axis direction and G_x and G_y are constants. This form defines a far-field pattern that is different in the X or Y directions. The larger G_x and G_y are, the narrower the distribution. If both G_x and G_y are zero, then all rays will emit from a virtual point source as collimated light.

The values of G_x and G_y are in parameters 10 and 11 of the *Source Ellipse* object.

Source Rectangle:

The *Source Rectangle* is a flat rectangular surface. The parameter of this object is identical to the *Source Ellipse*.

3.1.3 Source power calculation

3.1.3.1 Source power calculation for general use:

The value of the source power (parameter 3) is dependent on the solar irradiance (I_s) and the effective collection area (A_{ef}). Equation (3.3) is the generic solar source power for the full solar broadband wavelength. For example, considering an elliptical source with an effective area of 1 m^2, irradiated by 1000 W/m^2 solar irradiance, then the power of the source is 1000 W.

$$P_S = A_{ef}\, I_S \tag{3.3}$$

3.1.3.2 Source power calculation for solar-pumped laser:

For solar-pumped lasers, only a portion of the solar wavelength is useful for the laser medium. A 22 set of wavelengths on the source were configured to pump the absorption wavelength of Nd^{3+} from the Nd:YAG crystal, as shown in Figure 2.3. The source power of each laser material is recalculated through the amount of overlapping absorbing bands with the whole solar spectrum and the solar power provided from the effective source size at a constant solar irradiance.

3.1.3.2.1 Nd:YAG

In the case of Nd:YAG crystal, the amount of available energy is the overlapped solar energy with the absorption bands of Nd^{3+} ion ($\eta_{overlap,Nd^{3+}}$), which is roughly about 16% of the total solar power [52-54].

$$P_{Nd:YAG} = A_{ef}\, I_S\, \eta_{overlap,Nd^{3+}} \tag{3.4}$$

3.1.3.2.2 Ce:Nd:YAG

The Ce:Nd:YAG crystal has both Nd^{3+} and Ce^{3+} ions that contribute directly and indirectly to the output of the 1064 nm laser, as mentioned in section 6.3.2.1. The Ce:Nd:YAG is remarkably similar to the Nd:YAG in many aspects, therefore the Nd:YAG crystal can be used as a preliminary substitute for Ce:Nd:YAG, changing only the amount of energy available for absorption at the source. In Zemax® ray tracing, two separate sources considered to pump the crystal.

The first source emits all the relevant overlapped wavelengths of the solar spectrum with the Nd^{3+} ion absorption spectrum, as well as the wavelength data that includes the Ce^{3+} quantum cutting down conversion of non-radiative transfer to Nd^{3+}. The simulated power of source 1 ($P_{source1}$) follows Equation (3.5) [53].

$$P_{source1,Ce:Nd:YAG} = A_{ef}\, I_S(\eta_{overlap,Nd^{3+}} + \eta_{overlap,Ce^{3+}} \times \eta_{NR:Ce^{3+}\rightarrow Nd^{3+}}) \tag{3.5}$$

The $\eta_{overlap,Nd^{3+}}$ is the overlapped solar energy with the Nd^{3+} ion (~16%), $\eta_{overlap,Ce^{3+}}$ is the overlapped solar energy with the Ce^{3+} ion (~15.7%) and $\eta_{NR:Ce^{3+}\rightarrow Nd^{3+}}$ is the Ce^{3+} quantum cutting down conversion of non-radiative transfer to Nd^{3+} (~70%) [53-55].

The second source accounts for 30% of the absorbed energy by Ce^{3+} that was transferred radiatively to Nd^{3+} ($\eta_{R:Ce^{3+}\rightarrow Nd^{3+}}$), as shown in Equation (3.6) [53-55].

$$P_{source2,Ce:Nd:YAG} = A_{ef}\, I_S\, (\eta_{overlap,Ce^{3+}} \times \eta_{R:Ce^{3+}\rightarrow Nd^{3+}}) \tag{3.6}$$

3.1.4 Objects for solar-pumped laser

The solar-pumped laser modelling in Zemax® consists of various well-placed and optimized optical objects. The most used objects briefly are described in 3.1.4.1. Imported custom-made CAD objects are described in 3.1.4.2.

3.1.4.1 Zemax® objects

3.1.4.1.1 Primary concentrator

Large optical devices leverage their expansive surfaces to efficiently concentrate substantial amounts of solar radiation onto a highly localized and focused focal spot. These sophisticated optical systems harness the incoming solar energy, employing precision in their design to channel and intensify sunlight, maximizing the efficiency of energy collection. The concentrated solar radiation at the tight focal spot enables the generation of elevated temperatures and facilitates various applications, ranging from solar power generation to materials processing. This remarkable capability underscores the importance of large optical devices in harvesting and harnessing the immense power of the Sun for diverse technological and industrial purposes.

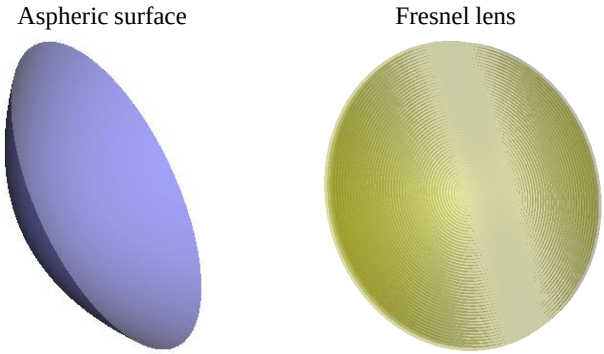

Figure 3.8 — Commonly used primary concentrator objects: Aspheric surface and Fresnel lens.

Aspheric Surface – This object commonly used as a parabolic mirror.
Fresnel lens – A general radial symmetric or cylindrical solid Fresnel lens constructed by modelling the detailed faces of the Fresnel surface.

3.1.4.1.2 Secondary concentrator

These sophisticated optical devices play a crucial role in the solar energy harvesting process by enhancing the concentration or distribution of solar radiation from the primary concentrator to the active medium crystal. Crafted from high-quality fused silica, these optical components are meticulously designed to ensure precision and efficiency in channelling sunlight. By skilfully manipulating and directing solar

rays, these components contribute to the optimization of energy transfer to the active medium crystal, thereby enhancing the overall performance of solar energy conversion systems.

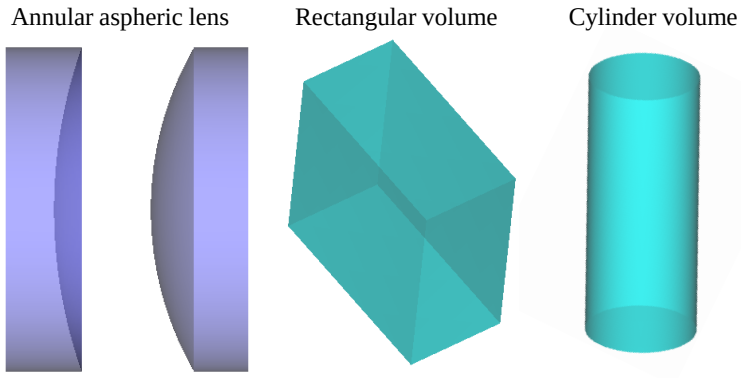

Figure 3.9 — Commonly used secondary concentrator objects: Annular aspheric lens, Rectangular volume, and Cylinder volume.

Annular Aspheric Lens – The *Annular aspheric lens* is an annular solid with a conic asphere with even aspheric polynomial terms. It further increases the concentration and reduce the size of the focusing solar radiation from the primary concentrator.
Rectangular volume – It used as an optical light guide to homogeneously distribute the focusing radiation onto the crystal. This object used as a body of water for cooling the active medium.
Cylinder volume – A cylinder can serve as a rod when both its front-end and back-end have equal radial sizes, and it can also operate as a light guide or an active medium. In cases where the front-end radius differs from the back-end radius, the cylinder can be transformed into a solid cone to serve as a focusing light guide or a pumping cavity when it's not solid.

3.1.4.1.3 Pumping cavity

Optical devices play a pivotal role in the intricate process of redirecting concentrated solar radiation into the crystal, facilitating multiple reabsorptions of energy within the crystal. Primarily in the form of mirrors, these surface-type objects are meticulously designed to efficiently capture and redirect sunlight. Through their reflective surfaces, these optical components ensure that solar energy is effectively channelled back into the crystal, promoting enhanced absorption and utilization of the radiant energy. This intricate interplay of optical components significantly contributes to optimizing the overall efficiency of solar energy absorption and conversion systems.

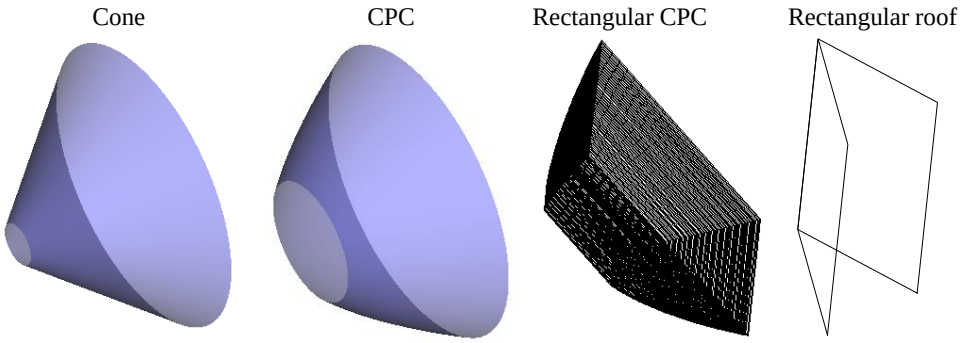

Figure 3.10 — Commonly used pumping cavity objects: Cone, CPC, Rectangular CPC, and Rectangular roof.

Cone – A hollow conic and reflective cavity used as end-side-pumping, an active medium.
CPC and Rectangular CPC – Compound parabolic concentrators used to concentrate light entering one end to another end. This type of CPC is the same as the “Basic CPC” described in [56].

Rectangular roof – A reflective folding surface with controllable folding angles. Used as a side-pumping cavity to achieve reabsorption by reflecting any light into the active medium rod.

3.1.4.1.4 Others

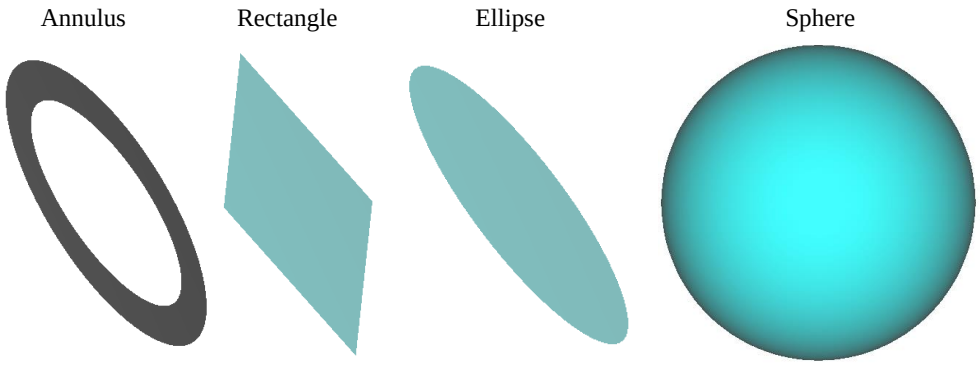

Figure 3.11 — Other useful objects: Annulus, Rectangle, Ellipse, and Sphere.

Annulus – An elliptical surface used as a reflective ring.
Rectangle and Ellipse – Used as folding mirrors or parts of an optical or mechanical apparatus.
Sphere –Used anywhere.

3.1.4.2 Imported CAD objects

Objects shapes not found in Zemax® objects database are imported from other Computer Aid Designs (CAD) programs, such as Standard Triangle Language (STL), Initial Graphics Exchange Specification (IGES), Standard for the Exchange of Product Data (STEP) and Standard ACIS Text (SAT). Zemax® also accepts dynamically linked objects such as Autodesk Inventor™, Creo Parametric™, and SolidWorks®.

There are no restrictions on the shape, complexity, or quantity of objects that can be imported. However, importing multiple objects in a single file can negatively impact ray tracing speed and potentially decrease the accuracy of the results.

The ray tracing accuracy of an imported CAD object depends on the complexity of its shape and the number of facets. For instance, an imported cylinder, if done correctly, would have the same optical accuracy as a native Zemax® cylinder object in ray tracing. Moreover, most CAD approximations are mostly suitable for mechanical designs, and not optimized for optical precision in ray tracing, where surfaces must be well known into tiny fractions due to the sensibility of ray wavelength into surface interaction. To increase the accuracy of the ray tracing with an imported Autocad® object, it is advisable to export with the largest number of facets possible. This can be achieved by modifying the object polygon count to the maximum with the *Facetress* command.

Some CAD objects may automatically convert an imported object into a Zemax® Object Format (ZOF), a native file format easily recognizable by Zemax® and improves the simulation time. This newly converted object will have an extra extension of *.ZOF at the end of the original file name. For example, if the original file name is Object.IGES then becomes an Object.IGES.ZOF. An imported CAD object in Zemax® used as any other object type.

- CAD Part: STEP/IGES/SAT – Uses imported CAD objects in IGES, STEP, and SAT format. The imported file will automatically convert into a ZOF (Zemax®'s native format).
- CAD Part: STL – The STL object is an open-ended user-defined object. It defines an open polygon surface or a closed polygon volume such as a prism or other solid. The STL Object format is based on a collection of 3D triangles. This format supported by mechanical CAD programs. There are no fixed limits to the total number of vertices or polygons imported.

3.1.4.3 Detectors for ray-tracing analysis

The detector object stores data. The qualitative data stored in the detector depends on the number of rays that touches its surface. The detector can be reflective, transparent, or absorbing, as in *MIRROR*, blank, or *ABSORB*, respectively. Each detector types offers unique analysis and functions. In this book, there are only two types of detectors used in solar-pumped lasers:

3.1.4.3.1 2D detectors

Detector Rectangle:

The detector rectangle object stores energy data from rays that strike or pass through it. The resulting data distributions viewed for incoherent light in spatial or angular domains, spatially coherent irradiance or phase, or coherent irradiance as a point spread function.

3.1.4.3.2 3D detectors

Detector Volume:

The amount of energy stored in each voxel depends on the material absorbance. The resulting data distributions viewed as incident flux, absorbed flux, or absorbed flux per unit volume. Detector volumes may be transparent or be any valid glass material. Detector volumes may also be nested within or straddled with other objects. The *Detector Volume* object shaped like a box, with its origin point at its center.

Note: In solar-pumped laser modelling, the laser crystal rod is nested inside of a water *Detector Volume*.

3.1.5 Raytracing

3.1.5.1 Ray Trace Control

The *Ray Trace Control* dialog box used to initialize ray tracing analysis. The controls within this dialog box are shown in Figure 3.12:

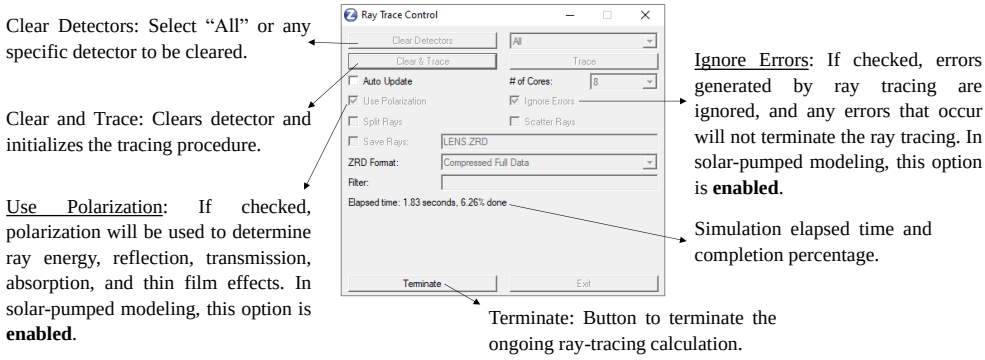

Figure 3.12 — Ray Trace Control dialog box.

Note: The ray tracing session should start with all the detectors cleared.
Note: If the ray tracing calculation terminated during tracing, then a new ray tracing must start with all detectors cleared.

3.1.5.2 Post-ray tracing: Detector Viewer

The *Detector Viewer* is a window that displays data of a detector in either a graphic or text format. This window accessed at the *Main Menu* → *Analysis* → *Ray Tracing* → *Detector Viewer*. Figure 3.13 shows the *Detector Viewer* window in Incoherent Irradiance after raytracing. Each pixel in the graph corresponds to an intensity color value. The bottom part of the detector viewer shows the information and summary of the detector, such as the detector object number (in this case, the 20th object), the size of the detector, the number of pixels per axis, the total number of rays hit, the peak irradiance and the accumulative total power.

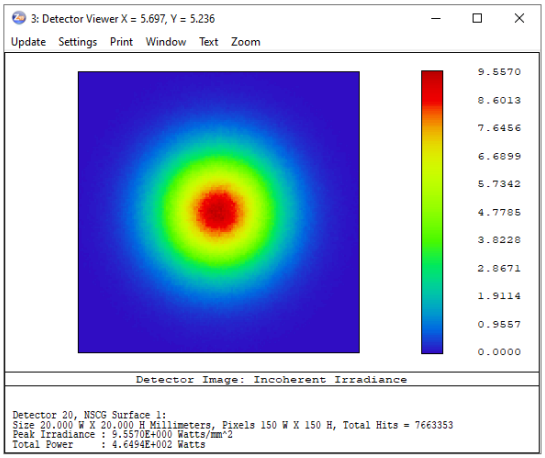

Figure 3.13 — *Detector Viewer* window.

3.1.5.3 Detector viewer Text window

Clicking the "Text" button on the menu in the *Detector Viewer* window in Figure 3.13 will opens a new text-based window shown in Figure 3.14 a). The text *Detector Viewer* shows all the relevant information related to the detector, such as the size, the position, and the type of power on each pixel or voxel, depending on the option chosen in "Show Data".

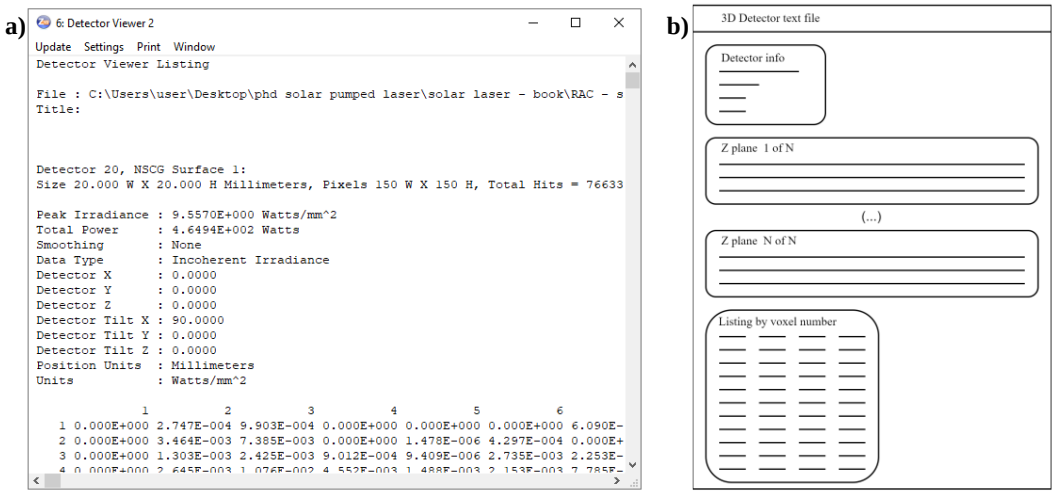

Figure 3.14 — (a) is the Text-based *Detector Viewer*. (b) is the 3D detector text file structure.

The data shown in text mode depends on the type of detector used:

- Two-dimension detector: Pixel data listed into a two-dimensional x-y matrix.
- The three-dimension detector: Voxel data listing is like a two-dimension detector, with a two-dimension x-y matrix listed in each z layer, and a list of voxels sorted by coordinates, as shown in Figure 3.14 b).
- Imported object as a detector: The pixelation data have the same order of sequence as the drawing coordinate sequence of the imported object.

Any text-based *Detector Viewer* can be saved into a text file from *Window* → *Save Text*.

The detector text file can be used as an intermediate file for importing into other software. A three-dimensional detector text file was required to load into LASCAD™ as a thermally loaded crystal and then used for calculating the laser power.

Important Note: Some software may only accept some type of text encoding architecture. LASCAD™ only accepts ANSI file encoding architecture, while ANSYS™ and other more advanced software can accept both ANSI and Unicode encoding architecture. In the Zemax® *Main Menu* → *File* → *Preference…* → *Miscellaneous* (tab) has the option to change the encoding architecture.

3.2 Evaluation of solid-state laser output performance by LASCAD™ software

This chapter introduces the calculation of laser power and the conditions required to achieve both multimode and single-mode (TEM_{00}) lasers using LASCAD™, a laser cavity modelling software. LASCAD™ software combines various simulation algorithms to optimize laser resonator design, including thermal and structural Finite Element Analysis (FEA), the ABCD Gaussian Beam Propagation Code, and the Beam Propagation Method (BPM) for non-Gaussian beams. It analyses resonant cavities, considering thermal lensing effects, multimode and TEM_{00} mode output power and efficiency, laser beam quality and profile, and laser beam propagation outside the cavity, considering parameters such as reflectivity, radius of curvature, distance between cavity components, diffraction losses, gain saturation, and more.

3.2.1 Standing Wave Resonator window

The *Standing Wave Resonator* window represents the laser cavity, as shown in Figure 3.15 a). This shows a single window with a black background with green horizontal lines (mode plot). If astigmatism is configured in the *Miscellaneous* tab in the *Parameter Field* window, then the *Standing Wave Resonator* window would present two mode plots, with the upper box in the x-z-plane, and the lower one in the y-z-plane, respectively.

The optical elements represented in vertical white lines with the center-numbered box as the number of that element. The y-axis value shows the maximum calculated spot size within the cavity. The x-axis value shows the distance between each optical element within the resonant cavity. The distance edited at the "distance (mm)" row at the *Parameter Field* window (Figure 3.15 b).

The optical elements represented by vertical lines within the mode plot represented by three types of elements, identified by triangular symbols.

- Mirrors: Filled rectangular triangles.
- Dielectric interfaces: Open rectangular triangles.
- Lenses: Filled isosceles triangles.

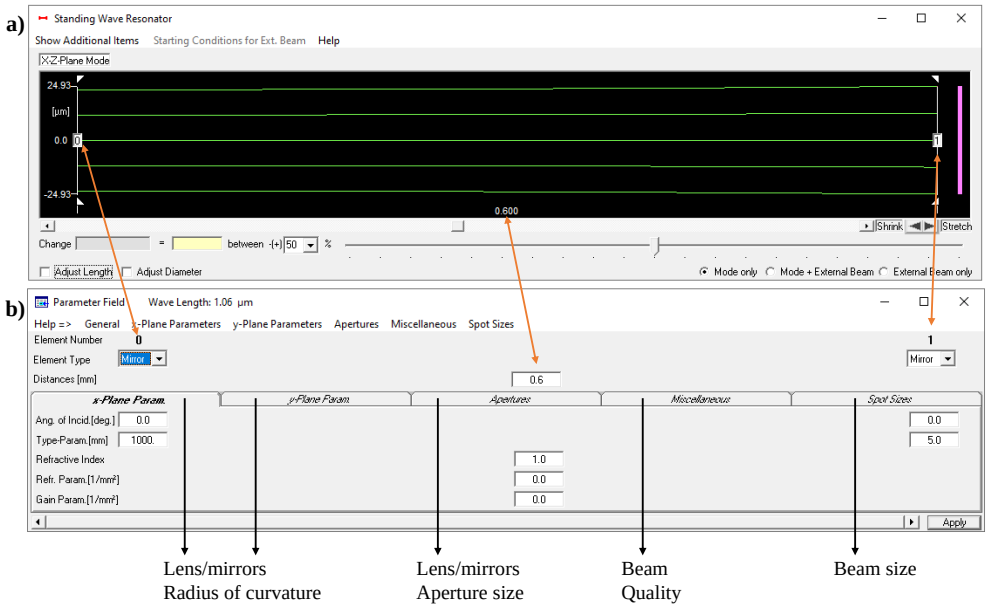

Figure 3.15 — (a) is the *Standing Wave Resonator* window, and (b) is the *Parameter Field* window.

3.2.2 Crystal, Pump Beam, and Material Parameter window

LASCAD™ uses Finite Element Analysis to compute the temperature distribution, deformation, and stress of a thermally loaded crystal. The dimension of the crystal is defined by the imported thermally loaded crystal data from Zemax®.

The *Crystal, Pump Beam, and Material Parameters* window or FEA window accessed through the *Main menu → FEA → FEA/Parameter Input & Start of FEA Code*, as shown in Figure 3.16.

Model: Choose "Cylindrical rod with numerical input of pump light distribution", then insert the size of the crystal.

Pump Light: Choose "ZEMAX – Product of ZEMAX Development corporation"

Boundaries: Cooling
- Insert the position of the colling surface of the rod

Material Param.:
- Change according to the figure

Doping & Mats.: Ignored

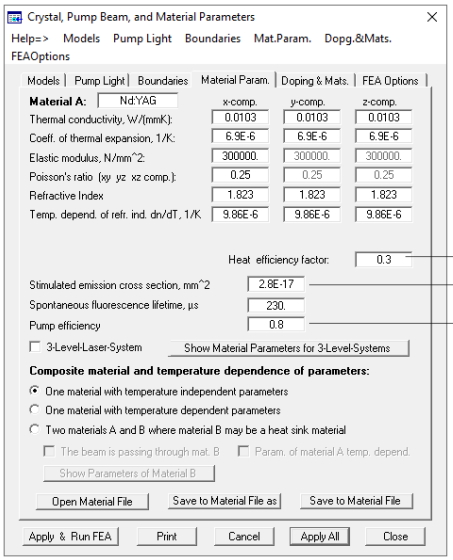

FEA Options:
- Insert mesh size same as the Zemax detector
- Increase the iteration from 10 to 300 for both Thermal and Structural analysis.

In between 0.5 to 0.8

From Data Sheet

Change from 0.8 to **1**

Figure 3.16 — Crystal, Pump Beam, and Material Parameters window.

This dialog box consists of six accessible tabs *Models*, *Pump Light*, *Boundaries*, and *Mat. Param*, *Doping & Mats*, and *FEA Options*.

Each tab serves as input conditions for FEA calculation for a single thermally loaded crystal and filled according to the physical conditions of the laser system to get an accurate numerical calculation.

"Apply & Run FEA" Button:

Clicking on the "Apply & Run FEA" button for the first time, without defining the FEA output directory, will prompt a window to save the FEA calculation directory. It is advisable to save within the same directory as the working LASCAD™ file. FEA output files are written in text file format.

After clicking on "Apply & Run FEA", it prompts a directory window to select the Zemax®'s detector data file. When the FEA calculation starts, a loading *Finite Element Analysis* dialog box will then pop up showing computational progress. During FEA calculation, it shows the iteration number, the maximum thermal analysis value, or the value of the maximum nodal displacement for the structural analysis. The "Skip" button stops the iteration process and finishes the numerical computation of thermal or structural analysis. A "FEA finished successfully!" message appears when the last iteration computation of structural analysis is complete.

3.2.3 Analysis of thermal lensing effects by FEA

3.2.3.1 2D data profiles & parabolic fit

This window accessed from the *Main menu → FEA → 2D data profiles & parabolic fit*. A directory window will then ask to load a *FEA_x_y.out* file, i.e., the FEA output files from the previous subsection. The window *2D data profiles & parabolic fit* shown in Figure 3.17. Each 2D profile has a single curved blue line, which represents the loaded FEA data. The x-axis is the same size as the crystal rod diameter and the y-axis changes depending on the selection of the Show Profile.

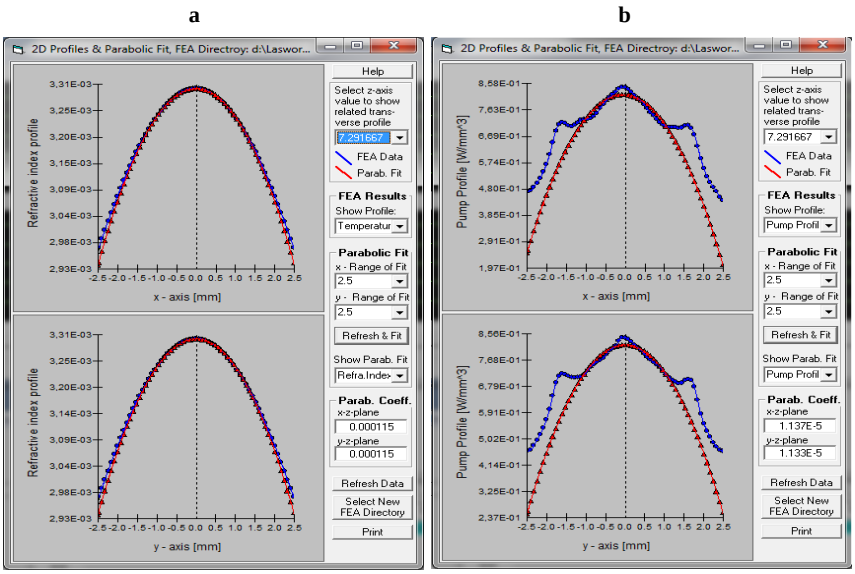

Figure 3.17 — 2D Profiles & Parabolic Fit windows. (a) Temperature fitting and (b) Pump Profile fitting.

After clicking on the "Refresh & Fit" button, a small yellow instruction dialog box will then prompt to remind the user to insert the calculated thermally loaded crystal in the *Standing Wave Resonator* window in between two elements by pressing both the ALT key and left clicking with the mouse. A yellow-coloured thermal lens (thermally loaded crystal) will add to the plot, as shown in Figure 3.18. The inserted crystal automatically changes the diameter for both elements and sets its distance based on its length in the *Parameter Field* window.

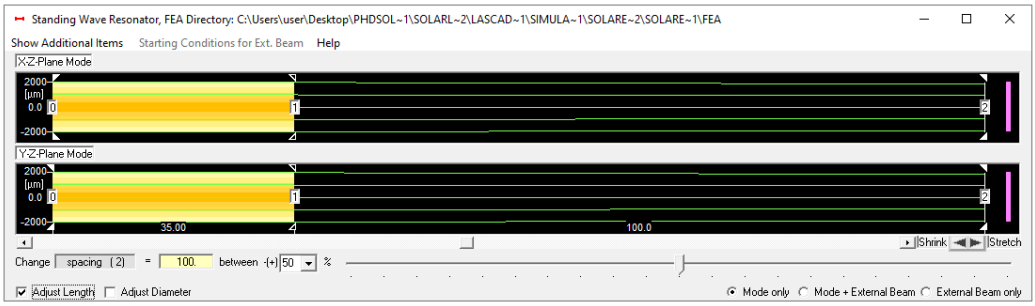

Figure 3.18 — Standing Wave Resonator windows after inserting the thermally loaded crystal (orange) between elements 0 and 1. The end-pump resonant cavity is defined by three elements: coated mirror (element 0), a dielectric interface (element 1), and an output mirror (element 2).

Note: The old thermal lens in the *Standing Wave Resonator* window must be cleared beforehand, by pressing the CTRL key and clicking with the left mouse button on the thermally loaded crystal.

3.2.3.2 3D Visualizer

The LASCAD™ *3D Visualizer* window, as shown in Figure 3.19, accessed after the FEA simulation at any time by selecting the *View* option in the LASCAD™ *Main menu* window. Various physical representations of thermally loaded crystal in terms of heat load, temperature, stress intensity, structural deformation, and absorption is changeable in the *View* menu.

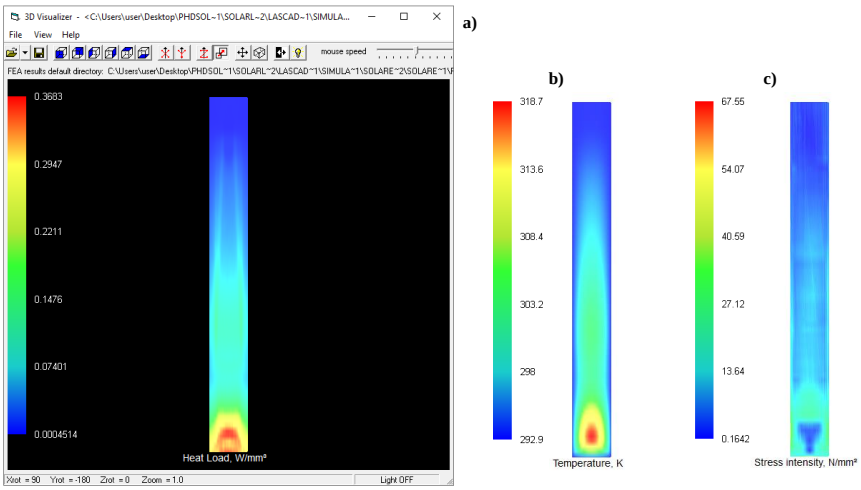

Figure 3.19 — (a) Heat load of the thermally loaded crystal in 3D Visualizer window. (b) is the temperature and (c) is the stress intensity of the thermally loaded crystal.

3.2.4 Laser beam propagation method (BPM)

The beam propagation method (BPM) is an alternative approximation that takes full advantage of the 3D distribution of the refractive index and the structural deformation obtained from the FEA by considering the physical optics code, based on FFT (Fast Fourier Transform). Unlike ABCD-based optical coding, the BPM does not consider parabolic approximation. This method takes wavefront propagation through each FEA crystal layer. The cavity configuration shaped by the Gaussian algorithm (at the *Parameter Field* window), and it used as an input for BPM. The beam profile is computed using an iterative computation of the Fox and Li round-trip procedure that involves a more complex computation method [57]. The iterative process shows the convergence of the theoretical approximated spot size generated in the cavity. Simultaneously, a 3D graphical representation of the intensity distribution windows in the output-coupling mirror after each round-trip. At the end of a single iteration process, it displays the phase profile.

3.2.4.1 Convergence of laser beam radius with cavity iteration window

The *convergence of laser beam radius at the cavity iteration* window appears after a single Fox and Li iteration, as shown in Figure 3.20 a), with the x-axis as the cavity iteration and the y-axis as the spot size of in micrometre. The y-axis information can be switched from radius at 1/e^2 or 1/e with the option control below the graph. The input text box can change the accuracy of the graph at box axes, respectively.

3.2.4.2 Laser beam profile on the right end mirror

The *Intensity Profile on the Transversal Plane – Compaq Array Viewer* window shows the laser beam intensity profile at the right end mirror, as shown in Figure 3.20 b). The plot refreshes each cavity iteration. The BPM menu item “View/Intensity along beam path” shows the intensity distribution along the resonator axis and x-axis.

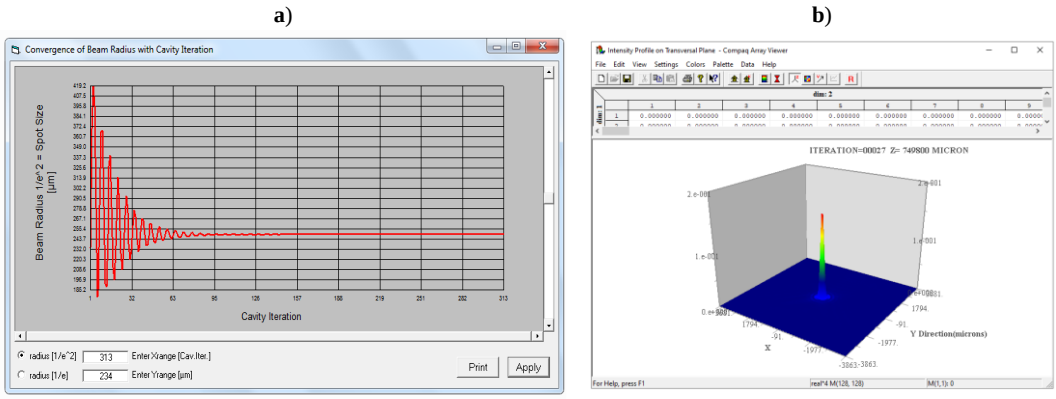

Figure 3.20 — (a) Convergence of Beam Radius with Cavity Iteration windows of 250 µm spot size at 313th Cavity iteration. (b) Intensity Profiled on Transversal Plane - Compaq Array Viewer window at 27th iteration.

3.2.5 Computation of laser output power

The *Laser Power Output* window (Figure 3.21) can be accessed from the LASCAD™ *Main* window.

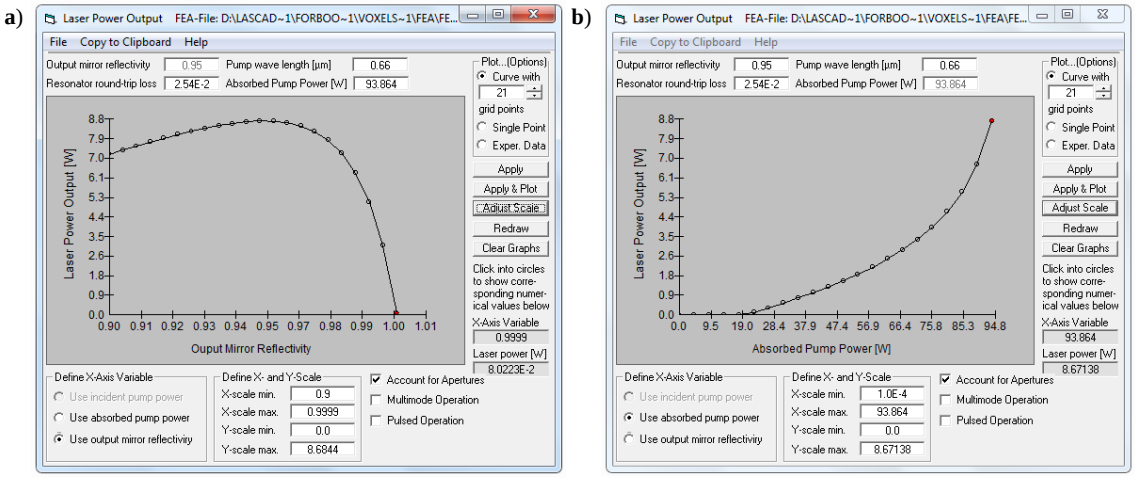

Figure 3.21 — Laser Power Output window. (a) Laser output power in function of output mirror reflectivity, and (b) Laser output power in function of absorbed pump power.

The top side of the window defines the lasing parameter of the cavity, such as the reflectivity of the output mirror, the percentage of a complete resonator round-trip loss, the pumping wavelength, and the absorbed pump power.

The complete resonator round-trip loss follows Equation (3.7).

$$Round\ trip\ loss\ (\%) = 2\ \alpha_s\ L_{rt} + I_{mp} + D_{Loss} \tag{3.7}$$

where the α_s is the scattering coefficient, the factor of laser power is lost inside of the crystal at a two-way roundtrip length (L_{rt}); I_{mp} is the imperfection of the crystal; and D_{loss} is the diffraction loss. For Nd:YAG crystal, the α_s is typically 0.002 cm^{-1} (or 0.2%) and I_{mp} is about 0.004 (or 0.4%).

Based on the numerical optimization of the solar laser systems in both Zemax® and LASCAD™, the solar laser heads and laser resonator mechanics were design in AUTOCAD® and then produced in Lisbon. The laser prototype cross-section image can be found in section 6.3.3.2, section 7.1.1.2, section 7.2.1.2, while the resulting solar-pumped laser measurements are presented in section 7.1 and 7.2.

3.3 Focal spot analysis of primary solar concentrators with ANSYS™ software

This chapter outlines the basic operating procedure for interfacing Zemax® with ANSYS™. The 2D detector data obtained from Zemax® at the focal point is superimposed on a cylinder of identical dimensions to calculate the temperature in ANSYS™ software. ANSYS™ is a simulation software used for engineering analysis, employing Finite Element Analysis (FEA) to simulate models of structures, electronics, machine components, and analyse their properties such as strength, toughness, elasticity, temperature distribution, electromagnetism, fluid flow, and other inherent or user-defined attributes.

All ANSYS™ simulations were carried out on the ANSYS™ workbench. Figure 3.22 illustrates the two sets of operations required to interact with the Zemax® data. Figure 3.22 a) depicts two connected analysis systems for FEA calculation. Group A, which includes external data, serves to import any external data. Group B is the transient thermal method of FEA calculation, which computes the propagation and distribution of temperature as a function of time.

a

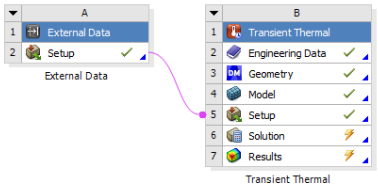

b

Table of File - C:\Users\user\Desktop\phd solar pumped laser\forno solar\re-done\Ansys - temperature\1B - d

	A	B	C	D	E
1	Column	Data Type	Data Unit	Data Identifier	Combined Identifier
2	A	X Coordinate	mm		File1
3	B	Y Coordinate	mm		File1
4	C	Heat Flux	W mm^-2	HeatFlux1	File1:HeatFlux1

Preview of File - C:\Users\user\Desktop\phd solar pumped laser\forno solar\re-done\Ansys - temperature\1B -

	A	B	C
1	X Coordinate	Y Coordinate	Heat Flux
2	0.	0.	0.2299
3	0.	0.2	0.2531
4	0.	0.4	0.2519
5	0.	0.6	0.282
6	0.	0.8	0.2512
7	0.	1.	0.2605
8	0.	1.2	0.3009
9	0.	1.4000000000000001	0.3805
10	0.	1.6	0.3964
11	0.	1.7999999999999998	0.3708

Figure 3.22 – a) ANSYS™ workbench project schematic setup for temperature calculation in Transient Thermal analysis system influenced by the imported Zemax® file at External data analysis system. b) ANSYS™ external data configuration by accepting three data columns extracted from the Zemax® detector data file.

The native Zemax® detector file is not compatible with ANSYS™ input, unlike LASCAD©. However, ANSYS™ can import any universal text-based file, such as a *.DAT file extension, through the External Data function. Figure 3.22 b) illustrates the reading configuration of the External Data from the file, which reads the content column by column. In this case, column A is considered the X-axis in millimetre length, column B as the Y-axis, and column C as the heat flux in W/mm^2. Each line corresponds to a single heat flux pixel at the X and Y coordinates on the detector.

Figure 3.23 illustrates how the matrix-formatted data shown on the detector in Zemax® can be easily converted into the necessary data format for ANSYS™. The conversion process can be automated using Microsoft Excel or programming languages such as Matlab®, Mathematica®, JavaScript, C++, and others.

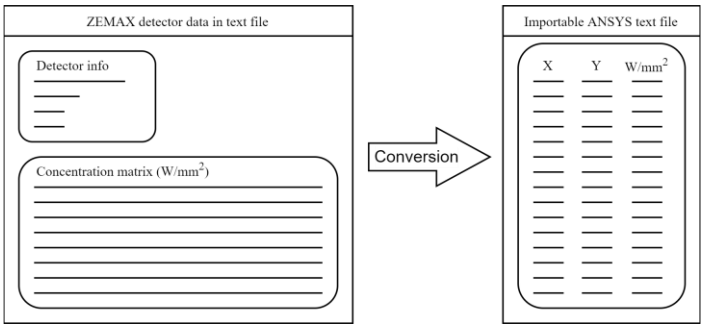

Figure 3.23 - Zemax® matrix data converted into importable/readable form for ANSYS™.

The imported heat flux map data from Zemax® overlaid on the cylindrical temperature detector is depicted in Figure 3.24 a). The cylinder was designed within the Geometry window of ANSYS™ and modelled with matching coordinates as found in the Zemax® data. It had a diameter of about 4 cm and was meshed using the Tetrahedrons method with an element size of 0.4 mm. The imported data was then incorporated into the Transient Thermal analysis system as one of the setup conditions.

Before executing the FEA simulation, other conditions were assigned to the cylinder object. It was considered as a Graphite material with an emissivity of 0.85, which is the average emissivity of graphite at a working temperature above 3000 K [58]. Additionally, boundary conditions of convection were used on the disk surface with a constant heat transfer of 5×10^{-6} W/mm^2/K, which was equivalent to natural stagnant air convection. The radiation exchange between the surface in ANSYS™ was restricted by a grey-diffuse surface. The simulated temperature is shown in Figure 3.24 b), where a maximum temperature of 3773.4 K is attained at the center of the cylinder [39].

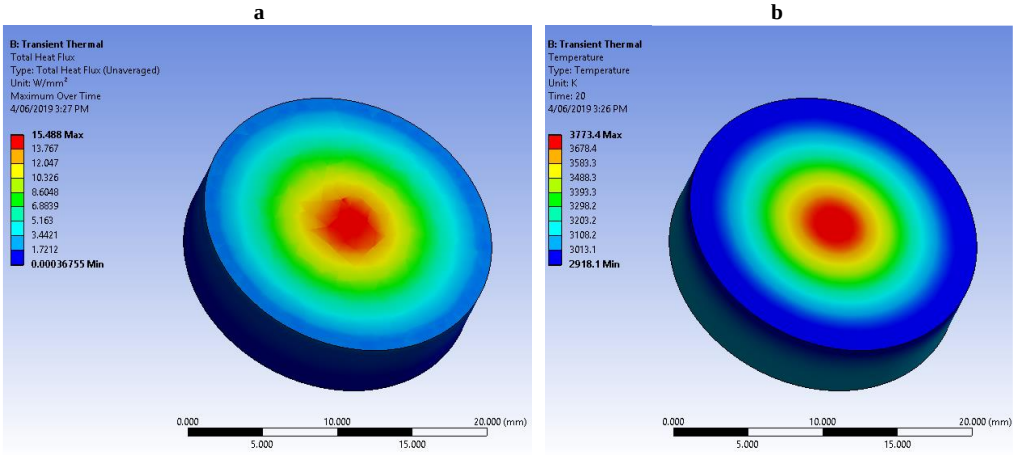

Figure 3.24 – **(**a) The imported heat flux data on top of the solid cylinder detector. (b) Temperature of the detector.

4

ELLIPTICAL SHAPED FRESNEL LENS DESIGN

4.1 State of the art

The shaped Fresnel lens, in contrast to its flat counterparts, exhibits enhanced concentration capabilities attributed to the reduction of chromatic aberration resulting from its curved design. Despite its promising potential, research in this field has been relatively limited, mainly due to the intricate process of integrating Fresnel equations onto a curved surface. Additionally, the existing body of research often relies on theoretical predictions, lacking real-world measurements for comparison.

This chapter introduces a novel, straightforward modelling approach for an elliptically shaped Fresnel lens. The method not only outlines the modelling process but also details the calculation of concentration. To validate the proposed model, a comparative analysis is conducted, juxtaposing the results with those obtained from a peer-reviewed article focused on a flat Fresnel lens. This approach aims to contribute to the existing body of knowledge by providing a more accessible and practical method for modelling and assessing the performance of elliptical-shaped Fresnel lenses.

A novel three-dimensional elliptical-shaped Fresnel lens (ESFL) analytical model is presented to evaluate and maximize the solar energy concentration of Fresnel-lens-based solar concentrators. AutoCAD®, Zemax® and Ansys™ software were used for the ESFL design, performance evaluation and temperature calculation, respectively. Contrary to the previous modelling processes, based on the edge-ray principle with an acceptance half-angle of ±0.27° as the key defining parameter, the present model uses, instead, a Gaussian distribution to define the solar source in Zemax®. The results were validated through the numerical analysis of published experimental data from a flat Fresnel lens. An in-depth study of the influence of several ESFL factors, such as focal length, arch height, and aspect ratio, on its output performance is carried out. Moreover, the evaluation of the ESFL output performance as a function of the number/size of the grooves is also analysed. Compared to the typical 1–16 grooves per millimetre reported in the previous literature, this mathematical parametric modeling allowed a substantial reduction in grooves/mm to 0.3–0.4, which may enable an easy mass production of ESFL. The concentrated solar distribution of the optimal ESFL configuration was then compared to that of the best flat Fresnel lens configuration, under the same focusing conditions. Due to the elliptical shape of the lens, the chromatic aberration effect was largely reduced, resulting in higher concentrated solar flux and temperature. Over 2360 K and 1360 K maximum temperatures were found for ESFL and flat Fresnel lenses, respectively, demonstrating the great potential of the three-dimensional curved-shaped Fresnel lens on renewable solar energy applications that require high concentrations of solar fluxes and temperatures.

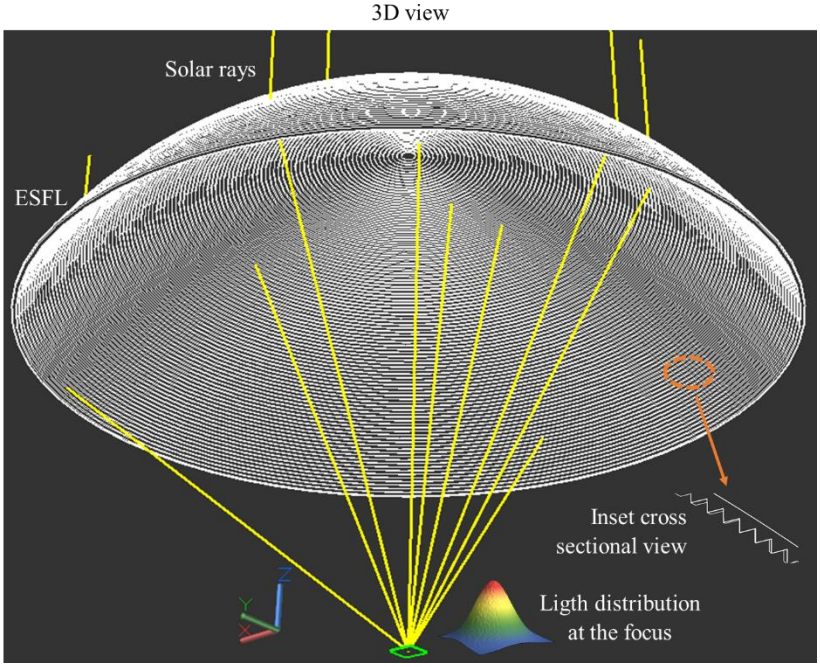

Figure 4.1 — 3D view of the ESFL in AutoCAD®.

4.2 Introduction

According to [59], optical concentration can significantly reduce the cost of photovoltaic cells. By using mirrors and lenses, high-concentration photovoltaic technology concentrates sunlight from a large area onto a smaller area of active semiconductor cells, resulting in direct conversion of sunlight into electricity [60, 61]. The Fresnel lens, known for its simple structure, light weight, low cost, and ease of processing [62], has been widely employed in the field of concentrated photovoltaics. However, its strong achromatic aberration limits its concentration ratio.

To overcome this issue, non-flat Fresnel lenses have been widely studied by many researchers, proposing new modelling methods and configurations with the aim of increasing the solar energy concentration. The shaped Fresnel lens conception was initiated in 1977 by Cosby [63]. One year later, a patent was filed by O'Neill [64], while Kritchman published his finding [21]. Since then, many other researchers throughout the world have been proposing their own non-flat Fresnel lens models and modelling processes [3, 22-25, 65]. Currently, the most notable work in this field is a published book by Leutz et al. [26], who presented an in-depth study of the non-flat shaped Fresnel lens.

The modelling process of the shaped Fresnel lens follows Snell's law (or law of refraction). The half-angle subtended by the Sun is the key parameter to set the size of the refractive prism facets by using the edge-ray principle, which adjusts the number of grooves required for the concentrator. It dictates the absolute angle at which the solar rays arrive at the surface of the Earth globe. The Sun–Earth subtended acceptance half-angle of 0.27° can be determined by the mathematical relationship between the radial size of the Sun and its distance to the Earth [20, 27, 35]. It stands valid from a theoretical and mathematical perspective, being considered by many researchers in the field of solar energy

concentration [3, 20-33, 35]. However, this angle could only be accepted if the Earth had no atmosphere. The sudden change from vacuum to Earth's atmosphere significantly alters the trajectory of solar rays due to the law of refraction. The solar rays pass through various atmospheric layers, such as the thermosphere, mesosphere, stratosphere, and troposphere. Each individual layer's gaseous composition has its own refractive index, influencing the refraction angle. Moreover, the half-angle subtended by the Sun can be different depending on geographical location, time zone, and local atmospheric conditions, such as the presence of clouds, humidity, sand particles and pollution in the troposphere. Therefore, within the Earth's atmosphere, the acceptance half-angle should be larger than 0.27°. These complex systems that influence the refraction of sunlight on Earth were neglected by most researchers in this field, who had adopted the half-angle of 0.27° as a standard for their works [3, 21-35]. This oversimplification in the acceptance half-angle calculation paired with the edge-ray principle has set and cemented the number and size of grooves in the production of Fresnel lenses in the market [66].

There are two categories of simulation methods for evaluation of the concentration systems: one by ray tracing and the other by analytical approach [67, 68]. The ray-tracing method simulates a vast number of discrete and well-defined rays of different wavelength, energy and traveling trajectory. Each ray has its own trajectory, which is influenced by the transmission, reflection, or refraction in a medium within its path. It is only numerically completed when the ray hits an absorbing detector or reaches an annihilation condition. This category has an accurate prediction of the flux distribution, but with the cost of high computing complexity, power, and time. Several pre-existing reputable ray-tracing tools are available in the market, such as Zemax® [39, 69, 70], LightTools® [29, 71-73] and Soltrace® [74]. The existing software are reliable, robust, user friendly, easy to learn and allow repeatability, making them great tools to expand new fields of research.

The analytical method, which uses self-developed computational codes and programs to outline the distribution of flux density, has been widely adopted in the field to greatly reduce computing time [22-25, 31, 32]. However, each research group has their own unique source code, which may differ greatly from others, and there is no guarantee that the code has been correctly implemented or that all critical parameters or functions have been incorporated. Therefore, the outcomes of this method may vary greatly due to these uncertainties.

Analysing the focused solar image is crucial in solar concentration research as it helps determine the achievable maximum concentration and flux distribution at the focal zone. It is essential to carefully examine and present these key features. To ensure the accuracy of numerical or analytical results, they should be experimentally validated or compared with existing experiments.

In this work, a parametric modelling procedure of a three-dimensional elliptical-shaped Fresnel lens is presented, using Snell's law. The ESFL is designed in AutoCAD®, and then imported into Zemax® non-sequential ray-tracing software for numerical evaluation of the ESFL output performance. In this evaluation, a Gaussian distribution based on measured data from the literature [36] is considered to define the solar source, instead of the classical edge-ray principle method with a solar acceptance half-angle of 0.27°. To validate the analytical model, this was applied in the performance evaluation of a flat Fresnel lens with published experimental data [75], whose results were in accordance with those

obtained through the proposed model. An in-depth study of the influence of the ESFL parameters, such as focal length, arch height, and aspect ratio on its output performance, in terms of concentrated solar flux, optical efficiency and full width at half maximum (FWHM), is also carried out. Furthermore, to the best of our knowledge, this is the first time that the ESFL concentration efficacy is evaluated as a function of the number of grooves, with optimal 0.4–0.3 groove numbers per millimetre being found.

This study reveals that the number of grooves necessary to maximize the concentrated solar flux could be significantly reduced in relation to that reported by the literature and market, which may enhance the cost efficiency of the manufacturing process of Fresnel lens solar concentrators. From the abovementioned studies, the best ESFL design is found. The optimal concentrated solar flux value within its focal cone is then analysed and compared to that of a flat Fresnel lens, which proved the effectiveness of the ESFL in substantially reducing the chromatic aberration and, consequently, on maximizing the solar flux.

The temperature analysis of both concentrators is also performed by ANSYS™. The maximum temperatures of 2360 K and 1360 K were attained from the ESFL and the flat Fresnel lens, respectively, demonstrating once more the potential of the ESFL in many solar energy research and applications that require high solar flux and temperature.

4.2.1 Advantages and disadvantages

The advantages of a shaped Fresnel lens compared with a flat Fresnel lens are:

- Reduction of the chromatic aberration effect.
- Have higher structural integrity and mechanical stability.
- Non-imaging lens.

The disadvantages of the shaped Fresnel lens include:

- The complexity of manufacturing this type of lens, and the precision required would be quite expensive.
- Non-imaging lens.

4.3 Modelling

The shaped Fresnel lens is characterized as a chain of a well-defined prism (grooves) aligned along an outline, such as a semicircle or an ellipse. Each prim individual prism is designed and optimized so that most of the refracted light will focus on the same focal position.

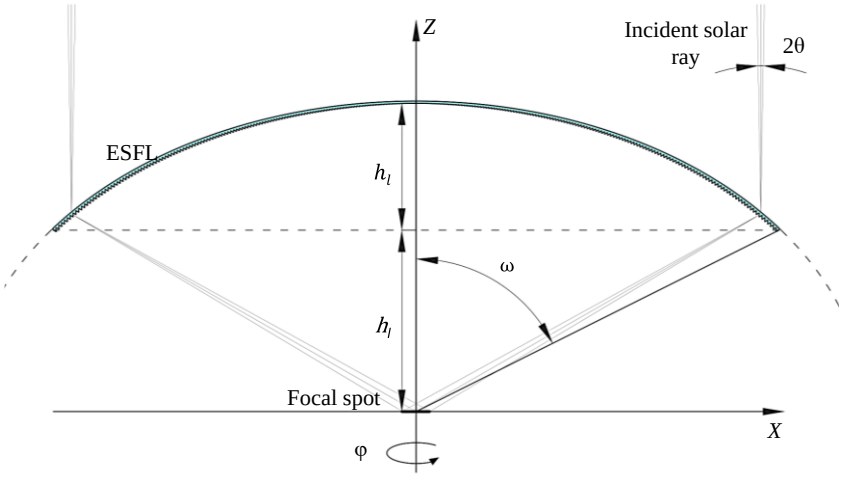

Figure 4.2 — Elliptical-shaped Fresnel lens. θ is the half angle from the Sun to Earth, ω is the aperture angle, f_l is the focal length, h_d is the height of the lens, and φ the angular rotation of the lens.

The general parameters to model an ESFL are:

- r – Radial aperture (mm) defines the size of the concentrator.
- h_f – Focal length (mm), which defines the vertical distance between the focus and the outmost prism of the concentrator.
- h_l – Lens height (mm) defines the height of the "arch".
- d_t – Lens thickness (mm), is the thickness of the substrate below the grooves.
- n_λ – Refraction index of medium and wavelength dependents.
- $\delta\omega$ – Division angle (°), defines the size of each groove.
- θ_P – Pitch angle (°), or "draft angle".

4.3.1 Defining the size of the ellipse

The shape of the elliptical arch depends on r, h_f and h_l. These parameters are required to draft the elliptical shell. The mathematical model of the ellipse is described at Equation (4.1), with "a" being the major axis length and "b" as the minor axis length, as shown in Figure 4.3. The curved segment of the parabola is used as the outline for the shaped Fresnel lens. Within the minor axis "b", h_f defines the focal distance of the lens, and the h_l is the height of the lens.

$$\frac{x^2}{a^2} + \frac{y^2}{b^2} = 1 \tag{4.1}$$

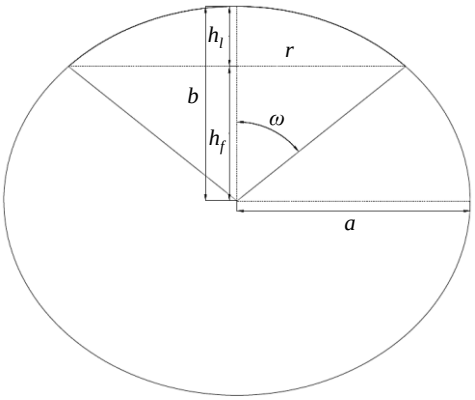

Figure 4.3 — The ellipse with major axis length of $\underline{a}$ and minor axis length of $\underline{b}$. The useful elliptical arch is defined by a radial aperture r and arch height of h_l. This arch has a focal length of h_f and aperture angle of ω.

Both major and minor axes are calculated at Equation (4.2):

$$\begin{cases} a = \dfrac{b \times r}{\sqrt{b^2 - {h_f}^2}} \\ b = h_f + h_l \end{cases} \tag{4.2}$$

4.3.2 Numbers of prisms

The prims are aligned or chained through the outline of the ellipse arch with the input facets facing toward the Sun. The number of prims or grooves (N) is defined by the divisions of the aperture angle with the angular segments ($\delta\omega$), shown in Equation (4.3).

$$N = \frac{\omega}{\delta\omega} \tag{4.3}$$

4.3.3 Single prism modelling

In Figure 4.4 shows a single arbitrary prism and a ray traveling vertically. The incoming solar ray comes from top to bottom into the input facet. The ray is then bend within the medium through Snell's law and is then further bent outward at the exiting facet toward to origin point (focal point), as described in Equation (4.4).

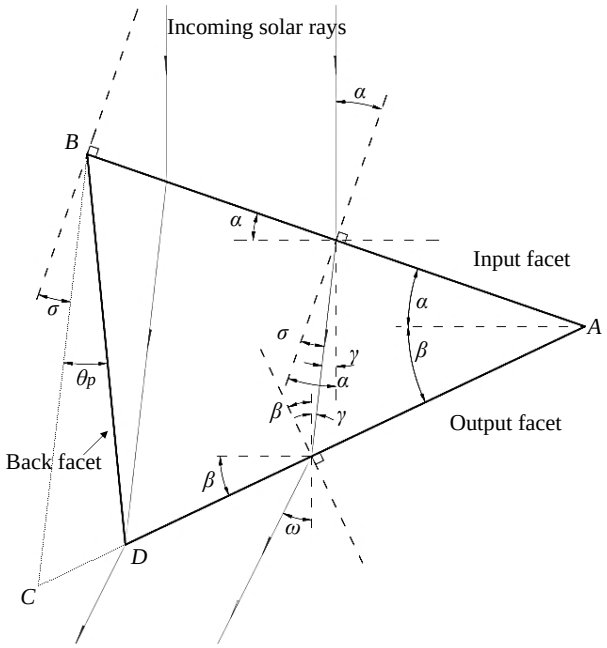

Figure 4.4 — The light path getting in and out through an *ABD* prism. The angles α, β, γ, σ, θ_p and ω are the characteristic angles for the Snell's law equations that the vertical incoming ray would exit at angle ω.

In this case, the incoming ray with the prism can be simply described by the Snell's law at the following equation:

$$\begin{cases} \sin(\alpha) = n_\lambda \ \sin(\alpha - \gamma) \\ n_\lambda \sin(\beta + \gamma) = \sin(\beta + \omega) \end{cases} \tag{4.4}$$

The angle α is the input angle originated from the difference of the normal angle from the input facet with the angle of incidence. The difference of $\alpha - \gamma$ is the changed angle within the medium at refractive index of n_λ. The angle β is the slope angle of the exiting facet in relation to the horizontal line. The sum of both $\beta + \gamma$ is the angle normal to the exiting facet, while $\beta + \omega$ is the exiting angle in relation to the exiting facet toward to the focus.

4.3.3.1 Input facet coordinate

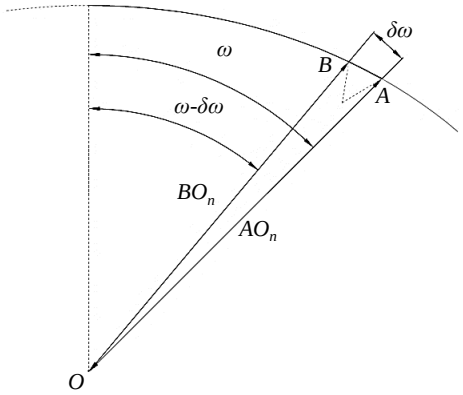

Figure 4.5 — A small segment of facet *AB* is acquired by defining a division angle of $\delta\omega$. The point *A* starts at angle ω, and point *B* ends at angle ω-$\delta\omega$ on the arch. *AO* and *BO* are the length between point *A* and *B* to *O* origin.

Knowing the size of the shaped Fresnel lens, then the outmost prism is the first to be modelled, as shown in Figure 4.5. The point *A* is defined as the vertex of the prism which binds the input and output facet. The point *B* is the other end of the input facet which binds with the back facet. The Equations (4.5) and (4.6) calculates the distance between *A* and *B* in relation to origin point (focal point). The size of the input facet *AB* is defined by size of the $\delta\omega$. A larger $\delta\omega$, means a larger input facet. The parameter *n* is the prism number, hence, $n = 1$ is the first prism (farthest prism of the lens), then $n = 2$ is the second prism, and so on, up until $n = N$ (central prism of the lens). The total number of grooves represents only half of the arch, since other the side is symmetrically identical.

$$AO_n = \frac{a \times b}{\sqrt{a^2 \cos(\omega - (n-1)\delta\omega)^2 + b^2 \sin(\omega - (n-1)\delta\omega)^2}} \tag{4.5}$$

$$BO_n = \frac{a \times b}{\sqrt{a^2 \cos(\omega - (n)\delta\omega)^2 + b^2 \sin(\omega - (n)\delta\omega)^2}} \tag{4.6}$$

The coordinates of point *A* and *B* are described in Equation (4.7) and (4.8).

$$\begin{cases} x_{n,A} = AO_n \ \sin(\omega - (n-1)\ \delta\omega) \\ y_{n,A} = AO_n \ \cos(\omega - (n-1)\ \delta\omega) \end{cases} \tag{4.7}$$

$$\begin{cases} x_{n,B} = BO_n \ \sin(\omega - (n)\ \delta\omega) \\ y_{n,B} = BO_n \ \cos(\omega - (n)\ \delta\omega) \end{cases} \tag{4.8}$$

The Figure 4.6 a) shows a single collimated ray incoming from top to bottom, arriving at angle α perpendicular to the prism input facet (AB_n). Through the diffraction of the material n_i, the ray is then turned by an angle of γ within the medium.

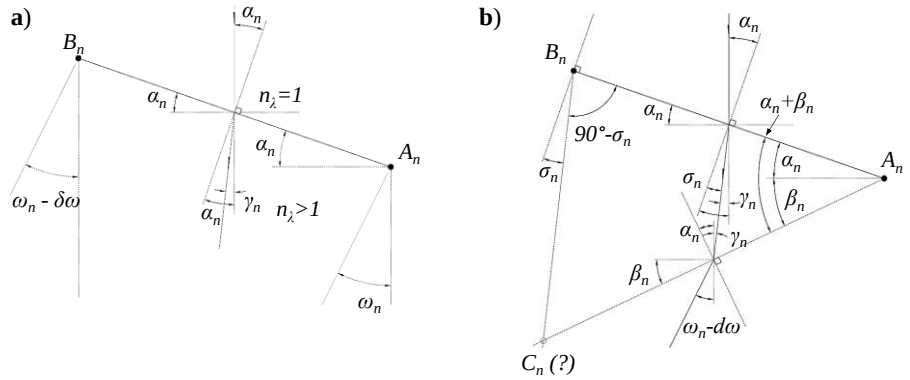

Figure 4.6 — (a) Collimated light ray interacting with the input facet (*AB*). α is the input light angle perpendicular to the facet *AB*. γ is the angle of the turned light path inside of the refractive material. (b) Exiting light ray from the output facet *AC* at output angle β.

With both coordinate of point, *A* and *B* known, then the facet length *AB* is trivially calculated by Equation (4.9):

$$AB_n = \sqrt{(x_{n,B} - x_{n,A})^2 + (y_{n,B} - y_{n,A})^2} \tag{4.9}$$

The input angle α at any given prism *n* is shown in Equation (4.10).

$$\alpha_n = \tan^{-1}\left(\frac{y_{n,A} - y_{n,B}}{x_{n,A} - x_{n,B}}\right) \tag{4.10}$$

The γ is obtained through Equation (4.11) by isolating the Snell's equation.

$$\gamma_n = \alpha_n - \sin^{-1}\left(\frac{\sin(\alpha_n)}{n_\lambda}\right) \tag{4.11}$$

4.3.3.2 Output facet coordinate and completing the prism

The output facet is determinate by the output angle β_n, which is determined by the refractive index of the material and output angle ω_n. In Figure 4.6 b) shows the exiting ray from the medium to the exterior through facet *AC* to the focus. The rays arrive at the focus at angle ω-$d\omega$, which is the angle in between ω and ω-$\delta\omega$. The back-facet *BC* adapts the same slope as the ray-path within the medium with the angle σ.

The output angle β_n can be calculated from inverting the Equation (4.4), as shown in Equation (4.12):

$$\beta_n = \tan^{-1}\left(\frac{n_\lambda \sin(|\gamma_n|) - \sin(\omega_n)}{\cos(\omega_n) - n_\lambda \cos(|\gamma_n|)}\right) \tag{4.12}$$

The exiting angle ω_n at n^{th} prism is presented in Equation (4.13):

$$\omega_n = \omega - (n-1)\delta\omega \tag{4.13}$$

To calculate the size of the output facet *AC* and the coordinate *C*, then a change of coordinate of the prism at point A_o as the origin point and B_o as the base coordinate is then needed, as shown in Figure 4.7 a). The coordinate of point C_o can be found at the intersection of the both lines coming out from the prism's vertex at point A_o and point B_o with angles α+β and 90°-σ, respectively.

The intersection of the two lines is shown at the following intersection condition at Equations (4.14) and the generic strait line of (4.15):

$$y_{AC} = y_{BC} \tag{4.14}$$

$$y = m(x - d) + c \tag{4.15}$$

The slope at point A_o and B_o are represented at following equations:

$$m_{A_{n,o}} = \tan(|\alpha_n| + |\beta_n|) \tag{4.16}$$

$$m_{B_{n,o}} = -\tan(90° - \sigma_n) \tag{4.17}$$

Then the output facet length ($AC_{n,o}$) has the following coordinates.

$$C_{n,o} = \begin{cases} x_{c_{n,o}} = \dfrac{m_{B_{n,o}}\, AB_n}{m_{A_{n,o}} - m_{B_{n,o}}} \\ y_{c_{n,o}} = m_{A_{n,o}}\, x_{c_{n,o}} \end{cases} \tag{4.18}$$

The facet $Ca_{n,o}$ length is the same as the following equation:

$$AC_{n,o} = \sqrt{(x_{c_{n,o}})^2 + (y_{c_{n,o}})^2} \tag{4.19}$$

The coordinate $C_{n,o}$ of the isolated prism is then integrated into the ESFL coordinated system; thus, the coordinate C is presented by following Equation (4.20):

$$\begin{cases} x_{n,C} = x_{n,A} - AC_{n,o}\cos(\beta_n) \\ x_{n,C} = y_{n,A} - AC_{n,o}\ \sin(\beta_n) \end{cases} \tag{4.20}$$

With all the coordinate A, B and C, then the prim is graphically formed, as shown in Figure 4.7 b).

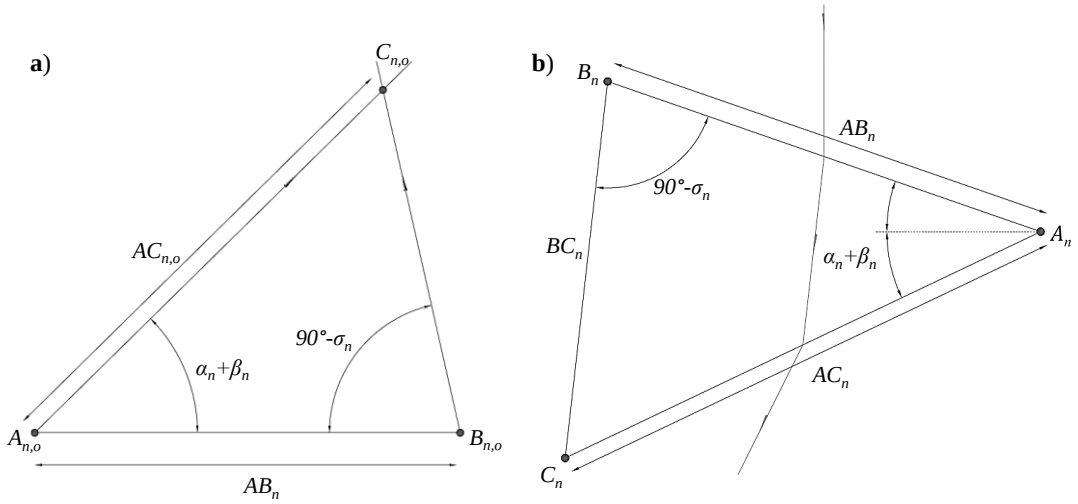

Figure 4.7 — **(**a) The point $C_{n,o}$ is acquired by the interception the two lines projected from $A_{n,o}$ and $B_{n,o}$ at angle $\alpha_n+\beta_n$ and 90°-σ_n. The point $A_{n,o}$ is considered an origin point (0, 0) and point $B_{n,o}$ with (*AB*, *0*). (b) A complete prism with all coordinates A_n, B_n, C_n localized and all facet size of AB_n, AC_n and BC_n known.

4.3.3.3 Pitch angle

As any real Fresnel lens composition, the pitch angle is an inevitable variable caused by the production process, as exemplified in Figure 4.8. Most of the mass-produced Fresnel lens were made by etching of a metallic mould of the injected hot plastic, such as PMMA. The original substrate shown at Figure 4.8 cannot be etched due to the inner hooked shape the groove. During fabrication process, a small part of the unused segment would be gone by means of etching or mechanically lathed, leaving a pitch angle.

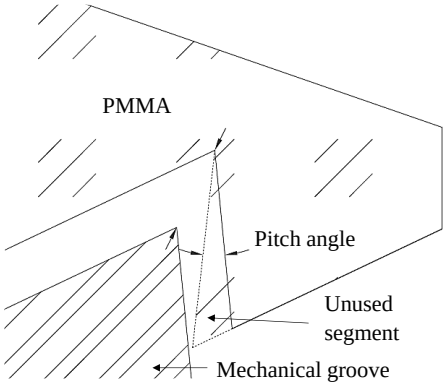

Figure 4.8 — Etching process of a Fresnel lens. The etching by vertical pressing leaves a mechanical groove print at the back facet of the prism. The pitch angle is formed by the characteristic of the mechanical groove.

One of the possible integrations of the pitch angle into the model is presented and shown in Figure 4.9 a), the pitch angle (θ_p) is subtracted from the angle at point *B*. Then point D_n is the intersection between the line AC_n and BD_n.

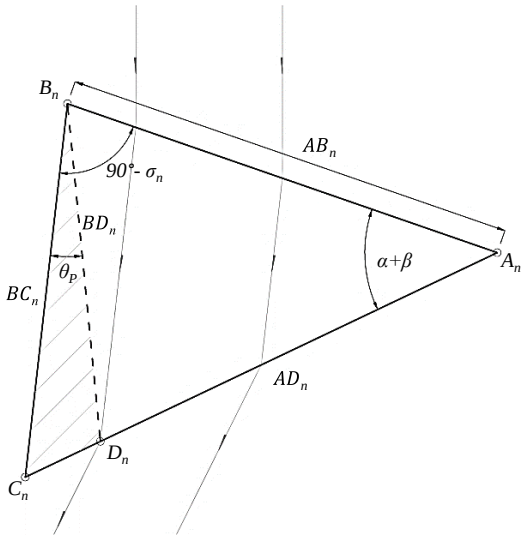

Figure 4.9 — The prism modification from ABC_n to ABD_n by the influence of pitch angle (θ_P).

The same procedure of changing the orientation of the prism done for Figure 4.7 a). The modified slope including the pitch angle ($m_{B_{n,o},p}$) is shown in Equation (4.21).

$$m_{B_{n,o},p} = -\tan(90° - \sigma_n - \theta_P) \tag{4.21}$$

The Equation (4.22) gives the coordinate of the isolated prims at point $D_{n,o}$.

$$D_{n,o} = \begin{cases} x_{D_{n,o}} = \dfrac{m_{B_{n,o},p}\, AB_n}{m_{A_{n,o}} - m_{B_{n,o},p}} \\ y_{D_{n,o}} = m_{A_{n,o}} x_{D_{n,o}} \end{cases} \tag{4.22}$$

The Equation (4.23) is the facet length of BD_n.

$$BD_n = \sqrt{(x_{D_{n,o}})^2 + (y_{D_{n,o}})^2} \tag{4.23}$$

Then coordinate of the reduced facet by including the pitch angle is presented in Equation (4.24).

$$\begin{cases} x_{n,D} = x_{n,A} - BD_n \cos(\beta_n) \\ x_{n,D} = y_{n,A} - BD_n \sin(\beta_n) \end{cases} \tag{4.24}$$

4.3.3.4 Thickness

The ideal prism shown in Figure 4.9 is not physically capable of joining a neighbouring prism. Expanding the output and the back facet at thickness (d_t) in relation to the input facet, changes the triangular prism shape into a new type of prism, as shown in Figure 4.10. Vertex *E* and *F* is the direct increment of d_t of point *B* and *A*, respectively.

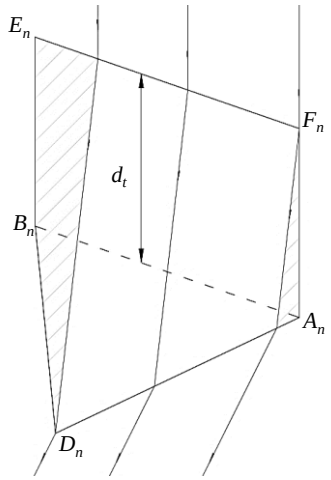

Figure 4.10 — Extension of thickness at BA_n facet to EF_n by length of d_t.

4.3.3.5 Prism chaining

The chaining process starts with joining the facet BE_n to the next prism facet AF_{n+1}, as shown in Figure 4.11. The strings of input facets EF_n maintains the original curvature elliptical shape obtained from the Equation (4.2).

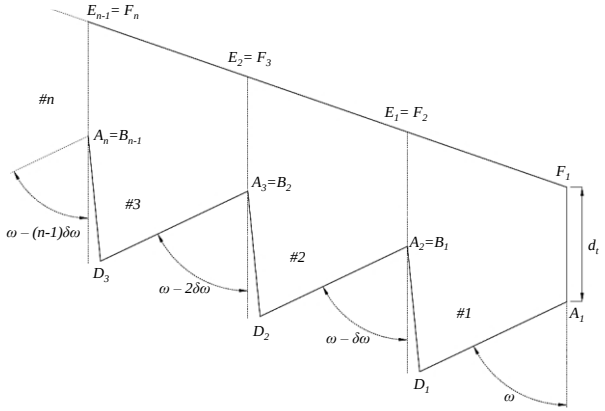

Figure 4.11 — The prism chaining process of the first three polygon.

4.3.3.6 Automation and coordinate extraction

The Figure 4.11 shows the first four segments of an ESFL coordinates imported into AutoCAD®. The coordinates are automatically drawn *Polyline* command. A complete ESFL would be drawn from

coordinates A_1, D_1, A_2, D_2, until D_N, then it continues from F_N to F_1 and finally ending by closing the *Polyline*. If done correctly, all the coordinates of the ESLF should be drawn in the positive quadrant of the cartesian space.

The conceptual model of the ESFL is no more than a list of coordinates of prisms chained together at one end to another end, forming a semi-arch. The coordinates of the ESFL can be automated with a simple recursive code, where all the vertices of the prism are calculated incrementally achieving the calculated number of prisms. In Figure 4.12 shows the flowchart for ESFL modelling.

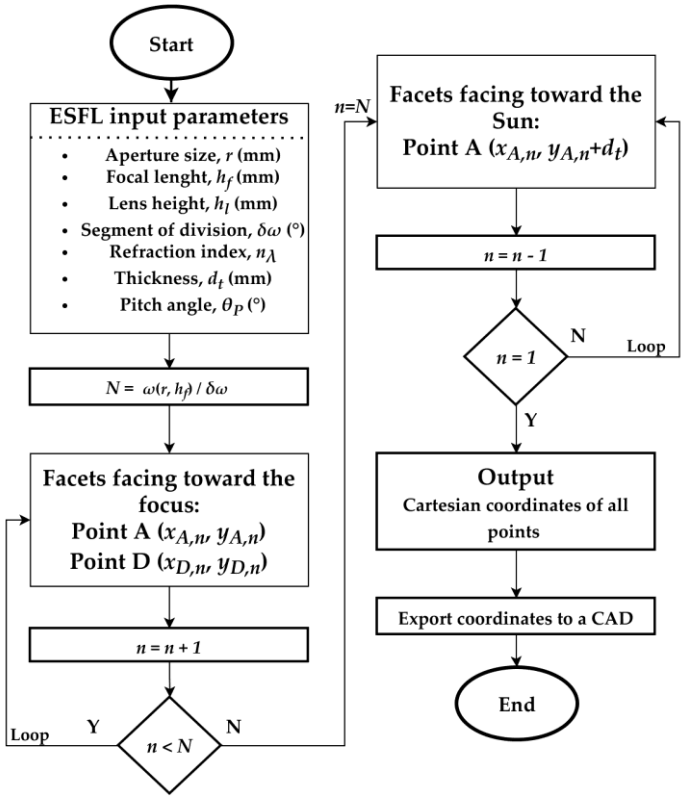

Figure 4.12 — Flowchart of ESFL modelling process.

The newly drawn 2D wire shaped ESFL can be converted into a 3D form of some shape or slab shape.

- Dome shape: Use the Revolve command on the 2D ESFL outline and revolve it for 360° along the Y axis to make a dome shape solid object, as shown in Figure 4.13 a).
- Slab shape: Use the mirror command on the 2D ESFL outline along the Y axis to make a duplicate, then use Extrude command to make a 3D slab ESFL, as shown in Figure 4.13 b).

Note 1: Use *Facetress* command then change the value to maximum (10) to achieve highest polygon count possible before exporting. Any optical design intended to be exported form a CAD should be as fine as possible.

Note 2: ESFL can only be correctly exported in IGES format.

Note 3: The CAD program or any imported program may become slow with too many grooves.

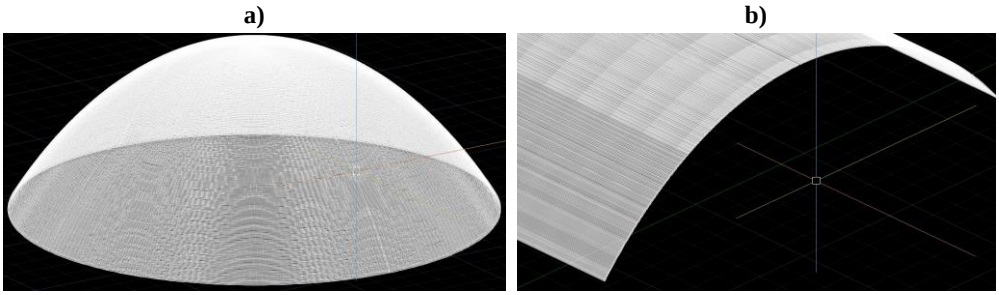

Figure 4.13 — 3D view of the ESFL in AutoCAD™. (a) The ESFL in dome shape. (b) The ESFL in slab shape.

4.4 Numerical Simulation Method

Figure 4.14 shows the sequence of the numerical simulation process in Zemax®. The sequence was the same for each ESFL configuration, but each output was unique in terms of concentrated solar flux, optical efficiency, and focal size at FWHM.

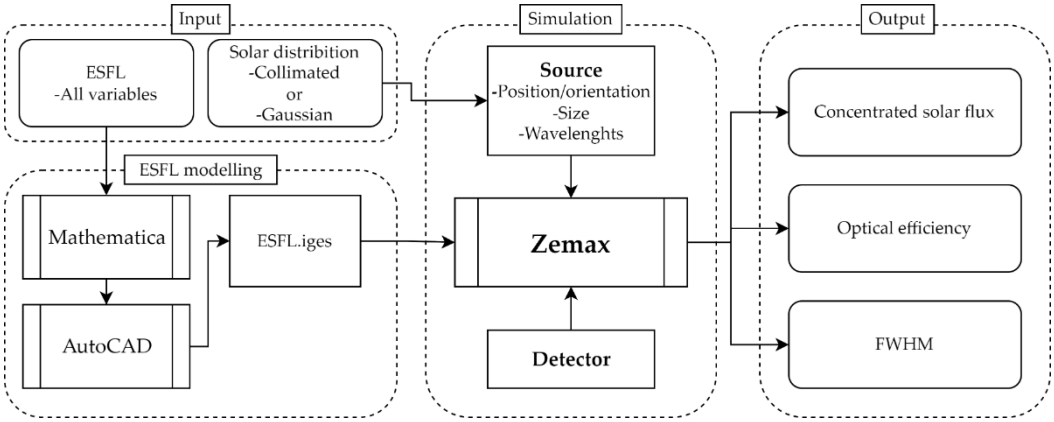

Figure 4.14 — Sequence diagram of a single numerical simulation.

Each individual coordinate of the ESFL was calculated with the Mathematica® programming language. Then, the coordinates of all the relevant Cartesian points were exported into AutoCAD® and linked as straight lines by the *polyline* command. The enclosed object was then revolved into a solid with the highest polygon count possible by adjusting the *facetres* command to its maximum. The object was then exported to Zemax® as an *IGES* file. Both AutoCAD® and the imported Zemax® object shares the same coordinates, as seen in X, Y, Z position of object 2 (the CAD imported object) in the non-sequential component editor windows as shown in Figure 4.15.

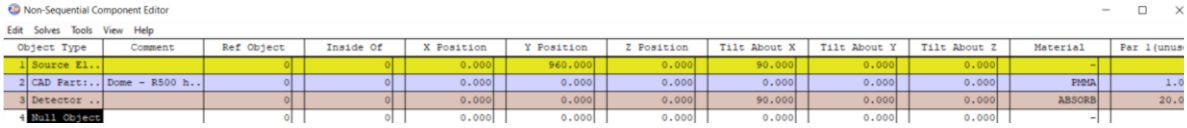

Figure 4.15 — The Non-sequential component editor window of Zemax® for the ESFL numerical simulation. The object 1 is the source positioned above the imported CAD ESFL object 2, the object 3 is the detector object.

4.4.1 Focal characteristics

Depending on the refractive index of the material used, the focal image of the elliptical shaped Fresnel lens (ESFL) is sensitive to wavelength and can experience chromatic Snell's deviation (achromatic aberration). Figure 4.16, which depicts the ESFL object in Zemax® under the same conditions as Figure 2.14, demonstrates some achromatic aberration issues as expected, similar to the flat Fresnel lens. However, the most concentrated focal spot produced by the ESFL is located closer to the mathematical focal length (Y = 0 mm), which reduces chromatic scattering when compared to a flat Fresnel lens of the same size and focal length [42].

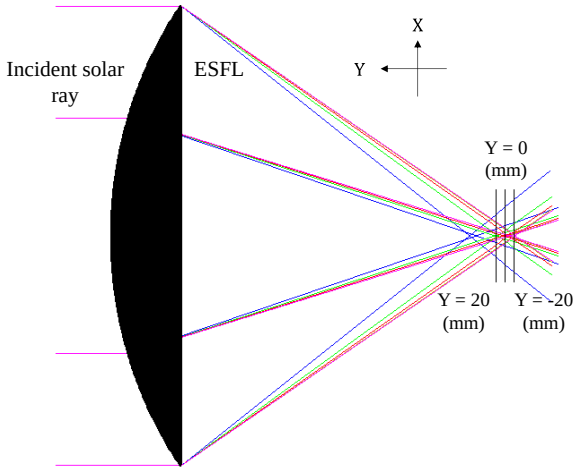

Figure 4.16 — Achromatic aberration caused by various collimated wavelengths onto the ESFL.

4.5 Results

4.5.1 Output solar distribution at the focal zone of the ESFL

To analyse the solar distribution at the focal zone of each ESFL configuration, over 60 million rays were employed per simulation. The output data were obtained from an absorbing detector with dimensions 20 × 20 mm^2 and resolution 150 × 150 pixels, positioned at the mathematical origin. The obtained data contained the solar distribution characteristics in terms of concentrated solar flux, optical efficiency (the total number of rays that strike the detector over the total emitted rays from the source) and FWHM.

Figure 4.17 shows the comparison of the three-dimensional focal distributions from a Gaussian source with $G_x = G_y = 35276$ and a collimated source with $G_x = G_y = 0$ (or infinite). In this case, an arbitrary ESFL model with 1 m diameter, $h_f = 400$ mm, $h_l = 400$ mm, $d_t = 3$ mm, and $\delta\omega = 0.20°$ (256 grooves), with $\theta_p = 12°$, was used. The focal shape formed by the Gaussian source, shown in Figure 4.17 a) has a

wide normal distribution with 10.8 mm FWHM and a concentrated solar flux of 5.0 W/mm^2, while the collimated source, shown in Figure 4.17 b) has a needle-shaped distribution with 0.3 mm FWHM, resulting in a peak concentrated solar flux of more than 100 W/mm^2. The collimated source offers the highest concentration intensity and its FWHM is nearly as tight as a laser beam. However, this is not possible to obtain with incoherent light provided from the Sun.

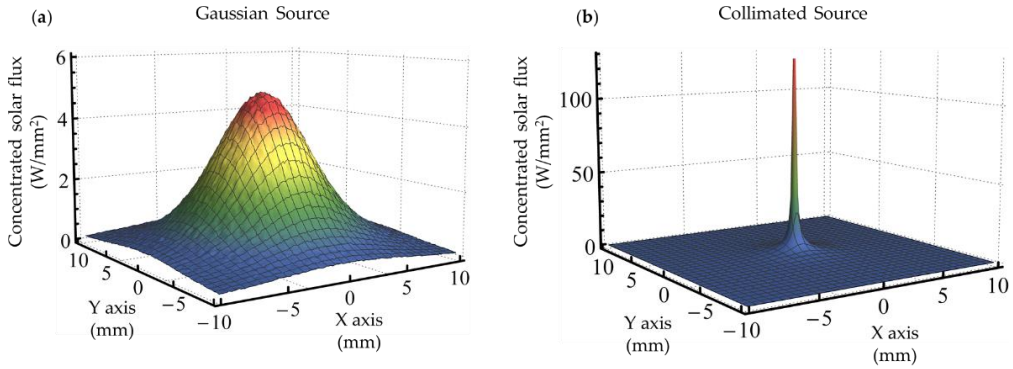

Figure 4.17 — The focal image formed by ESFL modelled at 1000 W/mm^2 irradiance with the (a) Gaussian source and (b) collimated source.

4.5.2 Comparative study of the ESFL output performance with the measured output performance of a Fresnel lens

Figure 4.18 shows the simulated layout and the focal output of the ESFL and a flat Fresnel lens [75] at the same focusing conditions. Ferriere et al. used a flat Fresnel lens of 900 mm diameter with 757 mm focal length, 20 grooves/cm (1800 grooves), and 31.7 mm thickness [75]. The measurement was conducted in PROMES-CNRS, where the irradiance can reach 1000 W/m^2 [44, 75, 76]. The remaining Fresnel lens parameters were adjusted to achieve the same output performance of the publication, by assuming a conic constant of −1.95 and a modest pitch angle of 2°. By using the solar source Gaussian distribution from [36], the simulated focal output of the flat Fresnel lens in Zemax® matched well with the measured data [75]. An ESFL with same collection size and focal length, and h_l = 300 mm, $\delta\omega$ = 0.0017° (1807 grooves), d_t = 3 mm and θ_p = 12°, was numerically simulated and compared. Figure 4.18 a) and b) presents the cross-sectional view of the light rays from five concentric annulus solar sources (with same area and power) passing through the ESFL and the Ferriere Fresnel lens, respectively. Area 1 represents the solar rays from the outmost concentric annulus source, while Area 5 corresponds to the solar rays of the innermost circular source. Figure 4.18 c) and d) show the contribution of each source on the concentrated solar flux of the ESFL and Ferriere Fresnel lens, respectively, as well as the combined concentrated solar fluxes distribution. As shown in Figure 4.18 b), it is noticeable that the solar rays at the external annulus area of the flat Fresnel lens (Area 1 and 2) are barely detected, leading to solar fluxes close to zero, as shown in Figure 4.18 d). The curved shaped of the ESFL overcomes this problem, allowing the solar rays from the external annulus area to be more efficiently focused, as demonstrated in Figure 4.18 a) and c). Since the external annulus areas collect most of the incoming solar power, the advantage of the ESFL concentrator in attaining higher solar flux becomes evident.

Chromatic aberration is also significantly reduced, leading finally to a higher concentrated solar flux of 4.5 W/mm^2 in Figure 4.18 c) compared to that of the flat Fresnel lens with 2.6 W/mm^2 in Figure 4.18 d) [75]. In addition to the elliptical shape of the Fresnel lens, there are also important factors that can contribute to the better performance of this concentrator, such as the aspect ratio and the number/size of grooves.

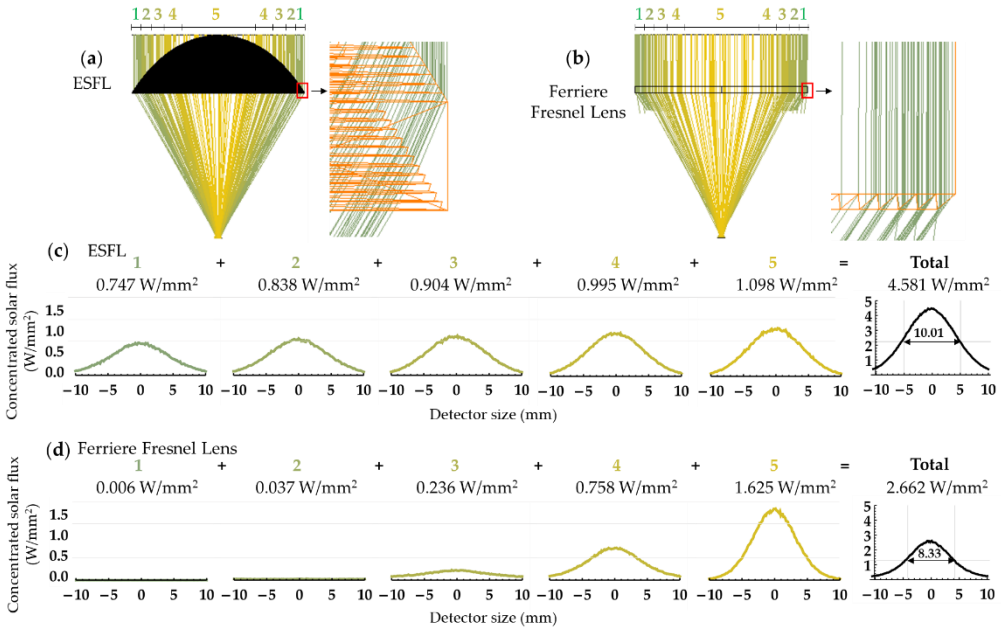

Figure 4.18 — (a) The ESFL and (b) the Ferriere Fresnel lens irradiated by five concentric solar sources with identical area and power. (c) and (d) are the concentrated solar fluxes and the combined solar fluxes for the ESFL and the Ferriere lens, respectively.

4.5.3 Comparative study of the ESFL output performance with other concentrators

Table 4-1 presents a summary of various analytical and experimental studies of other types of concentrators. It is crucial to keep in mind that when designing and simulating other concentrators, the experimental data from existing concentrators should be used as a reference to ensure an accurate and unbiased evaluation of their performance.

The parabolic mirror of the MSSF had a measured peak concentration of 16 W/mm^2 with 2000 mm diameter, 850 mm focal length and a focal size of 10 mm FWHM [37]. This parabolic concentrator has currently the highest known concentrated solar flux. However, based on analytical predictions, some authors have claimed higher concentrations with focal width like that presented in Figure 4.17 b) [25, 28, 72, 77], which is not possible with the incoherent solar light. The focal distribution measurements of linear-shaped Fresnel lenses by O'Neill and McDanal [64] and Leutz et al. [78] had both resulted in much lower concentration solar fluxes of 0.065 W/mm^2 and 0.045 W/mm^2, respectively, with the corresponding focal widths of 30 mm and 20 mm. It is common to find much lower concentrations from linear Fresnel lenses. The measured output performance of the flat Fresnel lens presented by Ferriere et al. had a concentrated solar flux of 2.6 W/mm^2 and a focal size of 8.3 mm at FWHM with a solar

irradiance of 1000 W/m^2 [75]. The present ESFL, at the same conditions of the flat Fresnel lens from [75], had a better focal solar flux of 4.5 W/mm^2.

Table 4-1 — Focal concentration and size from various concentrator types found in some publications.

Publications	Concentrator Type	Concentration	Focal Width (mm)	Lens Width (mm)	Focal Length (mm)	Grooves per mm	Method
Nelson et al., 1975 [79]	Fresnel lens	4.3–5.0 (ratio)	~30	137	140	~0.1	Analytical
Cosby, 1977 [63]	Shaped Fresnel lens (linear)	~70 (ratio)	~20	~914	~509	~1.0	Analytical
Kritchman et al., 1979 [21]	Shaped Fresnel lens (linear)	172 (ratio)	N/A	vary	vary	Infinitely small grooves	Analytical
O'Neill et al., 1993 [64]	Shaped Fresnel lens (linear)	0.065 (W/mm^2)	~30	850	726	N/A	Experimental
Flamant et al., 1999 [37]	Parabolic mirror	16.0 (W/mm^2)	~16 ~10 (FWHM)	2000	850	N/A	Experimental
Leutz et al., 2000 [78]	Shaped Fresnel lens (linear)	0.045 (W/mm^2)	~20 ~ 5-6 (FWHM)	~300	~150	N/A	Experimental
Ferriere et al., 2004 [75]	Flat Fresnel lens	2.644 (W/mm^2)	~20 ~8.3 (FWHM)	900	757	2.0	Experimental
Yeh, 2009, [34]	Shaped Fresnel lens (linear)	0.060 (W/mm^2)	~5–6 (FWHM)	300	446	1.0	Analytical
Pan et al., 2011 [72]	Fresnel lens	1,367,704,600 (W/mm^2)	<0.25	189	189	N/A	Analytical
Akisawa et al., 2012 [24]	Shaped Fresnel lens	0.506 (W/mm^2)	<1	45	60	4.0	Analytical
Cheng et al., 2013 [28]	Fresnel lens	N/A	<0.1	88	50	0.22	Analytical
Languy et al., 2013 [25]	Shaped Fresnel lens	8500 (ratio)	<1	N/A	N/A	N/A	Analytical
Yeh, 2016 [31]	Shaped Fresnel lens (linear)	0.070 (W/mm^2) (at 1135 nm)	~20 ~4 (FWHM)	300	223	2.0	Analytical
Yeh et al., 2016 [32]	Shaped Fresnel lens	~5.0 (W/mm^2)	~20 ~4 (FWHM)	460	280	4.3	Analytical
Zhao et al., 2018 [73]	Shaped Fresnel lens (linear)	40.6 (ratio)	16	650	950	N/A	Experimental
Garcia et al., 2019 [39]	RAC[1]	16.0 (W/mm^2)	~20 ~10 (FWHM)	2000	500	N/A	Analytical
Liang et al., 2021 [77]	AFSCFL[2]	46.7 (W/mm^2)	<1	734	593	N/A	Analytical
Present work	Shaped Fresnel lens	4.5 (W/mm^2)	~10.0 (FWHM)	900	757	0.34	Analytical

[1] Ring array concentrator.
[2] Annular Fresnel solar concentrator coupled with a circular Fresnel lens.

4.5.4 Output performance of the ESFL regarding the concentrated solar flux, the optical efficiency and the FWHM

4.5.4.1 ESFL configurations with fixed total height of 700 mm

As any lens, the shape of the ESFL concentrator has direct influence on its output performance. Figure 4.19 shows some of the possible configurations of the ESFL with a combined h_f and h_l of 700 mm total height.

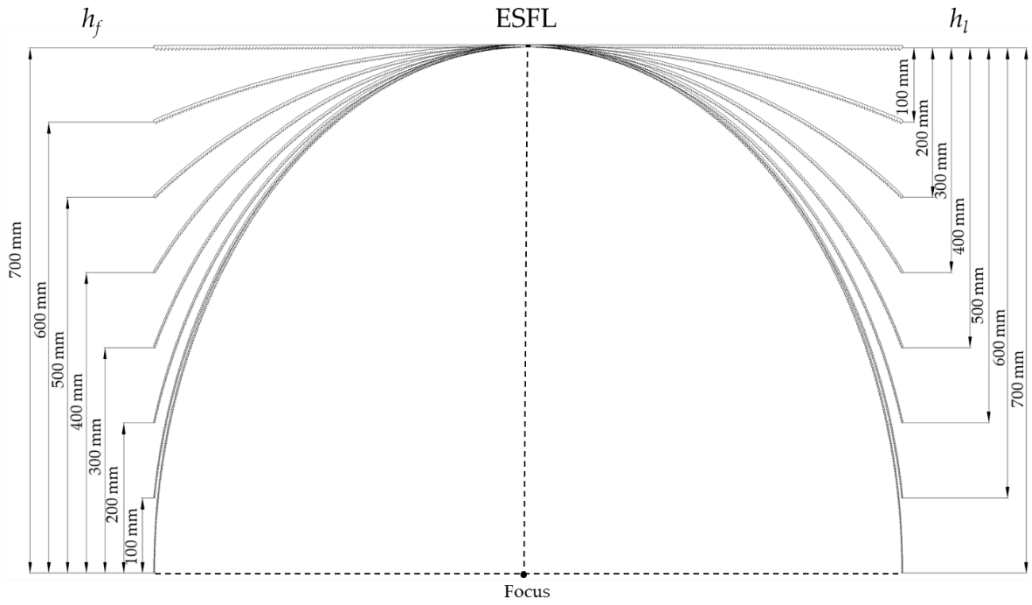

Figure 4.19 — ESFL configuration with a combination of h_f and h_d for a total height of 700 mm.

The ESFL has a similar configuration of a flat Fresnel lens at h_f = 700 mm, h_l = 0 mm. As h_l increases, the lens becomes more curved, and the aspect ratio becomes larger. The aspect ratio (*AR*) of the ESFL is given by the quotient of h_l and *D* (diameter of the lens):

$$AR = \frac{h_l}{D} \tag{4.25}$$

Figure 4.20 shows the variation of the concentrated solar flux as a function of the aspect ratio of ESFL and h_l, with 700 mm total height. All the ESFL configurations had *D* = 1 m, δ_ω = 0.28°, θ_p = 12° and d_t = 3 mm. The concentrated solar flux starts with 3.9 W/m^2 at h_l = 0 mm, which closely resembles that of a flat Fresnel lens. It gradually increases with h_l, at which point the Fresnel lens is shaped into a parabola. The concentrated solar flux is maintained over 5.2 W/mm^2 from h_l of 500 mm to 700 mm, i.e., with aspect ratio from 0.603 to 0.702.

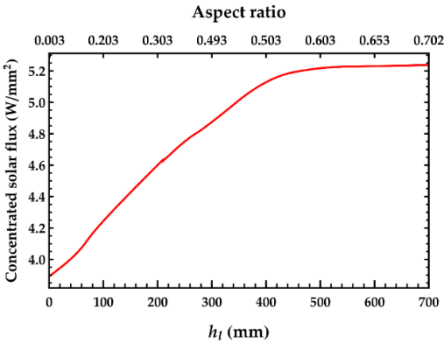

Figure 4.20 — Concentrated solar flux of the ESFL with a combined $h_f + h_d$ of 700 mm as a function of h_l and aspect ratio.

4.5.4.2 Concentrated solar flux, optical efficiency and FWHM as a function of the aspect ratio and several combinations of $h_f + h_l$

Figure 4.21 shows the concentrated solar flux, optical efficiency and FWHM at various combinations of h_f and h_l with ESFLs of D = 1 m, δ_ω = 0.28°, θ_p = 12° and d_t = 3 mm. h_f ranges from 200 mm to 600 mm and h_l ranges from 50 mm to at least 500 mm.

Each h_f has its own peak concentrated solar flux at different h_l (Figure 4.21 a). For example, in the ESFL configuration with h_f = 200 mm, the concentrated solar flux varies from 4.2 W/mm^2 at h_l = 50 mm to 5.2 W/mm^2 at h_l = 500 mm, above which it starts to decrease. The highest concentrated solar flux was attained by the lowest h_f = 200 mm at h_l = 500 mm (aspect ratio of 0.603). The increase in h_f resulted in a lower concentrated solar flux, whose peak value shifted to a lower h_l, decreasing the aspect ratio of the concentrator. For example, the ESFL with h_f = 600 mm has an aspect ratio of 0.500 with h_l = 350 mm and a concentrated solar flux of 4.4 W/mm^2.

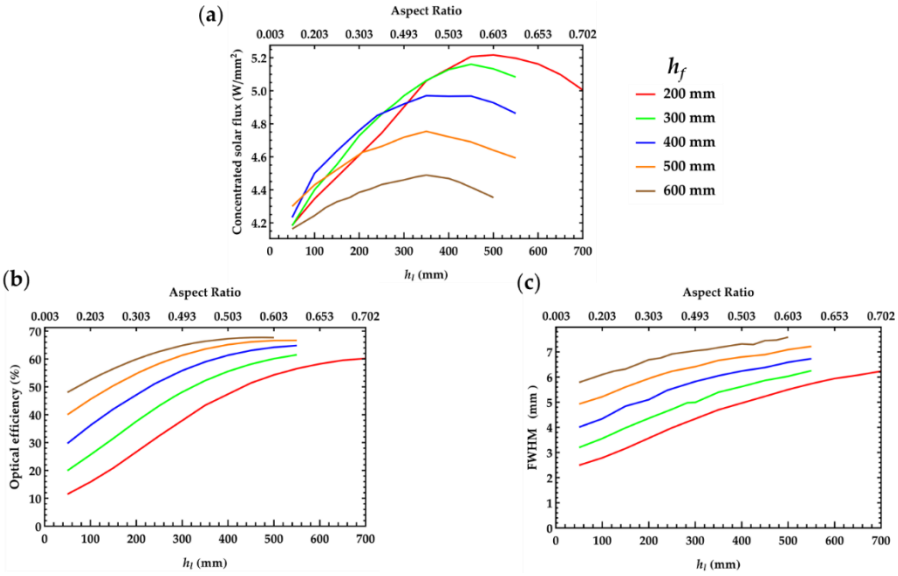

Figure 4.21 — (a) Concentrated solar flux, (b) optical efficiency and (c) FWHM of the ESFL configurations with D = 1 m at various h_f and h_l combinations.

The optical efficiency tends to stagnate at larger h_l, as shown in Figure 4.21 b). The highest optical efficiency of about 60% was attained at the higher h_f of 600 mm. The FWHM enlarges in a near linear fashion with the increase in h_l, and it also expands with the increase in h_f, as shown in Figure 4.21 c).

4.5.4.3 Influence of size/number of grooves on the ESFL output performance

The influence of different sizes of $\delta\omega$ on the ESFL output performance was analysed for the most favourable combinations of h_f and h_l that achieved the highest concentrated solar fluxes, shown in Figure 4.21 a). The variation of $\delta\omega$ changes the size of each groove/prism within the ESFL concentrator, mainly changing the size of the input (A_nB_n) and the output (A_nD_n) facets, as calculated in Equations (4.9) and (4.23). A range of $\delta\omega$, from 0.05° to 1°, was used for the conception of the ESFL model. Figure 4.22 a) shows the number of grooves per $\delta\omega$ at different h_f. The number of grooves drops exponentially independently of the h_f with the increase in $\delta\omega$. A gap in the number of grooves between h_f is observed at a smaller $\delta\omega$, while it converges closer into the same number of grooves at a larger $\delta\omega$.

Figure 4.22 b) shows the concentrated solar flux as a function of $\delta\omega$. Regardless of h_f, the maximum concentrated solar flux was found at $\delta\omega$ = 0.3°, which is equivalent to 210 to 132 grooves for h_f 200 mm to 600 mm, respectively. As shown in Figure 4.22 c), the increase in $\delta\omega$ lowers the optical efficiency from 66% to 56% and 53% to 50% at h_f of 600 mm and 200 mm, respectively. The FWHM shows a minimum within a certain $\delta\omega$ range, as shown in Figure 4.22 d). For example, at h_f = 600 mm, more than 10.7 mm FWHM was found at $\delta\omega$ = 0.35°, while at h_f = 200 mm, the minimum FWHM of about 8 mm was found at $\delta\omega$ = 0.2°. In all cases, the largest FWHM is located at $\delta\omega$ = 1°.

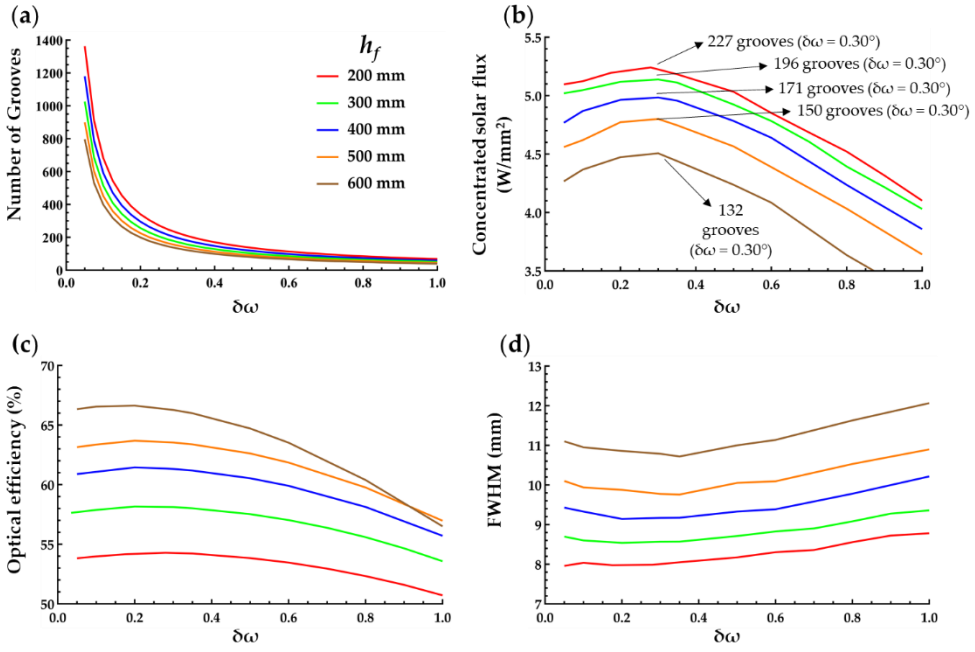

Figure 4.22 — Characteristics of the Gaussian distribution source at the focal zone: (a) number of grooves per $\delta\omega$, (b) concentrated solar flux, (c) optical efficiency and (d) FWHM.

The number of grooves has a direct influence on the focal characteristics of the concentrator, as demonstrated in Figure 4.23 a). On the one hand, with the increasing number of grooves (lower $\delta\omega$), each prism becomes smaller, which reduces the refraction space within the prism. Consequently, above a certain number of grooves, the number of effective rays that could be refracted onto the targeted focal position is diminished, causing the decrease in the concentrated solar flux, as illustrated in Figure 4.23 b). On the other hand, the reduction in the number of grooves (higher $\delta\omega$) leads to an increment in the size of

the prism, hence broadening the final output focal shape, as shown in Figure 4.23 d). Therefore, the concentration solar flux also diminishes with the decrease in the number of grooves, as shown in Figure 4.23 b). Maximum concentrated solar flux was numerically found at $\delta\omega$ = 0.30° for all the ESFLs, regardless the h_f, as demonstrated in both Figure 4.22 b) and Figure 4.23 b). However, the optimum number of grooves varies with h_f. Consequently, for $\delta\omega$ = 0.30°, the optimum number of grooves varied from 227 grooves with h_f = 200 mm to 132 grooves with h_f = 600 mm, corresponding to 0.42 grooves/mm and 0.26 grooves/mm, respectively. This variation is even more pronounced with smaller $\delta\omega$ (higher number of grooves). The optimum groove number per size is by far lower than that of other Fresnel lenses (Table 4-1), such as the shaped Fresnel lens with 4.3 groove/mm at D = 460 mm [32], flat Fresnel lens with 2 grooves/mm at D = 900 mm [75], 2 grooves/mm at D = 889 mm [49], and a range of 15.7 grooves/mm to 1 grooves/mm at various sizes of Fresnel lenses found at the market, such as the Fresneltech [66]. The improved performance of the ESFL, which utilizes larger prisms and a lower number of grooves, is since the design process was not based on the edge-ray principle, which is commonly used in modelling processes, but rather on the solar Gaussian distribution. Reducing the number of grooves and increasing the prism size may be advantageous for the manufacturer as it can minimize losses caused by manufacturing inaccuracies, such as blunt tips and deformed grooves.

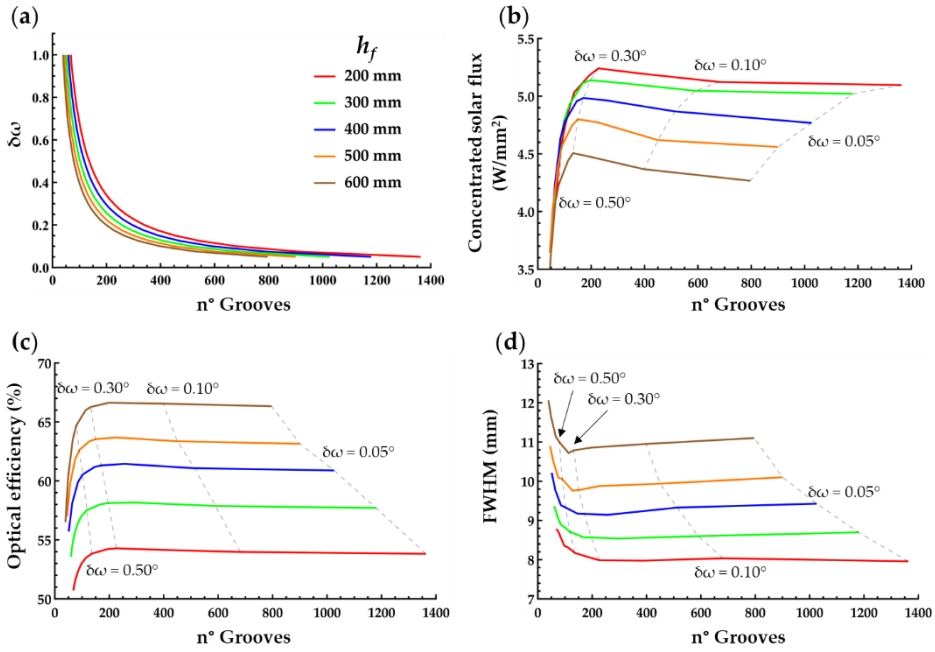

Figure 4.23 — Characteristic of the Gaussian distribution source at the focal zone: (a) $\delta\omega$, (b) concentrated solar flux, (c) optical efficiency and (d) FWHM as a function of the number of grooves.

4.5.5 Comparison between ESFL and a flat Fresnel lens

4.5.5.1 Optimal focal position analysis of both the ESFL and a flat Fresnel lens

Figure 4.24 and Figure 4.25 show the three-dimensional light distribution along the focal zone of the ESFL and a flat Fresnel lens with the same collection size, respectively. The ESFL had D = 1 m, δ_ω = 0.28° (171 grooves), θ_p = 12°, d_t = 3 mm, h_f = 300 mm, and h_l = 450 mm. The flat Fresnel lens with

the highest concentration flux configuration was chosen, with D = 1 m, h_f = 400 mm, 0.3 grooves per mm (150 grooves) and θ_p = 12°. The focal cones, as shown in Figure 4.24 a) and Figure 4.25 a), were represented by a detector volume with 100 × 100 × 100 voxels in vacuum, where each voxel accumulates and stores the energy data from each ray that passes through it, with the associated wavelength and power. Figure 4.24 b) shows the top view focal distribution of the ESFL in the detector positioned at the origin (Z = 0 mm), with a concentrated solar flux of 5.08 W/mm^2, while Figure 4.24 c) shows the focal distribution at Z = −5 mm in relation to the origin, with a maximum concentrated solar flux of 5.48 W/mm^2. Figure 4.25 b) shows the focal distribution of the flat Fresnel lens at Z = 0 mm, with a concentrated solar flux of 0.75 W/mm^2. At Z = +30 mm in relation to the origin, the maximum concentrated solar flux of only 1.86 W/mm^2 was reached, as shown in Figure 4.25 c).

For both the ESFL and the flat Fresnel lens, the focal distributions at the origin (Z = 0 mm) do not correspond to the positions where the concentrated solar flux is maximum, as shown in Figure 4.24 a) and Figure 4.25 a). This phenomenon occurs due to the chromatic aberration, which is more abundant in the flat Fresnel lens. It is important to note that a parabolic concentrator (a concentrator with no chromatic aberration effect) has its maximum concentration exactly at the origin point [39].

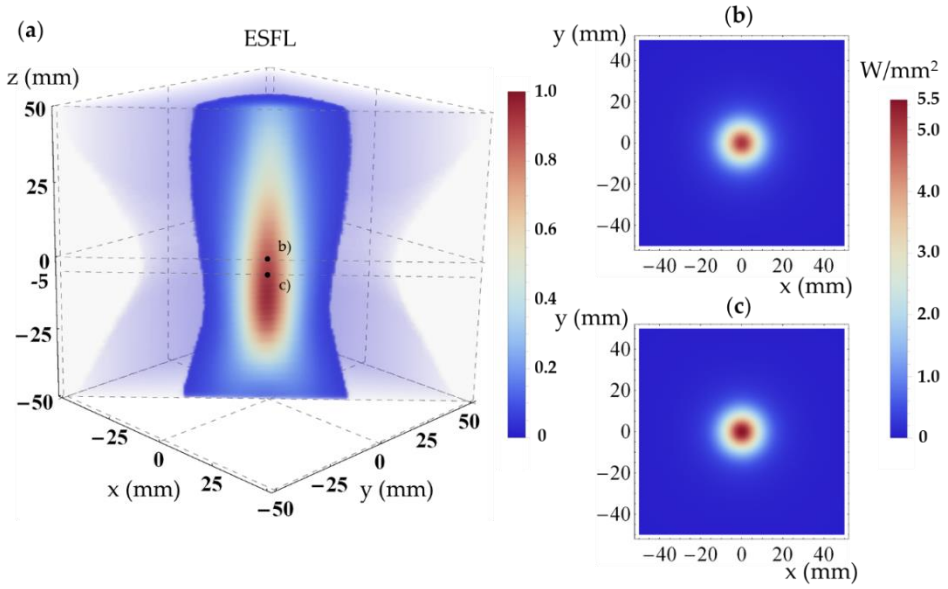

Figure 4.24 — (a) Three-dimensional focal distribution of the ESFL. (b) Top view of the light distribution at the focal point (Z = 0 mm). (c) Top view of the light distribution with the highest concentrated solar flux (Z = −5 mm).

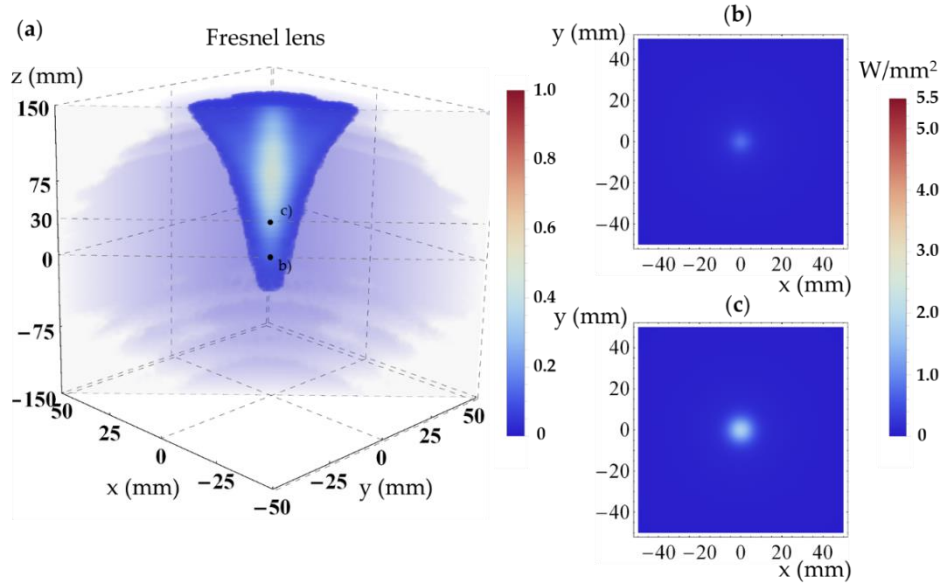

Figure 4.25 — (a) Three-dimensional focal distribution of the flat Fresnel lens. (b) Top view of the light distribution at the focal point (Z = 0 mm). (c) Top view of the light distribution with the highest concentrated solar flux (Z = 30 mm).

4.5.5.2 Temperature analysis of both the ESFL and the flat Fresnel lens

Zemax® non-sequential raytracing and Ansys finite element analyses were both used to evaluate the temperature of both the ESFL and the flat Fresnel lens at the Z position with the highest concentration solar flux found in the previous section. ANSYS™ allows thermo-optical calculations that deal with complex geometric shape and boundary conditions, enabling the approximation of variables in a volume or surface element that changes across the matrix [80-82].

A 20 × 20 mm^2 detector with an emissivity (ε) of 1 [80] was used in Zemax® to calculate the concentrated solar flux at the optimal focal positions of the ESFL and the flat Fresnel lens. The detector

was divided into 150 × 150 pixels. The resulting matrix data was exported to the ANSYS™ workbench using the "External data" component and loaded as a heat flux source.

In ANSYS™ 2021 finite element analysis, a graphite disk receiver of 20 mm diameter and 5 mm thickness was used to obtain the temperature of both concentrators. The graphite of 2250 kg/m^3 constant density, 24 W/m K thermal conductivity and 709 J/Kg K specific heat were chosen from the ANSYS™ internal material library. The disk receiver was divided by the tetrahedrons meshing method with a sizing element of 0.4 mm. The sample size was relatively small, containing around 1600 elements, which provided sufficient data for finite element analysis calculations with good approximation. The boundary conditions set for the convection applied onto the disk were the same as the natural stagnant air convection, representing a heat transfer coefficient of 5×10^{-6} W/mm^2/K. The radiation exchange between surfaces was restricted by a grey-diffused surface and the emissivity for the graphite disk surface was confined to $\varepsilon = 0.85$. A room temperature of 295.15 K was considered.

The respective temperatures of the ESFL and the flat Fresnel lens are shown in Figure 4.26. Both temperatures were generated from the focal distributions of Figure 4.24 c) and Figure 4.25 b), respectively. The ESFL attained maximum and minimum temperatures of 2362 K and 1945 K, respectively, which were 1.73 and 1.60 times more than that of the Fresnel lens with the maximum temperature of 1363 K and minimum temperature of 1217 K, respectively.

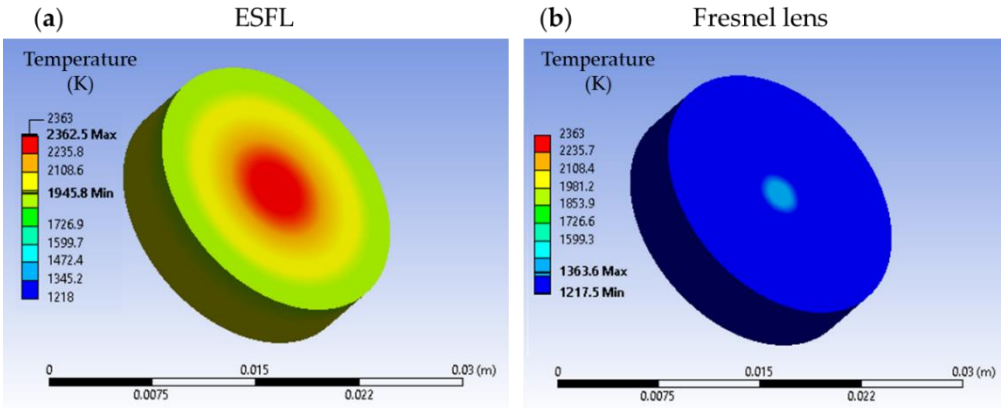

Figure 4.26 — Focal temperature of ESFL (a) and flat Fresnel lens (b).

4.5.6 Conclusions

A new approach to addressing the chromatic aberration issue in Fresnel lens concentrators involved the creation and analysis of a three-dimensional Elliptical-Shaped Fresnel lens parametric model. The modelling process was based on the solar Gaussian distribution using the parameters measured by Vittitoe and Biggs [36], rather than the traditional edge-ray principle method and a solar acceptance half-angle of 0.27°. The design was developed using CAD software and later subjected to numerical calculations in Zemax®. The precision of the model was validated by comparing the output performance of a flat Fresnel with experimental data, which yielded good agreement [75]. The ESFL was also evaluated under the same focusing conditions, and its performance was compared to these results. The analysis revealed that the ESFL has an advantage in efficiently focusing solar rays from the external annulus area at the

external annulus collection area, where a significant portion of the incoming solar power is collected. Consequently, the ESFL results in a considerable increase in concentrated solar flux.

The study of different combinations of ESFL focal length and arch height, and their influence on the output performance was carried out. The highest peak solar flux of about 5.2 W/m^2 was attained for the ESFL with a shorter focal length of h_f = 200 mm and high arch height of h_l = 500 mm, resulting in a large aspect ratio of 0.603. As h_f increased, the solar concentration decreased, but maximum solar fluxes were attained with a smaller h_l, hence lowering the aspect ratio.

The optimal concentrated solar flux value within the focal cone of the best ESFL was then studied and compared to that of a flat Fresnel lens at its best output performance configuration. This study demonstrated the effectiveness of the ESFL in reducing the chromatic aberration, leading to a significant enhancement of the concentrated solar flux and temperature, as compared to that of the flat Fresnel lens.

Furthermore, this study conducted a thorough investigation on the impact of prism size and groove count on the performance of ESFL. Results indicated that the ideal number of grooves per millimetre could be significantly decreased compared to previous research and industry standards. This finding could simplify the manufacturing process of Fresnel lens concentrators and boost its solar concentration ability, highlighting the potential of ESFL in numerous solar energy applications and research endeavours.

5
RING ARRAY CONCENTRATOR

5.1 State of the art

Traditionally, mirror-type solar concentrators have been regarded as the optimal choice for achieving higher temperature concentrations. This superiority is attributed to their complete elimination of chromatic aberration at the focus, a contrast to Fresnel lenses that are affected by the constraints of Snell's law. Among the mirror concentrators, the parabolic mirror stands out as the most commonly utilized. While the parabolic mirror demonstrates promising theoretical and practical outcomes in generating substantial energy at a confined focus, its efficiency diminishes as the size of the receiver and its mechanical support increases, primarily due to the cast shadow effect.

In this chapter, a novel solar concentrator configuration is introduced, featuring a combination of concentric rings of mirrors along with a Fresnel lens. Notably, the receiver and its mechanical support are strategically positioned behind the concentrator, aiming to address the challenges associated with shadowing effects and enhance the overall performance of the solar concentrator system.

5.2 Introduction

Solar energy is a promising resource to replace fossil energy in the future. Photovoltaic technologies dominate the current solar energy market due to their cost [83]. Solar concentrators are used to boost the photo-energy conversion efficiency while decreasing the overall cost, by reducing the size of the photovoltaic system. This is prompt to receive more solar energy and thus being more efficient [84, 85]. Fresnel lens concentrator technology is widely used in photovoltaic technology; however, these lenses have a limited concentration ratio due to their strong chromatic aberration issue [86, 87]. The use of high solar flux benefits heat-to-electricity conversion by Stirling engines [82, 88, 89]; direct light-to-material interaction, energetic transition from other non-renewable sources [3]; solar-pumped high power lasers [12, 13]; energy heat storage [90-93].

The existing parabolic mirrors have their own specific characteristics depending on their size and application, as shown in Figure 5.1 [44, 94-99].

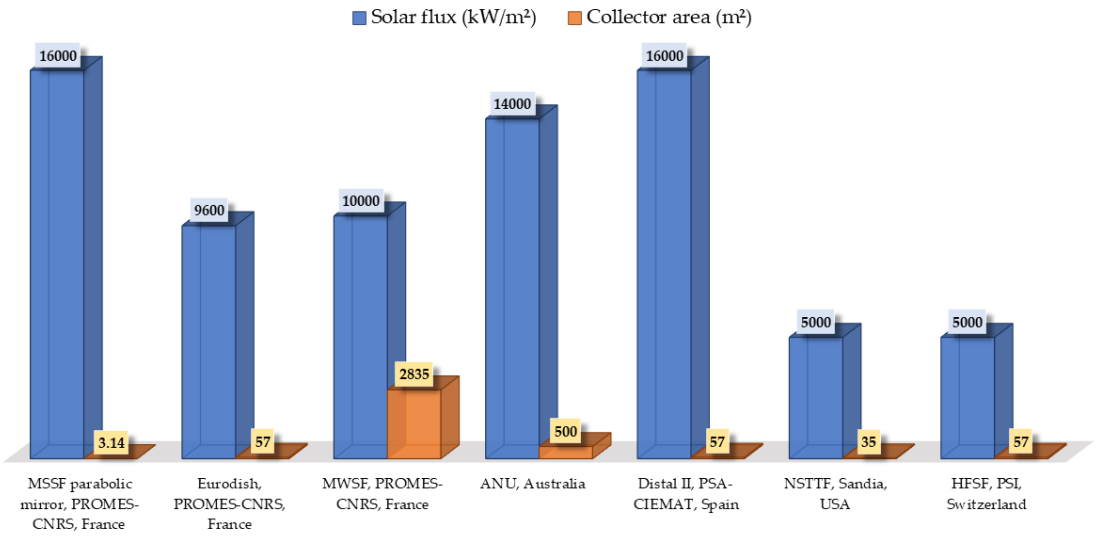

Figure 5.1 — The state-of-the-art concentrated solar fluxes. MSSF: Medium Size Solar Furnace [44]; Eurodish [94]; MWSF: Mega Watt Solar Furnace [95]; PROMES- CNRS: Procédés, Matériaux et Énergie Solaire - Centre National de la Recherche Scientifique; ANU: Australian National University [99]; PSA-CIEMAT: Plataforma Solar de Almería- Centro de Investigaciones Energéticas, Medio ambientales y Tecnológicas NSTTF: National Solar Thermal Test Facility [97]; HFSF: High Flux Solar Furnace; PSI: Paul Scherrer Institute [98].

Although parabolic mirrors can achieve higher solar fluxes than Fresnel lenses, they have a disadvantage in that the receiver and its mechanical support must be positioned in front of the solar concentrator, which casts shadows and reduces the overall efficiency [100].

Currently, there are other types of solar concentrators that have been developed to advance research in solar energy. One of these is the dome-shaped Fresnel lens, which has a higher concentration ratio than a flat Fresnel lens. However, this type of lens is not yet available for commercial use [25, 28, 101].

Ring-array concentrator (RAC) is an alternative concentrator that combines the advantages between the reflective nature of a parabolic mirror and the focusing method of a Fresnel lens. The RAC consists of a set of parabolic reflective rings mounted coaxially to avoid shading effect from either incoming or reflected light among parabolic rings, as shown in Figure 5.2 a). The focal spot is created by the superposition of the concentrated solar rays from the ring mirrors. The RAC modelling methodology requires positioning and sizing of each ring, ensuring no shadows between them. The possible shadowing in RAC derives from its mechanical support and it is far less compared to the shadow caused by a receiver and its associated mechanical support in front of a parabolic mirror, shown in Figure 5.2 b).

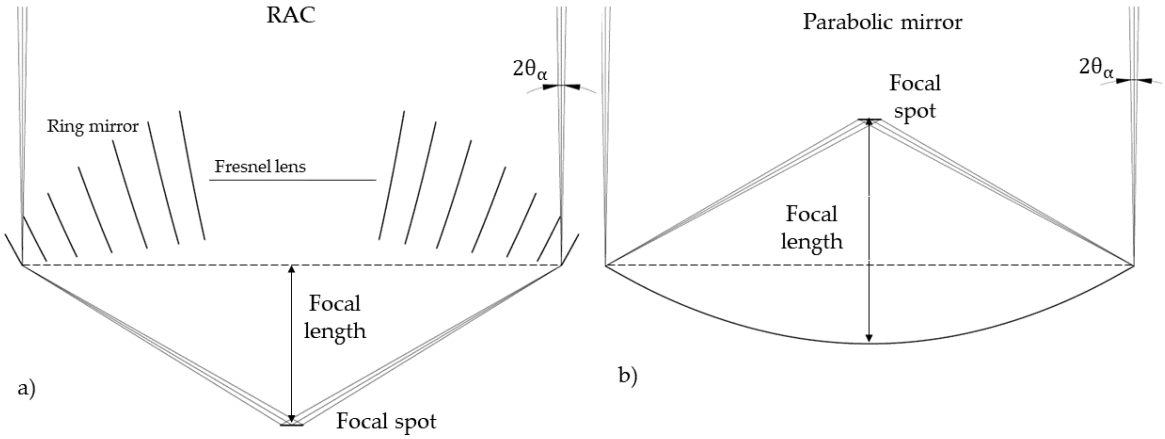

Figure 5.2 — (a) The seven-ring ring-array concentrator and (b) the medium size solar furnace parabolic mirror. Both concentrators have the same collection area of 3.14 m^2. θ_α is the Sun-Earth acceptance half-angle.

More importantly, the RAC shows no chromatic aberration along its focal spot, hence providing much higher solar concentration efficiencies than those by a Fresnel lens. The first RAC concept occurred at as early as the end of the 19th century by Manuel Gomes with the Pyreheliophoro [102, 103], further studied by Vasylyev and Oleg in 2003 [104], Mouzouris et al. in 2009 [105], and Garcia et al. in 2019 [39, 70]. The latter reported a novel 3D RAC solar furnace model and its temperature calculation. The RAC concept was also used for improving solar laser efficiencies [106-109].

A previous publication explored the RAC model with all rings resting onto the same focal level, creating some odd and impossible shapes for some of the concentrator's specifications [39]. The present article addresses the influence of the RAC configuration on its output performance by integrating a new variable that changes the ring position within the RAC. A fixed collection area of 3.14 m^2 (radius of 1 m) and focal length of 0.3 m was used for the analytical process of the RAC, while changing the ring width and the ring height position. A comparative study, conducted by the ray-tracing program of Zemax®, about concentrated solar flux and optical efficiency, in combination with total ring surface area and aspect ratio, was developed for different RAC configurations. Consequently, an equilibrium between the RAC output performance and its cost-effective design was presented for the first time. Additionally, the influence of the solar divergence half-angle and tracking error on the RAC performance was studied.

5.3 RAC design methodology

The seven-ring RAC incorporates both reflection and refraction mechanisms by utilizing the surface of the parabolic ring mirror section and Fresnel lens, respectively, to redirect incoming solar rays. The design of the RAC is depicted in Figure 5.3, where each ring section of the parabolic mirror was mathematically positioned and sized to prevent obstruction of the light path. The central solar rays were then focused towards the focal spot with the assistance of the Fresnel lens.

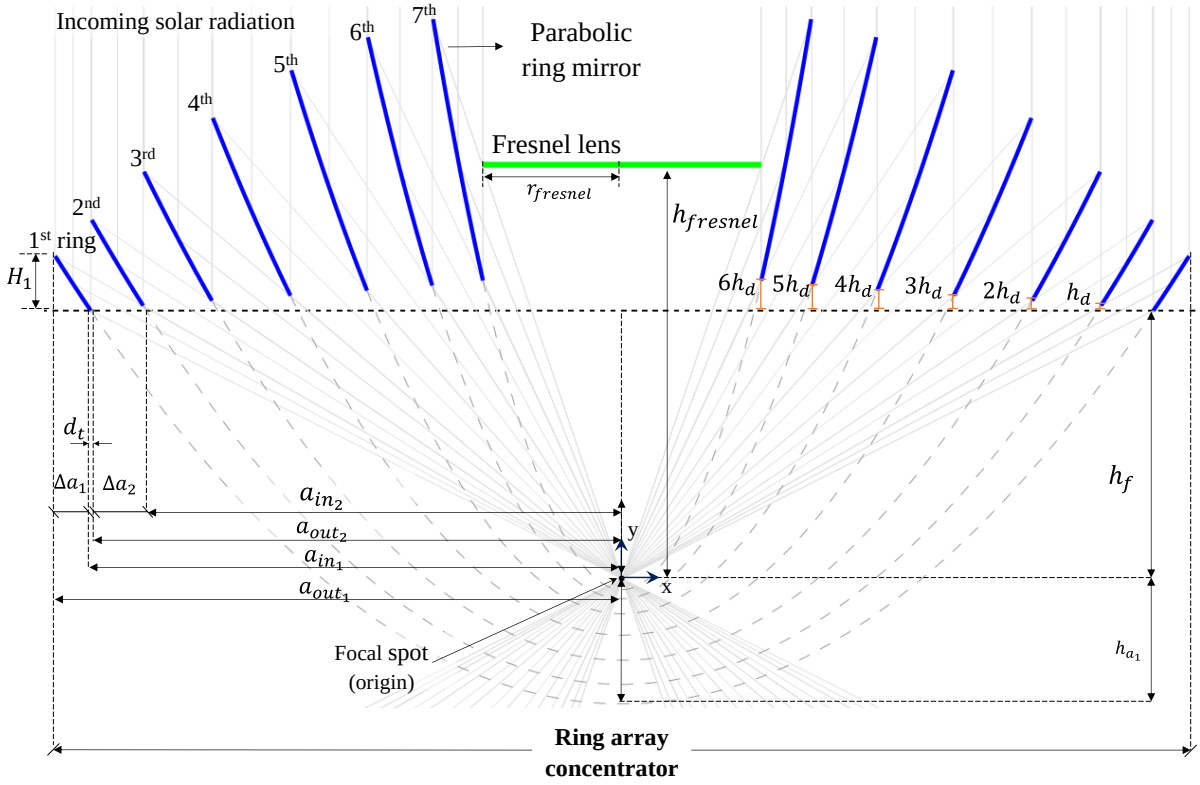

Figure 5.3 — Schematics of the ring-array concentrator unit with seven rings. The blue lines represent the cross section of the parabolic rings, and the green line represents the cross section of the Fresnel lens. Δa1 and Δa2 are the ring width of the first and second ring, respectively; a_{out_1} is the outer radial aperture of the first ring; a_{in_1} is the inner radial aperture of the first ring; hf is the focal length; dt is the thickness of the ring, rfresnel is the radius of the Fresnel lens; hd is the ring height modifier parameter; H1 is the height of the first ring; h_{a_1} is the ring height correction and hfresnel is the height of the Fresnel lens in relation to the origin.

The general parameters to model a RAC are:

- a_{out_1} – Radial aperture (mm) defines the size of the concentrator.
- h_f – Focal length (mm), which defines the vertical distance between the focus and the outmost ring.
- h_d – Ring height modifier (mm).
- d_t – Lens thickness (mm).
- $\Delta a_1(d_w)$– First ring width.

5.3.1 General equations

A parabolic ring is a section of a parabolic aspheric surface. Equation (5.1) shows the sag equation of a general geometric aspheric surface (z), where c is the curvature of the surface, a is the radial coordinate or aperture and α_i is the aspheric coefficient. In this study, the constant k (curvature constant) is set as -1 for a pure parabolic configuration, and c is the inverse of the radius of curvature ($c = 1/RoC$).

$$z_n = \frac{c \times a_n^2}{1 + \sqrt{1 - (1+k)c^2 a_n^2}} + \sum_{i=1}^{M} \alpha_i a^i = \frac{1}{2}\frac{a_n^2}{RoC} \tag{5.1}$$

Equation (5.2) defines the radius of curvature (RoC_n) for a given n^{th} ring with a desired focal length (h_f), inner aperture (a_{in_n}) and ring height modifier (h_d). n is the index number of the ring, $n \in [1, N]$, with N being the maximum desired number of rings within the RAC.

$$RoC_n = \sqrt{(h_f + (n-1)\,h_d)^2 - {a_{in_n}}^2} - (h_f + (n-1)\,h_d) \tag{5.2}$$

The h_d parameter changes the vertical position of each ring. Where $h_d = 0$ mm means that all rings had the same focal length. While, $h_d > 0$ mm, the vertical position of each inner ring increases linearly according to the ring number by $(h_f + (n-1)\,h_d)$, thus changing the ring focal length by $(n-1)\,h_d$ per ring number. The first ring ($n = 1$) always starts its focal length at h_f.

5.3.1.1 First ring

The RAC model is highly dependent on the initial parameters of the first ring. The implementation of the first ring in a Cartesian space is illustrated in Figure 5.4.

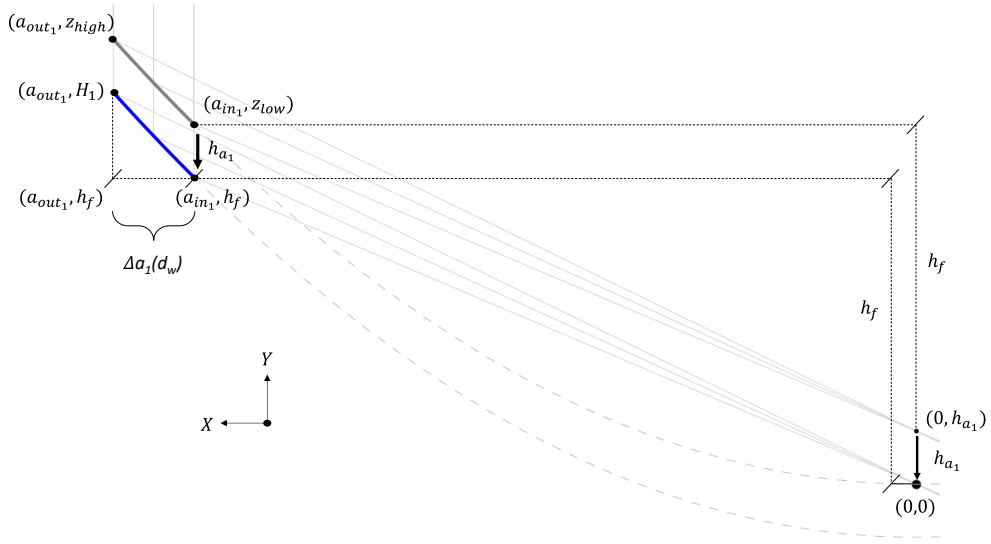

Figure 5.4 — Parametric positioning of the first parabolic ring. A virtual parabolic ring mirror is indicated as solid grey sag line from a_{out_1} to a_{in_1} and has its focus at (0, h_{a_1}). The remaining parabola is drawn by extending the sag line from a_{in_1} to a_1 = 0 mm (represented as dashed grey line) and has its vertex on the origin point (0, 0). The parabolic ring segment of the RAC model (solid blue sag line) is found by subtracting the h_{a_1} in Y axis from the virtual parabola, which ensures the focus in the origin point.

The initial procedure of the RAC modelling is to define the outmost radial aperture of the first ring (a_{out_1}), which also defines the maximum size of the RAC. Next, it is defined the size of the first ring, Δa_1, which is the width of the first ring. In this article, Δa_1 is defined as a scalable product that changes with the size of the RAC model, as shown by Equation (5.3).

$$\Delta a_1 = d_w \frac{a_{out_1}}{R} \tag{5.3}$$

d_w is the initial ring width variable; the constant R is the base radius of the RAC, which is considered as 1000 mm in this study. The Δa_1 output changes with d_w and a_{out_1}. For example, if a_{out_1} is 1000 mm, then the Δa_1will have the same value as d_w. However, if a_{out_1} is 2000 mm, then Δa_1 will be double the

value of d, as shown in Table 5-1. This equation ensures a linear scalability for any RAC size in relation to a 1000 mm base radius RAC.

Table 5-1 – The variation of Δa_1 with d_w at different a_{out1} and R of 1000 mm.

d_w (mm)	Δa_1 (mm) a_{out_1} (mm)			
	500	**1000**	**1500**	**2000**
60	30	60	90	120
80	40	80	120	160
100	50	100	150	300

With both a_{out_1} and Δa_1, the inner radial aperture (a_{in_1}) can be found by the difference of the outer radial aperture with the ring width, as shown in Equation (5.4).

$$a_{in_1} = a_{out_1} - \Delta a_1 \tag{5.4}$$

The parabolic ring segment can be designed from both the outer and inner radial apertures in the sag equation (Equation (5.1)). In this case, the vertex of the virtual parabolic sag will be positioned onto the origin point (0, 0), and its focal point at (0, h_{a_1}), as shown in Figure 5.4 by the solid and dashed grey sag lines.

The h_{a_n} is used to correct the position of any n^{th} ring in the vertical axis, as shown in Figure 5.4. This ensures the focus of each ring at the origin point. The corrected ring mirror position is represented by the solid blue sag line (Figure 5.4). h_{a_n} is half of the radius of curvature of the ring, as shown in Equation (5.5).

$$h_{a_n} = \frac{RoC_n}{2} \tag{5.5}$$

The first ring is then defined by the coordinates of the blue sag line, starting at (a_{out_1}, H_1) and ending at (a_{in_1}, h_f).

The H_n is the height of the ring, given by Equation (5.6).

$$H_n = z_n - h_{a_n} \tag{5.6}$$

5.3.1.2 Other rings

For the second ring and other successive rings, the sequence of modelling is shown in Figure 5.5.

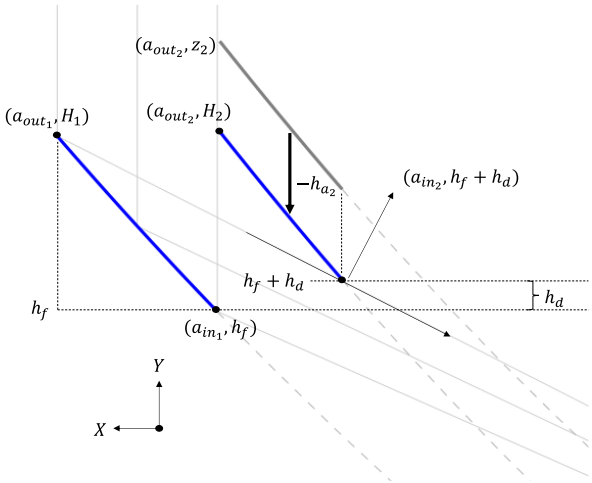

Figure 5.5 — Parametric positioning of the second ring. The outer radial aperture of the next ring (a_{out_2}) is found through the inner radial aperture of the previous ring. The inner radial aperture of the next ring is found at the intersection of the focal length of the next ring (XX, $h_f + h_d$) with the reflected light from (a_{out_2}, H_1) to origin (0, 0).

The outer radial aperture of the next ring (a_{out_n}) is found by subtracting the width of the ring thickness (d_t) from the inner radial aperture of the previous ring ($a_{in_{n-1}}$), as shown in Equation (5.7) and represented in Figure 5.5. This ensures the physical ring thickness within the RAC model.

$$a_{out_n} = a_{in_{n-1}} - d_t \tag{5.7}$$

To complete the next ring, the inner radial aperture (a_{in_n}) can be found at the intersection of the reflected light ray from the top of the previous ring at ($a_{out_{n-1}}, H_{n-1}$) with the focal length of the next ring at (XX, $h_f + h_d$), as shown in Equation (5.8).

$$a_{in_n} = \frac{h_f + (n-1)h_d}{\frac{H_{n-1}}{a_{out_{n-1}}}} - d_t \tag{5.8}$$

With both outer and inner radial aperture found; then it is possible to draft the virtual parabolic ring (solid grey sag line, shown in Figure 5.5) through Equation (5.1). Then the RAC parabolic ring segment (solid blue sag line) can be found with the corrected vertical ring height position, given by h_{a_n} from Equation (5.5), ensuring the focus at the origin.

5.3.1.3 Fresnel lens

The next inner rings are modelled with the same procedure, until the desired number of rings is completed. The last ring's inner aperture, a_{in_N}, (innermost ring of the RAC) leaves a "hole" in the middle of the concentrator. A Fresnel lens is used to complete the remaining space. Its radius is represented by $r_{fresnel}$ in Equation (5.9).

$$r_{fresnel} = a_{in_N} \tag{5.9}$$

The height of the Fresnel lens, $h_{fresnel}$, is given by the product of the interception of the reflected light ray from the top of the last ring (a_{out_N}, H_N) to the origin point with the position of the inner aperture of the last ring (a_{in_N}, YY), as shown in Equation (5.10).

$$h_{fresnel} = \frac{H_N}{a_{out_N}} a_{in_N} \tag{5.10}$$

5.3.2 RAC Design

According to the above-mentioned equations, the design of the desired RAC configuration is governed mainly by the following parameters:

- N, the number of rings.
- a_{out_1}, the radial size of the first parabolic ring, which defines the collection area of the RAC.
- h_f, the focal length of the lens.
- d_w, the initial width of the ring, which defines the size of each parabolic ring.
- h_d, the ring height modifier, which modifies the height of each successive ring.
- d_t, the thickness of the parabolic ring.

5.3.2.1 Number of rings, N

The RAC model depends on the number of rings which is composed. Figure 5.6 shows the cross-sectional view of three RACs with six to eight rings. These three RACs shared the same parameter of a_{out_1} = 1000 mm, h_f = 300 mm, d_w = 100 mm, and h_d = 40 mm.

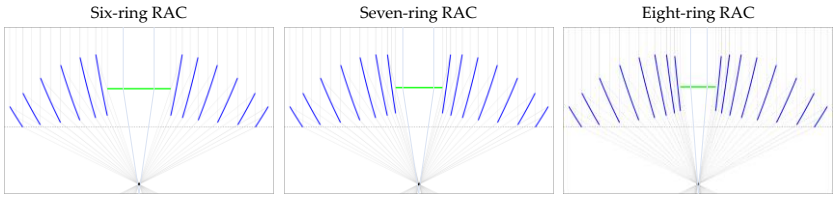

Figure 5.6 — Cross-sectional view of six-ring, seven-ring, and eight-ring RACs.

This thesis mainly focused on the RAC configurations with seven rings, which has shown to be the most suitable for designing an efficient RAC concentrator [39].

5.3.2.2 Initial ring width, d_w

The width of the first ring, (Δa_1), is a key parameter for the RAC modelling. However, this parameter is a product of a scalable function with d_w in Equation (5.3). Figure 5.7 shows the influence of d_w on the design of the RACs with h_f = 300 mm, a_{out_1} = 1000 mm and h_d = 27.5 mm. A smaller d_w led to a shorter first ring width and a larger Fresnel lens at the center, while a larger d_w resulted in a wider first ring width and a smaller Fresnel lens at the center.

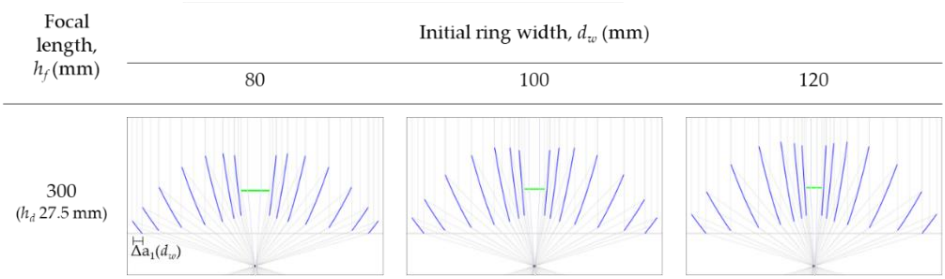

Figure 5.7 — Cross-sectional view of the seven-ring RAC configuration at different d_w of 80, 100 and 120 mm, with h_f = 300 mm, collection area of 3.14 m^2 and h_d = 27.5 mm.

5.3.2.3 Ring height modifier, h_d

The ring height modifier is a critical design parameter which was not discussed in [39]. This parameter modifies the focal length of each individual ring by changing its height. It yields a significant modification of the size and position of each ring, which is crucial for the conception of a physically acceptable RAC. Figure 5.8 shows the cross-sectional view of seven-ring RAC configurations with three different h_d (15 mm, 25 mm, and 35 mm), but all with fixed parameters of a_{out_1} = 1000 mm, h_f = 300 mm, and d_w = 100 mm. As h_d increased, the size of each ring section reduced both in height and width, thus increasing the size of the Fresnel lens.

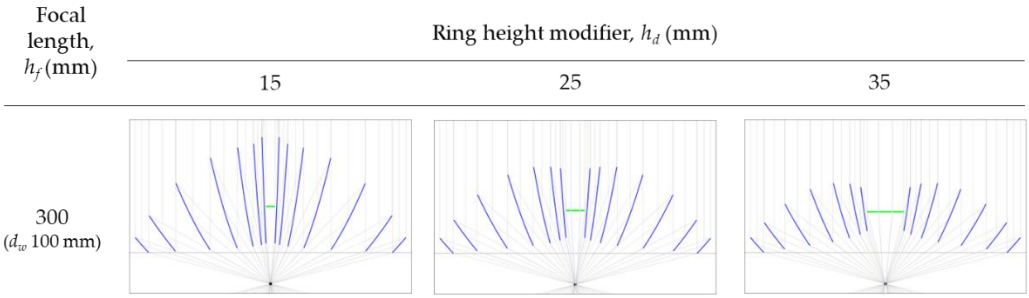

Figure 5.8 — Cross-sectional view of the seven-ring RAC configuration at different h_d of 15, 25 and 35 mm, with h_f = 300 mm, collection area of 3.14 m^2 and d_w = 100 mm.

5.3.2.4 Total ring surface area

The surface area of a concentrator is pivotal for building a cost-effective concentrator. Equation (5.11) shows the total surface area (A_r) of all rings within a RAC. The integral section refers to the calculation of each ring surface area. The sum section refers to the sum of the surface areas of all N rings.

$$A_r = \sum_{n=1}^{N} \int_{z_{n,low}}^{z_{n,high}} \frac{\pi \times RoC_n}{6 \times z^2} \left[\left({RoC_n}^2 + 4 \times z^2 \right)^{3/2} - {RoC_n}^3 \right] dz \qquad (5.11)$$

This equation is applicable for designing all the RAC configurations. Table 5-2 shows the total surface area of various RAC configurations at a fixed collection area of 3.14 m^2 and h_f = 300 mm, but with different d_w, ranging from 60 mm to 180 mm, and h_d, ranging from 0 mm to 65 mm. The total surface ring area reduced with the increase of h_d, with fixed d_w. This reduction is mainly due to the decrease of the ring width and height from each inner ring. When h_d was too high, the innermost ring (the last ring) became so small that either its ring width or height became negative. In this situation, the mathematical

model for the RAC became invalid and the RAC ceased to exist. This problem could be easily avoided if a restriction had been previously imposed, such as a minimum ring width (min Δa_n) and/or a minimum ring height (min H_n). However, in this study, no restriction was imposed for the RAC composition at any configuration. The largest surface area was obtained at h_d = 15 mm and d_w = 180 mm, and it decreased as d_w was reduced. Near h_d threshold, the overall RAC ring surface area was significantly reduced.

Table 5-2 — Surface area of a RAC with 3.14 m^2 collection area and h_f = 300 mm at different d_w and h_d.

d_w (mm)	Total surface ring area (m^2) h_d (mm)						
	15	**27.5**	**35**	**45**	**55**	**60**	**65**
60	8.52	7.08	4.61	-	-	-	-
80	8.84	7.89	6.97	3.97	-	-	-
100	9.08	9.08	7.70	6.36	-	-	-
120	9.28	8.63	8.13	7.22	5.62	-	-
140	9.46	8.88	8.46	7.74	6.66	-	-
160	9.64	9.10	8.74	8.13	7.30	6.73	-
180	9.82	9.31	8.98	8.46	7.77	7.32	6.77

5.3.2.5 Aspect ratio

The aspect ratio is the ring height divided by the diameter of the concentrator. It is one of the most important parameters for solar concentrator design and applications. Equation (5.12) gives the aspect ratio (*AR*) of a RAC, illustrated in Figure 5.9. *D* is the diameter of the RAC and max H_n is the highest ring height of all the rings.

$$AR = \frac{\max H_n}{D} = \frac{\max H_n}{2\, a_{out_1}}, n = [1, \dots, N] \tag{5.12}$$

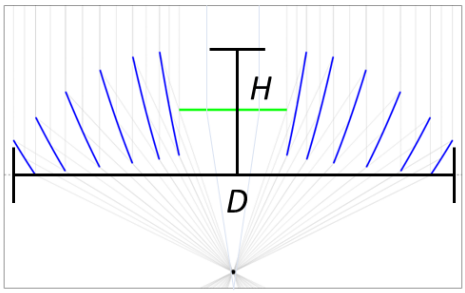

Figure 5.9 — Aspect ratio of a RAC. *H* is the maximum height and *D* is the diameter of the RAC.

Table 5-3 shows the aspect ratio of the seven-ring RAC with the same collection area of 3.14 m^2 and h_f = 300 mm, but with different h_d, ranging from 15 mm to 65 mm, and d_w, ranging from 60 mm to 180 mm. The aspect ratio decreased drastically with the increase of h_d, at fixed d_w. It also decreased with the reduction of d_w; however, at a lower rate than that with h_d variation.

Table 5-3 — Aspect ratio of a RAC at different d_w and h_d with 3.14 m^2 collection area and h_f = 300 mm.

d_w (mm)	Aspect ratio h_d (mm)						
	15	**27.5**	**35**	**45**	**55**	**60**	**65**
60	0.48	0.33	0.19	-	-	-	-
80	0.52	0.37	0.30	0.16	-	-	-
100	0.56	0.40	0.34	0.25	-	-	-
120	0.60	0.42	0.37	0.30	0.22	-	-
140	0.66	0.44	0.39	0.33	0.27	-	-
160	0.72	0.46	0.41	0.36	0.30	0.28	-
180	0.81	0.48	0.44	0.38	0.33	0.31	0.29

5.4 RAC modeling process in Zemax®

Figure 5.10 displays the non-sequential component editor within Zemax® used to model a seven-ring RAC. The initial six objects are control objects that are not shown and do not directly function within the ray-tracing sequence. The first object (named as BSPSEU) sets the solar irradiance at parameter 3, the parameter 6 sets the size of the RAC (a_{out1}) and the size of the source, the parameter 10 and 11 (not shown in the image) sets the Gaussian distribution of the source. The second object's (named as BYREF) "Y Position" sets the focal length (h_f) of the lens. The third object's (named BRING) "Y position" defines the rings thickness (d_t), the "Tilt about x" defines the first ring with d_w, it is important to note that this parameter is read by a customed made ZPL that builds the whole RAC system into the NSC editor in real time. The fourth object (named as "ring size B") "X position" defines the h_d for all rings. Object 6 serves a reference for moving the whole RAC at any axis.

Object 7 to 13 are "aspheric surface" objects that acts as reflective rings, named b1 to b7, respectively. The *RoC* (parameter 1), a_{in} (parameter 3), a_{out} (parameter 4) and d_w are calculated through a standalone ZPL code. The Y position of each ring was calculated using Equation (5.5), which is precisely negative half of the RoC value, as determined by the "pick-up" function. Object 14 represents the Fresnel lens, with its Y position being calculated via Equation (5.10), while its RoC is precisely half of its value, which is inserted in Parameter 6. The size of the Fresnel lens matches that of the last ring inner aperture, and Objects 16 and 17 represent the sources of the parabolic mirrors and the Fresnel lens, respectively. The calculation of the source powers follows Equation (3.3), while the detector is positioned at the origin.

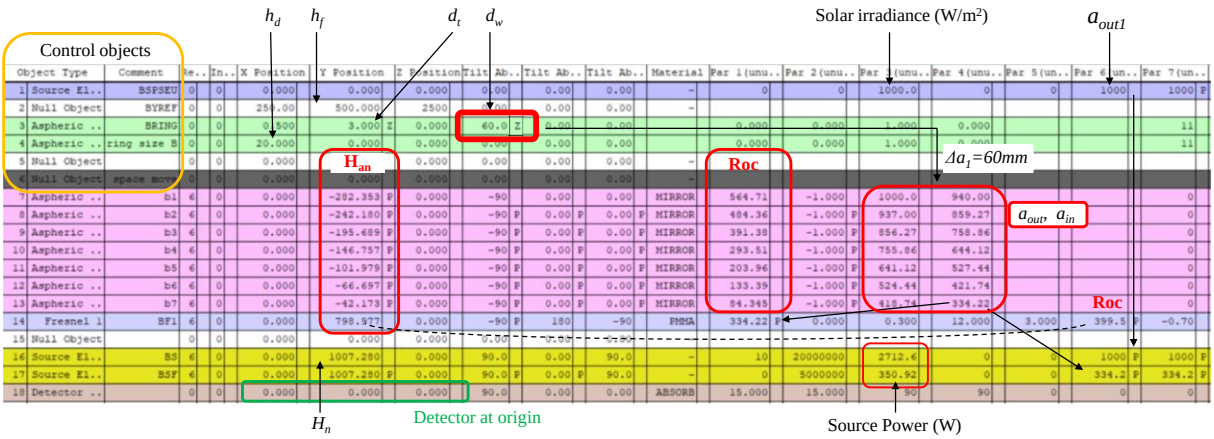

Figure 5.10 — non-sequential component window of the Zemax® for modeling the RAC.

The resulting built RAC model are shown in Figure 5.11, a) in layout model and b) in shaded model.

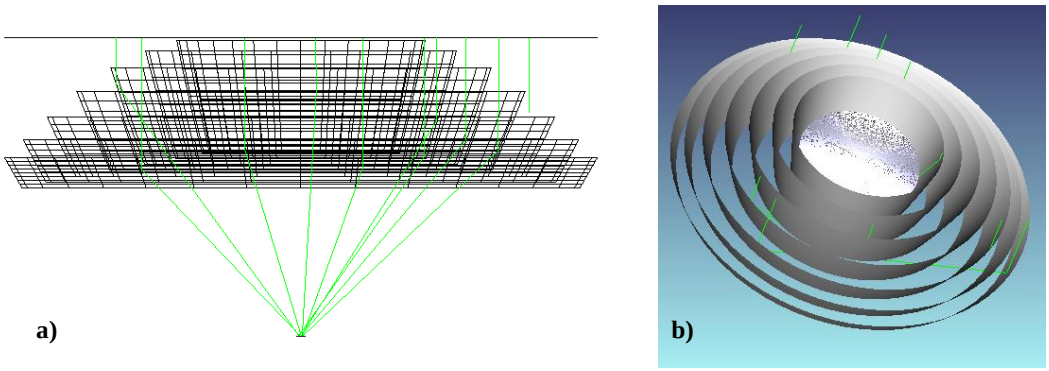

Figure 5.11 — (a) Layout window and (b) shaded model window of the seven-ring RAC.

5.5 Zemax® numerical evaluation of the RAC performance

To evaluate the optical efficiency and concentrated solar flux of different RAC configurations, we used Zemax® non-sequential ray-tracing software. Since a RAC object is not available in Zemax®, I created a virtual macro using Zemax® programming language to automate the design process. This macro included all relevant equations and added four 10 mm thick mechanical supports for both parabolic rings and the PMMA Fresnel lens, as shown in Figure 5.12. The parabolic rings were 1.5 mm thick, while the Fresnel lens was 3 mm thick.

In order to have a fair comparison with the concentrated solar flux of the MSSF parabolic mirror system in PROMES-CNRS [12], 59% mirror reflectance was here assumed for the parabolic ring mirrors. This 59% reflectance of the MSSF resulted from the 78% reflectivity from the heliostat and the 76% reflectivity from the MSSF parabolic mirror. The typical solar irradiance of 1000 W/m^2 in Odeillo, France, in clear sunny days was also considered. Sixteen key solar wavelengths, ranging from 0.325 μm to 2.223 μm, with their respective weight consulted in the standard solar spectrum for one-and-a-half air mass (AM1.5), were used as the wavelength data [110]. An absorbing flat rectangular detector of 15×15 mm^2 with 100×100 pixels resolution was used for the simulation and data acquisition at the focus of the RACs. Over 20 million analysis rays were used for each ray-tracing simulation to evaluate the performance of the RAC.

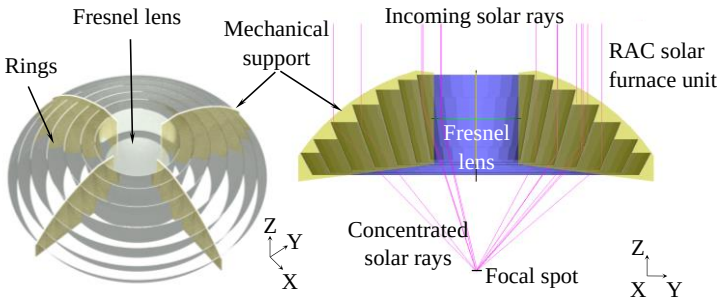

Figure 5.12 — (a) General view and (b) Cross-sectional view of an example of the RAC design.

The incoming solar light follows a gaussian distribution that was calibrated from the MSSF parabolic mirror at PROMES-CNRS within Zemax® to match the concentrated solar flux and focal size. The solar divergence half-angle (θ_a) of 0.27° was assumed. The same gaussian distribution was then used for the numerical analysis of the RAC. Figure 5.13 shows the interaction of a portion of the non-normal incident solar rays with the first two rings. A portion of the solar rays ($-\theta_a$) is reflected by the 1st ring (1), while a small portion is lost by the physical thickness of the ring (2). The remaining portion of the solar rays ($+\theta_a$) is reflected by the 2nd ring (3). Only a small portion of the solar rays, at the input edge of the 2nd ring, are blocked by the back-surface of the 3rd rings (4), representing a loss less than 1%.

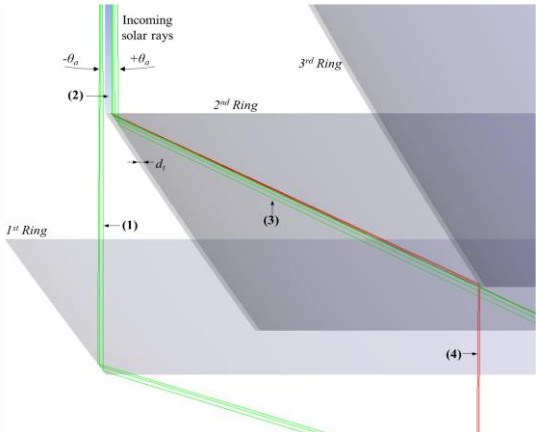

Figure 5.13 — Cross-sectional view of the interaction of one part of the incoming solar rays with the first two rings of the RAC in Zemax® non-sequential workspace. (1) The transmitted solar rays with divergence half-angle $-\theta_a$. (2) The blocked solar rays by the physical thickness of the ring. (3) The reflected solar rays with divergence half-angle $+\theta_a$. (4) The reflected/blocked solar rays due to the thickness of the 3rd ring from the reflected rays at the edge of the 2nd ring.

5.5.1 Concentrated solar flux

The concentrated solar flux represents the amount of solar power per unit area at the focus of the concentrator. Figure 5.14 shows the concentrated solar flux of a seven-ring RAC with collection area of 3.14 m^2 and h_f of 300 mm, at different d_w, ranging from 60 mm to 180 mm, and h_d, ranging from 15 mm to 65 mm.

Concentrated solar flux higher than 18 W/mm^2 was achieved within a certain range of h_d at any value of d_w. For example, for d_w = 60 mm, concentrated solar fluxes higher than 18 W/m^2 were obtained at h_d ranging from 0 mm to 32.5 mm. Smaller d_w attained a slightly increased concentrated solar flux as compared to that with larger d_w. For example, with d_w = 60 mm at h_d = 27.5 mm, maximum concentrated

solar flux of 18.72 W/mm^2 was attained, while with d_w = 80 mm at h_d = 32.5 mm, the solar flux decreased to 18.64 W/mm^2. For the same d_w, the solar flux varied significantly with h_d. For example, with d_w = 120 mm and h_d = 45 mm, 18.3 W/mm^2 solar flux was obtained, while with d_w = 120 mm and h_d = 54 mm, the flux value decreased to 16 W/mm^2. Nevertheless, at larger d_w, the concentration solar flux was kept above the 18 W/mm^2 within a larger range of h_d. Figure 5.14 offers a wider range of choice for RAC modelling.

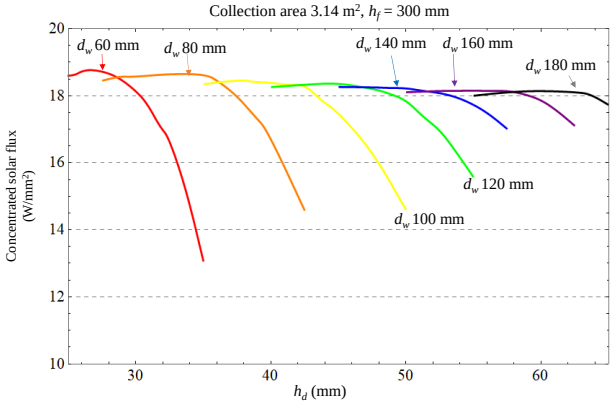

Figure 5.14 — Concentrated solar flux of seven-ring RACs with collection area of 3.14 m^2 at h_f = 300 mm with different d_w and h_d.

5.5.2 Optical efficiency

The optical efficiency is given by $\eta = P_2/P_1$, where P_1 is the initial radiative energy reaching the input area of the concentrator, and P_2 is the concentrated radiative energy at the focus [110]. The RAC optical efficiency depends on the concentration efficiency of both the parabolic rings and Fresnel lens. Figure 5.15 shows the optical efficiency of the seven-ring RAC with fixed collection area of 3.14 m^2 and h_f of 300 mm, at different d_w, ranging from 60 mm to 180 mm, and h_d, ranging from 15 mm to 65 mm. The maximum optical efficiencies are shown in Figure 5.15. Unlike the concentrated solar flux mentioned in the previous section, the optical efficiency approached the maximum value for large values of h_d and d_w. The maximum optical efficiency stopped at d_w of 180 mm, where the RAC model ceased to exist.

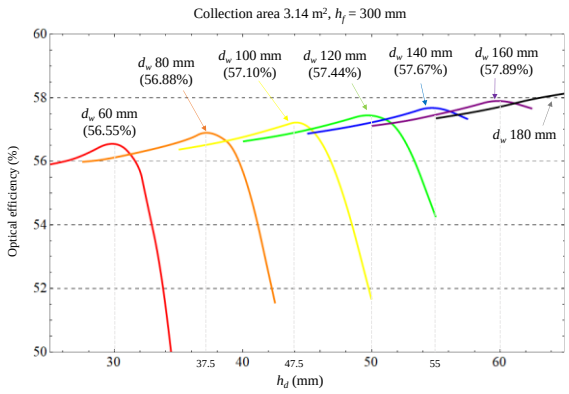

Figure 5.15 — Optical efficiency of the seven-ring RAC with collection area of 3.14 m^2 at h_f = 300 mm with different d_w and h_d.

5.6 Seven-ring discussion

The concentrated solar flux, optical efficiency, total ring area, and aspect ratio of the seven-ring RAC with a collection area of 3.14 m^2 and a focal length of 300 mm are strongly influenced by the initial RAC parameters, which dictate the model's outcome. Figure 5.16 illustrates the output performance of the RAC under various combinations of d_w and h_d, showing the concentrated solar flux, optical efficiency, total ring area, and aspect ratio.

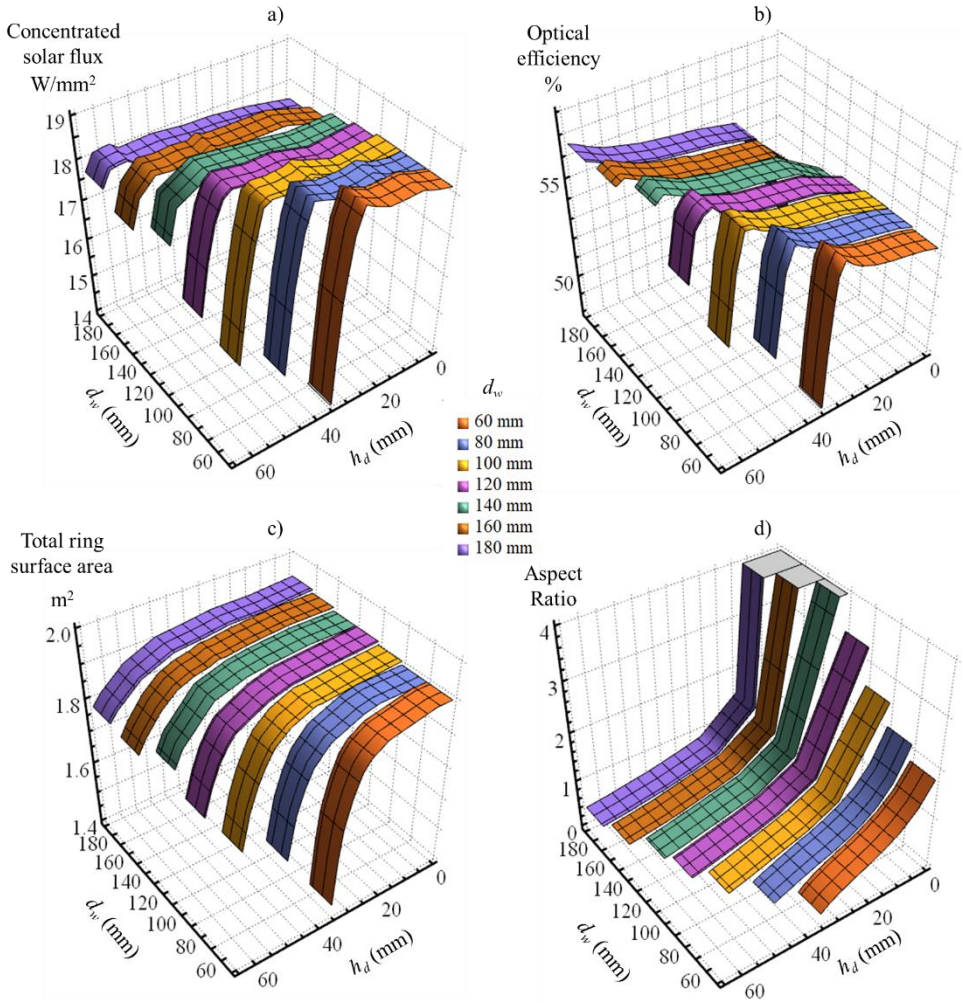

Figure 5.16 — Representation of the output characteristics of: (a) concentrated solar flux (W/mm^2), (b) optical efficiency (%), (c) total ring surface area (m^2) and (d) aspect ratio, from the seven-ring RAC configurations with 3.14 m^2 collection area, h_f = 300 mm at d_w of 60, 80, 100, 120, 140, 160, 180 mm and h_d of 0, 20, 40 to 60 mm.

The concentrated solar flux benefits from an increase in h_d value, at fixed d_w. This is valid until a certain h_d threshold, from which it starts to decrease. For example, in Figure 5.16 a), at d_w 60 mm, the concentrated solar flux started with 18.20 W/mm^2 for h_d = 0 mm, increasing to 18.72 W/mm^2 for h_d = 27.5 mm, and then it dropped to 13.05 W/mm^2 at h_d = 35 mm. For a fixed h_d value, the concentrated solar flux has a decreasing trend with the increase of d_w.

Similarly, the optical efficiency rises with the increase of the h_d value, at fixed d_w, up to a certain h_d threshold, from which it starts to decrease. This example could be seen at Figure 5.16 b) at d_w 60 mm, where the optical efficiency started with 53.45% for h_d = 0 mm, increasing to 55.11% at h_d = 30 mm, and then it dropped to 46.61% at h_d = 35 mm.

The total ring surface area of the RAC has its maximum at h_d = 0 mm, at any d_w, and it is reduced with the increase of h_d, as shown in Figure 5.16 c). This steady reduction became more abrupt with the decrease of d_w.

The aspect ratio of the RAC rapidly decreases with the increase of h_d, as shown in Figure 5.16 d). With the increase of d_w, this sudden decline acquires a more gradual reduction rate.

The interaction of d_w and h_d has a direct influence on the width and height of all the rings of the RAC, influencing the concentrator's aesthetical composition and output. Figure 16 shows the strong influence of d_w and h_d on the RAC cross-sectional profile and its respective output performance.

The d_w has a direct tie with the width of a ring. A small d_w value not only sets a smaller width of the first ring, but also leads to a smaller width for each successive inner ring. The last ring would normally leave a hole in the middle, and it would be occupied by a Fresnel lens, as shown in Figure 5.17. At larger d_w, the width of the inner rings was larger, which leaves a smaller gap at the centre of the concentrator, as shown in Figure 5.17, for d_w = 100 mm, and h_d = 15 mm.

At the extreme case of d_w = 180 mm, the width of the second and third ring is larger, and their size occupied most of the inner space. The width of the next rings decreased for smaller h_d in such a way that the last ring would become unrealistically long and there would be practically no space to add a Fresnel lens at the centre, as shown in Figure 5.17 for d_w = 160 mm and d_w = 180 mm, at h_d = 15 mm. Due to the long length of the innermost ring, the total ring surface area and aspect ratio increases. Moreover, this configuration does not offer the best performance in terms of concentrated solar flux and optical efficiency.

The variation of h_d modifies the internal ring's height position, and it influences the width and height of all internal rings. The increment of this value generally leads to a decrease in size of all rings and, consequently, to a larger gap on the centre of the concentrator, as shown in Figure 5.17 for d_w = 100 mm, at h_d from 15 mm to 35 mm. This not only changes the aesthetical aspect of the concentrator, but also vastly improves its desirability by reducing the aspect ratio from 1.03 to 0.53, the total ring surface area from 1.90 m^2 to 1.86 m^2, increasing the concentrated solar flux from 18.10 W/mm^2 to 18.40 W/mm^2 and the optical efficiency from 54.31% to 54.93%, respectively. However, any further increment of the h_d may cause some of the innermost rings to become too small and physically impossible to produce, as shown in Figure 16 for d_w 160 mm and h_d 60 mm. In this case, the innermost ring could be removed, as well as the vertically long innermost ring of the RAC with h_d 15 mm, since in both cases the collection area was so small that it has little influence on the total output of the concentrator.

The output performance of the concentrator is largely dependent on both h_d and d_w variables. Most of the h_d/d_w combinations proved to be equally efficient, but the practicability of the concentrator should be also considered. It is favourable for a cost-effective concentrator to have a smaller aspect ratio and a lower total ring surface area, which is more practical, cheaper, and lighter. Therefore, a compromise between d_w and h_d is needed to attain a balance between high concentrated solar flux and optical efficiency, accompanied by a reasonable aspect ratio and low total ring surface area. For example, the d_w = 60 mm and h_d = 27.5 mm configuration had the highest concentrated solar flux of 18.72 W/mm^2, associated with a moderate optical efficiency of 54.75%, while it had a total ring surface area of 1.81 m^2 and a moderate aspect ratio of 0.50.

Figure 5.17 — Summary of the concentrated solar flux (W/mm^2) / optical efficiency (%) / total ring surface area (m^2) / aspect ratio from the seven-ring RAC configurations with 3.14 m^2 collection area and h_f = 300 mm at different d_w and h_d of 15, 27.5, 35, 45 and 60 mm.

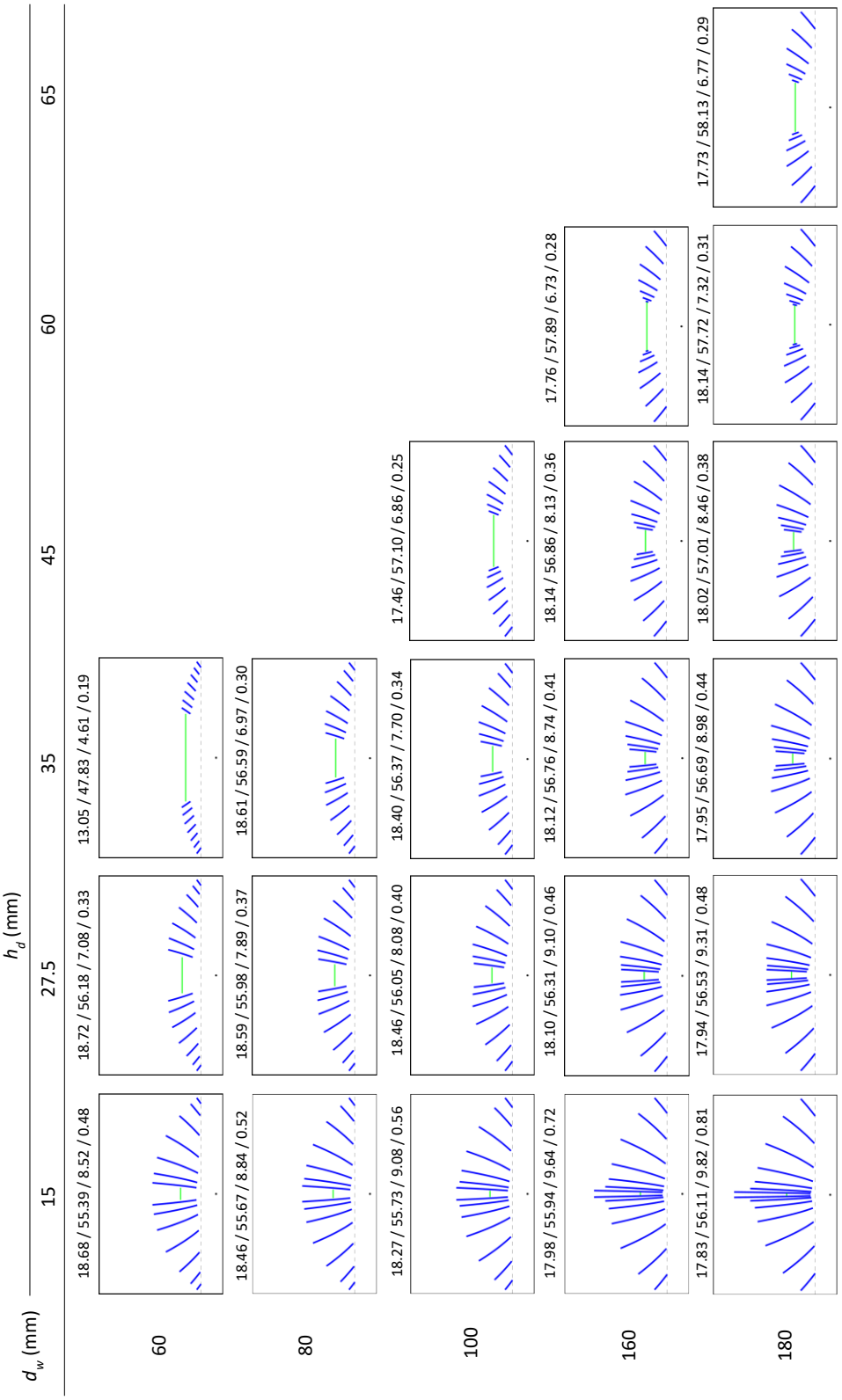

5.7 3D RAC

Figure 5.18 illustrates the 3D RAC solar furnace proposed in this study, which consists of five RAC units that focus incoming solar light onto a shared focal spot. These RACs are arranged to form a compact box-shaped solar furnace, which has a rear opening for easy access to the focal spot in the center. Figure 5.19 shows the concentrating process, with the primary RAC receiving incoming solar light that has been reflected by the heliostat, while the four lateral RACs receive reflected sunlight that has been first reflected by the heliostat and then by the four plane folding mirrors, which have a reflectivity of 95%.

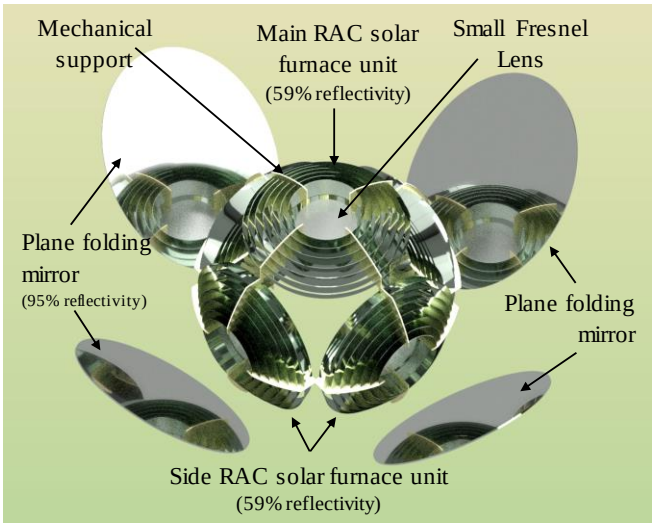

Figure 5.18 — 3D RAC solar furnace composed of five identical seven-ring RACs and four folding mirrors.

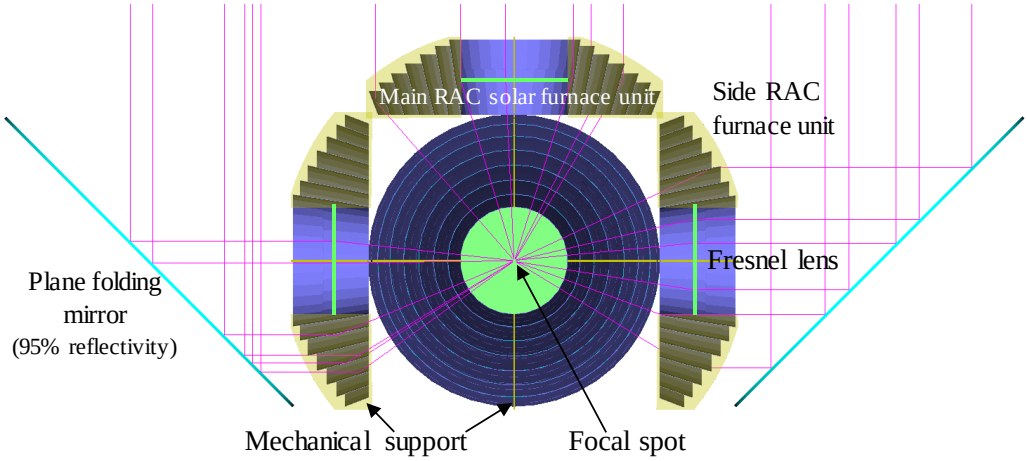

Figure 5.19 — Schematics of the cross-sectional view of the 3D RAC solar furnace with solar rays being concentrated to a common spot.

5.7.1 Heat load analysis of the 3D RAC, the MSSF parabolic mirror and the Fresnel lens solar furnaces.

The heat load analysis of the solar furnaces was conducted with a 15 mm × 15 mm × 15 mm volume detector in ZEMAX®. To ensure an accurate comparison with the performance of the 3.14 m^2 (1 m

radius) MSSF parabolic mirror, each RAC unit had 0.447 m radius, corresponding to 0.628 m^2 collection area; therefore, a combined 3.14 m^2 collection area was achieved for the five RAC units mounted together to form the 3D RAC solar furnace. 59% reflectivity was assumed for all the rings and 95% reflectivity for the folding mirrors.

The heat load distributions and the FWHM dimensions of the focal spots of the 3D RAC, the MSSF parabolic mirror and the Fresnel lens solar furnaces are shown in Figure 5.20.

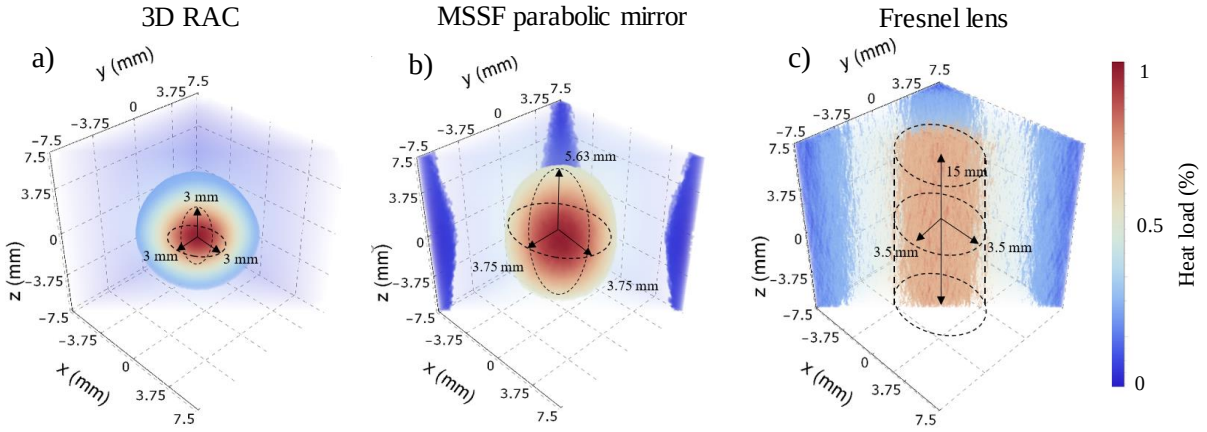

Figure 5.20 — Cross-sectional view of the heat load distribution at the focal spot of (a) the 3D RAC, (b) the MSSF parabolic mirror and (c) the Fresnel lens solar furnaces.

Due to the short focal length of 0.447 m for each 3D RAC unit, a considerably small spherical focal volume of 3 mm × 3 mm × 3 mm (27 mm^3) was obtained, as compared to that of the MSSF parabolic mirror, which obtained a large ellipsoidal-shape focal volume of 3.75 mm × 3.75 mm × 5.63 mm (41.45 mm^3). The Fresnel lens presented a significantly large cylindrical focal volume of 3.5 mm × 3.5 mm × 15 mm (577 mm^3).

The unique combination of the five RAC's units ensured therefore a considerably enhanced solar flux as compared to that of the conventional parabolic mirror solar furnace. This also may open a door for the high flux solar pumping of laser media, such as Alexandrite that requires very high pumping flux within a small volume [111].

5.7.2 Improvement of solar concentration ratio by the 3D RAC furnace

The concentration ratio C is defined by the input aperture area of the focusing collector over the receiver area ($C = S_{concentrator}/S_{receiver}$) [20]. By using the edge-ray principle [112] and assuming $\theta_a = 0.265°$ Sun-Earth acceptance half-angle subtended by the Sun [20], the maximum radius of a spherical receiver (r_{sphere}) at the focus of a parabolic mirror can be determined by the parabola's radial aperture ($r_{parabola}$) and its rim angle (ω) [3, 113], as indicated by Equation (5.13) and Figure 5.21 a).

$$r_{sphere} = r_{parabola}\,\frac{\sin\theta_a}{\sin\omega} \tag{5.13}$$

The maximum solar concentration ratio for an ideal perfectly specular 3D paraboloid rim angle aligned to the Sun, is given by Equation (5.14) [20].

$$C_{parabola} = \frac{S_{parabola}}{S_{sphere}} = \frac{\pi\, r_{parabola}^2}{4\,\pi\, r_{sphere}^2} = \frac{sin^2\omega}{4\, sin^2\, \theta_a} \tag{5.14}$$

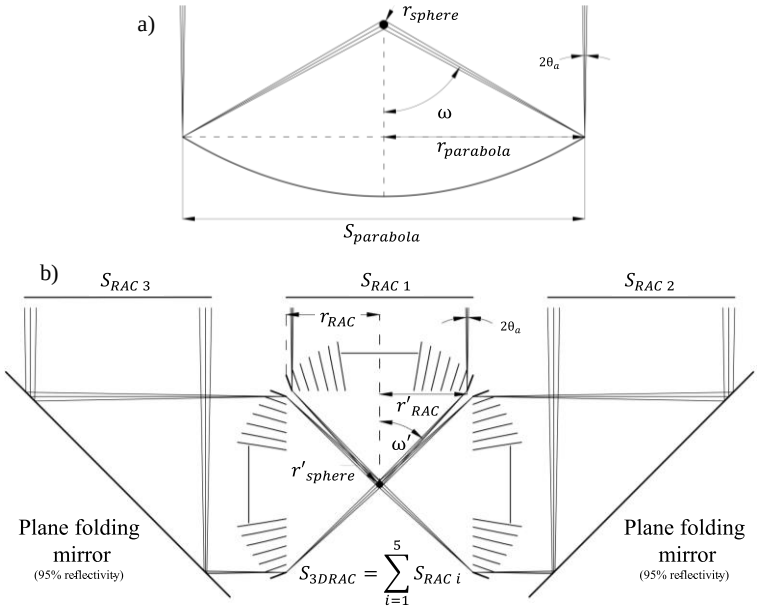

Figure 5.21 — Solar concentration schemes of (a) the parabolic mirror and (b) the 3D RAC solar furnaces, both with the same collection area *S*; S_{RAC1}, S_{RAC2}, S_{RAC3}, and $S_{RAC4,}$ S_{RAC5} are the collection areas of each single RAC; r_{RAC} is the radius of a single RAC; r'_{RAC} is the inner radius of the outmost ring of the RAC; r_{sphere} and r'_{sphere} are the radius of the receiver spheres of the parabolic mirror and the 3D RAC solar furnaces, respectively ; ω and ω' are the rim angles of the parabolic mirror and the 3D RAC solar furnaces, respectively; θ_a is the Sun-Earth acceptance half-angle.

The 3D RAC furnace total collection area (S_{3DRAC}) is given by the combination of the five single RACs collection area (S_{RACi}), as shown in Figure 5.21b and Equation (5.15).

$$S_{3DRAC} = \sum_{i=1}^{5} S_{RACi} \tag{5.15}$$

Since the 3D RAC furnace is composed of five single RACs with the same aperture and focal length, by the edge-ray principle, the radius of the spherical receiver of the 3D RAC (r'_{sphere}) can be determined by the inner radius of the outmost ring of a RAC (r'_{RAC}), its rim angle (ω') and the Sun-Earth acceptance half-angle (θ_a = 0.265°), as shown in Equation (5.16):

$$r'_{sphere} = r'_{RACi}\, \frac{sin\, \theta_a}{sin\, \omega'} \tag{5.16}$$

From Equations (5.8) and (5.9), the concentration ratio of the 3D RAC can then be calculated by:

$$C_{3DRAC} = \frac{S_{3DRAC}}{S'_{sphere}} = \frac{\sum_{i=1}^{5} S_{RAC\,i}}{4\,\pi\, r'^2_{sphere}} = \frac{\sum_{i=1}^{5} \pi\, r_{RACi}^2\ sin^{\,2}\omega'}{4\,\pi\, r'^2_{RAC}\, sin^2\, \theta_a} = \frac{5}{4}\frac{r_{RAC}^2 sin^{\,2}\omega'}{r'^2_{RAC} sin^2\, \theta_a} \tag{5.17}$$

The MSSF parabolic mirror with $r_{parabola}$ = 1000 mm has 60° rim angle and 850 mm focal distance. For the same collection area (S = 3.14 m^2), each RAC has r_{RAC} = 447 mm, r'_{RAC} = 420 mm, 447 mm focal distance and 43° rim angle. By using the edge-ray principle, the spherical receiver surface areas of 358.42 mm^2 (r_{sphere} = 5.34 mm) and 101.47 mm^2 (r'_{sphere} = 2.84 mm) were calculated for the MSSF

parabolic mirror and the 3D RAC furnaces, respectively. The concentration ratios of 8765 for the MSSF parabolic mirror and 30962 for the 3D RAC solar furnace were finally obtained, respectively, as summarized by Table 5-4.

Table 5-4 — Comparison of the MSSF parabolic mirror concentration ratio with that of the 3D RAC furnace

	3D RAC furnace	MSSF parabolic mirror
Collection area (m^2)	3.14	3.14
Sphere radius (mm)	2.84	5.34
Concentration ratio	30962	8765

Figure 5.22 shows the incident solar flux distribution onto the spherical receivers of both the MSSF parabolic mirror (r_{sphere} = 5.34 mm) and the 3D RAC (r'_{sphere} = 2.84 mm) solar furnaces. The large receiver surface of the MSSF parabolic mirror has one single light spot with high flux at its top, while little or no presence of light irradiance at its bottom, as shown in Figure 5.22 a). For the small 3D RAC receiver, most of its surface area is irradiated more uniformly than that of the MSSF parabolic mirror by high flux solar power, as shown in Figure 5.22 b).

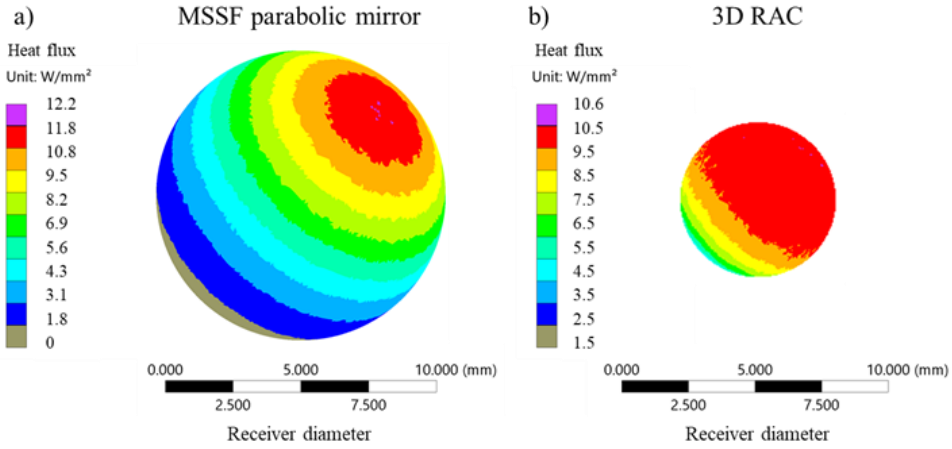

Figure 5.22 — The solar flux distribution profile on the surface of the spherical receivers from (a) the MSSF parabolic mirror and (b) the 3D RAC solar furnace.

5.7.3 Improvement in optical efficiency by the 3D RAC solar furnace

The optical efficiency is defined as the ratio between the absorbed solar power by a receiver and the incoming solar power of a solar collector. Figure 5.23 shows the comparison of the optical efficiencies of the MSSF parabolic mirror and 3D RAC furnace, for various spherical receiver sizes. For the MSSF parabolic mirror, 37.8% optical efficiency was numerically achieved for the $2r_{sphere}$ = 10.68 mm diameter spherical receiver, while less optical efficiency of 29.5% was numerically attained for the $2r'_{sphere}$ = 5.68 mm diameter spherical receiver of the 3D RAC. However, for receiver spheres of same diameter, the 3D RAC furnace offered a significantly higher optical efficiency compared to that of the MSSF parabolic mirror. For example, for the 10.68 mm diameter, 51.0% optical efficiency was numerically

achieved by the 3D RAC, which is 1.35 times more than that of the parabolic mirror. For receiver sphere larger than 15 mm diameter, the 3D RAC suffers from a slight decrease in optical efficiency.

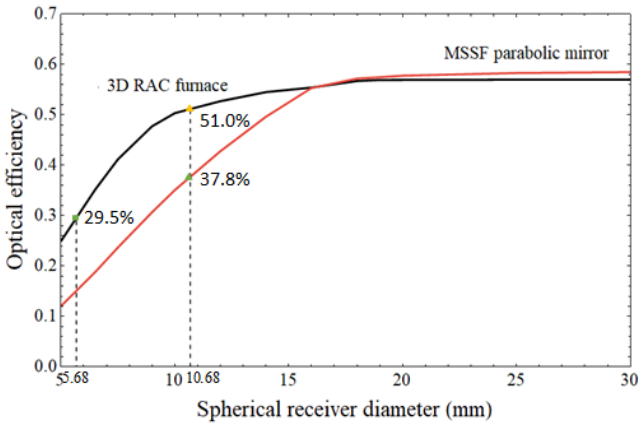

Figure 5.23 — Optical efficiency comparisons between the 3D RAC and the MSSF parabolic mirror at different receiver diameters.

5.7.4 Temperature performance analysis of the solar furnaces

Since the focused solar light at the focal spot of the 3D RAC are from five different directions (Figure 5.18), the use of the disk receiver is not suitable to analyse the temperature. Therefore, a spherical receiver was used to analyse the temperature for both the MSSF parabolic mirror and the 3D RAC solar furnaces.

Initially, a stereolithographic (STL) sphere with a radius of 2.84 mm and a total of 5624 superficial pixels was employed in Zemax® to substitute the disk receiver at the MSSF parabolic mirror's focus. The sphere's center was aligned with the focal spot's center, as demonstrated in Figure 5.24 a). Through numerical simulations, a maximum temperature of 3582 K, a minimum temperature of 2371 K, and an average temperature of 2841 K were achieved, as presented in Figure 5.24.

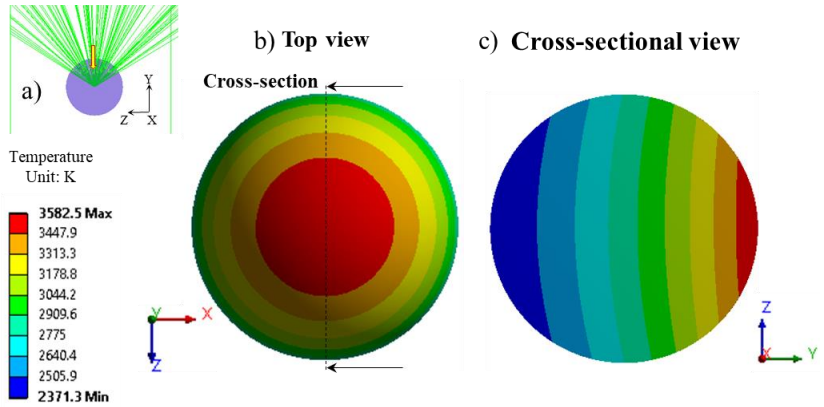

Figure 5.24 — (a) Spherical graphite receiver at the focal spot. (b) Top view and (c) cross-sectional view of the temperature distribution at the focal spot of the MSSF parabolic mirror.

A 2.84 mm radius spherical STL detector was then used for the temperature analysis of the 3D RAC furnace. The maximum temperature of 3756 K, the minimum temperature of 3344 K and the average temperature of 3632 K were numerically achieved, as shown in Figure 5.25.

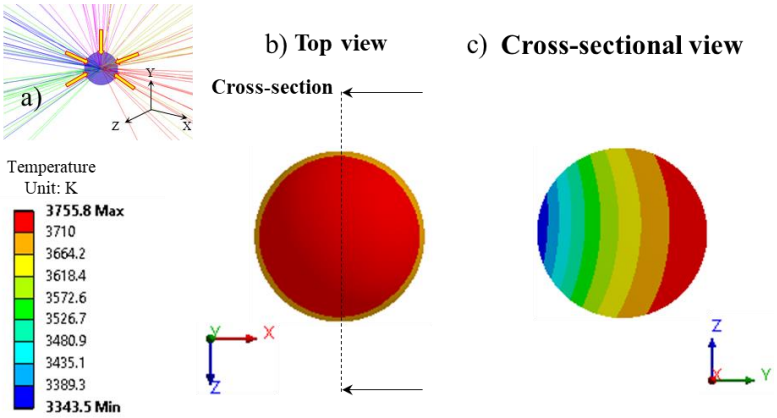

Figure 5.25 — (a) Spherical graphite receiver at the focal spot. (b) Top view and (c) cross-sectional view of the temperature distribution at the focal spot of the 3D RAC furnace.

The collection area of the solar furnace and the size of the receiver are critical factors to determine the amount of solar radiation reaching the focal spot. The 3D RAC, the parabolic mirrors and the Fresnel lens furnaces were analysed for the temperature comparison at their focal spot. Figure 5.26 shows the maximum attainable temperature for collection area up to 100 m^2. 5.68 mm, 10.68 mm, 15 mm, and 20 mm diameter spherical receivers were used.

For collection areas smaller than 3.14 m^2, the MSSF offered the highest temperature, and the 3D RAC furnace provided a slightly reduced temperature, while the Fresnel lens produced the lowest temperature. However, for the 5.68 mm diameter receiver, the 3D RAC exceeded the maximum temperature of the MSSF parabolic mirror, when the collection area was larger than 3.14 m^2. For collection areas varying from 3.14 m^2 to 100 m^2, 1.1 times gradual enhancement in maximum attainable temperature were numerically calculated. The maximum temperature of the 3D RAC furnace also increased faster than that of the MSSF parabolic mirror for all receivers, as shown in Figure 5.26.

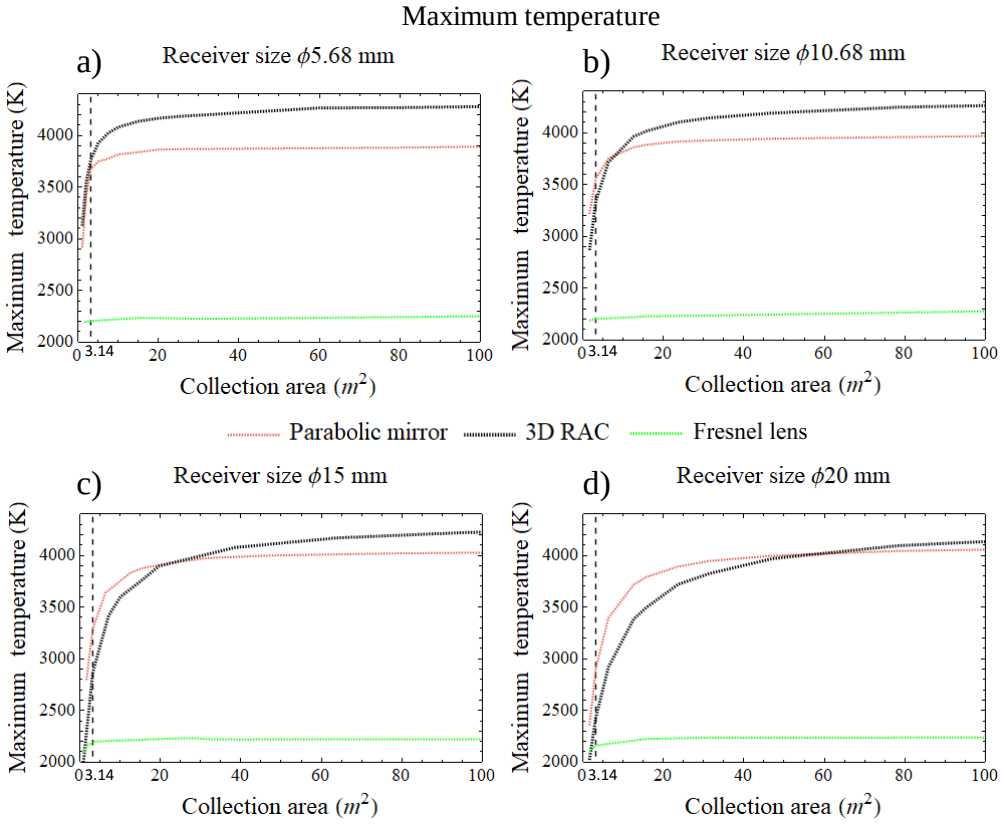

Figure 5.26 — Maximum temperature of 3D RAC, parabolic mirror, and Fresnel lens as a function of the collection area for receiver diameter of (a) 5.68 mm, (b) 10.68 mm, (c) 15 mm and (d) 20 mm.

Due to its short focal length, the 3D RAC furnace had the advantage of achieving effective solar concentration within a smaller focal spot and only a small portion of the focused rays missed the smaller diameter receiver, when compared to that of the parabolic mirror with an enlarged focal spot. For large collection area, the 3D RAC had an evident tendency for attaining higher temperature than that of the parabolic mirror. Moreover, a multiple side heating together with less heat dissipation from the small focal spot of the 3D RAC furnace also enabled a higher temperature than that of the parabolic mirror.

The Fresnel lens presented about 45% reduction in the maximum temperature performance, as compared to the above-mentioned parabolic mirror and 3D RAC schemes. No significant variation in temperature was attained neither with more collection area nor with a larger receiver.

Besides the importance of the maximum temperature, average and minimum temperatures are also vital parameters to characterize the working temperature capacity of a solar furnace. Figure 5.27 shows the influence of the receiver size and the collection area on average and minimum temperatures for each type of solar furnace. The 3D RAC furnace presented advantages in average and minimum temperatures for all collection areas.

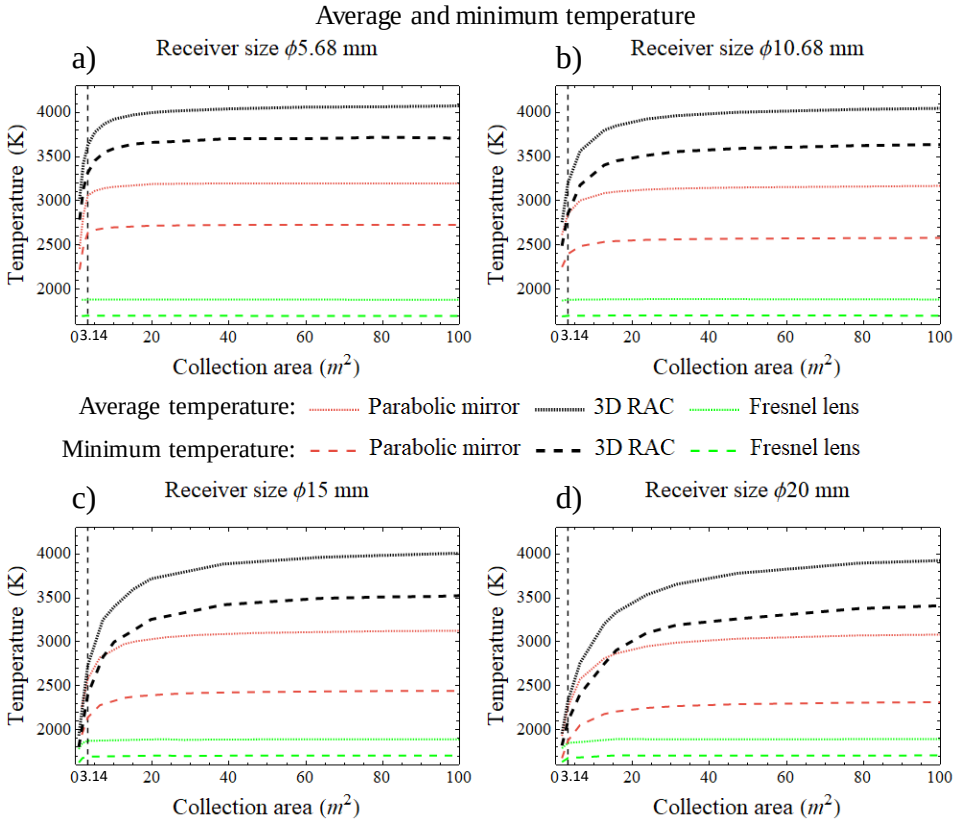

Figure 5.27 — Average and minimum temperature of 3D RAC, MSSF parabolic mirror and Fresnel lens as a function of the collection area for receiver diameter of (a) 5.68 mm, (b) 10.68 mm, (c) 15 mm and (d) 20 mm.

With the 5.68 mm diameter receiver and the collection area varying from 3.14 m^2 to 100 m^2, the average and minimum temperatures of the 3D RAC furnace were significantly improved by 870 K and 1140 K, respectively, as compared to that of the parabolic mirror, as shown in Figure 5.27 a). Even for a large diameter receiver, the superiority of the 3D RAC furnace in both average and minimum temperature operation remained. With the 20 mm diameter receiver and 100 m^2 collection area, for example, the 3D RAC furnace achieved about 870 K average temperature and 1140 K minimum temperature enhancements, respectively, over that of the parabolic mirror, as shown in Figure 5.27 d). The Fresnel lens presented significantly reduced average and minimum temperature values among these three types of solar furnaces.

5.7.5 Influence of convection coefficient on the temperature performances of both the 3D RAC solar furnace and the MSSF parabolic mirror

The temperature performances of both the 3D RAC and the parabolic mirror solar furnaces depend strongly on the convection coefficient. ANSYS™ simulation tool was used to analyse this dependency. For 5×10^{-6} W/mm^2/K convection coefficient, corresponding to the stagnant air situation in the previous sections, maximum, average and minimum temperatures of 3756 K, 3632 K and 3344 K, respectively, were numerically calculated for the 3D RAC furnace with 5.68 mm diameter receiver sphere; while maximum, average and minimum temperatures of 3582 K, 2841 K and 2371 K, respectively, were

numerically calculated for the parabolic mirror furnace with 10.68 mm diameter receiver sphere. Therefore, 4.6%, 21.8% and 29.1% more maximum, average, and minimum temperature, respectively, were obtained by the 3D RAC furnace. With the increase in convection coefficient, the advantage of the temperature performance of the 3D RAC solar furnace became more evident. For 1.2×10^{-3} W/mm^2/K convection coefficient, maximum, average, and minimum temperatures of 3321 K, 3182 K, 2865 K, respectively, were calculated for the 3D RAC furnace and 3014 K, 2137 K, 1580 K, respectively, for the parabolic mirror solar furnace. The receiver sphere with large surface area of the MSSF parabolic mirror resulted in more convection losses than that by the receiver sphere with small surface area of the 3D RAC furnace. The solar furnace using the 3D RAC design was able to generate significantly higher temperatures than the MSSF parabolic mirror scheme, with increases of approximately 9.2%, 32.8%, and 44.9% in maximum, average, and minimum temperature, respectively. This suggests that there were significant thermal losses in the parabolic mirror scheme.

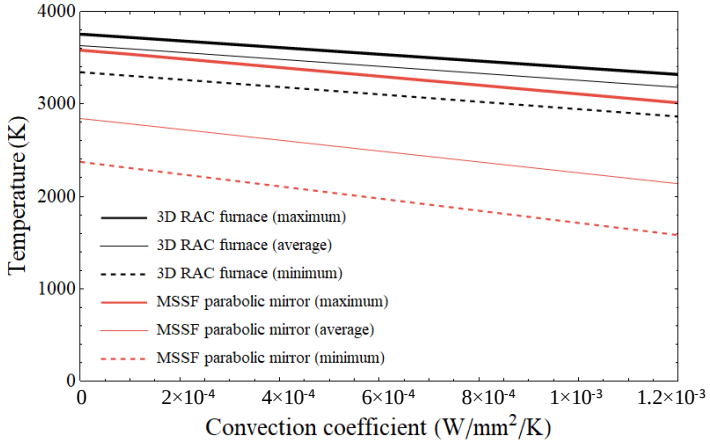

Figure 5.28 — Influence of convection coefficient on the temperature performances of both the 3D RAC solar furnace and the MSSF parabolic mirror.

5.7.6 Tracking error analysis of the 3D RAC and the parabolic mirror solar furnaces

The deviation in tracking (tracking error) results in the displacement of the focal spot from the ideal position, leading to a significant decrease in efficiency. Figure 5.29 a) demonstrates the reduction in efficiency of the 15 mm diameter spherical receiver as a function of tracking error in altitude and azimuth directions for both the MSSF parabolic mirror and the 3D RAC solar furnace.

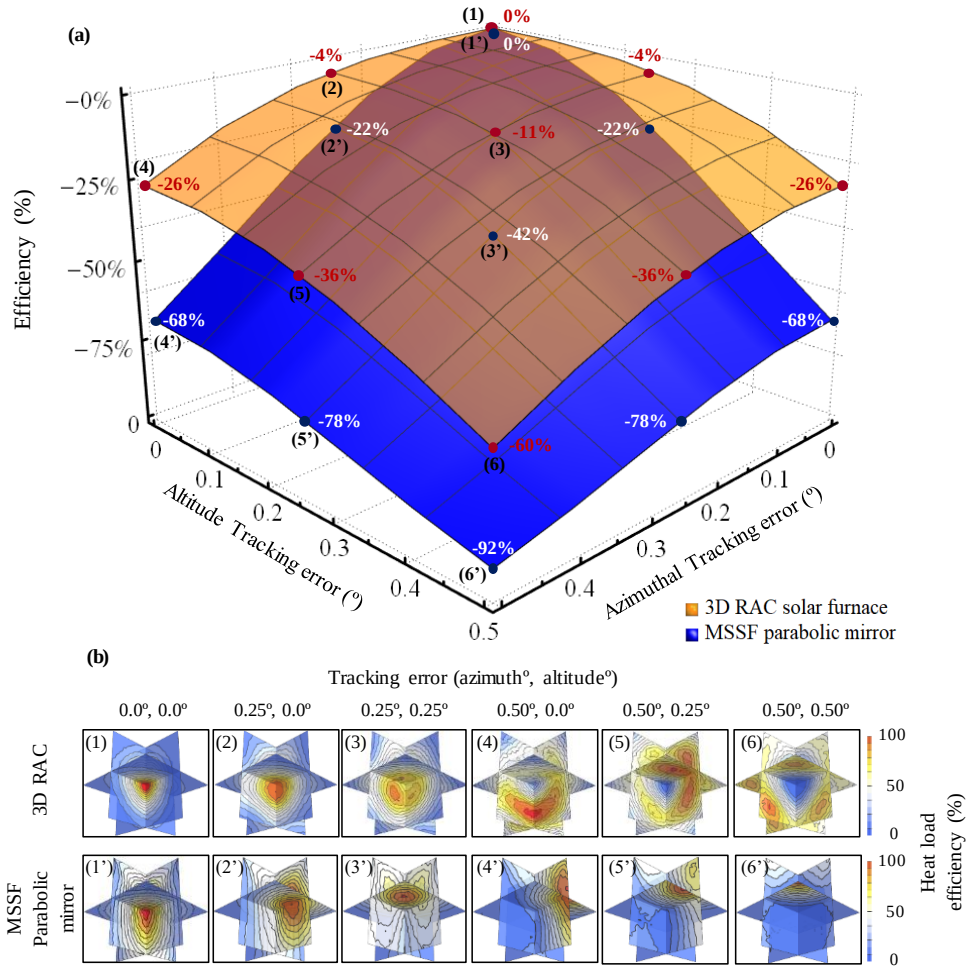

Figure 5.29 — (a) The absorbed energy by black body detector with the tracking error in altitude and azimuth directions. (b) The heat load distributions of the 3D RAC (1)(2)(3)(4)(5) and the MSSF parabolic mirror (1')(2')(3')(4')(5').

At 0.25° altitude and azimuthal tracking errors, about 11% and 42% loss were obtained for 3D RAC and MSSF parabolic mirror, respectively. However, at 0.50° on only one of the axes, a 26% and 68% power loss was obtained for 3D RAC and MSSF parabolic mirror, respectively. At the extreme case of tracking error by 0.50° on both axes, the efficiency was nearly extinguished for the MSSF parabolic mirror, and a 60% loss was obtained for 3D RAC. In summary, the 3D RAC furnace had a generally better tracking error performance as compared to the parabolic mirror furnace. Figure 5.29 b) shows the tracking error with heat load efficiency distribution at the focal spot by the 8 mm × 8 mm × 8 mm detector. For small tracking errors, the 3D RAC produced an enhanced heat load distribution at the center of the detector, as compared to that of the parabolic mirror furnace.

5.8 Conclusion

Analytical and numerical models were firstly used to optimize the single RAC solar furnace unit parameters. The single RAC, with seven ring-arrays and a small Fresnel lens at the center, provided nearly the same temperature range as that of the 3.14 m^2 MSSF parabolic mirror from PROMES-CNRS. The 3D RAC solar furnace, consisting of five RAC furnace units, was then proposed, and numerically optimized in Zemax® software. It formed a compact box-shaped solar furnace with an opening at the rear side for an easy access to the common focal spot at the center. By adopting the edge-ray principle, 3.53 times higher concentration ratio was calculated for the 3D RAC furnace, as compared to that of the parabolic mirror, leading to considerably improved thermal and optical efficiencies. The temperature performance of the 3D RAC and its dependency on both the receiver size and collection area were then numerically evaluated in ANSYS™ software and compared to that of the MSSF with same collection area. For the 6.5 mm diameter receiver, the 3D RAC exceeded the maximum temperature of the MSSF parabolic mirror for the collection area larger than 3.14 m^2. For large collection areas varying from 3.14 m^2 to 100 m^2, 1.1 times gradual enhancement in the maximum attainable temperature was numerically calculated. With the increase of the collection area, the maximum temperature of the 3D RAC furnace also increased faster than that of the MSSF parabolic mirror for all receivers. For a large size receiver (20 mm diameter for example), 870 K and 1140 K enhancements in average and minimum temperatures, respectively, in relation to that with MSSF, were numerically obtained. This shows the superiority of the 3D RAC, especially for achieving both average and minimum attainable temperatures. In addition, the 3D RAC solar furnace presented better temperature performance with convection loss and an overall enhanced tracking error compensation capacity, as compared to that of the MSSF.

6
SOLAR-PUMPED LASERS

6.1 State of the art

Laser technology has played a crucial role in various applications involving coherent light, such as material cutting, processing, and spectroscopy across diverse fields. However, conventional lasers of this kind are often characterized by their size, complexity, and high cost. The typical process involves exciting an active medium through lamps, then laser emission through the energy absorption by the active medium. This method demands a significant amount of electricity to generate a high-powered laser, and the configuration of the laser beam is achieved through intricate optics.

This chapter delves into the realm of solar-pumped lasers, a field that has evolved since the early 1960s. The technology involves concentrating solar light across all wavelengths onto the active medium through multiple stages of concentration. Subsequently, the laser is generated through the absorption of various wavelengths characteristic to the active medium. Notable advancements include the shift from the commonly used Nd:YAG crystal to the more recent Ce:Nd:YAG, as well as the transition from direct collectors of parabolic mirror then the use of Fresnel lenses to a heliostat-parabolic mirror system.

The focus of this chapter is on the modeling of an end-side-pump solar laser system, specifically targeting the pumping of Ce:Nd:YAG. The research aims to optimize solar laser production by utilizing a smaller solar collector. Key investigations include determining the minimum energy required for solar laser emission, exploring solar laser production under cloudy conditions, and studying the generation of a doughnut-shaped solar laser beam in such scenarios. These studies are crucial for the development of smaller-scale solar-pumped lasers capable of operating under cloudy conditions and providing flexibility in altering laser beam shapes.

6.2 Properties of light of solid-state lasers

Quantum properties dominate the fields of atomic and molecular physics. Radiation is quantized such that for a given frequency of radiation, there can be only one value of quantum energy for the photons of that radiation. The energy levels of atoms and molecules can have only certain quantized values. Transitions between these quantized states occur by the photon processes absorption, emission, and stimulated emission. All these processes require that the photon energy given by the Planck relationship is equal to the energy separation of the participating pair of quantum energy states.

6.2.1 Absorption and emission

The electron transitions associated with visible and ultraviolet interactions with matter, the absorption of a photon will only occur when the quantum energy of the photon matches the energy gap between the initial and final states, as shown in Figure 6.1.

$$\Delta E = E_2 - E_1 = h\nu_{21} \tag{6.1}$$

where E_2 and E_1 are two discrete energy levels, in which $E_2 > E_1$, υ_{21} is the frequency, and h is Planck's constant (6.626×10^{-34}J.s).

In the interaction of radiation with matter, if there is no pair of energy states such that the photon energy can elevate the system from the lower to the upper state, then the matter will be transparent to that radiation frequency.

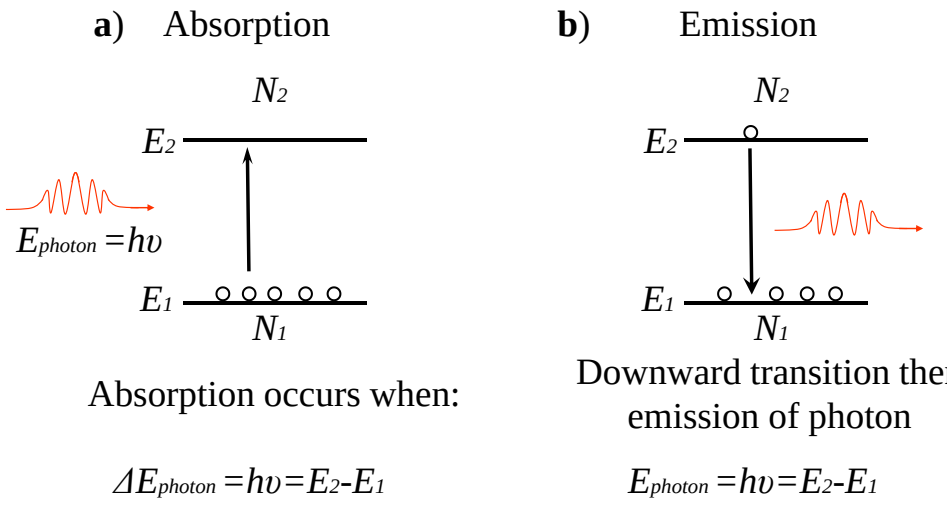

Figure 6.1 — Photon process of absorption in (a) and emission in (b).

Energy levels associated with molecules, atoms and nuclei are in general discrete, quantized energy levels and transitions between those levels typically involve the absorption or emission of photons. Electron energy levels have been used as the example here, but quantized energy levels for molecular vibration and rotation also exist. Transitions between vibrational quantum states typically occur in the infrared and transitions between rotational quantum states are typically in the microwave region of the electromagnetic spectrum.

At thermal equilibrium, the amount of population of N_1 in E_1 energy level should be populated, and none of N_2 at E_2 should be populated. The number of N_1 can be depleted proportionally due to the absorption of radiation at a density of $\rho(\upsilon)$ with a constant probability of B_{12}, shown in Equation (6.2):

$$\frac{\partial N_1}{\partial t} = -B_{12}\rho(\upsilon)N_1 \tag{6.2}$$

And the energy density is shown as:

$$\rho(\upsilon) = 8\pi h \frac{\upsilon^3}{c^3} \tag{6.3}$$

With c as speed of light at 299792458 m/s.

After an atom has been raised to the upper level by absorption, the population at the upper-level decays spontaneously to the lower level at a rate proportional to the upper-level population:

$$\frac{\partial N_2}{\partial t} = -A_{21}N_2 \tag{6.4}$$

where A_{21} is a constant related to the spontaneous transition probability to a lower level within a unit of time. Spontaneous emission can occur without the presence of an electromagnetic field, where the emitted quanta are incoherent. Thus, the A_{21} Einstein coefficient represents a loss term and introduces into the system photons that are not phase-related to the incident photon flux of the electric field, which means that the spontaneous process represents a noise source in a laser.

6.2.2 Stimulated emission

An electron already in excited state and an incoming photon with quantum energy is equal to the energy difference between its present level and a lower level, would stimulate a transition to that lower level, producing a second photon of the same energy, as shown in Figure 6.2.

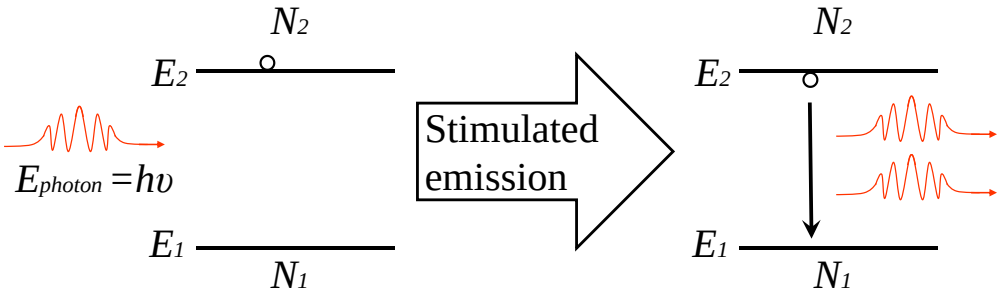

Figure 6.2 — Stimulated emission.

6.2.3 Population inversion

When a sizable population of electrons resides in upper levels ($N_2>>N_1$), this condition is called a "population inversion", and it sets the stage for stimulated emission of multiple photons. This is the precondition for the light amplification which occurs in a laser, and since the emitted photons have a definite time and phase relation to each other, the light has a high degree of coherence.

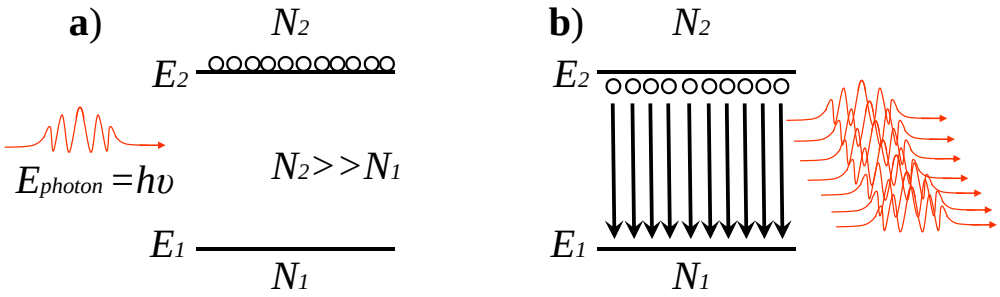

Figure 6.3 — (a) population inversion. (b) photons produced by stimulated emission, producing coherent light.

6.2.4 Fluorescence

If a high energy photon is absorbed by an atom or molecule by exciting an electron and then quickly undergoes some interaction with the crystal lattice or some collisional process, the excited electron can

be transferred to a lower quantum state. If the electron then makes a transition back to its original state, then the photon emitted will be of lower photon energy and longer wavelength.

The metastable state is an additional intermedial energy level between E_2 and E_1, defining the laser output frequency during the meta-state transition, as shown in Figure 6.4. Most transitions of ions show rapid non-radiative decay because the coupling of the internal atomic oscillations to the surrounding lattice is strong. Radiative decay processes occur, but most have short lifetimes and broad linewidths. Only a few transitions of selected ions in solids turn out to be decoupled from the lattice vibrations, which have a radiative decay that leads to relatively long lifetimes.

In three and four level laser systems, illustrated in Figure 6.4, the 3→2 and 1→0 transition frequencies fall within the frequency range of the vibration spectrum of the host crystal lattice. For this reason, these transitions can relax extremely rapidly by direct non-radiative decay, emitting a phonon to the lattice vibrations with lifetimes τ_{32}, $\tau_{10} \approx 10^{-8}$ to 10^{-11} s. Nevertheless, the transitions 3→0, 3→1, 2→0, and 2→1, with larger energy gaps, often correspond to transition frequencies that are higher than the highest possible vibration frequency of the crystal lattice. Since the lattice cannot accept phonons at those high frequencies, these transitions cannot relax via simple single-phonon spontaneous emission but relax either by radiative photon emission or by multiple-phonon processes, which are relatively weak compared to direct single-phonon relaxation. Therefore, these transitions will have much slower relaxation rates ($\tau_{21} \approx 10^{-5}$ to 10^{-3} s). The energy levels from the pump band, E_3, will then relax mostly into the metastable level, E_2, which has a long lifetime because there are no other levels located close below it, into which it can decay directly.

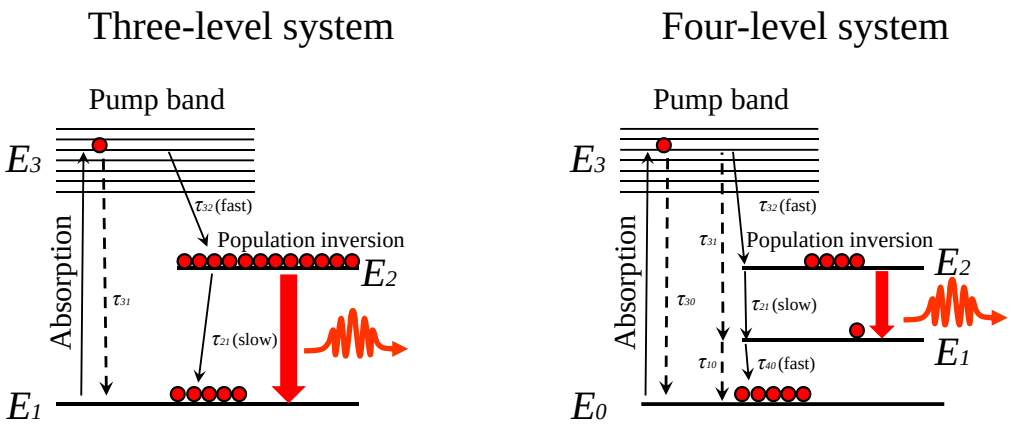

Figure 6.4 — Schematic energy level diagram of a three and four-level laser system.

6.2.5 Laser oscillator

For a laser device, in addition to a laser material and pump energy to maintain a non-equilibrium state, it is also necessary to have a feedback mechanism for radiation to build up the amplified optical field. This requirement can be obtained by placing the laser medium into a laser resonator, as shown in Figure 6.5.

The pump energy inverts the electron population in the laser material, leading to energy storage in the upper laser level, as shown in Figure 6.5 b) to f). The resonator, or resonant cavity, maintains the

electromagnetic field configuration by the amplifying medium through stimulated emission. Thus, the resonator defines the spectral, directional, and spatial characteristics of the laser radiation. The resonator is composed of two opposing mirrors (plane-parallel or curved) with the right radius of curvature, reflectivity of the mirror and relative distance to the axis of the active material. This enables the laser beam to travel back and forth through within the laser material, increasing the amplification of stimulated radiation, as shown Figure 6.5 c) to f). For laser emission at the desired wavelength, one of the cavity mirrors must be highly reflective, approaching 100% reflectivity, while the other lens (output coupler), must have a partially reflective coating for the same wavelength. A portion of the radiation will then "leak" out from the oscillator, and laser emission will occur if the feedback and gain are strong enough to compensate for the internal losses within the system.

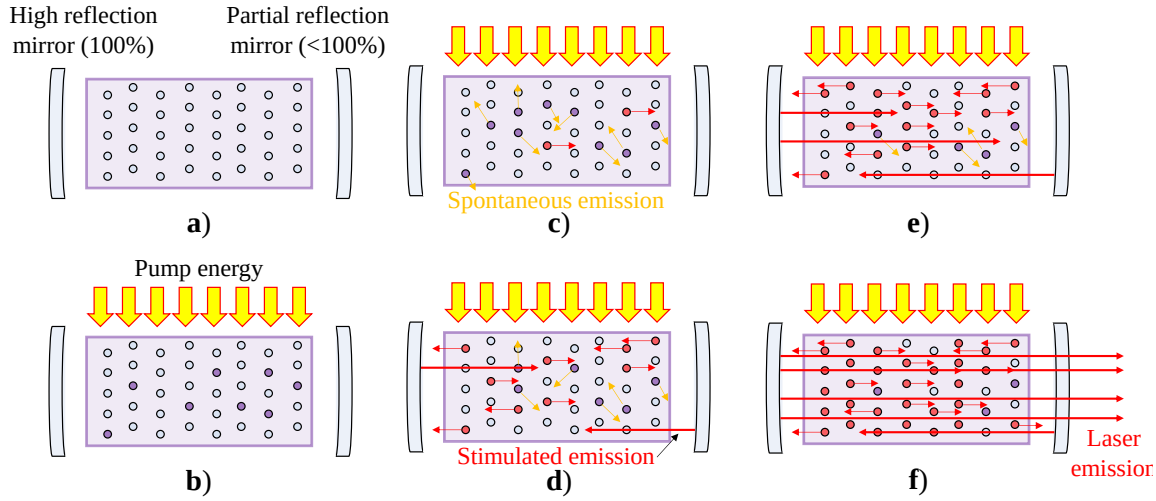

Figure 6.5 — Schematic scheme of laser oscillation operation through a resonant cavity.

6.3 Solar power conversion to laser output power

To achieve a desired output performance with the maximum system efficiency it is of utmost importance to understand the dependency and interrelationship of the laser system design parameters and design issues which may help in the optimization of the overall laser efficiency. This can be represented by the energy diagram schematically illustrated in Figure 6.6.

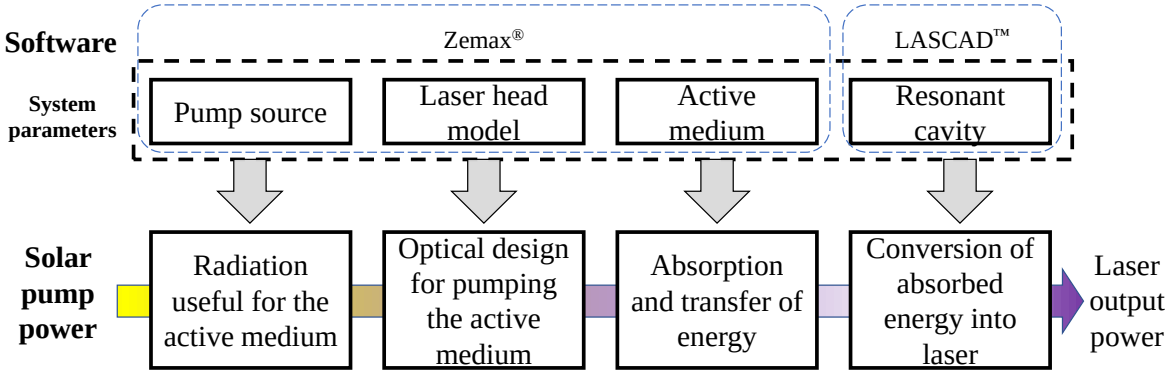

Figure 6.6 — Energy conversion process in a solar pumped laser system.

6.3.1 Absorption of pumped radiation by the active medium and transfer of energy to the upper laser level

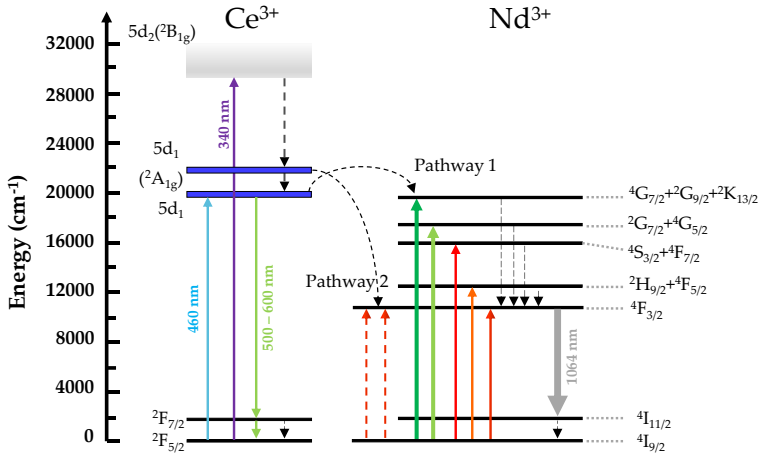

Figure 6.7 — Absorption and emission energy level of Ce^{3+} and Nd^{3+} ions. (1) the energy transfer by cross relaxation of Ce^{3+} to Nd^{3+}ion, and (2) the quantum cutting down conversion of Ce^{3+} ion from $5d_1$ energy level into two Nd^{3+} ions at $^4F_{3/2}$ energy level. Adapted from [55] and [51].

The strong UV and blue photons excite the Ce^{3+} 4f level (the $^2F_{5/2}$ ground state), towards the 5d sublevels of $5d_1$ and $5d_2$, as shown in Figure 6.7 [55, 114]. The consequent energy relaxation from $5d_1$ to both ground states $^2F_{7/2}$ and $^2F_{5/2}$ forms a yellow/green broad emission spectrum, overlapping with the excitation peaks of the Nd^{3+} ion at the $^4G_{7/2}$+$^2G_{9/2}$+$^2K_{13/2}$ energy levels between 510 nm and 540 nm and the $^2G_{7/2}$+$^4G_{5/2}$ energies levels between 566 nm and 595 nm [55, 115]. The radiative transfer mechanism by the transition 5d→4f of the Ce^{3+} ion and the transitions $^4I_{9/2}$→$^4G_{7/2}$+$^2G_{9/2}$+$^2K_{13/2}$ and $^4I_{9/2}$→$^2G_{7/2}$+$^4G_{5/2}$ through cross-relaxation process are indicated by pathway (1) in Figure 6.7 [55]. The pathway (2) represents the energy transfer from the Ce^{3+} excited state at $5d_1$ to the two Nd^{3+} ions at $^4F_{3/2}$ level through quantum cutting down-conversion process [55].

6.3.2 Conversion of input delivered from the pump source to useful pump radiation.

In solar-pump modelling process, the useful solar radiation is considered in the pumping source as the radiation absorbed by laser medium. The Ce:Nd:YAG is used through this thesis as the active medium and the main emission wavelength of 1064 nm from Nd^{3+}. The direct solar spectrum, the Ce:Nd:YAG absorption spectrum, the Ce^{3+} and Nd^{3+} ions' emission bands in YAG are represented in Figure 6.8. The broad absorption bands of the Ce^{3+} ion is located at the most energetic region of the electromagnetic spectrum, between 315 nm and 510 nm, corresponding to the excited energy level of $5d_1$ (centred at 341 nm) and $5d_2$ (centred at 458 nm). While the Nd^{3+} absorption bands are in between 510 nm and 888 nm, with five prominent absorbing bands, $^4G_{7/2}+^2G_{9/2}+^2K_{13/2}$ (centred at 530 nm), $^2G_{7/2}+^4G_{5/2}$ (centred at 580 nm), $^4S_{3/2}+^4F_{7/2}$ (centred at 770 nm), $^2H_{9/2}+^4F_{5/2}$ (centred at 805 nm) and $^4F_{3/2}$ (centred at 878 nm) [51, 55, 116].

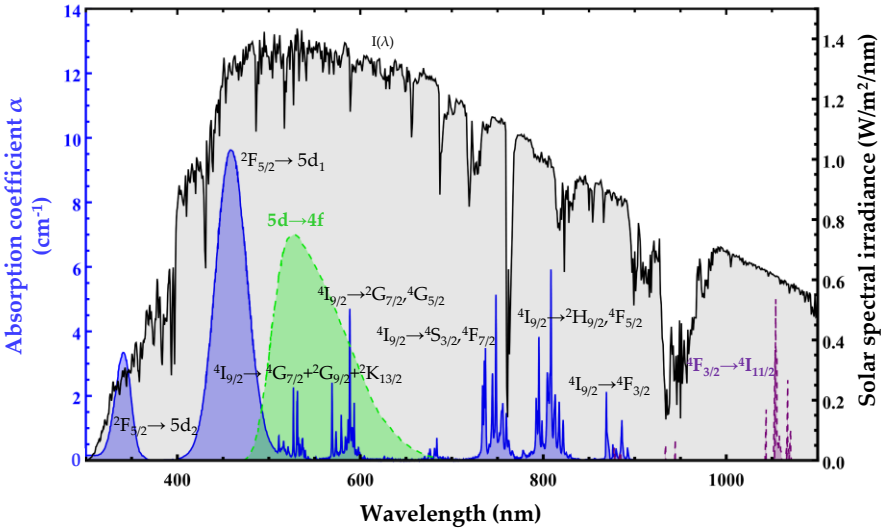

Figure 6.8 — AM1.5 direct solar spectrum (black), adapted from [117]. Ce(0.1 at%):Nd(1.1 at%):YAG absorption spectrum (blue), Ce^{3+} (green) and Nd^{3+} (purple) are emission spectra in YAG, adapted from [118].

The total absorbed solar power of an ion ($P_{abs,ion}$) of the active medium is calculated through Equation (6.5).

$$P_{abs,ion} = \int_{\lambda_i}^{\lambda_f} I(\lambda)\left(1 - e^{(-\alpha_{ion}(\lambda)\times L_c)}\right)d\lambda \qquad (6.5)$$

$I(\lambda)$ is the solar spectral irradiance (W/m^2/nm) of each wavelength λ, L_c is the effective absorption length of the laser rod and $\alpha_{ion}(\lambda)$ is the absorption coefficient of the ion for each wavelength. To effectively calculate the total power available from the Sun to feed both ions, L_c must be considered infinite. In this case, the total absorbed power by Ce^{3+} ($P_{abs,Ce}$) and Nd^{3+} ($P_{abs,Nd}$) ions is approximately 157 W and 162 W, respectively. Given the total solar irradiance of 1000 W/m^2, by integrating all the solar wavelength intensities, the overlap efficiency, i.e., the fraction of the available solar power that is absorbed by the Ce^{3+} ($\eta_{overlap,Ce}$) and Nd^{3+} ($\eta_{overlap,Nd}$) ions, is about 15.7% and 16.2%, respectively, as calculated through Equation (6.6).

$$\eta_{overlap,ion} = \frac{P_{abs,ion}}{\int I(\lambda) d\lambda} \tag{6.6}$$

The energy transfer efficiency of the non-radiative process ($\eta_{NR:Ce\text{-}Nd}$) is about 70% [55, 119], whereas for the radiative process ($\eta_{R:Ce\text{-}Nd}$) is about 30% [55].

6.3.2.1 The pump source defined in Zemax®

There are many possible and viable ways to calculate the absorbed power within the Ce:Nd:YAG with the prevalent wavelengths in the Zemax® software. A direct approach for calculation consists of using all the wavelengths of both the solar emission and the Ce:Nd:YAG absorption spectra. However, this method would require much more computing resources to achieve the same results as those by simulating with a few key solar wavelengths related to the absorption bands responsible for lasing [57].

A total available solar power of 249.05 W can be obtained by the NOVA parabolic mirror with an effective collection area (A_{ef}) of 0.293 m^2, at 850 W/m^2 solar irradiance (I). However, only 16.2% and 15.7% of the total power calculated from Equation (6.6) are useful for calculating the absorbed power by the Ce:Nd:YAG rod with finite dimensions. Consequently, in Zemax®, two sources were defined for solar pumping. The energy division is shown in Figure 6.9 a).

Source 1 emits all the relevant overlapped wavelengths of the solar spectrum with the Nd^{3+} ion absorption spectrum, as well as the wavelength data that includes the Ce^{3+} quantum cutting down conversion of non-radiative transfer to Nd^{3+}, described by pathway (1), as shown in Figure 6.9 b). The simulated power of source 1 ($P_{source1}$) follows the Equation (6.7) and has a total power of 67.72 W.

$$P_{source\ 1} = A\ I\ (\eta_{overlap,Nd^{3+}} + \eta_{overlap,Ce^{3+}} \times \eta_{NR:Ce-Nd}) \tag{6.7}$$

Source 2 accounts 30% of the absorbed energy by Ce^{3+} that was transferred radiatively to Nd^{3+}, as shown in Figure 6.7 by pathway (2). This source emits green and orange wavelengths useful for Nd^{3+} absorption, as shown in Figure 6.9 (c). The simulated power of source 2 ($P_{source2}$) follows the Equation (6.8) and has a total power of 11.73 W.

$$P_{source\ 2} = A\ I\ \eta_{overlap,Ce^{3+}} \times \eta_{R:Ce-Nd} \tag{6.8}$$

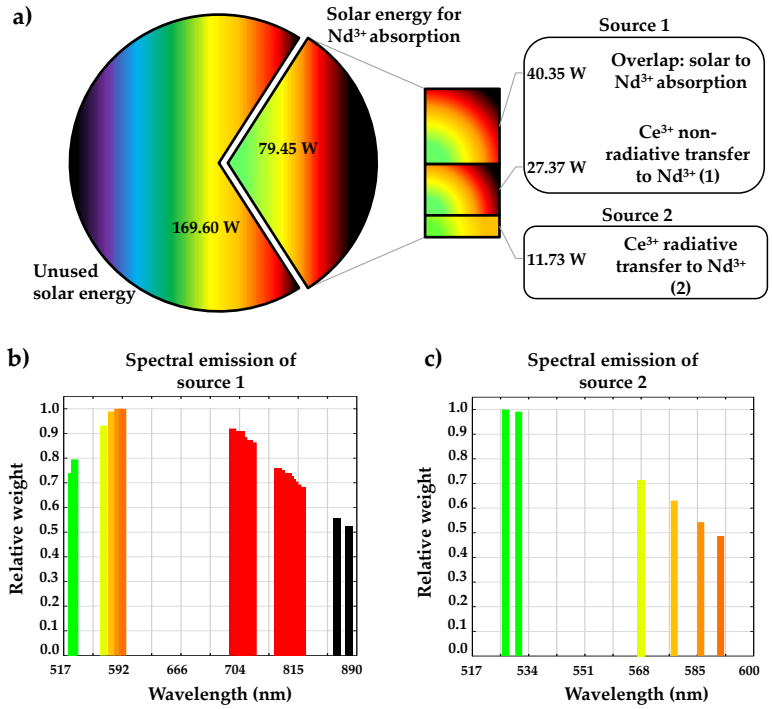

Figure 6.9 — (a) Solar energy division for Ce:Nd:YAG absorption from a total of 249.05 W. Spectral composition used in (b) source 1 and (c) source 2.

6.3.3 Laser head optics

6.3.3.1 Optical parameters

The transmission data for water and fused silica materials from Zemax® glass Catalog, along with the 22 transmission wavelengths of Ce(0.1 at%):Nd(1.1 at%):YAG at L_c=10 mm, are presented in Figure 6.10 a). Figure 6.10 b) displays the index of refraction of Ce(0.1 at%):Nd(1.1 at%):YAG, water, and fused silica as a function of the wavelength, which was utilized in Zemax®.

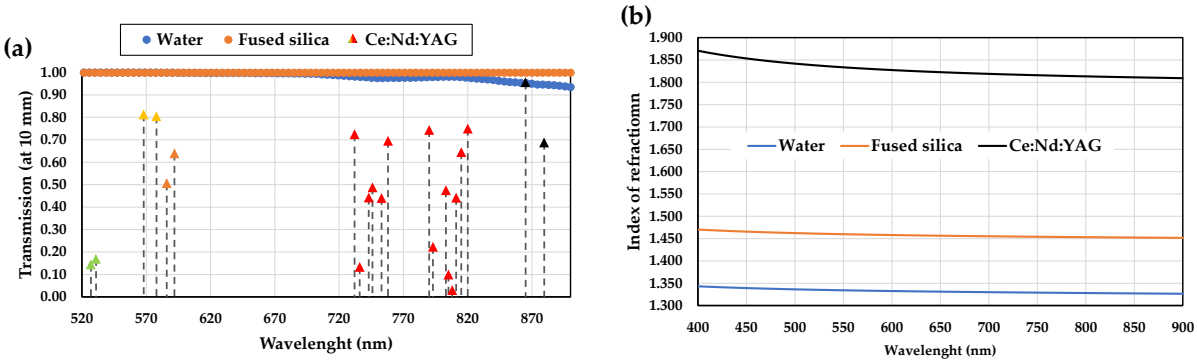

Figure 6.10 — Materials in Zemax®: Ce(0.1 at%):Nd(0.1 at%):YAG, water and fused silica. (a) Transmission of the materials at 10 mm depth. (b) Index of refraction of the materials at 20 °C and 1 atm.

The quantity of energy trapped within the Ce(0.1 at%):Nd(1.1 at%):YAG is determined by the transmission (*T*) characteristics of the Nd^{3+} active ion, water, and silica materials, as displayed in Equation (6.9):

$$T(\lambda) = e^{-\alpha(\lambda)\times L_c} \tag{6.9}$$

6.3.3.2 Pumping efficiency: Side-end-pumping

The transmission and the refractive index of the optical materials, the shape of each optical apparatus, the solar wavelengths and the angle of the concentrated solar rays determine the optical path of the solar rays from the source to the crystal rod. Figure 6.11 shows the optical path of the concentrated solar rays arriving at the laser head, through the fused silica aspheric lens, then into the cooling water and finally to the Ce:Nd:YAG crystal rod. Most of the concentrated solar rays enter the laser rod through its upper HR1064 nm end face, and travel within the rod through total internal reflection (due to the refractive index differences between the water and the active medium), as shown in Figure 6.11 by the red ray. Side-pumping occurs when rays enter the rod through its lateral surface. Multiple passes can be achieved by a single ray zigzagging back into the crystal through the conical pump cavity, which increases the path length of the ray inside the rod, L_p, and hence the amount of energy absorbed.

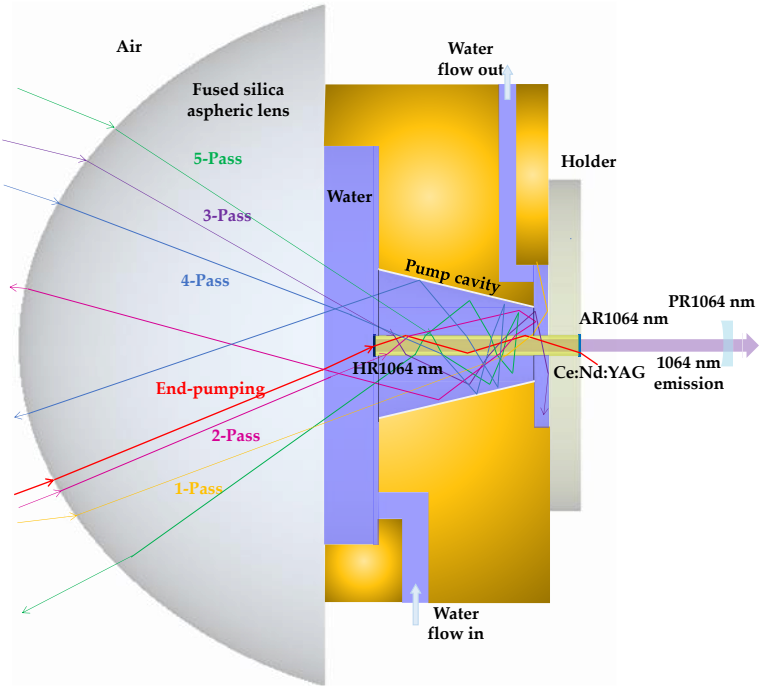

Figure 6.11 — Solar rays at various angles and wavelengths passing through the Ce:Nd:YAG medium inside the laser head. End-pumping occurs through total internal reflection within the rod. Side-pumping may have 1 to 5 or more passes through the rod.

Figure 6.12 shows the absorption of the laser rod as a function of the wavelength and the number of passes. The end-pump has a minimum L_p of 25 mm, the same as the length of the rod. The average L_p of 1-pass, 2-pass, 3-pass, 4-pass, and end-pumping is about 3.25 mm, 6.50 mm, 9.75 mm, 13 mm, and 35 mm, respectively. The absorption of a single ray increases gradually with each successive number of passes within the crystal. Some wavelengths, such as 527 nm, 531 nm, 736 nm, 793 nm, 805 nm, and 808 nm are totally absorbed by the rod if the ray is traveling within the rod by end-pumping regime.

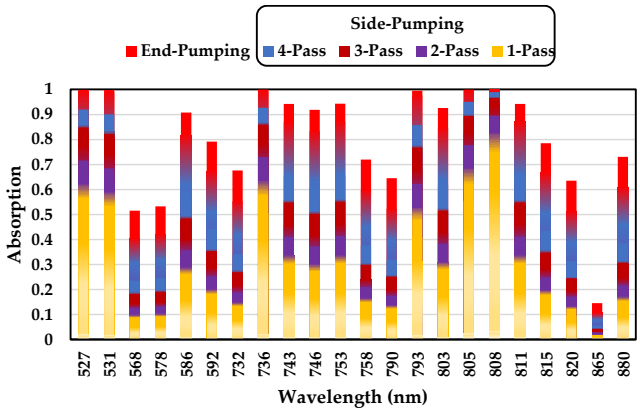

Figure 6.12 — Wavelength-dependent absorption versus number of passes within the crystal. Each pass covers an average absorption length travelled within the crystal rod.

The pump flux distribution along its longitudinal cross-section and five central transversal cross-sections are shown in Figure 6.13. Red color represents the maximum solar energy absorption, whereas blue represents little or no absorption. The most intensive absorbing region has a peak flux of 0.95 W/mm^3, located slightly below the input surface of the rod. The lower part of the rod also absorbs some radiation due to multiple passages of the solar rays by side-pumping with the help of the reflective cone. A total absorbed solar energy of 30.96 W was stored along the thermally loaded crystal.

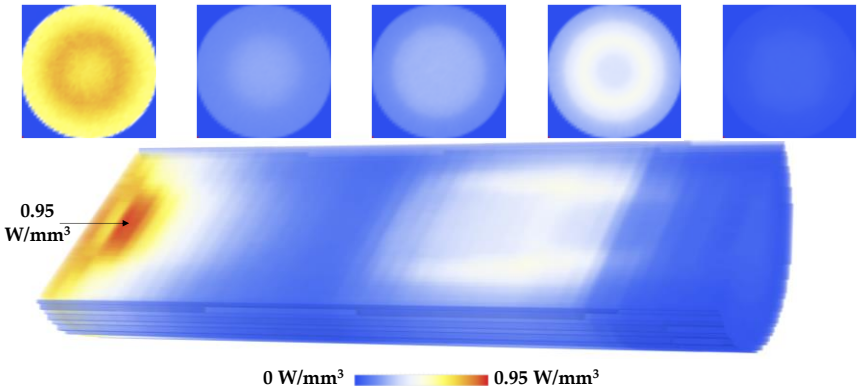

Figure 6.13 — Absorbed solar pump-flux distribution along the longitudinal at a central cross-section, and five separate transversal cross-sections of the Ce:Nd:YAG rod.

6.3.4 Conversion of the upper state energy to laser output

The beam overlap efficiency is strongly dependent on the resonator parameters, such as radius of curvature of the mirrors; dual cavity length of L_1 and L_2 for side-pumping solar lasers and single cavity length L_1 for side-end-pump solar lasers; rod diameter and length (L_r); and most importantly the pumping configuration, as shown in Figure 6.14.

Figure 6.14 – Schematic diagram of the TEM_{00}-mode beam propagation along the asymmetric laser resonator at side-pumping lasers with large RoC end mirrors. L_1 and L_2 represent the separation length of the high reflection (HR) mirror and partial reflection (PR) mirror, respectively, to the end face of the laser rod with length LR.

In solid-state lasers, optical pumping leads to a radial temperature gradient in the laser rod. As a result, in high-average laser power systems, the laser rod acts like a positive thick lens with an effective focal length, which is inversely proportional to pump power [120, 121]. Pump induced fluctuations on the rod focal length will hence exert strong influence on resonator modes configuration and stability, giving rise to thermally stable zones [120, 121]. Conventionally, lasers are designed to operate at the middle of thermally stable zones, where the fundamental mode size is insensitive to thermal perturbation [120]. Since the TEM_{00} mode Gaussian beam has the smallest beam radius and divergence in a resonator, if the transverse dimension of the gain region is much larger than the TEM_{00} mode size, laser oscillates at several modes [120]. However, to achieve laser operation in fundamental mode, classically a pinhole with a similar diameter to the fundamental mode size is inserted inside the laser resonant cavity to prevent higher-order modes from oscillating, considerably reducing the laser extraction efficiency because of poor utilization of the stored energy in the active medium. Thus, a suitable resonator design for efficient energy conversion to the TEM_{00} mode must maximize the overlap integral of the resonator TEM_{00} mode and the pump profile while simultaneously utilizing only the rod to higher-order spatial modes [122]. In side-pumped solar lasers, the adoption of an asymmetric resonator configuration with concave end mirrors of large radius of curvature has shown to provide a large spatial overlap between the fundamental mode and pump mode volumes, as shown in Figure 6.14. The use of small diameter laser rods played a crucial role. Since the laser rod acts as an aperture, high-order resonator modes can be easily suppressed with small diameter rod due to large diffraction losses, improving thus the beam quality and contributing largely on the efficient extraction of TEM_{00} laser power [12, 13, 108, 123-130].

6.4 Solar-pumped laser output classification

Through literatures, the solar-pumped lasers have various classifications, which all depends on the measured solar laser output power from a power meter, as identified in Figure 6.15.

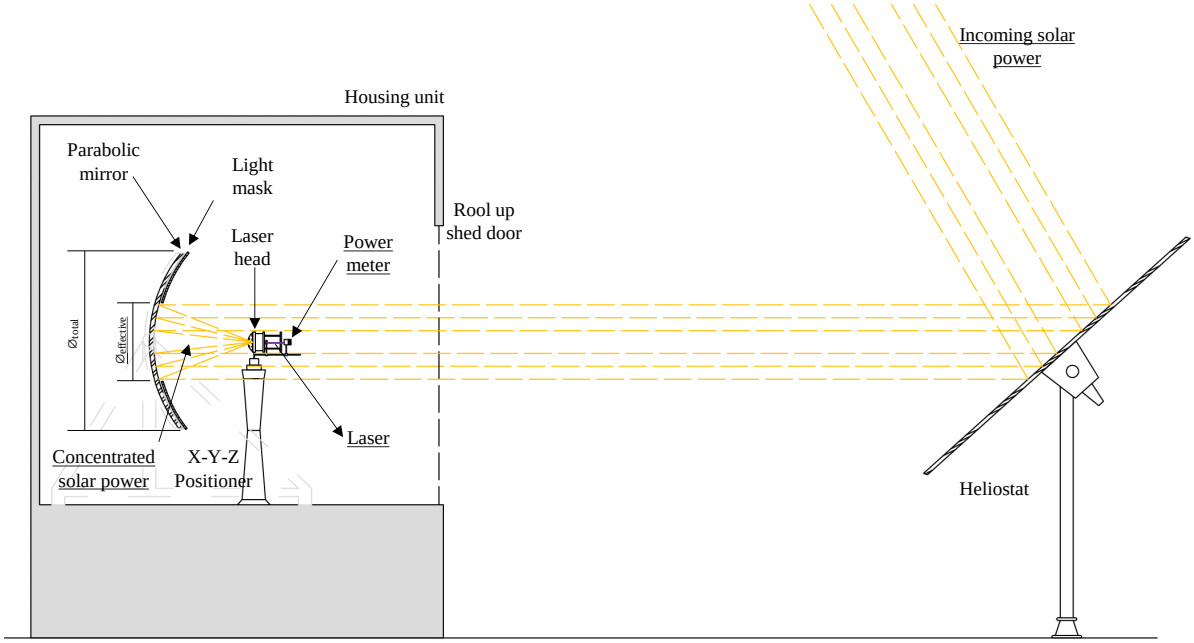

Figure 6.15 — Schematic of a heliostat-parabolic mirror solar energy collection and concentration system.

6.4.1 Solar laser output power

The final output power of the solar-laser measurement is impacted by various factors, including the active medium used, solar irradiance at the time of measurement, tracking method (direct or indirect), primary concentrator size and quality, side-pumping or side-end-pumping of the laser rod, energy distribution type (point focusing or homogenous), and resonant cavity configuration. Additionally, external factors such as ambient temperature, cooling water temperature and its quality, laboratory dust levels, heliostat tracking errors, laser head and/or other optical component positioning errors, and duration of exposure to concentrated light may also affect the output power. The solar laser output power is presented in Watts.

6.4.2 Solar laser collection efficiency

The collection efficiency (*CE*) is defined by the ratio between the laser output power and the effective area of the solar concentrator:

$$CE = \frac{P_{out}}{A_{effective}} \tag{6.10}$$

The *CE* is presented in Watts/m^2.

6.4.3 Solar-to-laser collection efficiency

The solar-to-laser collection efficiency (*SLCE*) is defined by the ratio between the laser output power and the input power useful for pumping:

$$SLCE = \frac{P_{out}}{I \times A_{effective}} \times 100\% \quad (6.11)$$

It is important to remember that the input power can be either the incoming solar power (which is calculated as the solar irradiance multiplied by the effective collector area) or the concentrating solar power (which is the result of incoming solar power and the optical quality loss of the system, such as a heliostat-parabolic mirror or Fresnel lens), as shown in Figure 6.15. The SLCE is expressed as a percentage.

6.4.4 Slope efficiency

The slope efficiency (SE) is calculated by performing a linear regression on solar laser measurements obtained at various input power levels. It provides an estimate of the scaling capability of the solar-pumped laser under an input power. It is worth noting that the calculation of slope efficiency depends on the type of power used in the X-axis, whether it is incoming solar power or concentrating solar power. The resulting slope efficiency is expressed as a percentage.

6.4.5 Threshold power

The minimum power required to initiate laser production is known as the threshold power (T_h). This can be determined by reducing the effective area of the primary concentrator through the use of a light mask, or by employing a controllable shutter or by adjusting the opening of the shed door, as depicted in Figure 6.15. It should be noted that the threshold power can be expressed as either incoming threshold power or concentrated threshold power.

6.4.6 Progress in multimode solar-pumped lasers

An historical progression solar-pumped lasers in multimode is summarized in Table 6-1. In 1963, Kiss et al first observed solar-pumped laser technology. Subsequently, Young produced a 1 W solar laser by employing a 0.29 m^2 parabolic mirror to pump a relatively large Nd:YAG crystal. Over time, advancements in pumping schemes utilizing smaller active mediums and alternative solar collectors led to an increase in solar laser output power. In 2003, Yabe achieved a multi-mode 24.4 W solar laser using a 9 mm diameter, 100 mm length Nd:YAG crystal pumped by a 1.3 m2 Fresnel lens.

Further innovations emerged in 2011 when Liang et al introduced a smaller active medium a 4 mm diameter, 25 mm length Nd:YAG rod end-side pumped by a 0.636 m^2 Fresnel lens, producing a 12.3 W laser with a solar laser collection efficiency of 19.3 W/m^2, demonstrating greater compactness and efficiency. In 2021, the first measurement of Ce:Nd:YAG crystal displayed promising results in solar laser production, utilizing at least 30% of solar energy. Since then, solar laser research has predominantly focused on Ce:Nd:YAG due to its higher solar laser output and the reduced collection area required for initiating laser production.

In 2022, Garcia et al employed a heliostat-parabolic collection system of 0.293 m^2, pumping a Ce:Nd:YAG rod with a diameter of 2.5 mm and length of 25 mm, achieving an 11.2 W laser with a

slope efficiency of 4.5%. A configuration with three rods reached a 16.5 W laser, equivalent to a remarkable 41.3 W/m^2 collection efficiency. In 2023, Garcia et al explored solar-pumped laser research under cloudy conditions, revealing improvements in slope efficiency and solar-to-laser conversion efficiency. Later in the same year, the production of a doughnut-shaped solar laser beam became achievable with a smaller collection area, facilitated by the presence of clouds.

Table 6-1. — Summary of the progress of solid-state solar-pumped laser efficiency in multimode regime.

Year Authors Reference	Primary concentrator (Collection area)	Pumping type Active medium (dimensions)	Laser output power (cw)	Laser collection efficiency	Slope efficiency (total / at the focus)	Solar-to-laser conversion efficiency (total / at the focus)
1963 Kiss *et al* **[131]**	Spherical mirror (0.099 m^2)	Dy:CaF_2 (6.35 mm × 3.16 mm × 25.4 mm)	---	---	--- / ---	--- / ---
1966 Young **[132]**	Parabolic mirror (0.29 m^2)*	Side-pumping Single Nd:YAG rod (Ø3 mm × 30 mm)	1.0 W	~3.4 W/m^2*	--- / ---	--- / ---
1984 Arashi *et al* **[133]**	Segmented parabolic mirror (13.1 m^2)*	Side-pumping Single Nd:YAG rod (Ø4 mm × 75 mm)	18.0 W	~1.4 W/m^2*	--- / ---	--- / ~1.6%
1988 Weksler and Schwartz **[134]**	Segmented mirror concentrator (12.8 m^2)*	Side-pumping Single Nd:YAG rod (Ø6.35 mm × 76.2 mm)	~ 66 W	~5.1 W/m^2*	--- / 2.1%	--- / ~1.5%*
1993 Krupkin *et al* **[135]**	Heliostats / Paraboloidal mirrors (660 m^2)	Side-pumping Array of Nd:YAG rods (---)	500 W	0.76 W/m^2	--- / ---	--- / ---
2003 Lando *et al* **[136]**	ACTA solar concentrator (6.75 m^2)	Side-pumping Single Nd:YAG rod (Ø6 mm × 72 mm)	46.0 W	6.7 W/m^2	--- / ---	--- / ---
2007 Yabe *et al* **[137]**	Fresnel lens (1.3 m^2)	End-side-pumping Single Cr:Nd:YAG rod (Ø3-9 mm × 100 mm)	24.4 W	18.7 W/m^2	~8.3±1%[1†] / 12.5±1.5[1]	~1.93%* / ~2.9%
2011 Liang and Almeida **[138]**	Fresnel lens (0.636 m^2)	End-side-pumping Single Nd:YAG rod (Ø4 mm × 25 mm)	12.3 W	19.3 W/m^2	2.75%* / 3.5%	2.17%* / 2.76%*
2012 Dinh *et al* **[139]**	Fresnel lens (4.0 m^2)	End-side-pumping Single Nd:YAG rod (Ø6 mm × 100 mm)	120 W	30 W/m^2	4.3% / 8.6%	3.26%* / 6.52%*

* The value is not indicated in the publication, but it can be assumed/calculated based on the reported parameters.

[1] The value is not indicated in the publication, but it can be calculated based on the reported parameters.

† The value was overestimated, considering only a few laser output data points at high solar input power to calculate the slope efficiency.

2014 Xu *et al* **[140]**	Fresnel lens (1.03 m^2)	End-side-pumping Single Nd:YAG grooved rod (Ø6 mm × 100 mm)	27 W	26.2 W/m^2	4.09%*/ 9.04%	2.91%*/ 6.44%
2017 Liang *et al* **[13]**	Parabolic mirror (1.18 m^2)	End-side-pumping Single Nd:YAG rod (Ø4 mm × 35 mm)	37.2 W	31.5 W/m^2	5.25%*/ 8.9%	3.14%* / 5.31%*
2018 Guan *et al* **[141]**	Fresnel lens (1.03 m^2)	End-side-pumping Single Nd:YAG/YAG rod (Ø6 mm × 95 mm)	33.1 W	32.1 W/m^2	5.4% / ---	3.3% / ---
2018 Liang *et al* **[142]**	Parabolic mirror (1.0 m^2)	End-side-pumping Single Nd:YAG rod (Ø4.5 mm × 35 mm)	32.5 W	32.5 W/m^2	6.7% / 8.96%*	3.74%* / 5.0%*
2019 Liang *et al* **[143]**	Parabolic mirror (0.9 m^2)	Side-pumping Single Nd:YAG rod (Ø3 mm × 30 mm)	15.3 W	17.0 W/m^2	5.4% / 7.22%[2]	2.43%* / 3.25%*
2020 Liang *et al* **[144]**	Parabolic mirror (1.0 m^2)	End-side-pumping Three Nd:YAG rods (Ø3 mm × 25 mm)	18.3 W (6.1 W each)	18.3 W/m^2	5.1% / 6.82%*	2.2%* / 2.95%*
2021 Vistas *et al* **[145]**	Parabolic mirror (0.7 m^2)	Side-pumping Ce:Nd:YAG rod (Ø4 mm × 35 mm)	16.5 W	23.6 W/m^2	4.4% / 5.88%*	2.8% / 3.73%*
2022 Garcia *et al* **[53]**	Parabolic mirror (0.293 m^2)	End-side-pumping Single Ce:Nd:YAG rod (Ø2.5 mm × 25 mm)	11.2 W	38.2 W/m^2	6.8% / 9.09%*	4.5% / 6.02%*
2022 Liang *et al* **[54]**	Parabolic mirror (0.4 m^2)	End-side-pumping Three Ce:Nd:YAG rods (Ø2.5 mm × 25 mm)	16.5 W (5.5 W each)	**41.3 W/m^2**	**7.64%** / 10.2%*	**4.64%** / 6.20%*
2023 Garcia et al **[188]**	Parabolic mirror (0.652-0.152 m^2)	End-side-pumping Single Ce:Nd:YAG rod (Ø2.5 mm × 25 mm)	14 W (with **clouds**)	21.47 W/m^2	7.71%	6.32%
2023 Garcia et al **[189]**	Parabolic mirror (0.226 m^2)	End-side-pumping Single Ce:Nd:YAG rod (Ø2.5 mm × 25 mm)	1.34 W (**Doughnut shape**)	5.93 W/m^2	-	1.08%

[2] The value is not indicated in the publication, but it can be calculated based on the reported parameters.

7
SOLAR PUMPED LASER CE:ND:YAG

Solar-pumped laser is an arrangement of well-defined and well-assorted optics that converts the incoherent solar spectrum radiation into collimated and coherent wavelength laser radiation. Solar laser technology is a promising candidate for space applications, such as deep-space communications, laser power beaming, space-to-Earth wireless power transmission and asteroid deflections [15, 146, 147]. On Earth, solar-pumped laser applications are highly conditioned by Earth's rotation and revolution, as well as atmospheric processes and phenomena. Still, a green and sustainable industry [148, 149], based on solar laser material processing [16, 150], can flourish in locations with abundant solar irradiance.

While the first solar-pumped laser was reported by Kiss et al. in the 1960s [131], optical pumping designs and gain media has largely improved over the last two decades. Substantial progress in this field of research has been carried out by a few research teams, mostly by using Nd:YAG laser crystal [12, 13, 123, 126, 127, 133, 134, 136, 139, 141-143, 151-159] and most recently with Ce:Nd:YAG laser crystal [53, 54, 145, 160-164].

The Nd:YAG crystal is the most used active medium for the solid-state laser industry, not only due to its relatively low price, availability in the market, but more so to its high quantum efficiency, exceptionally good thermal conductivity, and robust mechanical strength. However, the absorption efficiency of the Nd^{3+} ions in YAG is rather low when pumped by either flash lamps or sunlight. The introduction of the Ce^{3+} ion sensitizer into Nd:YAG benefits from the absorption of the ultraviolet (UV) and visible wavebands, whose energy is transferred to the absorption bands of the Nd^{3+} ion through cross-relaxation and quantum cutting down conversion from the Ce^{3+} $5d_1$ pump band [55], further increasing the number of Nd^{3+} ions into excitation state.

The use of the Ce:Nd:YAG active medium improved laser output efficiency not only through diode/lamp pump sources [115, 165, 166], but also through solar pumping [53, 54, 162-164]. In 2021, Vistas et al. reported an improvement of 1.5 times in Ce:Nd:YAG solar laser efficiency over that with Nd:YAG under the same pumping conditions [145]. However, this material is still not as matured as Nd:YAG, and during solar laser operation the thermal effects were more pronounced, resulting in the damage of the active medium at high input power levels [161, 163]. To minimize the thermal load in Ce:Nd:YAG, in 2022, Almeida et al. [162] and Vistas et al. [163] adopted a rectangular light guide homogenizer, instead of a classic aspheric lens [145, 163], to uniformly side-pump a Ce:Nd:YAG rod. Still, the efficiency was worse than the previous one [145]. In the same year, Liang et al. used a three-rod configuration to simultaneously end-side-pump three thin Ce:Nd:YAG rods within a single cavity, ensuring an equal redistribution and sharing of the solar pump light by the Ce:Nd:YAG media while substantially improving the solar laser collection and solar-to-laser conversion efficiencies to 41.25 W/m^2 and 4.64%, respectively [54]. Garcia et al. adopted a parabolic mirror with small collection area of only 0.293 m^2 to pump a single thin Ce:Nd:YAG rod with 2.5 mm diameter and 25 mm length [53].

High collection efficiency of 38.22 W/m^2 and high solar-to-laser conversion and slope efficiencies of 6.02% and 9.9% at the focus of the primary concentrator were respectively attained. Moreover, the lowest threshold solar power at the focus of 66 W was obtained [53]. In 2023, Cai et al. used a Fresnel solar collector and a 6 mm diameter 95 mm length Ce:Nd:YAG/YAG grooved bonded crystal rod which resulted a 200 W incoming threshold solar power, 3.85% solar-to-laser conversion efficiency, 38.8 W/m^2 collection efficiency [164].

7.1 Ce:Nd:YAG Solar Laser with 4.5% Solar-to-Laser Conversion Efficiency

The efficiency potential of a small-size solar-pumped laser is studied here. The solar laser head was composed of a fused silica aspheric lens and a conical pump cavity, which coupled and redistributed the concentrated solar radiation from the focal zone of a parabolic mirror with an effective collection area of 0.293 m^2 to end-side pump a Ce (0.1 at%):Nd (1.1 at%):YAG rod of 2.5 mm diameter and 25 mm length. Optimum solar laser design parameters were found through Zemax® non-sequential raytracing and LASCAD™ analysis. The utilization of the Ce:Nd:YAG medium with small diameter pumped by a small-scale solar concentrator was essential to significantly enhance the end-side pump solar laser efficiency and thermal performance. For 249 W incoming solar power at an irradiance of 850 W/m^2, 11.2 W multimode solar laser power was measured, corresponding to the record solar-to-laser power conversion efficiency of 4.50%, being, to the best of our knowledge, 1.22 times higher than the previous record. Moreover, the highest solar laser collection efficiency of 38.22 W/m^2 and slope efficiency of 6.8% were obtained, which are 1.18 and 1.02 times, respectively, higher than the previous records. The lowest threshold solar power of a Ce:Nd:YAG solar-pumped laser is also reported here.

7.1.1 Materials and method

7.1.1.1 Solar energy collection and concentration: NOVA heliostat-parabolic system

The NOVA heliostat-parabolic mirror solar laser system, as shown in Figure 7.1, is composed of a two-axis heliostat with four flat mirrors of 93.5% reflectivity, which are used for redirecting the incoming solar radiation towards a parabolic mirror of 80.0% reflectivity with a focal length of 660 mm. This whole system has a combined reflective capacity of 74.8%. By using an external annular mask, the collection diameter of the parabolic mirror was reduced from 1.50 m to 0.68 m. About 0.293 m^2 effective solar collection area was then calculated by discounting the shadowed area of approximately 0.07 m^2 caused by the laser head and its supporting mechanics, the *X-Y-Z* positioner, and the non-reflecting space between the two flat segments of the heliostat.

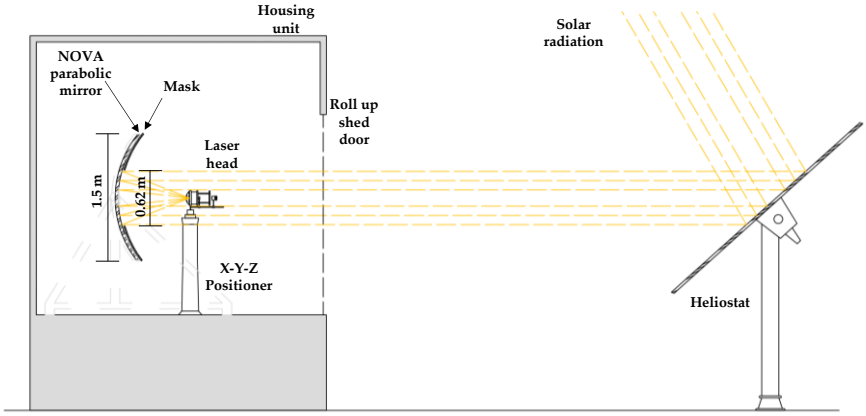

Figure 7.1 — Schematic of the NOVA heliostat-parabolic mirror solar energy collection and concentration system.

7.1.1.2 Solar laser head

Figure 7.2 shows the image of the solar laser head and its optical components, as well as the laser resonator components. The laser head was composed of a fused silica aspheric lens of 99.995% optical purity that focused the concentrated solar radiation onto the flat upper surface of the Ce(0.1 at%):Nd(1.1 at%):YAG rod of 2.5 mm diameter and 25 mm length, mounted within a single reflective conical pump cavity. The rod's flat upper surface had a highly reflective (HR) coating for the laser emission wavelength at 1064 nm (99.9% @ 1064 nm), while the other end surface had an anti-reflection (AR) coating for the laser emission wavelength (reflectivity (R) < 0.2% @ 1064 nm), supplied by Chengdu, Dongjun Laser Co., Ltd. (Chengdu, China). Cooling water constantly flowed into the laser head from an inlet and the heated water was extracted through the outlet. Maximum lasing could only be achieved when the laser head was correctly aligned at the focus of solar concentrator through the *X*-*Y*-*Z* positioner and the correct alignment of the laser resonator mirrors.

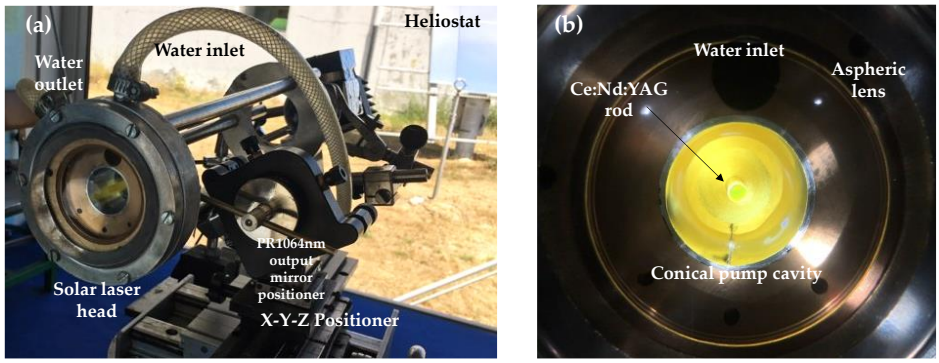

Figure 7.2 — Photograph of (a) the Ce(0.1 at%):Nd(1.1 at%):YAG solar laser head at the focus of the parabolic mirror, and (b) the front view of the laser head.

The fused silica aspheric lens had an 82 mm diameter and a thickness of 37 mm, with a curved input surface and a flat output surface. The curved feature of the aspheric lens follows the sag (z) in Equation (7.1), with radial aperture (r) of 41 mm, the parabolic constant $k = 0$, the radius of curvature (c) of -43 mm and the aspheric coefficient $\alpha_1 = -0.004$.

$$z = \frac{c \times r^2}{1+\sqrt{1-(1+k)c^2r^2}} + \alpha_1 r^2, \tag{7.1}$$

The flat output surface of the lens was 6 mm apart from the flat input surface of the crystal rod. This space was necessary for the laser rod to effectively absorb the concentrated solar radiation and to guarantee an abundant cooling for effective heat dissipation. The absorption efficiency was further enhanced by a silver-coated aluminium foil of 94% reflectivity that covered the conical pump cavity. The reflective conical surface allowed the reabsorption of the solar energy due to the crisscross of the solar rays into the laser rod, thus helping in the redistribution of the solar energy along the rod. This conical pump cavity was 19.5 mm in length with input and output aperture diameters of 18 mm and 9 mm, respectively.

Cooling water with 6 L/min flow rate was used as the heat extraction medium. The cooling system was designed to maximize the removal of the heat generated within the rod and the optical components, such as the fused silica aspheric lens and the conical pump cavity. Both the cooling water and the silica lens weaken the intensity of the UV solarization and IR heating arriving at the rod, which help to reduce the thermal lensing issue.

7.1.1.3 Solar laser model in Zemax®

The NSC editor for modelling the Ce(0.1 at%):Nd(1.1 at%):YAG solar pumped laser is shown in Figure 7.3. The solar source is represented by object 2, the parabolic mirror by object 3, the aspheric fused silica by object 7, the cooling water by object 8, the reflective cavity by object 9, the detector as water by object 13, the Ce:Nd:YAG crystal by object 14, and the mechanical holder by object 15. Reference objects 1, 5, 6, and 12 are also included for optimization purposes.

Non-Sequential Component Editor: Config 1/2

Edit Solves Tools View Help

	Object Type	Comment	Ref Ob..	Ins..	X Posit..	Y Posit..	Z Position	Tilt Ab..	Tilt Ab..	Tilt Ab..	Material	Par 1(un..	Par 2(un..	Par 3(un..	Par 4(..	Par 5(..	Par 6(u..	Par 7(..	Par
1	Source El..	ref source	0	0	0.00	0.00	0.000	0.00	0.00	0.00	-	0	0	1000	0	0	310	310 P	1
2	Source El..	CeNdYAG source	0	0	0.00	0.00	0.000	0.00	-180	0.00	-	100	20000000	37.00	0	0	310 P	310 P	
3	Aspheric ..	FCT	0	0	0.00	0.00	-850.0	0.00	0.00	0.00	MIRROR	1700	-1.000	310.0 P	50			0	
4	Null Object		0	0	0.00	0.00	0.000	0.00	0.00	0.00	-								
5	Null Object	pseu	0	0	0.00	0.00	1.300 V	0.00	0.00	0.00	-								
6	Null Object	pseu2	0	0	0.00	0.00	-7.000 V	0.00	0.00	0.00	-								
7	Annular A..	silica	-2	0	0.00	0.00	-7.000 P	180	0.00	0.00	SILICA	0.000	42.000	0.000	42	0.0	-60	0.00	3
8	Cylinder ..	water	-3	0	0.00	0.00	-7.000 P	0.00	0.00	0.00	WATER	30.00	28.000 P	30.00 P					
9	Cylinder ..	cavity	-4	-1	0.00	0.00	0.000 V	0.00	0.00	0.00	MIRROR	9.000	19.000	4.500					
10	Null Object		0	0	0.00	0.00	0.000	0.00	0.00	0.00	-								
11	Null Object		0	0	0.00	0.00	0.000	0.00	0.00	0.00	-								
12	Cylinder ..	control	-7	0	0.00	0.00	0.000	0.00	0.00	0.00		1.250	25.000	1.250					
13	Detector ..	water	-1	0	0.00	0.00	12.500 P	0.00	0.00	0.00	WATER	1.250 P	1.250 P	12.50	30	30	30	0	
14	Cylinder ..		-2	-1	0.00	0.00	0.000	0.00	0.00	0.00	NDYAG	1.250	25.000	1.250 P					
15	Annular V..	holder	-3	0	0.00	0.00	21.000	0.00	0.00	0.00	MIRROR			1.250	1.3	1.3	1.25	10.0	1

Figure 7.3 — Non-sequential component editor of the Ce:Nd:YAG solar pumped laser.

7.1.1.4 LASCAD™ simulation

The absorbed power in cubic matrix form was imported into LASCAD™ software to analyse the solar laser output performance. The material data of Ce(0.1 at%):Nd(1.1 at%):YAG crystal with a stimulated emission cross-section of 2.8×10^{-19} cm^2, a fluorescence lifetime of 230 µs and an absorption/scattering loss of 0.002 cm^{-1} was set in LASCAD™. The mean absorbed and intensity-weighted wavelength of 660 nm was considered in the analysis [134]. Figure 7.4 shows the laser resonator of the thermally loaded crystal rod and the associated dielectric lenses. The left end-face of the rod has a layer of HR 1064 mm coating, represented by the optical dielectric interface 0. The output end-face has an AR 1064 nm coating, represented by the optical dielectric interface 1. The partial reflection (PR) output mirror is positioned 17 mm apart from the AR coated end face ($L_{AR\text{-}PR}$=17 mm), represented by optical

dielectric interface 2. Different reflectivity and radii of curvature (RoC) of the PR mirror were tested to find the best combination to achieve the highest laser output power for the most efficiently solar-pumped Ce:Nd:YAG rod. A total round-trip loss of 1.6% was accounted in the LASCAD™ calculation.

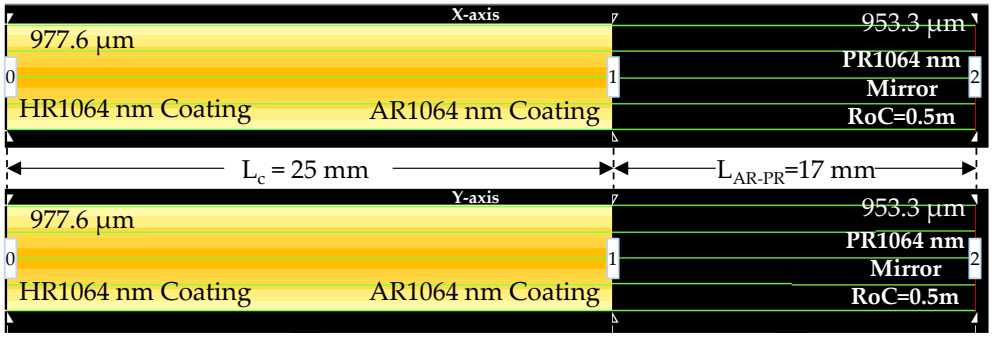

Figure 7.4 — Laser resonator configuration for multimode solar laser extraction from the Ce:Nd:YAG rod. The L_c is the laser rod length, and the L_{AR-PR} is the length between AR1064 nm end face of the rod and the PR1064 nm mirror.

The results of the LASCAD™ analysis for the 2.5 mm diameter and 25 mm length rod are presented in Figure 7.5, which shows the heat load, temperature, and stress intensity. The analysis was performed under ambient temperature and cooling boundary conditions of 300 K. The locally maximum heat load was found to be 0.385 W/mm^3. The tip of the input surface of the crystal attained a maximum temperature of 313.8 K. The highest thermal stress recorded was 24.23 N/mm^2, which is considered moderate.

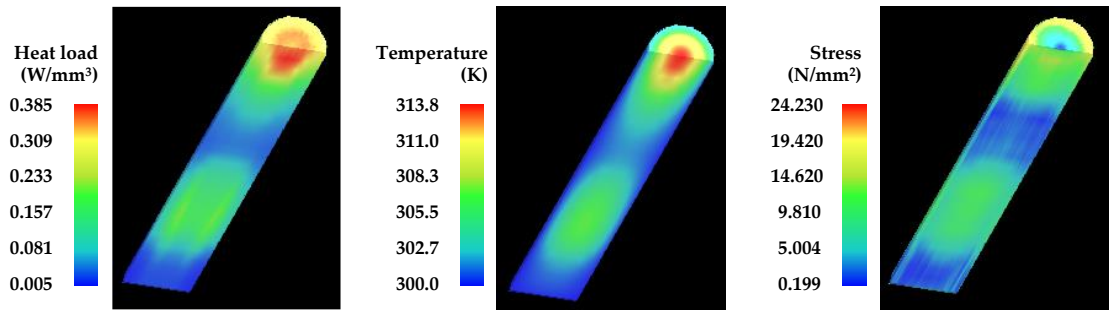

Figure 7.5 — Heat load, temperature and stress intensity of the 2.5 mm diameter, 25 mm length Ce:Nd:YAG rod, numerically acquired through LASCAD™ analysis.

Considering all the physical attributes of the stimulated active medium, our numerical calculations indicate that an optimal maximum multimode laser power of 11.3 W can be achieved. This is best attained using a PR1064 nm mirror with a reflectivity (R) of 96% and a Radius of Curvature (RoC) of 0.5 m. This configuration would result in an earlier laser emission with a lower solar energy input, as illustrated in Figure 7.6. It's noteworthy that a PR1064 nm mirror with reflectivity values of 98% and 96% would yield a lower solar laser output power compared to the 96% reflectivity configuration.

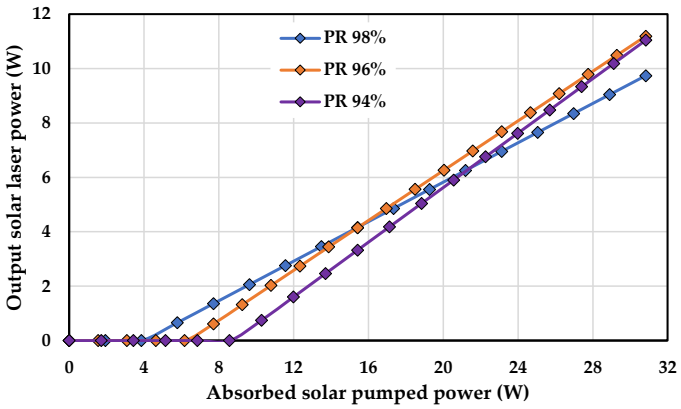

Figure 7.6 — Numerically calculated solar laser output power of the Ce:Nd:YAG as a function of the total amount of solar power absorbed in the crystal, at partial reflection (PR) mirror of 94%, 96% and 98%.

7.1.2 Results and discussion

The solar laser head prototype was built according to the model designed in Zemax® that provided the highest laser power extraction through LASCAD™. The laser head was tested at the NOVA solar facility in April of 2022. The solar irradiance of 850 W/m^2 was measured during that period, which is equivalent to a maximum incoming solar power of 249 W provided from the primary parabolic mirror with effective diameter of 0.68 m. A maximum multimode laser power of 11.2 W was successfully achieved using a PR ($R \geq 96\%$ @ 1064 nm) mirror with RoC of 0.5 m, as shown in Figure 7.7, which matches well with the numerical prediction (Figure 7.6). The lasing emission started with an incoming solar power of 88 W and grew linearly to 11.2 W at 249 W incoming solar power, leading to a slope efficiency of 6.8%.

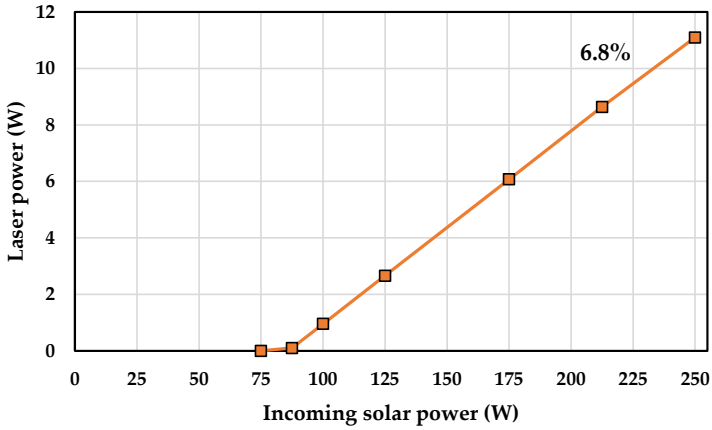

Figure 7.7 — Ce:Nd:YAG solar laser output power as a function of the incoming solar power, using a PR mirror of 96%.

Table 7-1 summarizes the most recent progress in solar-pumped lasers, regarding to the minimum threshold power, maximum solar-to-laser power conversion, solar laser collection and slope efficiencies. In this work, only 88 W solar power was needed to start the lasing process, which is 0.44 times below the record minimum threshold power of 200 W [141]. The solar lasing system was able to produce 11.2 W multimode laser power, equivalent to the highest solar-to-laser power conversion efficiency of

4.50%, to the best of our knowledge, which is 1.22 times more than the record of 3.69% [142]. Furthermore, the solar laser collection and slope efficiencies were 38.22 W/m^2 and 6.8%, respectively, being 1.18 and 1.02 times higher than the previous records of 32.5 W/m^2 and 6.7% through an end-side-pumped Cr:Nd:YAG rod [142].

Table 7-1 — Comparison of progress in solar efficiencies.

Parameters	Guan et al. 2018 [141]	Liang et al. 2018 [142]	Vistas et al. 2021 [145]	This work 2022	Improvements over **previous record (times)**
Primary concentrator	Fresnel lens	Parabolic mirror	Parabolic mirror	Parabolic mirror	-
Overall efficiency of the collection system	~45%	75%	75%	75%	-
Effective collection area	1.030 m^2	1.000 m^2	1.070 m^2	0.293 m^2	-
Tracking method	Direct tracking	Via heliostat	Via heliostat	Via heliostat	-
Solar irradiance	980 W/m^2	870 W/m^2	860 W/m^2	850 W/m^2	-
Active medium	Nd:YAG/YAG	Cr:Nd:YAG	Ce:Nd:YAG	Ce:Nd:YAG	-
Pumping method	End-side-pump	End-side-pump	Side-pump	End-side-pump	
Laser power	31.1 W	32.5 W	16.5 W	11.2 W	-
Minimum incoming threshold power	**200 W**	400 W	220 W	88 W	**0.44 [141]**
Solar-to-laser conversion efficiency	3.1%	**3.7%**	2.8%	4.5%	**1.22 [142]**
Solar laser collection efficiency	32.1 W/m^2	**32.5 W/m^2**	23.6 W/m^2	38.22 W/m^2	**1.18 [142]**
Slope efficiency	5.4%	**6.7%**	4.4%	6.8%	**1.02 [142]**

The laser beam M^2 quality factors of the Ce:Nd:YAG were measured according to ISO 11164-1 standards, with a CINOGY UV-NIR beam profiler using a CinCam CMOS. Figure 7.8 a) shows the multimode laser beam profile. The measured solar laser beam widths along the beam caustic and the associated extrapolated hyperbolic plot are shown in Figure 7.8 b). $M_x^2 = 32.16 \pm 2.62$ and $M_y^2 = 36.62 \pm 4.22$ factors were experimentally obtained.

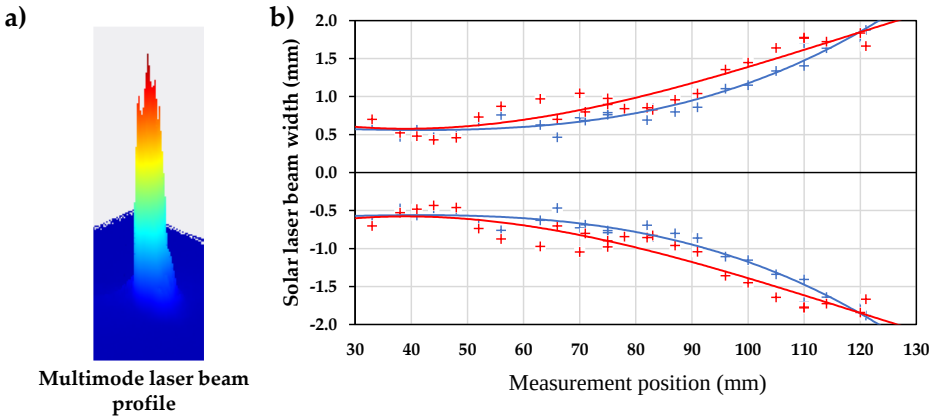

Figure 7.8 — (a) Multimode beam profile. (b) Caustic fit measurements of the multimode solar laser beam.

The highly efficient Ce:Nd:YAG solar laser was composed of the first-stage heliostat-parabolic mirror solar energy collection and concentration system; the second-stage fused silica aspheric lens that further concentrated the solar energy onto the end-face of the active medium by end-pumping; and the third-stage conical-shaped reflective pump cavity to efficiently side-pump the 2.5 mm diameter, 25 mm length Ce:Nd:YAG rod. The solar energy transfer for the Nd^{3+} and Ce^{3+} ions as well as the energy transfer of Ce^{3+} to Nd^{3+} were introduced and considered in Zemax®. The design parameters of the laser head were optimized to find the highest solar energy absorption by the active medium to then determine the best lasing conditions in LASCAD™. The Ce:Nd:YAG solar laser prototype was then built according to the simulated model. 11.2 W multimode laser output power was successfully measured, matching well with the numerical result. This, to the best of our knowledge, resulted in a record solar-to-laser conversion efficiency of 4.50%. The highest solar laser collection and slope efficiencies of 38.22 W/m^2 and 6.8%, respectively, were also obtained. Furthermore, low threshold power of 88 W was also reported. Since the NOVA solar energy collection and concentration facility has a limited transfer efficiency of 0.75, further research on small size Ce:Nd:YAG solar laser in direct solar tracking mode will, most hopefully, ensure further solar laser efficiency enhancement and enable promising space applications.

7.2 Lowest-threshold solar laser operation under cloudy sky condition

Classical solar-pumped lasers often demand a significant amount of concentrated solar power for laser emission, which is only attainable under clear sky condition, limiting their applicability. In this research, we report the first solar laser emission at very low threshold solar power under cloudy sky condition by end-side-pumping a 2.5 mm diameter, 25 mm length Ce:Nd:YAG rod at the focus of a parabolic mirror concentrator. The Ce:Nd:YAG solar laser performance was also evaluated under clear sky condition for comparison. Low threshold pump power of 32.4 W for continuous-wave solar-pumped laser was obtained under clear sky condition, being two times lower than the previous record. However, the cloud-filtered infrared sunlight enabled notable improvements in the solar laser performance by lessening the thermal lensing effects in the laser medium. The threshold pump power was further reduced to 29.2 W

and maximum solar laser output of 14 W was successfully measured. This nearly doubled the focal slope efficiency from 4.03% during clear weather to 7.71% under a cloudy sky. The solar-to-laser conversion efficiency of 6.32% was nearly tripled compared to the 2.32% on a clear sky, while the solar laser conversion efficiency of 21.47 W/m^2 was nearly twice the value of 12.62 W/m^2 obtained on a clear day. This demonstrates that a cloudy environment could be an asset for solar laser research.

7.2.1 Materials

7.2.1.1 Solar energy collection and concentration system

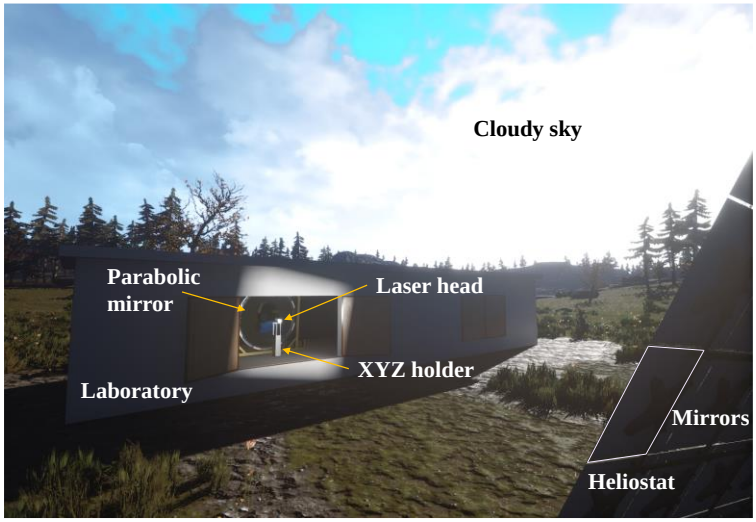

Figure 7.9 — Schematic depicting the solar pumped laser facility in three dimensions. It includes the laboratory, which houses the parabolic mirror, the laser head, and the XYZ holder. Additionally, there is a mirror-heliostat located outside the laboratory that reflects solar light filtered by the clouds.

The incoming solar radiation was redirected by a two-axis heliostat, constituted by 36 small flat back-surface silver-coated mirrors (0.5 m × 0.5 m each) with less than 80% reflectivity, to the MSSF parabolic mirror, also back-surface silver-coated, installed inside a laboratory as shown in Figure 7.9. Only 59% of the total combined effective incoming solar radiation is useful for pumping the laser head.

In these experiments, the external annular area of the MSSF parabolic mirror was masked to reduce the collection area as much as necessary. The total effective collection area discounts the shadow area caused by the space between the heliostat mirrors, the shutter blades, The X-Y-Z mechanical positioner and the laser head, leading to four different setups with total effective collection areas of 0.152 m^2, 0.110 m^2, 0.075 m^2, and 0.652 m^2.

The experiments were conducted on 16 September 2022 from 10:00 to 17:00. The solar irradiance was measured locally by a Kipp and Zonen CH1 pyrheliometer, on a Kipp and Zonen 2AP solar tracker, from Kipp and Zonen, Delft, The Netherlands. The resulting data of that day at Universal Time Coordinated (UTC) is shown in Figure 7.10.

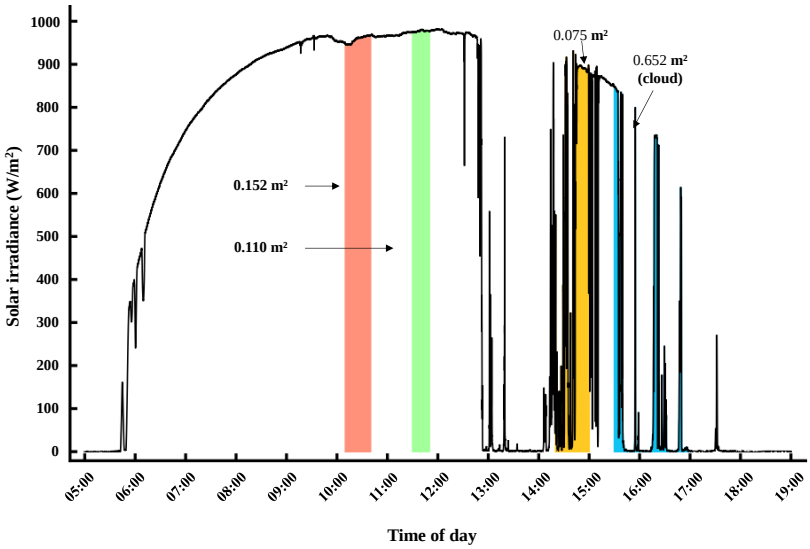

Figure 7.10 — The direct normal irradiance measured at the PROMES-CNRS on 16 September 2022 from 5:00 to 19:00 UTC time, and the experimental duration period for each parabolic mirror diameter size. Collector sizes of 1.520 m^2, 0.110 m^2, and 0.075 m^2 were used during the clear sky. 0.652 m^2 was used during the cloudy sky.

7.2.1.2 End-side-pumped solar laser head

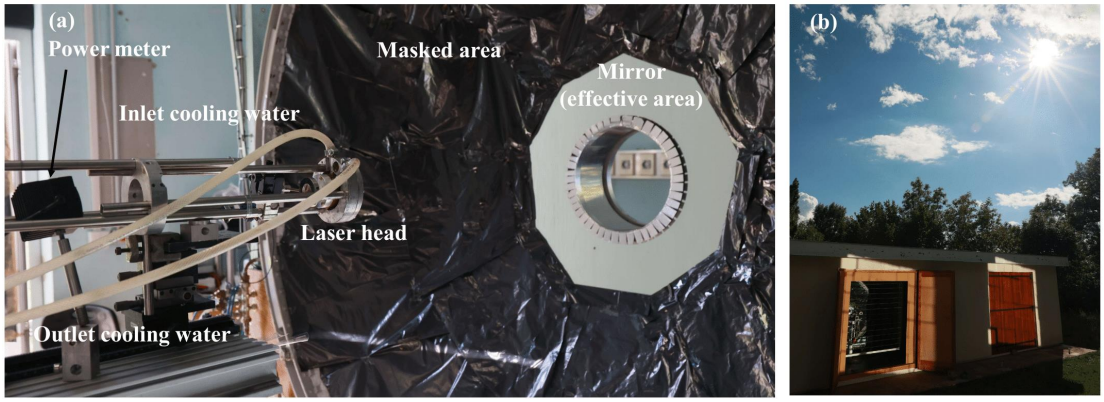

Figure 7.11 — Photograph of (a) the solar laser head housing the Ce:Nd:YAG crystal placed at the focus of the MSSF parabolic mirror with 0.075 m^2 effective collection area and (b) the sky on 16 September 2022 at 15:48 UTC in PROMES-CNRS.

The laser head was previously used at the NOVA facility [53]. It was composed of a large, fused silica aspheric lens of 99.995% optical purity, designed to effectively focus the concentrated solar radiation onto a 2.5 mm diameter, 25 mm length crystal rod, and used as a lid to enclose the laser head. The Ce(0.1 at%):Nd(1.1 at%):YAG crystal was centred in a conical pump cavity covered with silver-coated aluminium foil of 94% reflectivity, as shown in Figure 7.12. The pump cavity had a conical shape with 19.5 mm length and input/output diameters of 18.0 mm and 9.0 mm, respectively, whose dimensions were previously optimized numerically. This design not only facilitated the easy flow of cooling water, but most importantly enabled efficient multi-pass pumping to the laser rod, resulting in better pump energy absorption and distribution along the active medium. In our study, we were limited by the local open cooling system, which operated with a flow rate of 4 L/min and 4.5 bar pressure at ambient temperature. However, the future implementation of a laser chiller to regulate both the temperature and

pressure of the cooling water could further help to increase the solar laser output. Payziyev [167] observed that the increase of the water flow rate might result in a significant increase of the solar laser output, especially at high solar pump power level. Figure 7.11 a) and Figure 7.12 show the water-cooling system of the solar laser head.

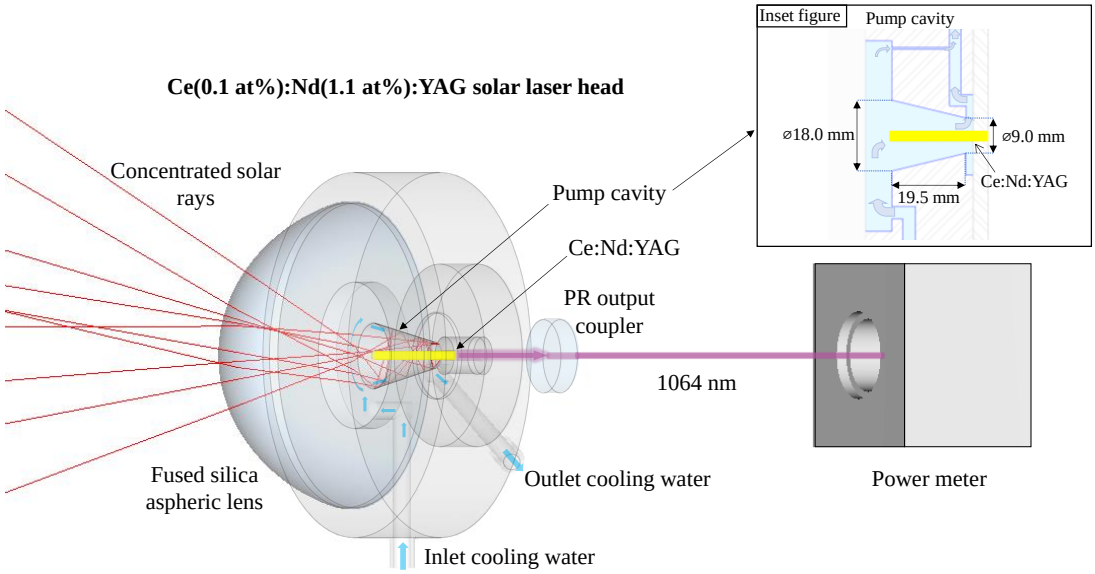

Figure 7.12 — Design of the laser head in end-side-pumping configuration, composed of the fused silica aspheric lens, the conical pump cavity, and the Ce:Nd:YAG laser rod actively cooled by water. Dimension of the pumping cavity in the inset figure.

The laser rod has one end-face with a high-reflection coating at the laser emission wavelength (99.9% @ 1064 nm), facing the output section of the aspheric lens, while the other end-face has an anti-reflection (AR) coating with less than 0.2% reflectivity (<0.2% @ 1064 nm). The active medium was acquired from Chengdu, Dongjun Laser Co., Ltd. (Chengdu, China). A partial-reflection (PR) coated output coupler for the 1064 nm laser emission with 95% reflectivity and a radius of curvature of -0.5 m was positioned 17 mm apart from the AR-coated end face of the laser rod. Solar-pumped laser emission could only be attained when all optical elements were correctly aligned. The solar laser power was then measured by the Thorlabs PM110D power meter.

7.2.2 Methods and measurements

7.2.2.1 Ce:Nd:YAG end-side-pumped solar laser experiment under a clear sky with different collection areas

The first set of solar-pumped laser measurements was conducted from 10:10 to 10:40 with an effective collection area of 0.152 m^2 and solar irradiance of 905-926 W/m^2; the second set from 11:30 to 11:50 with an effective collection area of 0.110 m^2 at 959-964 W/m^2; and the last set from 14:20 to 15:00 with an effective collection area of 0.075 m^2 at 972-974 W/m^2, as shown in Figure 7.10.

The data acquisition process consisted of the registration of the laser power as a function of the solar power at the focus for the three collection areas, as presented in Figure 7.13. The solar incoming power

was controlled by the shutter. Solar laser emission was firstly spotted with the shutter opened at 50%, 58% and 75% for 0.152 m^2, 0.110 m^2 and 0.075 m^2 collection areas, respectively, corresponding to 40.2 W, 36.1 W and 32.4 W minimum threshold solar powers at the focus. By fully opening the shutter, maximum solar laser output powers of 1.94 W, 1.24 W, and 0.43 W were respectively reached with solar powers at the focus of 82.87 W, 62.28 W, and 43.21 W, leading to laser slope efficiencies of 4.75%, 4.88%, and 4.03% for 0.152 m^2, 0.110 m^2 and 0.075 m^2 collection areas, respectively.

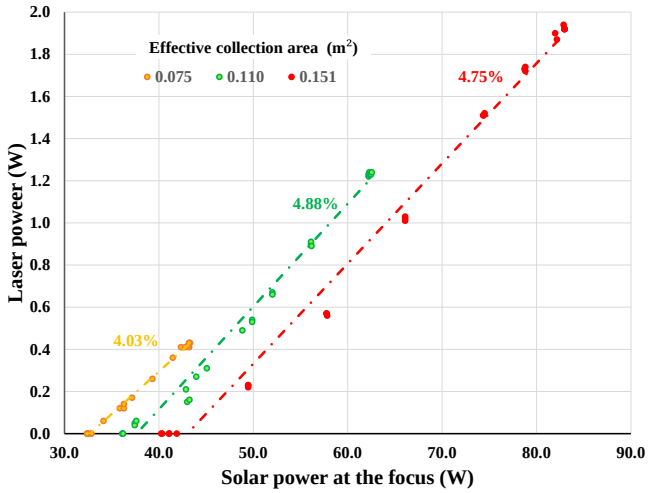

Figure 7.13 — Solar laser output power versus solar power at the focus and the respective slope efficiencies at effective collection areas of 0.151 m^2, 0.110 m^2, and 0.075 m^2.

7.2.2.2 First Ce:Nd:YAG end-side-pumped solar laser operation under a cloudy sky.

Figure 7.14 shows the solar irradiance values between 15:30 to 17:00 that were constantly changing, evidencing the cloud coverage of the sky. Thin clouds could momentarily increase the solar irradiance up to 700 W/m^2 (around 16:17 to 16:20), while thicker and darker clouds could reduce it to a minimum of only 1 W/m^2.

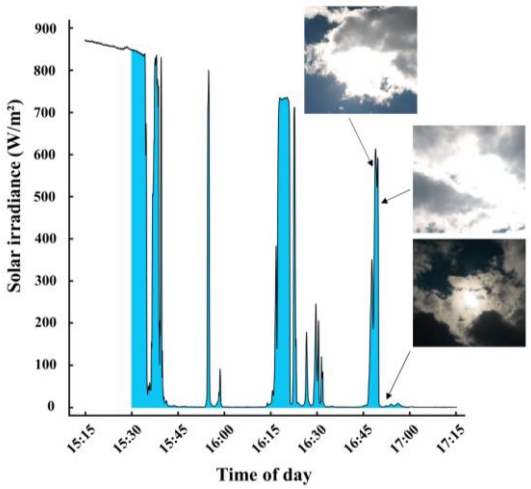

Figure 7.14 — The direct irradiance measured at the PROMES-CNRS on 16 September 2022 from 15:15 to 17:15 UTC time. The inset figures are photographs of the cloudy sky at certain periods.

Since the solar irradiance and the solar laser power were oscillating rapidly, reliable solar-pumped laser output power measurements were only considered when the solar irradiance values were steady for more

than two seconds. As shown in Figure 7.15, the solar laser output powers of 14.0 W, 11.0 W, 6.0 W, 5.5 W, and 1.0 W were successfully measured under solar irradiances of 211.6 W/m^2, 173.2 W/m^2, 111.6 W/m^2, 105.8 W/m^2 and 54.3 W/m^2, respectively.

The lowest incoming threshold powers at the focus of 34.48 W, 29.37 W, and 29.12 W were obtained with solar irradiances and opening of the shutter blades (in terms of percentage) of 160 W/m^2 at 56%, 212 W/m^2 at 36%, 150 W/m^2 at 41%, respectively. The slope efficiency calculated based on the receiving focal power was 7.71%.

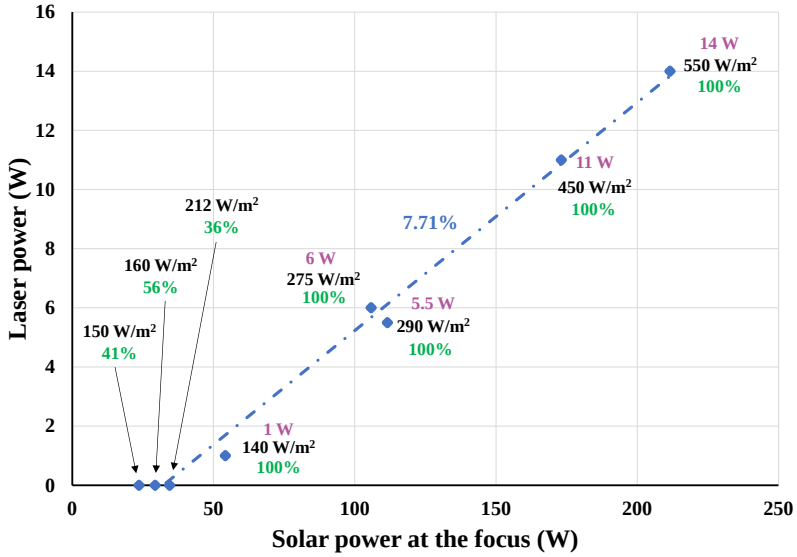

Figure 7.15 — Solar laser output power versus the solar power at the focus, and the respective slope efficiency, at an effective collection area of 0.652 m^2 during the cloudy period. The measured solar irradiance (black) and the shutter opening percentage (green) at each measured solar laser power (purple) instances are also displayed.

7.2.3 Discussion

The summary of the solar-pumped laser output performance with Ce:Nd:YAG active medium at different collector sizes are shown in Table 7-2.

Table 7-2 – Summary of the Ce:Nd:YAG end-pumped solar laser performance at different collection areas and periods of the day.

Day Status	Clear	Clear	Clear	Cloudy
Measurement period	10:30-11:10	11:30-12:40	14:00-15:00	16:20-17:40
Collection diameter	0.600 m	0.540 m	0.485 m	1.1 m
Effective collection area	0.152 m^2	0.110 m^2	0.075 m^2	0.652 m^2
Maximum solar power at the focus (Solar irradiance)	83 W (922 W/m^2)	62.7 W (960 W/m^2)	43.2 W (971 W/m^2)	221.6 W (550 W/m^2)
Maximum solar laser output power	1.92 W	1.24 W	0.42 W	14 W
Threshold solar power at the focus	40.2 W	36.1 W	**32.4 W**	**29.2 W**

Slope efficiency based on focal power	4.75%	4.88%	4.03%	**7.71%**
Solar-to-laser conversion efficiency at the focus	2.32%	1.98%	0.97%	6.32%
Solar laser collection efficiency	12.62 W/m^2	11.27 W/m^2	5.6 W/m^2	21.47 W/m^2

During the clear sky measurement period, the threshold solar power tends to be lower at a smaller collection area; the lowest threshold solar power at the focus was 32.4 W, achieved with the 0.075 m^2 collection area, while 40.2 W was found with 0.152 m^2. Both values were lower than the previous minimum threshold power at the focus of 66 W [53]. The slope efficiency at the focus changes with the collection area from 4.75% at 0.152 m^2 to 4.88% at 0.110 m^2, and then to 4.03% at 0.075 m^2. The solar-to-laser conversion efficiency and the solar laser collection efficiency decreased with the reduction of the concentrator's collection area.

The Ce:Nd:YAG solar-pumped laser performance measured under the cloudy sky revealed a substantial improvement in relation to the minimum threshold achieved with the clear sky. The slope efficiency from the focus of 7.71%, obtained with a large collection area of 0.625 m^2, is nearly twice the value of 4.03% under the clear sky with a small collection area of 0.075 m^2. The minimum threshold power at the focus was also reduced from 32.4 W with a clear sky to 29.2 W under the cloudy sky. The solar-to-laser conversion efficiency had also shown a notable improvement, from 2.32% with a clear sky to 6.32% with a cloudy sky, representing a threefold increase; while the solar laser collection efficiency had nearly doubled, from 12.62 W/m^2 to 21.47 W/m^2.

According to Bartlett et al. [168], the cloud interaction with the Sun increases light scattering. This helps in spreading the concentrated solar radiation along the active medium and pump cavity, changing the thermal lensing and, consequently, the laser output power. Moreover, the study of Andrews et al. [169] and Bird et al. [170] showed the influence of cloud thickness on solar spectral intensity. The solar intensity suffers a small loss in the UV to the middle of the visible light, in the range of 0.1 µm to 0.5 µm, but it reduces by half from 0.5 µm to 1.4 µm, while the IR waveband tends to be completely removed with a passage of a cloud. The removal of the IR waveband is a beneficial factor for the reduction of the amount of heat load in the laser head, lessening the thermal lensing effect in the active medium and, consequently, improving the laser output performance.

Although cloudy days are usually a disadvantage in the performance of solar systems, such as in photovoltaics technology, this work showed how beneficial the presence of clouds can be, to a certain extent, in the Ce:Nd:YAG solar-pumped laser performance. Indeed, the use of cloud forecasting technology in sky imagery [171-181], satellite imagery [174, 182, 183], and through machine learning [184], could help maintain a constant solar laser output by anticipating the potential reduction of solar irradiance with a passing cloud. From that, the solar input power could be compensated accordingly through the automatization of the shutter.

Table 7-3 compares the progress of the current solar-pumped laser performance with minimum threshold solar power with that of the previous Ce:Nd:YAG single-rod solar laser, regarding the threshold at

the focus, the slope efficiency, the solar-to-laser power conversion and the solar laser collection efficiencies.

Table 7-3 — Comparison of progress in Ce:Nd:YAG solar laser efficiency.

Parameters	Garcia et al. 2022 [53]	This work			
Sky status	Clear	Clear	Improvement (times)	**Cloudy**	Improvement (times)
Date	June 2022 (Summer)	September 2022 (Summer)		September 2022 (Summer)	
Primary concentrator	Parabolic mirror (NOVA)	Parabolic mirror (PROMES-CNRS)		Parabolic mirror (PROMES-CNRS)	
Total reflectivity of the collection system	75%	59%		59%	
Effective collection area	0.293 m^2	0.075 m^2		0.652 m^2	
Tracking method	Via heliostat	Via heliostat		Via heliostat	
Active medium Pumping method	Ce:Nd:YAG End-side-pump	Ce:Nd:YAG End-side-pump		Ce:Nd:YAG End-side-pump	
Laser rod dimensions	Ø2.5 mm×25 mm	Ø2.5 mm×25 mm		Ø2.5 mm × 25 mm	
Solar irradiance	~850 W/m^2	916-927 W/m^2		Varied	
Maximum solar power at the focus	186.3 W	43.2 W		221.6 W (at 550 W/m^2)	
Maximum laser power	11.2 W	0.42 W		14 W (at 550 W/m^2)	
Threshold power at the focus	66 W	32.4 W	**2.03**	29.2 W	**2.26**
Slope efficiency from the focus	9.06%	4.03%	0.44	7.71%	0.86
Solar-to-laser conversion efficiency at the focus	3.37%	0.97%	0.10	6.32%	0.68
Solar collection efficiency	38.22 W/m^2	5.57 W/m^2	0.15	21.47 W/m^2	0.56

The lasing conditions varied between the NOVA and PROMES-CNRS solar facilities. At the NOVA facility, the parabolic mirror had an effective collection area of 0.293 m2, a focal length of 660 mm, a total reflectivity of 75%, and a focal size of approximately 8 mm full width at half maximum. These measurements were taken in June 2022, under clear skies with a solar irradiance of 850 W/m2. In contrast, the PROMES-CNRS MSSF parabolic mirror had a focal length of 850 mm, lower reflectivity of 59%, and a focal size of 16 mm in diameter [37].

The laser head used in this study did not operate at its full potential due to the enlarged focal spot which changes the distribution of the solar energy throughout conical cavity and consequently the active medium. Despite these challenges, the threshold power achieved with the PROMES-CNRS facility, which had an effective collection area of 0.075 m^2, was half of that achieved at the NOVA facility with a larger collection area of 0.293 m^2 [53]. In cloudy weather conditions, the threshold solar power was further reduced to 29.2 W while using a larger collection area of 0.652 m^2 compared to that of the NOVA facility. The slope efficiency from the focus was nearly halved from 9.06% at the NOVA facility to

4.75% at the PROMES-CNRS facility during clear weather. However, it increased to 7.71% with the removal of IR wavebands during cloudy weather.

7.3 High-quality laser beam with lower-order modes with Ce:Nd:YAG pumped by a small collection area

A simple TEM_{00} mode solar system with a Ce:Nd:YAG rod pumped through a heliostat-parabolic mirror system at PROMES-CNRS during 08 of September of 2022. A solar laser head was composed of a aspheric fused silica lens and a conical pump cavity, which coupled and redistributed the concentrated solar radiation from the focal zone of a parabolic mirror into the Ce:Nd:YAG laser rod (Figure 7.11 and Figure 7.12).

7.3.1 Materials

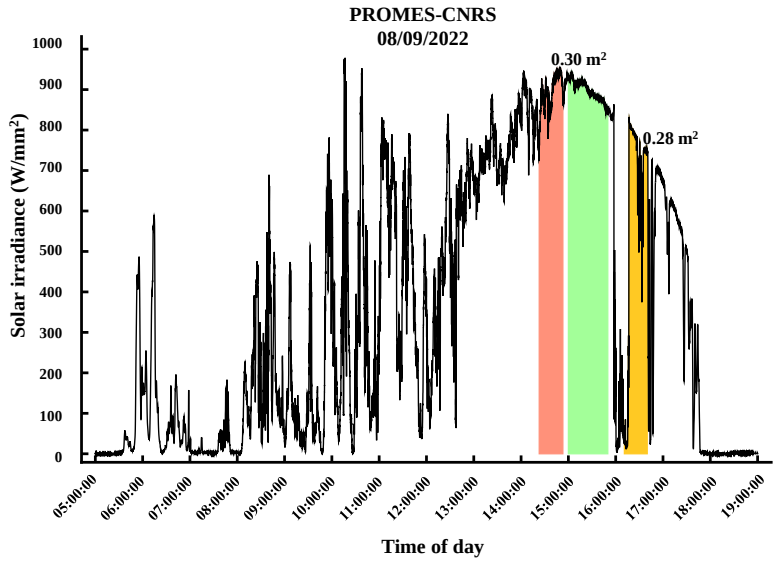

Figure 7.16 — The direct normal irradiance measured at the PROMES-CNRS on 08 September 2022 from 5:00 to 19:00 UTC time, and the experimental duration period for each parabolic mirror diameter size. Collector sizes 0.30 m^2 and 0.28 m^2 were used for the experiment. The measurement around 14:30 to 15:00 (red segment) were during a cloudy period.

The same material as in section 7.2.1 was used, and the laser head was pumped by the heliostat-parabolic concentrator. The experiment examined effective collection areas of 0.30 m^2 and 0.28 m^2. The optical materials used for TEM_{00} laser generation followed the design parameters optimized by Zemax® and LASCAD™ numerical methods, with a maximum solar irradiance of 1000 W/m^2.

Based on the numerically optimization of the solar laser system, the solar laser prototype was built and tested in the PROMES-CNRS heliostat–parabolic mirror system. The 2.5 mm diameter, 25 mm length Ce:Nd:YAG laser rod was HR1064 nm coated ($R \geq 99.8\%$@ 1064 nm) on the input end face and AR1064 nm coated ($R \leq 0.2\%$ @ 1064 nm) on the output end face. The resonator was designed to allow the displacement of the output mirror (from 25 mm to 1000 mm). By varying the rotation angle

of the shutter, different input solar power was measured with a Molectron PowerMax 500D. Output laser power was measured by a Thorlabs PM1100D power meter. Direct solar irradiance was measured simultaneously during lasing with a Kipp Zonen pyroheliometer. A CINOGY UV-NIR beam profiler CinCam CMOS, placed 40 mm away from the output coupler, was used for monitoring the laser beam profile during the experiments. The laser beam quality M^2 factors were measured according to ISO 11146-1 standard, by using the beam profiler. The output coupler of R=95% with RoC=−1 m, mounted L= 490 mm away from the AR1064 nm output face of the laser rod. A suitable resonator design for efficient energy conversion to the fundamental mode must maximize the overlap integral of the resonator fundamental mode and the pump profile while simultaneously utilizing the rod to apodized higher-order spatial modes [122]. This has been accomplished by the adoption of a long cavity length with concave end mirrors of large RoC [13]. Resonant cavity length (L) is a key parameter for achieving the optimum mode overlap. High-order mode laser output power levels can be achieved with relatively short L, where the fundamental mode volume poorly matches the pumped region. However, this comes at the expense of high M^2 factor beam quality values. By increasing the resonator length, high-order modes are suppressed, increasing the probability of low mode oscillation. Consequently, the beam brightness figure of merit increases, and high-quality laser beam can be achieved. Therefore, to obtain efficient extraction of low mode power, the laser should operate close to the edge of the optically stable region, where the fundamental mode size is more sensitive to thermal focus fluctuations.

7.3.2 Results

The study investigated the efficiency of the TEM_{00} solar laser by altering the solar power received at the focus, particularly during a cloudy period from 14:30 to 15:00. At the same time, the solar laser power and beam profiling were measured, and the solar power at the focus was calculated using the solar irradiance data with the shutter always fully open (in contrast to section 7.2.2.2, where the shutter was adjusted in sync with solar irradiance).

Figure 7.17 illustrates the laser output power at various solar power levels at the focus. The inset image depicts the formation process of TEM_{00} with increasing solar power. At 120.7 W solar power, the beam profile exhibited a combination of TEM_{10}, and at 140.3 W, the merging process became more apparent. Despite the constant beam size, the laser beam profile at 152.1 W pumping power displayed a form similar to the TEM_{00} mode. At the highest focal solar power of 169.0 W, a reduced size TEM_{00} laser beam of 1.3 W was observed. The slope efficiency achieved in this experiment was approximately 16.4%, the highest ever recorded for any solar pumped laser, with a threshold solar power at the focus of 113 W. The efficiency of the solar laser was considerably enhanced by filtering the solar wavelength.

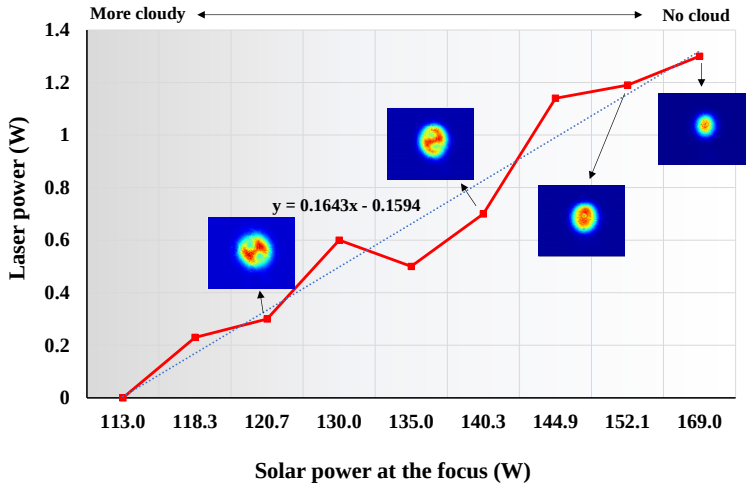

Figure 7.17 — Solar laser output power trend at various focal solar power and the associated laser beam profile during the cloudy sky period at 14:30 to 15:00 by using a 0.30 m^2 collection area.

In Figure 7.18, the solar laser beam profile is depicted at various levels of focal solar power under cloudless skies between 15:00 and 16:00. When the focal solar power was 157.0 W, a donut-shaped solar laser beam with a laser power of 1.07 W was produced. As the concentrated solar power increased, the laser power at the ring filled up and spread to the center, forming a TEM_{00}-shaped beam, as shown in the inset image of Figure 7.18 for focal solar powers of 159.4 W, 166.1 W, and 170.4 W. As the solar power at the focus increased further, the laser beam waist became smaller, particularly between 170.4 W and 180.1 W, and then 184 W. At a solar focal power of 184 W, the TEM_{00} laser mode was achieved with a solar laser power of 0.97 W.

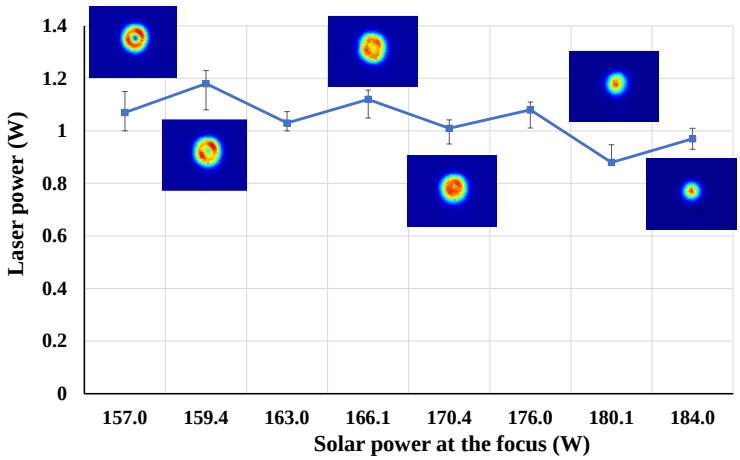

Figure 7.18 — Solar laser output power trend at various focal solar power and the associated laser beam profile during the cleared sky period at 15:00 to 16:00 by using a 0.30 m^2 collection area.

7.3.3 Discussion

To achieve high-efficiency and high-quality solar laser beams at a low order mode, the laser must operate near the edge of the optically stable region. This necessitates a long resonant cavity length, as it provides significant spatial overlap between the volume of lower-order modes and the pump mode

volume. Figure 7.18 demonstrates that only a few modes oscillated at a long cavity length. At an input focal solar power of 157 W, a doughnut-shaped solar laser beam with 1.07 W laser power was recorded, which corresponds to a collection efficiency of 3.8 W/m^2 and 16% of the maximum intensity at the center. The beam diameters and dark spot sizes [185] were also indicated in Figure 7.18 to characterize the radial intensity distribution of the doughnut-shaped beams. It is important to note that the angular adjustments of the output mirror did not change to achieve a 16% maximum intensity at the center, as was done in [157] to attain an 18% maximum intensity at the center. Low order modes have small beam diameter and divergence, resulting in a high-quality laser beam. The TEM_{01^*} doughnut-shaped mode is the second lowest order mode, having approximately 1.5 times smaller in diameter compared to the fundamental TEM_{00} mode, as confirmed the experimental measurements in Figure 7.19. The TEM_{00}-mode solar laser oscillation was obtained by increasing the input solar focal power, at the limit of thermally stable zone. Maximum TEM_{00}-mode solar laser power of 0.97 W was measured at solar focal power of 184.0 W.

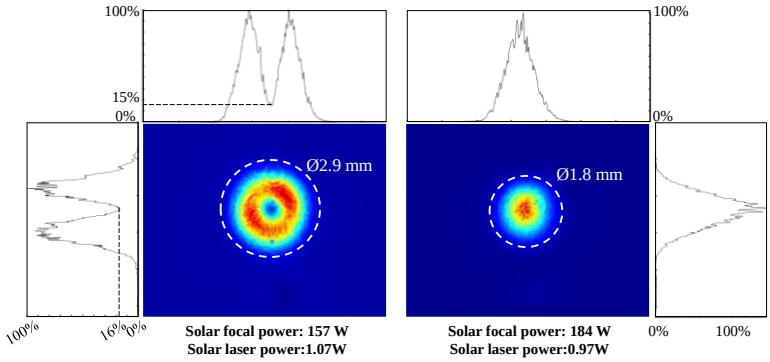

Figure 7.19 – Solar laser beam profile at two different solar focal power of 157 W (doughtnut shaped beam) and 184 W (TEM_{00} mode).

7.4 Uniform and non-uniform pumping effect on Ce:Nd:YAG side-pumped solar laser output performance

This study focuses on the influence of two secondary concentrators: a fused silica aspherical lens and a rectangular fused silica light guide; and consequent pump light distribution on the output performance of a Ce:Nd:YAG side-pumped solar laser. The solar laser head with the aspherical lens concentrated the incident pump light on the central region of the rod, producing the highest continuous-wave 1064 nm solar laser power of 19.6 W from the Ce:Nd:YAG medium. However, the non-uniformity of the absorbed pump profile produced by the aspherical lens led to the rod fracture because of the high thermal load, limiting the maximum laser power. Nevertheless, the solar laser head with the light guide uniformly spread the pump light along the laser rod, minimizing the thermal load issues and producing a maximum laser power of 17.4 W. Despite the slight decrease in laser power, the use of the light guide avoided the laser rod fracture, demonstrating its potential to scale to higher laser power. Therefore, the pumping distribution on the rod may play a fundamental role for Ce:Nd:YAG solar laser systems design.

7.4.1 Material and method

The MSSF of PROMES-CNRS was used for the solar laser experiments. The external annular area of the parabolic mirror was masked to avoid overheating the gain medium so that only 1.38 m in diameter of its central circular area was used. An effective solar collection area of 1.09 m^2 was calculated after discounting the shading effects of a shutter, X-Y-Z axis positioner, solar laser cavity and 0.3 m diameter central opening of the parabolic mirror. The shutter was used to control the input power. All the mirrors of the MSSF solar facility are back-surface silver-coated, and because of the iron impurities within the glass substrates and imperfections, only 59% of incoming solar radiation was focused to the focal zone. Direct solar irradiances between 1036 W/m^2 and 1061 W/m^2 were measured during the experiments in Odeillo (France), in February 2022.

Two solar laser heads were investigated using as secondary concentrator: (1) a fused silica aspherical lens, and (2) a fused silica light guide with rectangular cross-section, as shown in Figure 7.20.

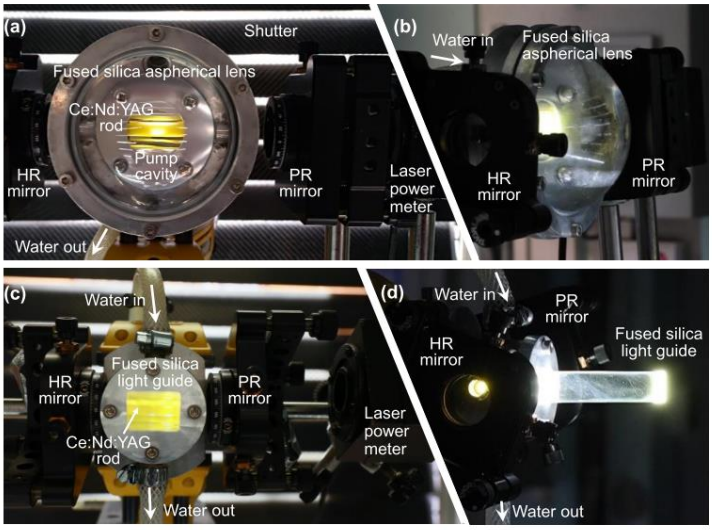

Figure 7.20 — Photographs of the front view (a,c) and side view (b,d) of the Ce:Nd:YAG solar laser heads using the fused silica aspherical lens (a,b) and the fused silica light guide (c,d). PR: partial reflection; HR: high reflection.

7.4.2 Result

The solar laser head with the fused silica aspherical lens produced a non-uniform absorbed pump profile within the rod, which is more concentrated on its central region, while the solar laser head with the rectangular fused silica light guide formed a uniform absorbed pump profile along the rod. The laser collection efficiency, solar-to-laser power conversion efficiency, and threshold pump power with the aspherical lens were 18 W/m^2, 1.7%, and 480 W, respectively, which were better than that with the light guide that had 16 W/m^2, 1.5%, and 577 W, respectively. However, the non-uniformity of the absorbed pump profile created by the aspherical lens increased the thermal load of the rod, creating hot pump spots. This led to the Ce:Nd:YAG rod fracture, limiting the maximum laser output power. At the expense of slightly lower solar laser power and efficiency, the use of light guide overcame this problem through the uniformity of the incident solar light on the rod. Therefore, the pumping distribution plays an

important role in the design of Ce:Nd:YAG solar laser systems, and the light guide technology may ensure successful solar laser power scaling.

7.5 Most efficient simultaneous solar laser emissions from three Ce:Nd:YAG rods within a single pump cavity

We report here, to the best of our knowledge, the most efficient simultaneous emissions of three continuous-wave 1064 nm solar laser beams. A fused silica aspheric lens was used to couple the concentrated solar radiation from the focal zone of a 0.4 m^2 effective collection area primary parabolic mirror into three 2.5 mm diameter, 25 mm length 0.1 at.% Ce:1.1 at.% Nd:YAG laser rods within a single conical pump cavity. For 356 W incoming solar power, 16.5 W continuous-wave total multimode solar laser power was measured, corresponding to 4.64% solar-to-laser conversion efficiency, 41.25 W/m^2 collection efficiency, and 7.64% slope efficiency, which are 1.24, 1.27, and 1.11 times, respectively, higher than previous records by pumping a single 4.5 mm diameter, 35 mm length 0.1 at.% Cr:1.0 at.% Nd:YAG ceramic laser rod. The three-rod Ce:Nd:YAG solar laser also provided 2.13, 2.25 and 1.50 times enhancements in solar-to-laser conversion efficiency, collection efficiency, and slope efficiency, respectively, as compared to previous records by pumping three 3.0 mm diameter, 25 mm length 1.0 at.% Nd:YAG rods within the same single conical pump cavity.

7.5.1 Materials and method

NOVA heliostat-parabolic mirror solar laser system was used. The solar power at the focus was limited by masking the external annular area of the 1.5 m diameter parabolic mirror, so that only 0.8 m diameter central circular area was utilized. 0.4 m^2 effective solar collection area was hence calculated by discounting the shadowing area of 0.1 m^2 caused by the laser head, its supporting mechanics, the X-Y-Z positioner, and the non-reflecting space between the two flat segments of the heliostat mirrors. For a typical solar irradiance of 890 W/m^2 in Lisbon and 0.4 m^2 collection area, about 265 W solar power was focused into a concentrated pump light spot with near-Gaussian distribution of 8 mm full width at half maximum.

Figure 7.21 a) presents the front image of the solar laser head composed of the large fused silica aspheric lens and the three 2.5 mm diameter, 25 mm length Ce:Nd:YAG rods mounted within the single conical pump cavity. Three small partial reflection (PR) 1064 nm output mirrors were accurately aligned with their corresponding laser rods, as shown in Figure 7.21b. Simultaneous cw 1064 nm solar laser emissions were produced. Accurate resonant cavity alignments were achieved by adjusting three output couplers individually by their respective positioners. For an accurate alignment in the focal zone, the laser head was mounted onto the X-Y-Z axes positioning system.

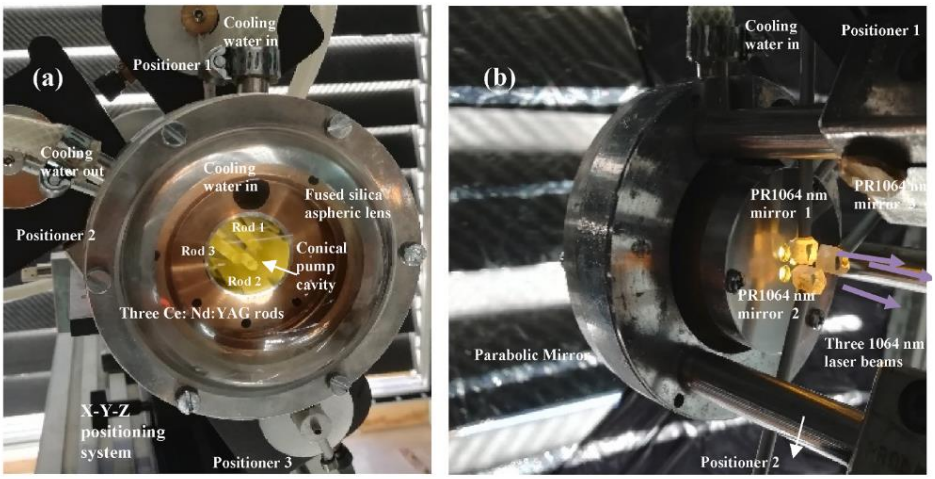

Figure 7.21 — (a) Front image showing the three-Ce:Nd:YAG rod solar laser head cooled by water. (b) Back image of the solar laser head with three small output couplers accurately aligned to their respective rods.

7.5.2 Results

The three-rod Ce: Nd:YAG solar laser was composed of the first-stage heliostat-parabolic mirror solar energy collection and concentration system, the second-stage fused silica aspheric lens and the third-stage conical-shaped pumping cavity, within which the three 2.5 mm diameter, 25 mm length Ce:Nd:YAG rods were efficiently pumped. Solar energy absorption by Ce^{3+}, Nd^{3+} ions and Ce^{3+} to Nd^{3+} energy transfer in Ce:Nd:YAG medium was analysed. Optimum optical pumping system design parameters were consequently found through Zemax® software. Optimum solar laser power and beam parameters were calculated through LASCAD™ numerical analysis. 16.5 W cw total solar laser power was measured, corresponding to 7.64% system slope efficiency and 41.25 W/m^2 solar laser collection efficiency. 4.64% solar-to-laser conversion efficiency was attained, which, to the best of our knowledge, which are 1.24, 1.27, and 1.11 times, respectively, higher than previous records. With the 2.5 mm diameter Ce:Nd:YAG rods, water cooling was more efficient, which avoided rod fracture issue that has hindered the efficiency improvement of Ce:Nd:YAG solar lasers. Most efficient and simultaneous cw solar laser emissions from the three 2.5 mm diameter Ce:Nd:YAG rods could, most hopefully, provide new solutions for multi-beam solar-powered lasers applications.

7.6 40 W Continuous wave Ce:Nd:YAG solar laser through a fused silica light guide

The solar laser power scaling potential of a side-pumped Ce:Nd:YAG solar laser through a rectangular fused silica light guide was investigated by using a 2 m diameter parabolic concentrator. The laser head was formed by the light guide and a V-shaped pump cavity to efficiently couple and redistribute the concentrated solar radiation from the parabolic mirror to a 4 mm diameter, 35 mm length Ce(0.1 at.%):Nd(1.1 at.%):YAG laser rod. The rectangular light guide ensured a homogeneous distribution of the solar radiation along the laser rod, allowing it to withstand highly concentrated solar energy. With

the full collection area of the parabolic mirror, the maximum continuous wave (cw) solar laser power of 40 W was measured. This, to the best of our knowledge, corresponds to the highest cw laser power obtained from a Ce:Nd:YAG medium pumped by solar radiation, representing an enhancement of two times over that of the previous side-pumped Ce:Nd:YAG solar laser and 1.19 times over the highest Cr:Nd:YAG solar laser power with a rectangular light-guide. This research proved that, with an appropriate pumping configuration, the Ce:Nd:YAG medium is very promising for scaling solar laser output power to a higher level.

7.6.1 Materials and method

The MSSF of PROMES-CNRS was used for the solar laser experiments. The external annular area of the parabolic mirror was masked to avoid overheating the gain medium so that only 2.0 m in diameter of its central circular area was used. The incoming solar power was regulated by a shutter with motorized blades. When the shutter was totally open, a 2.48 m^2 effective collection area was measured for the maximum diameter of the parabolic mirror. All the shadow effects in the MSSF caused by the space between the flat mirrors of the heliostat, the shutter blades, the laser head, and respective mechanical supports, have been accounted for.

A schematic design of the laser head is given in Figure 7.22. It is composed of a rectangular fused silica light guide and a two-dimensional (2D) V-shaped pump cavity, within which the Ce:Nd:YAG laser rod was fixed, being actively cooled by water.

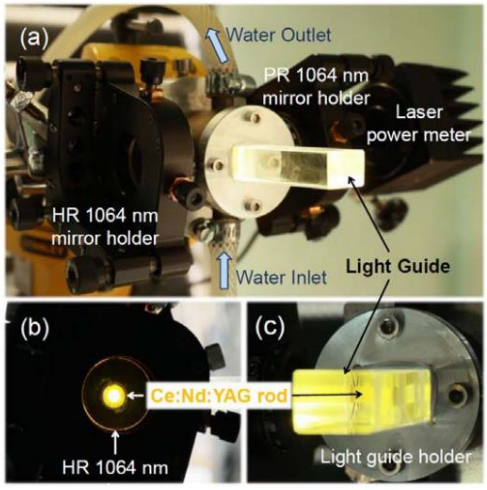

Figure 7.22 — Photograph of (a) the Ce:Nd:YAG solar-pumped laser head with the laser resonator and (b,c) the detailed view of the Ce:Nd:YAG laser medium in the experiments. HR, high reflection; PR, partial reflection.

7.6.2 Results

The potential of the Ce:Nd:YAG laser medium for solar laser power scaling was evaluated at the MSSF of PROMES-CNRS. The adoption of the side-pumping configuration with a rectangular light guide ensured a uniform pump light distribution along the laser rod. Thanks to this, the 4 mm diameter and 35 mm length Ce(0.1 at.%):Nd(1.1 at.%):YAG rod demonstrated a remarkable resistance to highly incoming solar powers, compared to the previous Ce:Nd:YAG solar lasers [145, 161, 163]. By using the

total incoming solar power of the MSSF, a 40 W cw solar laser power was registered. As far as we are aware, this was the highest laser power level reported from a solar powered Ce:Nd:YAG laser medium, being two times more than that from the most recent Ce:Nd:YAG laser rod side-pumped with an aspheric lens secondary concentrator at the MSSF [163]. It was also the highest side-pumped solar laser power through light guide [154, 186, 187]. Therefore, the side-pumping of the laser rod, with the help of the fused silica light homogenizer, proved to be a good solution for scaling the solar laser power with the Ce:Nd:YAG laser medium. In future work, either side-pumping or end-side-pumping configurations with lightguides could be employed for the simultaneous pumping of several Ce:Nd:YAG laser rods of smaller diameters within a common pumping cavity. The highly concentrated solar radiation could hence be evenly shared by the several laser rods, ensuring not only a substantial alleviation of the thermal lensing effects in solar-powered lasers [144], but also a significant rise in solar laser conversion efficiency. This may pave the way of Ce:Nd:YAG solar laser research into a new phase of development in terms of efficiency, laser beam quality, and stability at higher power levels.

8
CONCLUSION AND FUTURE RESEARCH

8.1 Conclusion

This doctoral dissertation offers an extensive exploration of novel models for RAC and ESFL, starting with their conceptual mathematical modelling and progressing through numerical simulations using Zemax® to ascertain their concentrated solar focal characteristics, as well as ANSYS™ for temperature calculation. Both models exhibit focal characteristics comparable to those of many practical results, but they also exhibit higher performance than what is currently available on the market. As a result, these concentrators could serve as a competitive alternative to the existing solar concentrator market.

In addition, it includes an assessment of solar-pumped lasers using Ce:Nd:YAG as the primary active medium, which was optimized through Zemax® and LASCAD™. The solar laser system underwent testing at both NOVA university and PROMES-CNRS, resulting in successful solar emission under cloudy conditions, the attainment of the lowest threshold power required for laser production, and TEM_{00} mode solar laser emission under a small collection area.

The main achievement addressed in this PhD thesis are summarized as follow:

1. **Advances of ring based solar concentrators:**

- In 2019, a peer-reviewed article was published introducing the concept of ring-based parabolic mirrors [39]. These mirrors offer a promising alternative to traditional parabolic concentrators by eliminating the shadow effect caused by the receiver. The 3D positioning of the ring-based parabolic mirrors was found to result in an extremely high temperature of 3755 K.
- An additional study [70] delved deeper into the modeling of RAC and included more parameters to explore its potential. Various configurations and shapes of RAC were analysed in this work to identify potential avenues for future research.

2. **Advances of curved shape Fresnel lens:**

- In 2022, a new methodology for the conceptual and mathematical modeling of shaped Fresnel lenses was published [42]. This innovative approach does not rely on the acceptance half angle or the edge-ray principle, which are commonly utilized in the Fresnel lens field. The analysis produced was rigorously compared to empirical research, revealing that the ESFL concentrates solar flux nearly twice as much as a flat Fresnel lens, while also addressing the issue of achromatic aberration.

3. **Advances in Ce:Nd:YAG solar pumped lasers**

- In 2022, a solar laser system was developed using a Ce(0.1 at%):Nd(1.1 at%):YAG rod, with dimensions of 2.5 mm diameter and 25 mm length, in a side-end pumped

configuration, achieving a new record-breaking solar threshold power of 88 W of incoming solar power at the NOVA facility [53]. This achievement surpassed the previous record of 200 W. The solar laser was able to utilize a 0.293 m^2 area of the NOVA parabolic mirror, achieving a collection efficiency of 38.22 W/m^2, which corresponds to a 4.5% conversion efficiency from solar energy to laser output.

- In September 2022, a research project supported by the SFERAIII European project (Grant Agreement N° 823802), SURPF1904040028, was conducted at PROMES-CNRS using the MSSF parabolic concentrator. The study measured a record solar threshold focal power of 32.4 W by limiting the parabolic mirror to 0.075 m^2. It was further reduced to 29.2 W when operated during a larger collection area of 0.293 m^2 under cloudy weather.
- Within this period, the solar-pumped Ce:Nd:YAG laser was measured to have attained the doughnut beam with the largest hole cavity and the smallest Gaussian single-mode.

8.2 Future visions:

The future developments of the work carried out are presented below, which are considered be of greater importance:

1. To expand the RAC and ESFL models, additional building variables and constraints will be incorporated, and all relevant numerical calculations related to these modifications will be explored and the findings will be published.
2. Create a standalone software for modeling a RAC and ESFL which will be available for free on Github.
3. Incorporate the RAC and ESFL concentrator as a built-in object in Zemax®, providing seamless integration with other optical components.
4. Constructing RAC and ESFL concentrators and utilizing either or both for energy generation and/or as a pumping medium for a solar laser.
5. The adoption of a newer numerical calculation software is recommended. The latest version of Zemax® has been acquired by ANSYS™. It also includes a more advanced and up-to-date laser cavity design and the newly added feature of photoluminescence simulation. Learning to use this software will result in a much more accurate solar pumped laser approximation and will eliminate the need for the outdated LASCAD® software.
6. Further investigation of the capabilities of Ce:Nd:YAG solar laser in a controlled environment is needed. This includes measuring solar laser emission under different cooling temperatures and selecting solar wavelengths using filters.
7. Achieve full automation of the solar laser generation process, which is crucial for bringing this technology to an industrial scale. At present, all solar laser experiments require at least two people to operate.

BIBLIOGRAPHY

1. Kalogirou, S.A., *Solar thermal collectors and applications.* Progress in Energy and Combustion Science, 2004. **30**(3): p. 231-295.
2. Islam, M.T., et al., *A comprehensive review of state-of-the-art concentrating solar power (CSP) technologies: Current status and research trends.* Renewable and Sustainable Energy Reviews, 2018. **91**: p. 987-1018.
3. Romero, M. and A. Steinfeld, *Concentrating solar thermal power and thermochemical fuels.* Energy & Environmental Science, 2012. **5**(11): p. 9234-9245.
4. Agrafiotis, C., et al., *Solar thermal reforming of methane feedstocks for hydrogen and syngas production—A review.* Renewable and Sustainable Energy Reviews, 2014. **29**: p. 656-682.
5. Datas, A., et al., *Ultra high temperature latent heat energy storage and thermophotovoltaic energy conversion.* Energy, 2016. **107**: p. 542-549.
6. Liu, G., J. Xu, and K. Wang, *Solar water evaporation by black photothermal sheets.* Nano Energy, 2017. **41**: p. 269-284.
7. Ahmed, F.E., R. Hashaikeh, and N. Hilal, *Solar powered desalination – Technology, energy and future outlook.* Desalination, 2019. **453**: p. 54-76.
8. Prieto, A., et al., *COOLFACADE: State-of-the-art review and evaluation of solar cooling technologies on their potential for façade integration.* Renewable and Sustainable Energy Reviews, 2019. **101**: p. 395-414.
9. Fend, T., et al., *Porous materials as open volumetric solar receivers: Experimental determination of thermophysical and heat transfer properties.* Energy, 2004. **29**(5): p. 823-833.
10. Funken, K.-H. and M. Becker, *Solar chemical engineering and solar materials research into the 21st century.* Renewable Energy, 2001. **24**(3): p. 469-474.
11. Fernández-González, D., et al., *Concentrated solar energy applications in materials science and metallurgy.* Solar Energy, 2018. **170**: p. 520-540.
12. Almeida, J., et al., *Highly efficient end-side-pumped Nd:YAG solar laser by a heliostat-parabolic mirror system.* Applied Optics, 2015. **54**(8): p. 1970-1977.
13. Liang, D., et al., *Solar-pumped Nd:YAG laser with 31.5 W/m2 multimode and 7.9 W/m2 TEM00-mode collection efficiencies.* Solar Energy Materials and Solar Cells, 2017. **159**: p. 435-439.
14. Lando, M., et al. *Solar-pumped solid state laser program*.

15. Vasile, M. and C.A. Maddock, *Design of a formation of solar pumped lasers for asteroid deflection.* Advances in Space Research, 2012. **50**(7): p. 891-905.
16. Yabe, T., et al., *Demonstrated fossil-fuel-free energy cycle using magnesium and laser.* Applied Physics Letters, 2006. **89**(26): p. 261107.
17. Takashi, Y., et al., *Demonstration of Solar-Pumped Laser-Induced Magnesium Production form Magnesium Oxide*, in *Magnesium Technology 2012*, S.N. Mathaudhu, et al., Editors. 2016, Springer International Publishing: Cham. p. 55-58.
18. International, A. *Standard Tables for Reference Solar Spectral Irradiance at Air Mass 1.5: Direct Normal and Hemispherical for a 37 Degree Tilted Surface*. 1992 21/12/2021]; Available from: https://www.nrel.gov/grid/solar-resource/spectra-am1.5.html.
19. Kalogirou, S.A., *Solar Energy Engineering: Processes and Systems*. 2013: Elsevier Science.
20. Rabl, A., *Active Solar Collectors and Their Applications*. 1985: Oxford University Press.
21. Kritchman, E.M., A.A. Friesem, and G. Yekutieli, *Highly concentrating Fresnel lenses.* Appl Opt, 1979. **18**(15): p. 2688-95.
22. Leutz, R., et al., *Design of a nonimaging Fresnel lens for solar concentrators.* Solar Energy, 1999. **65**(6): p. 379-387.
23. Yeh, N., *Analysis of spectrum distribution and optical losses under Fresnel lenses.* Renewable and Sustainable Energy Reviews, 2010. **14**(9): p. 2926-2935.
24. Akisawa, A., M. Hiramatsu, and K. Ozaki, *Design of dome-shaped non-imaging Fresnel lenses taking chromatic aberration into account.* Solar Energy, 2012. **86**(3): p. 877-885.
25. Languy, F. and S. Habraken, *Nonimaging achromatic shaped Fresnel lenses for ultrahigh solar concentration.* Opt Lett, 2013. **38**(10): p. 1730-2.
26. Leutz, R. and A. Suzuki, *Nonimaging Fresnel Lenses : Design and Performance of Solar Concentrators.* 2001.
27. Winston, R., *Principles of solar concentrators of a novel design.* Solar Energy, 1974. **16**(2): p. 89-95.
28. Cheng, Y., X.D. Zhang, and G.X. Zhang, *Design and machining of Fresnel solar concentrator surfaces.* International Journal of Precision Technology, 2013. **3**(4): p. 354-369.
29. Zheng, H., et al., *Design and experimental analysis of a cylindrical compound Fresnel solar concentrator.* Solar Energy, 2014. **107**: p. 26-37.
30. Viera-González, P.M., et al., *Mathematical Analysis of Nonimaging Fresnel Lenses Using Refractive and Total Internal Reflection Prisms for Sunlight Concentration.* Mathematical Problems in Engineering, 2018. **2018**: p. 4654795.
31. Yeh, N., *Illumination uniformity issue explored via two-stage solar concentrator system based on Fresnel lens and compound flat concentrator.* Energy, 2016. **95**: p. 542-549.
32. Yeh, N. and P. Yeh, *Analysis of point-focused, non-imaging Fresnel lenses' concentration profile and manufacture parameters.* Renewable Energy, 2016. **85**: p. 514-523.
33. Ma, X., et al., *Ideal shape of Fresnel lens for visible solar light concentration.* Opt Express, 2020. **28**(12): p. 18141-18149.
34. Yeh, N., *Optical geometry approach for elliptical Fresnel lens design and chromatic aberration.* Solar Energy Materials and Solar Cells, 2009. **93**(8): p. 1309-1317.
35. Kalogirou, S., *Solar energy engineering processes and systems.* 2014.
36. Vittitoe, C.N. and F. Biggs, *Six-gaussian representation of the angular-brightness distribution for solar radiation.* Solar Energy, 1981. **27**(6): p. 469-490.

37. Flamant, G., et al., *SOLAR PROCESSING OF MATERIALS: OPPORTUNITIES AND NEW FRONTIERS.* Solar Energy, 1999. **66**(2): p. 117-132.
38. Ferriere, A., et al., *Corrosion resistance of stainless steel coatings elaborated by solar cladding process.* Solar Energy, 2006. **80**(10): p. 1338-1343.
39. Garcia, D., et al., *A three-dimensional ring-array concentrator solar furnace.* Solar Energy, 2019. **193**: p. 915-928.
40. Wilbert, S., et al., *Measurement of Solar Radiance Profiles With the Sun and Aureole Measurement System.* Journal of Solar Energy Engineering, 2013. **135**(4).
41. Rabl, A. and P. Bendt, *Effect of Circumsolar Radiation on Performance of Focusing Collectors.* Journal of Solar Energy Engineering, 1982. **104**(3): p. 237-250.
42. Garcia, D., et al., *Elliptical-Shaped Fresnel Lens Design through Gaussian Source Distribution.* Energies, 2022. **15**(2).
43. Winter, C.J., R.L. Sizmann, and L.L. Vant-Hull, *Solar Power Plants*. 1991, Berlin, Heidelberg: Springer Berlin Heidelberg.
44. PROCÉDÉS, M.E.É.S.U. *MSSF horizontal - PROMES*. 2018 [cited 2019 7/3/2019]; Available from: https://www.promes.cnrs.fr/index.php?page=mssf-horizontal.
45. Hornung, T., M. Steiner, and P. Nitz, *Estimation of the influence of Fresnel lens temperature on energy generation of a concentrator photovoltaic system.* Solar Energy Materials and Solar Cells, 2012. **99**: p. 333-338.
46. N. Claytor, R., *Fresnel lens with apseheric grooves*, U.S. Patent, Editor. 1997, Fresnel Technologies Inc.: United State of America. p. 7.
47. *Zemax Manual*. Vol. 13. 2014, Radiant Zemax: Zemax.
48. López-Delgado, A., et al., *Dehydration of Gypsum Rock by Solar Energy: Preliminary Study.* Geomaterials, 2014. **4**: p. 82.
49. Sierra, C. and A. Vázquez, *NiAl coatings on carbon steel by self-propagating high-temperature synthesis assisted with concentrated solar energy: Mass influence on adherence and porosity.* Solar Energy Materials and Solar Cells - SOLAR ENERG MATER SOLAR CELLS, 2005. **86**: p. 33-42.
50. Sierra, C. and A. Vázquez, *NiAl coating on carbon steel with an intermediate Ni gradient layer.* Surface and Coatings Technology, 2006. **200**: p. 4383-4388.
51. Powell, R.C., *Physics of Solid-State Laser Materials*. 1998: Springer New York.
52. Zhao, B., et al., *Study of active medium for solar-pumped solid-state lasers.* Guangxue Xuebao/Acta Optica Sinica, 2007. **27**: p. 1797-1801.
53. Garcia, D., et al., *Ce:Nd:YAG Solar Laser with 4.5% Solar-to-Laser Conversion Efficiency.* Energies, 2022. **15**(14): p. 5292.
54. Liang, D., et al., *Most efficient simultaneous solar laser emissions from three Ce:Nd:YAG rods within a single pump cavity.* Solar Energy Materials and Solar Cells, 2022. **246**.
55. Tai, Y., et al., *Near-infrared quantum cutting of Ce^{3+}–Nd^{3+} co-doped $Y_3Al_5O_{12}$ crystal for crystalline silicon solar cells.* Journal of Photochemistry and Photobiology A: Chemistry, 2015. **303-304**: p. 80-85.
56. Welford, W.T. and R. Winston, *CHAPTER 4 - Nonimaging Concentrators: The Compound Parabolic Concentrator*, in *High Collection Nonimaging Optics*, W.T. Welford and R. Winston, Editors. 1989, Academic Press. p. 53-76.
57. *LASCAD 3.3.5 Manual*. 2007: LAS-CAD GmbH.

58. Kostanovskii, A.V., M.G. Zeodinov, and M.E. Kostanovskaya, *The determination of thermal conductivity and emissivity of graphite at high temperatures.* High Temperature, 2005. **43**(5): p. 793-795.
59. Price, J.S., et al., *Wide-angle planar microtracking for quasi-static microcell concentrating photovoltaics.* Nature Communications, 2015. **6**(1): p. 6223.
60. Coughenour, B.M., et al., *Dish-based high concentration PV system with Köhler optics.* Optics Express, 2014. **22**(S2): p. A211-A224.
61. El Majid, B., S. Motahhir, and A. El Ghzizal, *Parabolic bifacial solar panel with the cooling system: concept and challenges.* SN Applied Sciences, 2019. **1**(10): p. 1176.
62. Xie, W.T., et al., *Concentrated solar energy applications using Fresnel lenses: A review.* Renewable and Sustainable Energy Reviews, 2011. **15**(6): p. 2588-2606.
63. Cosby, R.M., *Solar concentration by curved-base Fresnel lenses*. 1977, Ball State Univ. Muncie, IN, United States.
64. Neill, M.J.O. and A.J. McDanal. *Manufacturing technology improvements for a line-focus concentrator module*. in *Conference Record of the Twenty Third IEEE Photovoltaic Specialists Conference - 1993 (Cat. No.93CH3283-9)*. 1993.
65. Ma, X., H. Zheng, and M. Tian, *Optimize the shape of curved-Fresnel lens to maximize its transmittance.* Solar Energy, 2016. **127**: p. 285-293.
66. *Fresneltech Brochure*. [cited 2021 June 17, 2021]; Fresnel lens Brochure]. Available from: https://www.fresneltech.com/fresnel-lenses.
67. Garcia-Segura, A., et al., *Durability studies of solar reflectors: A review.* Renewable & Sustainable Energy Reviews, 2016. **62**: p. 453-467.
68. He, C., et al., *An analytical flux density distribution model with a closed-form expression for a flat heliostat.* Applied Energy, 2019. **251**: p. 113310.
69. Lv, H., et al., *Non-uniform sizing of PV cells in the dense-array module to match the non-uniform illumination in dish-type CPV systems.* International Journal of Low-Carbon Technologies, 2020. **15**(4): p. 565-573.
70. Garcia, D., et al., *Analytical and numerical analysis of a ring-array concentrator.* International Journal of Energy Research, 2021. **45**(10): p. 15110-15123.
71. Yeh, P. and N. Yeh, *Design and analysis of solar-tracking 2D Fresnel lens-based two staged, spectrum-splitting solar concentrators.* Renewable Energy, 2018. **120**: p. 1-13.
72. Pan, J.-W., et al., *High concentration and homogenized Fresnel lens without secondary optics element.* Optics Communications, 2011. **284**(19): p. 4283-4288.
73. Zhao, Y., et al., *Development and performance studies of a novel portable solar cooker using a curved Fresnel lens concentrator.* Solar Energy, 2018. **174**: p. 263-272.
74. Shen, F. and W. Huang, *Study on the Optical Properties of the Point-Focus Fresnel System.* Sustainability, 2021. **13**(18).
75. Ferriere, A., G. Rogriguez, and J. Sobrino, *Flux Distribution Delivered by a Fresnel Lens Used for Concentrating Solar Energy.* Journal of Solar Energy Engineering, 2004. **126**: p. 654-660.
76. Gineste, J.M., G. Flamant, and G. Olalde, *Incident solar radiation data at Odeillo solar furnaces.* J. Phys. IV France, 1999. **09**(PR3): p. Pr3-623-Pr3-628.
77. Liang, K., et al., *Design and test of an annular fresnel solar concentrator to obtain a high-concentration solar energy flux.* Energy, 2021. **214**: p. 118947.

78. Leutz, R., et al., *Shaped nonimaging Fresnel lenses.* Journal of Optics A: Pure and Applied Optics, 2000. **2**(2): p. 112-116.
79. Nelson, D.T., D.L. Evans, and R.K. Bansal, *Linear Fresnel Lens Concentrators.* Solar Energy, 1975. **17**(5): p. 285-289.
80. An, W., et al., *Finite element method for radiative heat transfer in absorbing and anisotropic scattering media.* Journal of Quantitative Spectroscopy & Radiative Transfer, 2005. **96**(3-4): p. 409-422.
81. Li, B., et al., *Numerical and experimental study on improving temperature uniformity of solar furnaces for materials processing.* Solar Energy, 2015. **115**: p. 95-108.
82. Rinker, G., L. Solomon, and S.G. Qiu, *Optimal placement of radiation shields in the displacer of a Stirling engine.* Applied Thermal Engineering, 2018. **144**: p. 65-70.
83. Abbott, D., *Keeping the Energy Debate Clean: How Do We Supply the World's Energy Needs?* Proceedings of the IEEE, 2010. **98**(1): p. 42-66.
84. Katsuaki, T., *A Review of Ultrahigh Efficiency III-V Semiconductor Compound Solar Cells: Multijunction Tandem, Lower Dimensional, Photonic Up/Down Conversion and Plasmonic Nanometallic Structures.* Energies, 2009. **2**.
85. Parida, B., S. Iniyan, and R. Goic, *A review of solar photovoltaic technologies.* Renewable and Sustainable Energy Reviews, 2011. **15**(3): p. 1625-1636.
86. Chong, K.-K., et al., *Design and development in optics of concentrator photovoltaic system.* Renewable and Sustainable Energy Reviews, 2013. **19**: p. 598-612.
87. Rumyantsev, V.D., *Solar concentrator modules with silicone-on-glass Fresnel lens panels and multijunction cells.* Optics Express, 2010. **18**(S1): p. A17-A24.
88. Hafez, A.Z., et al., *Solar parabolic dish Stirling engine system design, simulation, and thermal analysis.* Energy Conversion and Management, 2016. **126**: p. 60-75.
89. Hachem, H., et al., *Technological challenges and optimization efforts of the Stirling machine: A review.* Energy Conversion and Management, 2018. **171**: p. 1365-1387.
90. Fernandez, A.G., et al., *Thermal characterization of HITEC molten salt for energy storage in solar linear concentrated technology.* Journal of Thermal Analysis and Calorimetry, 2015. **122**(1): p. 3-9.
91. Pelay, U., et al., *Thermal energy storage systems for concentrated solar power plants.* Renewable & Sustainable Energy Reviews, 2017. **79**: p. 82-100.
92. Gupta, M.K., et al., *Thermodynamic performance evaluation of solar and other thermal power generation systems: A review.* Renewable & Sustainable Energy Reviews, 2015. **50**: p. 567-582.
93. Schrader, K.N.A., Ronald L., *A Thermo-Optic Propagation Modeling Capability*. 2014, Sandia National Laboratories: Albuquerque, New Mexico 87185-MS0406.
94. Reinalter, W., et al., *Detailed performance analysis of a 10 kW dish/Stirling system.* Journal of Solar Energy Engineering-Transactions of the Asme, 2008. **130**(1).
95. PROCÉDÉS, M.E.É.S.U. *Mega Watt Solar Furnace - PROMES*. 2019 [cited 2019 7/3/2019]; Available from: https://www.promes.cnrs.fr/index.php?page=mega-watt-solar-furnace.
96. PSA-CIEMAT, *BIANUUAL REPORT 2008-2009*. 2009.
97. Camacho-Lopez, T. *National Solar Thermal Test Facility*. 2019; Available from: https://energy.sandia.gov/energy/renewable-energy/solar-energy/csp-2/nsttf/.

98. Haueter, P., T. Seitz, and A. Steinfeld, *A new high-flux solar furnace for high-temperature thermochemical research.* Journal of Solar Energy Engineering-Transactions of the Asme, 1999. **121**(1): p. 77-80.
99. Lovegrove, K., G. Burgess, and J. Pye, *A new 500 m(2) paraboloidal dish solar concentrator.* Solar Energy, 2011. **85**(4): p. 620-626.
100. Bianchini, A., et al., *Performance assessment of a solar parabolic dish for domestic use based on experimental measurements.* Renewable Energy, 2019. **133**: p. 382-392.
101. Pham, T.T., N.H. Vu, and S. Shin, *Novel Design of Primary Optical Elements Based on a Linear Fresnel Lens for Concentrator Photovoltaic Technology.* 2019. **12**(7): p. 1209.
102. A. Gomes, M., *The Pyreheliophoro*, INPI, Editor. 1899: France.
103. Meinel, A.B., *Applied solar energy. an introduction*. 1979, Reading: Addison-Wesley.
104. Vasylyev, V.P.T., Oleg G., *Expected Optical Performances of Novel Type Multi-element High-heat Solar Concentrators.* Conference Proceedings, 2003.
105. Mouzouris, M. and M.J. Brooks. *Nonimaging solar thermal collector for high temperature terrestrial and space applications*. in *SPIE Optical Engineering and Applications*. 2009. SPIE.
106. Tibúrcio, B.D., et al., *Improving solar-pumped laser efficiency by a ring-array concentrator.* Journal of Photonics for Energy, 2018. **8**(01).
107. Matos, R., et al., *High-efficiency solar laser pumping by a modified ring-array concentrator.* Optics Communications, 2018. **420**: p. 6-13.
108. Tibúrcio, B.D., et al., *Enhancing TEM00-Mode Solar Laser With Beam Merging and Ring-Array Concentrator.* Journal of Solar Energy Engineering, 2022. **144**(6).
109. Tibúrcio, B.D., et al., *Improving side-pumped solar lasers using ring-array concentrators.* International Journal of Sustainable Energy, 2022. **41**(7): p. 868-888.
110. Leutz, R. and A. Suzuki, *Nonimaging Fresnel lenses : design and performance of solar concentrators*. 2011, Berlin; London: Springer.
111. Kerridge-Johns, W.R. and M.J. Damzen, *Temperature effects on tunable cw Alexandrite lasers under diode end-pumping.* Optics Express, 2018. **26**(6): p. 7771-7785.
112. Welford, W.T. and R. Winston, *Optics of nonimaging concentrators. Light and solar energy*. 1978, United States: Academic Press Incorporated,New York, NY.
113. Goswami, D.Y., *Principles of Solar Engineering, Third Edition*. 2015: Taylor & Francis.
114. Ueda, J. and S. Tanabe, *(INVITED) Review of luminescent properties of Ce3+-doped garnet phosphors: New insight into the effect of crystal and electronic structure.* Optical Materials: X, 2019. **1**: p. 100018.
115. Samuel, P., et al., *Efficient energy transfer between Ce^{3+} and Nd^{3+} in cerium codoped Nd: YAG laser quality transparent ceramics.* Journal of Alloys and Compounds, 2010. **507**(2): p. 475-478.
116. Möller, S., et al., *Determination of vis and NIR quantum yields of Nd3+-activated garnets sensitized by Ce3+.* Journal of Luminescence, 2015. **158**: p. 365-370.
117. International, A., *Standard Tables for Reference Solar Spectral Irradiances: Direct Normal and Hemispherical on 37° Tilted Surface.*, in *ASTM G173 - 03(2012)*. 2012.
118. Payziyev, S., et al., *Luminescence sensitization properties of Ce: Nd: YAG materials for solar pumped lasers.* Optics Communications, 2021. **499**: p. 127283.
119. Yamaga, M., et al., *Energy transfer from Ce to Nd in Y3Al5O12 ceramics.* 2012. **9**(12): p. 2300-2303.

120. Koechner, W., *Solid-State Laser Engineering*. 2006: Springer.
121. Magni, V., *Resonators for solid-state lasers with large-volume fundamental mode and high alignment stability.* Applied Optics, 1986. **25**(1): p. 107-117.
122. Welford, D., D.M. Rines, and B.J. Dinerman, *Efficient TEM00-mode operation of a laser-diode side-pumped Nd:YAG laser.* Optics Letters, 1991. **16**(23): p. 1850-1852.
123. Liang, D. and J. Almeida, *Solar-Pumped TEM00 Mode Nd:YAG laser.* Opt Express, 2013. **21**(21): p. 25107-12.
124. Liang, D., et al., *Solar-pumped TEM_{00} mode Nd:YAG laser by a heliostat—Parabolic mirror system.* Solar Energy Materials and Solar Cells, 2015. **134**: p. 305-308.
125. Vistas, C.R., D. Liang, and J. Almeida, *Solar-pumped TEM_{00} mode laser simple design with a grooved Nd:YAG rod.* Solar Energy, 2015. **122**: p. 1325-1333.
126. Vistas, C.R., et al., *TEM_{00} mode Nd:YAG solar laser by side-pumping a grooved rod.* Optics Communications, 2016. **366**: p. 50-56.
127. Liang, D., et al., *High-efficiency solar-pumped TEM_{00}-mode Nd:YAG laser.* Solar Energy Materials and Solar Cells, 2016. **145**: p. 397-402.
128. Catela, M., et al., *Six-rod/six-beam concept for revitalizing TEM00 mode lamp-pumped lasers.* Optical Engineering, 2020. **59**(12).
129. Catela, M., et al., *Renovating electrical power-to-TEM_{00} mode laser power conversion efficiency with four-lamp/four-rod pumping scheme.* Journal of Modern Optics, 2021. **68**(17): p. 895-905.
130. Almeida, J., et al., *Numerical modeling of a four-rod pumping scheme for improving TEM00-mode solar laser performance.* Journal of Photonics for Energy, 2019. **9**(1): p. 018001.
131. Kiss, Z.J., H.R. Lewis, and R.C. Duncan, *Sun Pumped Continuous Optical Maser.* Applied Physics Letters, 1963. **2**(5): p. 93-94.
132. Young, C.G., *A Sun-Pumped cw One-Watt Laser.* Applied Optics, 1966. **5**(6): p. 993-997.
133. Arashi, H., et al., *A Solar-Pumped cw 18 W Nd:YAG Laser.* Japanese Journal of Applied Physics, 1984. **23**(8R): p. 1051.
134. Weksler, M. and J. Shwartz, *Solar-Pumped Solid-State Lasers.* Ieee Journal of Quantum Electronics, 1988. **24**(6): p. 1222-1228.
135. Krupkin, V., J. Kagan, and A. Yogev, *Nonimaging optics and solar laser pumping at the Weizmann Institute*. SPIE's 1993 International Symposium on Optics, Imaging, and Instrumentation. Vol. 2016. 1993: SPIE.
136. Lando, M., et al., *A solar-pumped Nd:YAG laser in the high collection efficiency regime.* Optics Communications, 2003. **222**(1-6): p. 371-381.
137. Yabe, T., et al., *High-efficiency and economical solar-energy-pumped laser with Fresnel lens and chromium codoped laser medium.* Applied Physics Letters, 2007. **90**(26): p. 261120.
138. Liang, D. and J. Almeida, *Highly efficient solar-pumped Nd:YAG laser.* Optics Express, 2011. **19**(27): p. 26399-26405.
139. Dinh, T.H., et al., *120 watt continuous wave solar-pumped laser with a liquid light-guide lens and an Nd:YAG rod.* Optics Letters, 2012. **37**(13): p. 2670-2672.
140. Xu, P., et al., *High-efficiency solar-pumped laser with a grooved Nd:YAG rod.* Applied Optics, 2014. **53**(18): p. 3941-3944.

141. Guan, Z., et al., *32.1 W/m² continuous wave solar-pumped laser with a bonding Nd:YAG/YAG rod and a Fresnel lens.* Optics & Laser Technology, 2018. **107**: p. 158-161.
142. Liang, D., et al., *Solar-pumped Cr:Nd:YAG ceramic laser with 6.7% slope efficiency.* Solar Energy Materials and Solar Cells, 2018. **185**: p. 75-79.
143. Liang, D., et al., *Side-pumped continuous-wave Nd:YAG solar laser with 5.4% slope efficiency.* Solar Energy Materials and Solar Cells, 2019. **192**: p. 147-153.
144. Liang, D., et al., *Simultaneous solar laser emissions from three Nd:YAG rods within a single pump cavity.* Solar Energy, 2020. **199**: p. 192-197.
145. Vistas, C., et al., *Ce:Nd:YAG side-pumped solar laser.* Journal of Photonics for Energy, 2021. **11**(1): p. 018001.
146. Mordechai, L., et al. *Solar-pumped solid state laser program*. in *Proc.SPIE*. 1997.
147. Abdel-Hadi, Y.A., *Space-based solar laser system simulation to transfer power onto the earth.* NRIAG Journal of Astronomy and Geophysics, 2020. **9**(1): p. 558-562.
148. *The Global Goals. Goal 9: Industry, Innovation and Infrastructure.* [The Global Goals. Goal 9: Industry, Innovation and Infrastructure.] [cited 2022 1-4]; Available from: https://www.globalgoals.org/goals/9industry-innovation-and-infrastructure/.
149. Motohiro, T., et al., *Concept of the solar-pumped laser-photovoltaics combined system and its application to laser beam power feeding to electric vehicles.* Japanese Journal of Applied Physics, 2017. **56**(8S2): p. 08MA07.
150. Yabe, T., et al., *100 W-class solar pumped laser for sustainable magnesium-hydrogen energy cycle.* Journal of Applied Physics, 2008. **104**(8).
151. Guan, Z., et al., *Low threshold and high efficiency solar-pumped laser with Fresnel lens and a grooved Nd:YAG rod*. 2016. 1001609.
152. Lando, M., et al., *Visible solar-pumped lasers.* Optical Materials, 1999. **13**(1): p. 111-115.
153. Almeida, J., et al., *A 40 W cw Nd:YAG solar laser pumped through a heliostat: a parabolic mirror system.* Laser Physics, 2013. **23**(6).
154. Almeida, J., et al., *5.5 W continuous-wave TEM00-mode Nd:YAG solar laser by a light-guide/2V-shaped pump cavity.* Applied Physics B, 2015. **121**(4): p. 473-482.
155. Liang, D., J. Almeida, and C.R. Vistas, *25 W/m2 collection efficiency solar-pumped Nd:YAG laser by a heliostat-parabolic mirror system.* Applied Optics, 2016. **55**(27): p. 7712-7717.
156. Zhe, G., et al., *5.04% system slope efficiency solar-pumped Nd:YAG laser by a heliostat–parabolic mirror system.* Journal of Photonics for Energy, 2018. **8**(2): p. 027501.
157. Vistas, C.R., et al., *A doughnut-shaped Nd:YAG solar laser beam with 4.5 W/m² collection efficiency.* Solar Energy, 2019. **182**: p. 42-47.
158. Bouadjemine, R., et al., *Stable TEM_{00}-mode Nd:YAG solar laser operation by a twisted fused silica light-guide.* Optics & Laser Technology, 2017. **97**: p. 1-11.
159. Mehellou, S., et al., *Stable solar-pumped TEM00-mode 1064 nm laser emission by a monolithic fused silica twisted light guide.* Solar Energy, 2017. **155**: p. 1059-1071.
160. Payziyev, S., K. Makhmudov, and Y.A. Abdel-Hadi, *Simulation of a new solar Ce:Nd:YAG laser system.* Optik, 2018. **156**: p. 891-895.
161. Vistas, C.R., et al., *Ce:Nd:YAG continuous-wave solar-pumped laser.* Optik, 2020. **207**.
162. Almeida, J., et al., *40 W Continuous Wave Ce:Nd:YAG Solar Laser through a Fused Silica Light Guide.* Energies, 2022. **15**(11).

163. Vistas, C.R., et al., *Uniform and Non-Uniform Pumping Effect on Ce:Nd:YAG Side-Pumped Solar Laser Output Performance*. Energies, 2022. **15**(10).
164. Cai, Z., et al., *Efficient 38.8 W/m2 solar pumped laser with a Ce:Nd:YAG crystal and a Fresnel lens.* Optics Express, 2023. **31**(2): p. 1340-1353.
165. Li, Y., et al., *Intense 1064nm emission by the efficient energy transfer from Ce3+ to Nd3+ in Ce/Nd co-doped YAG transparent ceramics.* Optical Materials, 2010. **32**(9): p. 1223-1226.
166. Villars, B., E. Steven Hill, and C.G. Durfee, *Design and development of a high-power LED-pumped Ce:Nd:YAG laser.* Optics Letters, 2015. **40**(13).
167. Payziyev, S. and A. Sherniyozov, *Influence of thermal population of lower laser levels on the performance of end-side-pumped Ce:Nd:YAG solar laser.* Journal of Photonics for Energy, 2022. **12**(04).
168. Bartlett, J.S., et al., *The spectral effects of clouds on solar irradiance.* Journal of Geophysical Research: Oceans, 1998. **103**(C13): p. 31017-31031.
169. Andrews, R.W. and J.M. Pearce, *The effect of spectral albedo on amorphous silicon and crystalline silicon solar photovoltaic device performance.* Solar Energy, 2013. **91**: p. 233-241.
170. Bird, R.E., et al., *Solar spectral measurements in the terrestrial environment.* Applied Optics, 1982. **21**(8): p. 1430-1436.
171. Logothetis, S.-A., et al., *Solar Irradiance Ramp Forecasting Based on All-Sky Imagers.* Energies, 2022. **15**(17).
172. Juncklaus Martins, B., et al., *Systematic review of nowcasting approaches for solar energy production based upon ground-based cloud imaging.* Solar Energy Advances, 2022. **2**.
173. Terrén-Serrano, G. and M. Martínez-Ramón, *Multi-layer wind velocity field visualization in infrared images of clouds for solar irradiance forecasting.* Applied Energy, 2021. **288**.
174. Rodríguez-Benítez, F.J., et al., *Assessment of new solar radiation nowcasting methods based on sky-camera and satellite imagery.* Applied Energy, 2021. **292**: p. 116838.
175. Wang, F., et al., *A minutely solar irradiance forecasting method based on real-time sky image-irradiance mapping model.* Energy Conversion and Management, 2020. **220**: p. 113075.
176. Espinosa-Gavira, M.J., et al., *Cloud motion estimation from small-scale irradiance sensor networks: General analysis and proposal of a new method.* Solar Energy, 2020. **202**: p. 276-293.
177. Cheng, H.-Y., *Cloud tracking using clusters of feature points for accurate solar irradiance nowcasting.* Renewable Energy, 2017. **104**: p. 281-289.
178. Tzoumanikas, P., et al., *The effect of clouds on surface solar irradiance, based on data from an all-sky imaging system.* Renewable Energy, 2016. **95**: p. 314-322.
179. Li, M., et al., *Quantitative evaluation of the impact of cloud transmittance and cloud velocity on the accuracy of short-term DNI forecasts.* Renewable Energy, 2016. **86**: p. 1362-1371.
180. Peng, Z., et al., *3D cloud detection and tracking system for solar forecast using multiple sky imagers.* Solar Energy, 2015. **118**: p. 496-519.
181. Cazorla, A., et al., *Multi-exposure adaptive threshold technique for cloud detection with sky imagers.* Solar Energy, 2015. **114**: p. 268-277.

182. Frincu, M., M. Penteliuc, and A. Spataru, *A Solar Radiation Forecast Platform Spanning over the Edge-Cloud Continuum.* Electronics, 2022. **11**(17).
183. Hammer, A., et al., *Short-term forecasting of solar radiation: a statistical approach using satellite data.* Solar Energy, 1999. **67**(1): p. 139-150.
184. Nespoli, A., et al., *Machine Learning techniques for solar irradiation nowcasting: Cloud type classification forecast through satellite data and imagery.* Applied Energy, 2022. **305**.
185. Yin, J., W. Gao, and Y. Zhu, *Chapter 3 - Generation of dark hollow beams and their applications*, in *Progress in Optics*, E. Wolf, Editor. 2003, Elsevier. p. 119-204.
186. Almeida, J., D. Liang, and E. Guillot, *Improvement in solar-pumped Nd:YAG laser beam brightness.* Optics & Laser Technology, 2012. **44**(7): p. 2115-2119.
187. Liang, D., J. Almeida, and E. Guillot, *Side-pumped continuous-wave Cr:Nd:YAG ceramic solar laser.* Applied Physics B, 2013. **111**(2): p. 305-311.
188. Garcia, D., et al., *Lowest-threshold solar laser operation under cloudy sky condition.* Renewable Energy, 2023.
189. Garcia, D., et al., *Efficient Production of Doughnut-Shaped Ce:Nd:YAG Solar Laser Beam.* Sustainability, 2023. **15**(18): p. 13761.
190. Catela, M., et al., *Stable emission of solar laser power under non-continuous solar tracking conditions.* Appl Opt, 2023.
191. Costa, H., et al., *Seven-Rod Pumping Concept for Highly Stable Solar Laser Emission.* Energies, 2022. **15**(23): p. 9140.
192. Catela, M., et al., *Highly Efficient Four-Rod Pumping Approach for the Most Stable Solar Laser Emission.* Micromachines, 2022. **13**(10): p. 1670.
193. Tibúrcio, B.D., et al., *Tracking error compensation capacity measurement of a dual-rod side-pumping solar laser.* Renewable Energy, 2022. **195**: p. 1253-1261.
194. Liang, D., et al., *Seven-Rod Pumping Approach for the Most Efficient Production of TEM00 Mode Solar Laser Power by a Fresnel Lens.* Journal of Solar Energy Engineering, 2021. **143**(6).
195. Catela, M., et al., *Doughnut-Shaped and Top Hat Solar Laser Beams Numerical Analysis.* Energies, 2021. **14**(21): p. 7102.
196. Costa, H., et al., *Zigzag Multirod Laser Beam Merging Approach for Brighter TEM_{00}-Mode Solar Laser Emission from a Megawatt Solar Furnace.* Energies, 2021. **14**(17): p. 5437.
197. Costa, H., et al., *Quasi-Gaussian Multibeam Solar Laser Station for a Megawatt Solar Furnace.* Journal of Solar Energy Research Updates, 2021. **8**: p. 11-20.
198. Vistas, C.R., et al., *32 W TEM_{00}-Mode Side-Pumped Solar Laser Design.* Applied Solar Energy, 2020. **56**(6): p. 449-457.
199. Almeida, J., et al., *Seven-rod pumping concept for simultaneous emission of seven TEM00-mode solar laser beams.* Journal of Photonics for Energy, 2020. **10**(3): p. 038001.
200. Costa, H., et al., *Design of a multibeam solar laser station for a megawatt solar furnace.* Optical Engineering, 2020. **59**(8): p. 086103.
201. Tibúrcio, B.D., et al., *Highly efficient side-pumped solar laser with enhanced tracking-error compensation capacity.* Optics Communications, 2020. **460**: p. 125156.
202. Tibúrcio, B.D., et al., *Dual-rod pumping concept for TEM_{00}-mode solar lasers.* Applied Optics, 2019. **58**(13): p. 3438-3446.

203. Tibúrcio, B., et al., *Dual-rod pumping approach for tracking error compensation in solar-pumped lasers.* Journal of Photonics for Energy, 2019. **9**(2): p. 028001.

A

ACHIEVEMENTS

Book:

Responsible for two book chapter.

- Chapter 2 Numerical tools for solid-state laser design
- Chapter 5 Primary solar concentrators

Book information:

Solar-Pumped Lasers: With Examples of Numerical Analysis of Solid-State Lasers

Authors: Dawei Liang, Joana Almeida, Cláudia Vistas, Bruno Tibúrcio, Dário Garcia

ISBN-13:9783031247842

Publisher: Springer International Publishing

Series: Green Energy and Technology

Edition description: 1st ed. 2023

Highlights:

- Featured content in Journal of Photonic for Energy 2019 with "Dual-rod pumping approach for tracking error compensation in solar-pumped lasers".
- Featured content in Journal of Photonic for Energy 2019 with "Numerical modeling of a four-rod pumping scheme for improving TEM_{00}-mode solar laser performance".
- Contract for two book chapters on "Solar-pumped lasers" with Springer 2020.
- Cover page in Journal of Photonics for Energy 2021 with "Seven-rod pumping concept for simultaneous emission of seven TEM_{00}-mode solar lasers beam".
- Featured in Laser focus world web site in https://www.laserfocusworld.com/lasers-sources/article/14283698/solar-pumping-converts-broadband-sunlight-into-efficient-laser-light with "A novel three Ce:Nd:YAG rod solar-pumped laser achieves 4.64% solar-to-laser energy conversion efficiency".
- Featured book coverage for "Challenge and Research Trends of Solar Concentrators" in 2022, ISBN 978-3-0365-6038-0, Doi.org/10.3390/books978-3-0365-6038-0.
- Reviewer for Energies.

Conferences:

- J. Almeida, D. Liang, B. D. Tiburcío, **D. Garcia**, R. Matos, C. R. Vistas, Recent Advances in Renewable Solar-Pumped Lasers, presented in Encontro com a Ciência e Tecnologia em Portugal, 2019.
- B. D. Tiburcío, D. Liang, J. Almeida, C. R. Vistas, **D. Garcia**, R. Matos, M. Catela, Recent Advances in Solar-Pumped Lasers, presented in NOVA science Day, 2019.
- H. Costa, J. Almeida, **D. Garcia**, B. D. Tiburcío, M. Catela, C. R. Vistas, Novel concepts in solar-pumped lasers, presented in Ciência 2020 – Encontro com a Ciência e Tecnologia em Portugal 2020.

Publications during the PhD thesis:

I. **Garcia, D.**, Liang, D., Almeida, J., Catela, M., Costa, H., Tibúrcio, B. D. & Vistas, C. R. (2023). Lowest-threshold solar laser operation under cloudy sky condition. *Renewable Energy*. DOI: 10.1016/j.renene.2023.03.124 [188]

II. **Garcia, D.**, Liang, D., Almeida, J., Catela, M., Costa, H., Tibúrcio, B. D. & Vistas, C. R. (2023). Efficient Production of Doughnut-Shaped Ce:Nd:YAG Solar Laser Beam. *Sustainability*. DOI: 10.3390/su151813761[189]

III. Catela, M., Liang, D., Vistas, C. R., **Garcia, D.**, Costa, H., Tibúrcio, B. D., & Almeida, J. (2023). Stable emission of solar laser power under non-continuous solar tracking conditions. *Apply Optics*. DOI:10.1364/AO.53.001856 [190]

IV. Costa, H., Liang, D., Almeida, J., Catela, M., **Garcia, D.**, Tibúrcio, B. D., & Vistas, C. R. (2022). Seven-Rod Pumping Concept for Highly Stable Solar Laser Emission. Energies, 15(23), 9140. DOI:10.3390/en15239140 [191]

V. Catela, M., Liang, D., Vistas, C. R., **Garcia, D.**, Costa, H., Tibúrcio, B. D., & Almeida, J. (2022). Highly Efficient Four-Rod Pumping Approach for the Most Stable Solar Laser Emission. Micromachines, 13(10), 1670. DOI:2072-666X/13/10/1670 [192]

VI. Tibúrcio, B.D., Liang, D., Almeida, J., **Garcia, D.**, Catela, M., Costa, H., Vistas, C.R.: Enhancing TEM_{00}-Mode Solar Laser With Beam Merging and Ring-Array Concentrator. Journal of Solar Energy Engineering 144(6) (2022). DOI:10.1115/1.4054666 [108]

VII. Tibúrcio, B. D., Liang, D., Almeida, J., **Garcia, D.**, Catela, M., Costa, H., & Vistas, C. R. (2022b). Tracking error compensation capacity measurement of a dual-rod side-pumping solar laser. *Renewable Energy*, *195*, 1253-1261. DOI:10.1016/j.renene.2022.06.114 [193]

VIII. Tibúrcio, B. D., Liang, D., Almeida, J., **Garcia, D.**, Catela, M., Costa, H., & Vistas, C. R. (2022a). Improving side-pumped solar lasers using ring-array concentrators. *International Journal of Sustainable Energy*, *41*(7), 868-888. DOI:10.1080/14786451.2021.1987435 [109]

IX. Liang, D., Vistas, C. R., **Garcia, D.**, Tibúrcio, B. D., Catela, M., Costa, H., Guillot, E., & Almeida, J. (2022). Most efficient simultaneous solar laser emissions from three Ce:Nd:YAG rods within a single pump cavity. *Solar Energy Materials and Solar Cells*, *246*. DOI:10.1016/j.solmat.2022.111921 [54]

X. **Garcia, D.**, Liang, D., Vistas, C. R., Costa, H., Catela, M., Tibúrcio, B. D., & Almeida, J. (2022). Ce:Nd:YAG Solar Laser with 4.5% Solar-to-Laser Conversion Efficiency. *Energies*, *15*(14), 5292. DOI:1996-1073/15/14/5292 [53]

XI. Almeida, J., Liang, D., **Garcia, D.**, Tibúrcio, B. D., Costa, H., Catela, M., Guillot, E., & Vistas, C. R. (2022). 40 W Continuous Wave Ce:Nd:YAG Solar Laser through a Fused Silica Light Guide. *Energies*, *15*(11). DOI:10.3390/en15113998 [162]

XII. Vistas, C. R., Liang, D., **Garcia, D.**, Catela, M., Tibúrcio, B. D., Costa, H., Guillot, E., & Almeida, J. (2022). Uniform and Non-Uniform Pumping Effect on Ce:Nd:YAG Side-Pumped Solar Laser Output Performance. *Energies*, *15*(10). DOI:10.3390/en15103577 [163]

XIII. **Garcia, D.**, Liang, D., Almeida, J., Tibúrcio, B. D., Costa, H., Catela, M., & Vistas, C. R. (2021). Analytical and numerical analysis of a ring-array concentrator. *International Journal of Energy Research*, *45*(10), 15110-15123. DOI:10.1002/er.6787 [42]

XIV. Liang, D., Almeida, J., Tibúrcio, B. D., Catela, M., **Garcia, D.**, Costa, H., & Vistas, C. R. (2021). Seven-Rod Pumping Approach for the Most Efficient Production of TEM00 Mode Solar Laser Power by a Fresnel Lens. *Journal of Solar Energy Engineering*, *143*(6). DOI:10.1115/1.4051223 [194]

XV. Vistas, C., Liang, D., Almeida, J., Tibúrcio, B., **Garcia, D.**, Catela, M., Costa, H., & Guillot, E. (2021). Ce:Nd:YAG side-pumped solar laser. *Journal of Photonics for Energy*, *11*(1), 018001. DOI:10.1117/1.JPE.11.018001 [145]

XVI. Catela, M., Liang, D., Vistas, C. R., **Garcia, D.**, Tibúrcio, B. D., Costa, H., & Almeida, J. (2021a). Doughnut-Shaped and Top Hat Solar Laser Beams Numerical Analysis. *Energies*, *14*(21), 7102. DOI:1996-1073/14/21/7102 [195]

XVII. Catela, M., Liang, D., Vistas, C. R., **Garcia, D.**, Tibúrcio, B. D., Costa, H., & Almeida, J. (2021b). Renovating electrical power-to-TEM_{00} mode laser power conversion efficiency with four-lamp/four-rod pumping scheme. *Journal of Modern Optics*, *68*(17), 895-905. DOI:10.1080/09500340.2021.1904155 [129]

XVIII. Costa, H., Almeida, J., Liang, D., Catela, M., **Garcia, D.**, Tibúrcio, B. D., & Vistas, C. R. (2021). Zigzag Multirod Laser Beam Merging Approach for Brighter TEM_{00}-Mode Solar Laser Emission from a Megawatt Solar Furnace. *Energies*, *14*(17), 5437. DOI:1996-1073/14/17/5437 [196]

XIX. **Garcia, D.**, Liang, D., Almeida, J., Tibúrcio, B. D., Costa, H., Catela, M., & Vistas, C. R. (2021). Analytical and numerical analysis of a ring-array concentrator. *International Journal of Energy Research*, *45*(10), 15110-15123. DOI:10.1002/er.6787 [70]

XX. Costa, H., Almeida, J., Liang, D., Tibúrcio, B. D., **Garcia, D.**, Catela, M., & Vistas, C. R. (2021). Quasi-Gaussian Multibeam Solar Laser Station for a Megawatt Solar Furnace. *Journal of Solar Energy Research Updates*, *8*, 11-20. DOI:10.31875/2410-2199.2021.08.02 [197]

XXI. Catela, M., Liang, D., Vistas, C. R., **Garcia, D.**, Tibúrcio, B. D., Costa, H., & Almeida, J. (2020). Six-rod/six-beam concept for revitalizing TEM_{00} mode lamp-pumped lasers. *Optical Engineering*, *59*(12). DOI:10.1117/1.Oe.59.12.126108 [128]

XXII. Vistas, C. R., Liang, D., **Garcia, D.**, Tibúrcio, B. D., & Almeida, J. (2020). 32 W TEM00-Mode Side-Pumped Solar Laser Design. *Applied Solar Energy*, *56*(6), 449-457. DOI:10.3103/S0003701X20060122 [198]

XXIII. Almeida, J., Liang, D., Costa, H., **Garcia, D.**, Tibúrcio, B. D., Catela, M., & Vistas, C. R. (2020). Seven-rod pumping concept for simultaneous emission of seven TEM00-mode solar laser beams. *Journal of Photonics for Energy*, *10*(3), 038001. DOI:10.1117/1.JPE.10.038001 [199]

XXIV. Costa, H., Almeida, J., Liang, D., **Garcia, D.**, Catela, M., Tibúrcio, B. D., & Vistas, C. R. (2020). Design of a multibeam solar laser station for a megawatt solar furnace. *Optical Engineering*, *59*(8), 086103. DOI:10.1117/1.OE.59.8.086103 [200]

XXV. Tibúrcio, B. D., Liang, D., Almeida, J., **Garcia, D.**, Vistas, C. R., & Morais, P. J. (2020). Highly efficient side-pumped solar laser with enhanced tracking-error compensation capacity. *Optics Communications*, *460*, 125156. DOI: 10.1016/j.optcom.2019.125156 [201]

XXVI. Liang, D., Almeida, J., **Garcia, D.**, Tibúrcio, B. D., Guillot, E., & Vistas, C. R. (2020). Simultaneous solar laser emissions from three Nd:YAG rods within a single pump cavity. *Solar Energy*, *199*, 192-197. DOI:/10.1016/j.solener.2020.02.027 [144]

XXVII. Vistas, C. R., Liang, D., **Garcia, D.**, Almeida, J., Tibúrcio, B. D., & Guillot, E. (2020). Ce:Nd:YAG continuous-wave solar-pumped laser. *Optik*, *207*. DOI:10.1016/j.ijleo.2019.163795 [161]

XXVIII. **Garcia, D.**, Liang, D., Tibúrcio, B. D., Almeida, J., & Vistas, C. R. (2019). A three-dimensional ring-array concentrator solar furnace. *Solar Energy*, *193*, 915-928. DOI:10.1016/j.solener.2019.10.016 [39]

XXIX. Tibúrcio, B. D., Liang, D., Almeida, J., **Garcia, D.**, & Vistas, C. R. (2019). Dual-rod pumping concept for TEM_{00}-mode solar lasers. *Applied Optics*, *58*(13), 3438-3446. DOI:10.1364/AO.58.003438 [202]

XXX. Vistas, C. R., Liang, D., Almeida, J., Tibúrcio, B. D., & **Garcia, D.** (2019). A doughnut-shaped Nd:YAG solar laser beam with 4.5 W/m2 collection efficiency. *Solar Energy*, *182*, 42-47. DOI:10.1016/j.solener.2019.02.030 [157]

XXXI. Tibúrcio, B., Liang, D., Almeida, J., **Garcia, D.**, & Vistas, C. R. (2019). Dual-rod pumping approach for tracking error compensation in solar-pumped lasers. *Journal of Photonics for Energy*, 9(2), 028001. DOI:10.1117/1.JPE.9.028001 [203]

XXXII. Liang, D., Vistas, C. R., Almeida, J., Tibúrcio, B. D., & **Garcia, D.** (2019). Side-pumped continuous-wave Nd:YAG solar laser with 5.4% slope efficiency. *Solar Energy Materials and Solar Cells*, *192*, 147-153. DOI:10.1016/j.solmat.2018.12.029 [143]

XXXIII. Almeida, J., Liang, D., Tibúrcio, B. D., **Garcia, D.**, & Vistas, C. R. (2019). Numerical modeling of a four-rod pumping scheme for improving TEM00-mode solar laser performance. *Journal of Photonics for Energy*, *9*(1), 018001. DOI:10.1117/1.JPE.9.018001 [130]

Publications under review and revision:

1. Hugo Costa, Dawei Liang*, Joana Almeida, Miguel Catela, **Dário Garcia**, Bruno D. Tibúrcio and Cláudia R. Vistas (2023). Seven-Grooved-Rod Side-Pumping Concept for Highly Efficient TEM_{00}-Mode Solar Laser Emission through Fresnel Lenses. *Photonics*. (Submitted).
2. Cláudia R. Vistas, Dawei Liang*, Miguel Catela, Hugo Costa, **Dário Garcia**, Bruno D. Tibúrcio and Joana Almeida (2023). Fresnel lens solar pumping approach for uniform and stable emission of six laser beams under tracking error condition. *Sustainability*. (Submitted).

2023

Dário Machado Garcia

Solar concentrators and solar-pumped lasers